

THE EFFECT OF OVERBURDEN AND HORIZONTAL CONFINING STRESS STATE ON CAVE MINING PROPAGATION

Nicholas Kyle Schoeman

A Dissertation presented for the degree of
Master of Structural Engineering



UNIVERSITEIT VAN PRETORIA
UNIVERSITY OF PRETORIA
YUNIBESITHI YA PRETORIA

Department of Civil Engineering
University of Pretoria
South Africa
September 2020

Abstract

Title: The Effect of Overburden and Horizontal Confining Stress State on Cave Mining Propagation
Author: Nicholas Schoeman
Supervisor: Professor E.P. Kearsley
Co-supervisor: Professor S.W. Jacobsz
Department: Civil Engineering
University: University of Pretoria
Degree: Master of Engineering (Structural Engineering)

The mechanism of cave mining propagation still requires a better understanding to be attained outside the industry-accepted Duplancic conceptual model. While this model suggests a continuous damage profile to be followed when an orebody is undercut in cave mining operations, the research of Cumming-Potvin (2018) describes an extended conceptual model to cave propagation which highlights a different failure mechanism whereby discontinuous damage occurs through the advancing events of parallel fracturing termed ‘fracture banding’.

In this dissertation, a physical modelling approach was adopted in an attempt to simulate the process of cave mining propagation at various stress states in order to observe the resulting failure mechanism. Four centrifuge tests were conducted utilising manufactured artificial rock material sample panels that were subjected to various ratios of horizontal to vertical stress. Before the applicability of this material to represent actual rock found in cave mines could be deemed adequate, a full characterisation of the properties of this artificial rock material was performed. The material testing included uniaxial compression strength tests, triaxial tests and Brazilian disc tests. These values were compared to typical corresponding parameters of various rock types in order to establish a suitable range of scale factors. Particle Image Velocimetry (PIV) was integrated into determining the critical extensional strain for the material which was used to establish a strain-based failure criteria for the artificial rock material using the model developed by Stacey (1981).

Once the artificial rock material was manufactured to replicate the characteristics rock by a standard deemed acceptable; a scale factor range of 12–9 291 was achieved using an absolute critical extensional strain value of 0.014 %. The following set of conditions were achieved when conducting physical modelling: negligible horizontal confinement using sand with zero overburden pressure, minimal horizontal confinement with zero overburden pressure, maximum horizontal confinement with minimal overburden pressure, and lastly maximum horizontal confinement with maximum overburden pressure following the same proportion in lateral earth pressure (K ratio) as the previous test.

Even though the results, with regard to the geometry of cave formation, in each of the tests were different; all four tests displayed an indication of ‘fracture banding’. In terms of the different geometries that had formed during cave progression, it was found that models with lower K ratios showed a higher development of the caving mechanism (at the same vertical stress), whilst models with higher K ratios suppresses this. Moreover, models conditioned with larger vertical stresses saw cave formation forming in a longer time period, but ultimately exhibited caves with a larger perimeter and area once the full undercut width had been reached. Total collapse occurred when the cave advanced vertically reaching the top surface of the sample through the formation of a ‘chimney’.

On further investigation of mapping strains in models throughout common time-steps, the results showed that regions of high minor principal strains from PIV analysis of cave propagation correlated well with identified fractures. In all test cases, cracks propagated at the point of the material matching or exceeding the absolute critical extensional strain value in either new cracks opening via cave-back progression or reaching pre-existing fractures. In most cases, regions of these tensile strain values were observed to have been bisected by visual cracks in models which suggest that the perceived behaviour of parallel fracturing is tensile in nature.

Declaration

I, the undersigned hereby declare that:

- I understand what plagiarism is and I am aware of the University's policy in this regard;
- The work contained in this thesis is my own original work;
- I did not refer to work of current or previous students, lecture notes, handbooks or any other study material without proper referencing;
- Where other people's work has been used this has been properly acknowledged and referenced;
- I have not allowed anyone to copy any part of my thesis;
- I have not previously in its entirety or in part submitted this thesis at any university for a degree.

Signature of student: 

Name of student: Nicholas Schoeman

Student number: 14074428

Date: 28 September 2020

Acknowledgements

First and foremost, I would like to thank My Lord and Saviour for strength, determination and perseverance during my postgraduate studies and for the privilege of studying at the University of Pretoria.

I would like to express my deepest gratitude to my supervisor Prof. Kearsley for her advice, commitment and financial support in helping me complete this dissertation. Her enthusiastic mindset and rich knowledge in the field of materials played a crucial role in aiding my experimental work in this investigation.

I would like thank my co-supervisor Prof. Jacobsz for his guidance, motivation and support during this investigation. His knowledge of physical modelling, geotechnical laboratory testing and problem-solving skills in the laboratory was essential in helping me to conduct the centrifuge experiments and material tests.

I would like express an immense appreciation to Prof Wesseloo for his financial support and opening the opportunity for research on the topic of Cave Mining. I would like to thank him for his guidance during his visits to the University of Pretoria and his advice on modelling rock in the centrifuge.

A special thanks to Tiaan Bosman for all of his hard work and assistance in the research project to provide fixes, reinforcement and modifications to the centrifuge test frame used in the experiments. His assistance in preparing samples before centrifuge spin-up was invaluable.

I would like to thank the postgraduate group of 2018 and 2019 for their help and support. A special thanks to Tiago Gaspar, Rick Vandoorn, Sophia Smit for the knowledge and advice in their areas of assistance. Also to Andre Broekman who wrote the programs to run and implement the Fly-by-Pi for controlling the actuators during the experiments.

Thanks to the Civil Laboratory staff of the University of Pretoria — Mr. Johan Scholtz and Mr. Jaco Botha for their assistance during laboratory testing, Mr. Jurie van Staden for his patience and guidance in helping me conduct many triaxial tests, Mr. Rikus Kock and Mr. Jan Vermaak for their assistance with setting up the electronics needed in the centrifuge, and Mrs. Vanessa Doman for her assistance in sample testing and procurement.

Last but certainly not least, I would like to express my appreciation and gratitude to my lovely partner Ashleigh as well as my family, for their patience, continual love and moral support during the years of postgraduate studies.

Contents

| | |
|--|------------|
| Abstract | ii |
| Declaration | iv |
| Acknowledgements | v |
| 1 Introduction | 1-1 |
| 1.1 Background | 1-1 |
| 1.2 Objectives of the Study | 1-2 |
| 1.3 Scope of the Study | 1-3 |
| 1.4 Methodology | 1-3 |
| 1.5 Outline of the Dissertation | 1-4 |
| 2 Literature Review | 2-1 |
| 2.1 In-Situ and Induced Stresses | 2-1 |
| 2.1.1 The Theory of Plate Tectonics | 2-1 |
| 2.1.2 World Stress Map Project | 2-1 |
| 2.1.3 Stress Orientations of Cave Mines around the World | 2-2 |
| 2.2 Rock Mass Modelling | 2-4 |
| 2.2.1 Scale Effects | 2-4 |
| 2.2.2 Hoek-Brown Strength Criterion | 2-6 |
| 2.2.3 The Hoek-Brown Model | 2-7 |
| 2.2.3.1 Strength of Intact Rock | 2-8 |
| 2.2.3.2 Tensile Failure | 2-9 |
| 2.2.3.3 The Geological Strength Index | 2-11 |
| 2.2.3.4 Estimation of rock deformation modulus | 2-13 |
| 2.2.3.5 The Disturbance factor | 2-14 |
| 2.2.4 Cohesion and Tension Softening | 2-15 |
| 2.2.5 The Mohr-Coulomb Model | 2-18 |
| 2.2.6 Modified Mohr-Coulomb Characterisation | 2-20 |
| 2.2.7 Extensional Strain Criterion | 2-22 |
| 2.2.8 Hard Brittle Rock Failure | 2-27 |
| 2.2.9 Typical Rock Properties | 2-28 |
| 2.2.10 Synthetic Rock | 2-33 |
| 2.3 Caving Mechanics | 2-44 |
| 2.3.1 Fundamentals of Caving Mining Propagation | 2-44 |
| 2.3.2 The Duplancic Conceptual Model | 2-48 |
| 2.4 Empirical Cave Propagation Assessment | 2-49 |
| 2.5 Physical Cave Propagation Assessment | 2-52 |
| 2.5.1 Two-Dimensional Scaled Models | 2-52 |
| 2.5.2 Centrifuge Modelling | 2-55 |
| 2.5.3 Cave Mine Site Observations | 2-60 |
| 2.6 Numerical Cave Propagation Assessment | 2-61 |
| 2.6.1 Two-Dimensional Elastic Models | 2-61 |
| 2.6.2 Two-Dimensional Plasticity Models | 2-63 |
| 2.7 Literature Review Summary | 2-68 |
| 3 Rock Material Characterisation | 3-1 |
| 3.1 Development Process for the Artificial Rock Mass | 3-1 |
| 3.2 Particle Size Distributions | 3-2 |
| 3.3 Mixing and Curing Procedure | 3-3 |
| 3.4 Uniaxial Compressive Strength Testing | 3-4 |
| 3.5 Triaxial Testing | 3-6 |
| 3.6 Brazilian Disc Tests | 3-8 |
| 3.6.1 Indirect Tensile Strength | 3-8 |
| 3.6.2 Particle Image Velocimetry | 3-9 |

| | | |
|----------|---|------------|
| 3.6.3 | Critical Extensional Strain | 3-11 |
| 3.7 | Summary of Material Properties | 3-17 |
| 3.8 | Mohr-Coulomb Characterisation | 3-18 |
| 3.9 | Hoek-Brown Characterisation | 3-22 |
| 3.10 | Artificial and Actual Rock-Mass Comparison | 3-25 |
| 4 | Physical Modelling | 4-1 |
| 4.1 | Background on the Geotechnical Centrifuge | 4-1 |
| 4.2 | Scaling Relationships | 4-1 |
| 4.3 | Centrifuge Test Setup and Equipment | 4-5 |
| 4.3.1 | Test Frame | 4-7 |
| 4.3.2 | Water Bladders | 4-8 |
| 4.3.3 | Brass Weights | 4-11 |
| 4.3.4 | Electric Actuators | 4-11 |
| 4.3.5 | Data Capturing Instrumentation | 4-12 |
| 4.4 | Centrifuge Test Procedure | 4-14 |
| 4.5 | Experimental Models | 4-15 |
| 4.5.1 | Centrifuge Model 1 | 4-15 |
| 4.5.2 | Centrifuge Model 2 | 4-16 |
| 4.5.3 | Centrifuge Model 3 | 4-17 |
| 4.5.4 | Centrifuge Model 4 | 4-18 |
| 4.6 | Centrifuge Model Summary | 4-19 |
| 5 | Experimental Results and Discussion | 5-1 |
| 5.1 | Data Capturing Procedure | 5-1 |
| 5.1.1 | Qualitative Image Analysis | 5-1 |
| 5.1.2 | Quantitative Image Analysis | 5-2 |
| 5.2 | Image Analysis Results | 5-3 |
| 5.2.1 | Cave Progression Test 1 | 5-4 |
| 5.2.2 | Cave Progression Test 2 | 5-7 |
| 5.2.3 | Cave Progression Test 3 | 5-10 |
| 5.2.4 | Cave Progression Test 4 | 5-13 |
| 5.3 | Discussion of Results | 5-16 |
| 5.3.1 | Cave Progression Geometry | 5-16 |
| 5.3.2 | Lateral Earth Pressure | 5-20 |
| 5.3.3 | Critical Extensional Strain in Caving Mechanics | 5-21 |
| 5.3.4 | Summary of Discussion | 5-34 |
| 6 | Conclusions and Recommendations | 6-1 |
| 6.1 | Conclusions | 6-1 |
| 6.1.1 | Applicability of the Artificial Rock Material | 6-1 |
| 6.1.2 | Cave Geometry and Lateral Earth Pressure | 6-2 |
| 6.1.3 | Critical Extensional Strain in Mapping Cave Propagation | 6-3 |
| 6.2 | Recommendations | 6-4 |
| A | Appendix A | A-1 |
| B | Appendix B | B-1 |
| C | Appendix C | C-1 |
| D | Appendix D | D-1 |

List of Tables

| | | |
|-----|---|------|
| 2.1 | A general summary various rock type properties (from various sources*) | 2-29 |
| 2.2 | Examples of critical extensional strain values for various rock types (Stacey, 1981). | 2-31 |
| 2.3 | Summary of authors replicating rock-mass for various applications in literature | 2-33 |
| 2.4 | Material properties for plaster of Paris samples (cast with 62.5 % water). | 2-36 |
| 2.5 | Chemical composition of fly ash and kaolin by percentage mass (Yahya et al., 2018) | 2-42 |
| 2.6 | Mix design of fly ash-based geo-polymer concrete (Yahya et al., 2018) | 2-42 |
| | | |
| 3.1 | Final Mix Design of Kaolin-Fly Ash Artificial Rock Material | 3-3 |
| 3.2 | Average Extensional Strain values for subset rows in Brazilian disc tests | 3-16 |
| 3.3 | Principal Stress values from triaxial testing results of the artificial rock material | 3-17 |
| 3.4 | Upper and lower bound Mohr-Coulomb parameters of the artificial rock material. | 3-19 |
| 3.5 | Summary of Hoek-Brown Parameters for peak and residual failure envelopes | 3-23 |
| | | |
| 4.1 | Scaling law parameters for the prototype and model | 4-4 |
| 4.2 | Comparison for the range of scale factors for various scaling relationships | 4-4 |
| 4.3 | Summary of horizontal, vertical stresses and K ratios for centrifuge models | 4-19 |

List of Figures

| | | |
|-------------|--|------|
| Figure 1.1 | Schematic of a typical block cave mine (Sainsbury, 2012). | 1-1 |
| Figure 2.1 | Distribution of both operating and planned block and panel cave mines, together with historic (closed) mines. Not included are sub-level caving operations (Brown, 2007). Note locations are not geographically accurate. | 2-2 |
| Figure 2.2 | Various types of faulting at the boundaries of the tectonic plates (Van der Pluijm and Marshak, 2004). | 2-3 |
| Figure 2.3 | Measured rock strength-scale effect including large size specimens of in-situ test (Pratt et al., 1972). | 2-5 |
| Figure 2.4 | Applicability of the Hoek-Brown empirical rock mass strength criterion at different scales (Li et al., 2008). | 2-6 |
| Figure 2.5 | Development of equivalent Mohr-Coulomb property estimates from a fit to the Hoek-Brown curve (Sainsbury, 2012). | 2-7 |
| Figure 2.6 | Dimensionless plot of triaxial test data for Carrara marble showing the use of the generalised Griffith theory for tensile failure and the Hoek-Brown criterion for shear failure (Hoek and Brown, 2019). | 2-10 |
| Figure 2.7 | Relationship between the ratio of $\frac{\sigma_{ci}}{ \sigma_i }$ and m_i (Hoek and Brown, 2019). | 2-11 |
| Figure 2.8 | Geological Strength Index (GSI) chart (Marinos et al., 2007). | 2-12 |
| Figure 2.9 | Comparison between field measurements and deformation modulus values predicted by several authors (Hoek and Brown, 2019). | 2-14 |
| Figure 2.10 | Plot of normalised in situ rock mass deformation modulus from China and Taiwan against Hoek and Diederich's Equation (2.13 and 2.14). Each data point represents the average of multiple tests at the same site in the same rock mass (Hoek and Diederichs, 2006). | 2-15 |
| Figure 2.11 | Idealised stress-strain curves representing different material behaviour used in numerical modelling (Sainsbury, 2012). | 2-16 |
| Figure 2.12 | Damage stages of a three-dimensional, strain-softening specimen (Pierce et al., 2006). | 2-17 |
| Figure 2.13 | Development of equivalent linear Mohr-Coulomb strength parameters based on a fit to the Hoek-Brown strength envelope (Sainsbury, 2012). | 2-18 |
| Figure 2.14 | Schematic diagram of the mobilisation of the strength components cohesion and friction (a) in the laboratory (b) around an underground opening; c_i and c_r and ϵ_c^P and ϵ_f^P represent the plastic strain components when the friction and cohesion strength components have reached ultimate values (Hajiabdolmajid et al., 2002). | 2-19 |
| Figure 2.15 | Modified Mohr-Coulomb criterion (Singh et al., 2011). | 2-21 |
| Figure 2.16 | Polyaxial failure data for Shirahama Sandstone and KTB Amphibolite with the adoption of Hoek-Brown strength criterion (Benz et al., 2008) and extension strain criterion (Wesseloo and Stacey, 2016). | 2-26 |
| Figure 2.17 | Mohr-circle representation of rock material passes through various structural stages when loaded in compression (Gramberg, 1965). | 2-27 |
| Figure 2.18 | Typical UCS stress-strain curves for three igneous rocks (adapted from Wawersik and Fairhurst (1970) as well as Siratovich et al. (2012)). | 2-29 |
| Figure 2.19 | Typical UCS stress-strain curves for three sedimentary rocks (adapted from Wawersik and Fairhurst (1970), Chuanliang et al. (2015) and Sygala et al. 2013)). | 2-30 |
| Figure 2.20 | Typical UCS stress-strain curves for three metamorphic rocks (adapted from Wawersik and Fairhurst (1970), Chen et al. (2016) and Rao et al. (2011)). | 2-30 |
| Figure 2.21 | Typical triaxial compression test stress-strain curves for sandstone (Li et al., 2018). | 2-31 |
| Figure 2.22 | Typical ranges of values for Poisson's ratio of various rock types (Vutukuri et al. (1974), Hatheway and Kiersch (1986) and Gercek (2007)). | 2-32 |
| Figure 2.23 | The structure of the plaster of Paris: (a) 50 % relative density and (b) 70 % relative density specimens (Vekinis et al., 1993). | 2-35 |
| Figure 2.24 | The PTFE cell used in the hydrostatic compression experiments (Vekinis et al., 1993). | 2-37 |
| Figure 2.25 | Load contraction curve for a specimen tested in uniaxial compression (lower curve) and in hydrostatic compression (upper curve) (Vekinis et al., 1993). | 2-37 |
| Figure 2.26 | Fracture initiation and hole collapse initiation stress and strain as a function of relative density (Vekinis et al., 1993). | 2-38 |
| Figure 2.27 | Micro-graphs for the uniaxial specimens (left) and biaxial specimens (right) (Vekinis et al., 1993). | 2-39 |

| | |
|---|------|
| Figure 2.28 (a) Fracture initiation, and (b) final collapse surfaces for plaster of Paris, for three relative densities (Vekinis et al., 1993). | 2-39 |
| Figure 2.29 Microscopic images of Kaolin (left) and Fly Ash (right) side-by-side (Yahya et al., 2018). Scale not specified. | 2-40 |
| Figure 2.30 Compressive strength of geopolymers with age (after Yahya et al., 2018). | 2-43 |
| Figure 2.31 Typical caving stress-paths representing stress and gravity caving mechanisms (Sainsbury, 2012). | 2-45 |
| Figure 2.32 Conceptual stress-state development around a propagating cave (adapted from Sainsbury, 2012). | 2-46 |
| Figure 2.33 The influential zones of the Duplancic model (Duplancic and Brady, 1999) | 2-48 |
| Figure 2.34 Empirical method for predicting caveability: Laubscher’s Stability Chart (Laubscher, 1994). | 2-50 |
| Figure 2.35 Empirical method for predicting caveability: Extended Mathews Stability Chart (Trueman and Mawdesley, 2003). | 2-51 |
| Figure 2.36 Model of caving simulated using the base friction technique (Baumgartner and Stimpson 1979). | 2-54 |
| Figure 2.37 Typical subsidence (cave-in) test to model sinkhole development (Nishida et al., 1988). | 2-55 |
| Figure 2.38 Parallel fractures ahead of the cave back and on the cave periphery — test 1 (left) and test 2 (right) (Cumming-Potvin et al., 2016a). | 2-57 |
| Figure 2.39 Parallel fractures ahead of the cave front and on the cave periphery — test 3 (left) and test 4 (right) (Cumming-Potvin et al., 2016a). | 2-58 |
| Figure 2.40 Parallel fractures ahead of the cave front and on the cave periphery — test 5 (left) and cave progression (test 3) (right) (Cumming-Potvin et al., 2016a). | 2-58 |
| Figure 2.41 Fractures lining up with the edges of pistons (solid red lines) and those that do not (dashed orange lines) (Cumming-Potvin et al., 2016a). | 2-59 |
| Figure 2.42 Centrifuge model stress distributions (adapted from Cumming-Potvin, 2018). | 2-59 |
| Figure 2.43 Parallel fractures in a circular zone around an active cave (Panek, 1981). | 2-60 |
| Figure 2.44 Impact of principal stress orientation in relation to an undercut as defined by two-dimensional numerical modelling (Palma and Agarwal, 1973). | 2-62 |
| Figure 2.45 Conceptual diagram of effect of principal stress direction and undercut footprint dimensions on cavability (after Sainsbury, 2012). | 2-63 |
| Figure 2.46 Development of two-dimensional numerical modelling approaches for cave propagation analysis (A) Model mesh (B) section through the mining geometry (C) simulated undercutting process (D) contours of resultant mobilized strength – the shaded area represents a fully softened or caved rock mass (Barla et al., 1980). | 2-64 |
| Figure 2.47 Methodology for the application of a continuum based numerical model for the prediction of onset of caving (Rech and Lorig, 1992) | 2-65 |
| Figure 2.48 Cave Propagation Factor at Northparkes Lift 1 Mine (Karzulovic and Flores 2003) | 2-67 |
| Figure 3.1 Particle size distributions for the raw material as well as artificial rock material. | 3-2 |
| Figure 3.2 Experimental setup for uniaxial compressive strength testing. | 3-4 |
| Figure 3.3 Uniaxial compressive strength repeatability tests for the artificial rock material. | 3-5 |
| Figure 3.4 Typical setup of a triaxial cell (Knappett and Craig, 2012). | 3-6 |
| Figure 3.5 Axial stress-strain plot of the artificial rock material for various confining pressures. | 3-7 |
| Figure 3.6 Tensile stress-displacements curves of the artificial rock material. | 3-9 |
| Figure 3.7 General overview of the PIV–DIC method (Stanier et al., 2016). | 3-10 |
| Figure 3.8 Linear elastic range of the artificial rock material. | 3-12 |
| Figure 3.9 Tensile strain-displacements curves of the artificial rock material. | 3-13 |
| Figure 3.10 Extensional Strains plotted from PIV row data for Brazilian disc tests 3 and 4. | 3-14 |
| Figure 3.11 Extensional Strains plotted from PIV row data for Brazilian disc tests 5 and 7. | 3-14 |
| Figure 3.12 Extensional Strains plotted from PIV row data for Brazilian disc tests 11 and 13. | 3-15 |
| Figure 3.13 BDT Test setup (left) and failed specimen indicating subsets (right). | 3-16 |
| Figure 3.14 Plot of peak strengths in s and t stress space for all triaxial tests. | 3-20 |
| Figure 3.15 Plot of residual strengths in s and t stress space for all triaxial tests. | 3-20 |
| Figure 3.16 Plot of peak strength Mohr circles with defined failure envelope. | 3-21 |
| Figure 3.17 Plot of residual strength Mohr circles with defined failure envelope. | 3-21 |
| Figure 3.18 Hoek-Brown failure envelope in principal stress space. | 3-24 |
| Figure 3.19 Hoek-Brown failure envelope for peak strength values in $\sigma_n - \tau$ stress space. | 3-24 |
| Figure 3.20 Hoek-Brown failure envelope for residual strength values in $\sigma_n - \tau$ stress space. | 3-25 |

| | | |
|-------------|---|------|
| Figure 3.21 | Visual comparison between the artificial rock material and shale in their intact and fragmented forms. | 3-26 |
| Figure 4.1 | The front of the test frame (left) and the back of the test frame (right). | 4-6 |
| Figure 4.2 | Water bladders housed within the test frame (left) and the test frame positioned on the centrifuge swing (right). | 4-6 |
| Figure 4.3 | Labelled schematic of the test frame used during centrifuge testing. | 4-7 |
| Figure 4.4 | The piping and water flow diagram for the test setup. | 4-9 |
| Figure 4.5 | Water piping system for supplying a static head to experimental models. | 4-10 |
| Figure 4.6 | The undercutting procedure of material removal. | 4-12 |
| Figure 4.7 | Actuator head displacements during a typical centrifuge test. | 4-13 |
| Figure 4.8 | Distribution of stresses and K ratio of the sample in centrifuge test 1 at 80 g. | 4-15 |
| Figure 4.9 | Distribution of stress state and K ratio in sample of centrifuge test 2 at 80 g. | 4-16 |
| Figure 4.10 | Distribution of stress state and K ratio in sample of centrifuge test 3 at 80 g. | 4-17 |
| Figure 4.11 | Distribution of stress state and K ratio in sample of centrifuge test 4 at 80 g. | 4-18 |
| Figure 5.1 | Overview of cave progression test 1 over steps 0–5 (zero confinement). | 5-4 |
| Figure 5.2 | Binary Image of cave progression test 1 highlighting cracks over steps 0–5. | 5-5 |
| Figure 5.3 | Minor principal strain surface plots during cave mining propagation over steps 0–5. | 5-6 |
| Figure 5.4 | Overview of cave progression test 2 over steps 0–5 (minimum confinement). | 5-7 |
| Figure 5.5 | Binary Image of cave progression test 2 highlighting cracks over steps 0–5. | 5-8 |
| Figure 5.6 | Minor principal strain surface plots during cave mining propagation over steps 0–5. | 5-9 |
| Figure 5.7 | Overview of cave progression test 3 over steps 0–5 (minimum confinement and overburden). | 5-10 |
| Figure 5.8 | Binary Image of cave progression test 3 highlighting cracks over 6 steps. | 5-11 |
| Figure 5.9 | Minor principal strain surface plots during cave mining propagation over 6 steps. | 5-12 |
| Figure 5.10 | Overview of cave progression test 4 over steps 0–5 (maximum confinement and overburden). | 5-13 |
| Figure 5.11 | Binary Image of cave progression test 4 highlighting cracks over 6 steps. | 5-14 |
| Figure 5.12 | Minor principal strain surface plots during cave mining propagation over 6 steps. | 5-15 |
| Figure 5.13 | Derivation of geometry parameters used in the investigation (Step 5 of test 3). | 5-17 |
| Figure 5.14 | Caved perimeter during cave mining propagation over steps 1–5. | 5-18 |
| Figure 5.15 | Caved area during cave mining propagation over steps 1–5. | 5-18 |
| Figure 5.16 | Caved hydraulic radius during cave mining propagation over steps 1–5. | 5-19 |
| Figure 5.17 | Cave height vs. cavity width plot during cave mining propagation over steps 1–5. | 5-19 |
| Figure 5.18 | Plot of K values against H/B ratios for tests 1, 2 and 3. | 5-20 |
| Figure 5.19 | Step 3 of test 1 — superimposed surface plot. | 5-22 |
| Figure 5.20 | Step 3 of test 1 — superimposed contour plot. | 5-22 |
| Figure 5.21 | Step 4 of test 1 — superimposed contour plot. | 5-23 |
| Figure 5.22 | Step 5 of test 1 — superimposed contour plot. | 5-24 |
| Figure 5.23 | Step 1 of test 2 — superimposed surface plot. | 5-25 |
| Figure 5.24 | Step 2 of test 2 — superimposed contour plot. | 5-25 |
| Figure 5.25 | Step 3 of test 2 — superimposed contour plot. | 5-26 |
| Figure 5.26 | Step 3 of test 2 — superimposed surface plot. | 5-27 |
| Figure 5.27 | Step 4 of test 2 — superimposed surface plot. | 5-27 |
| Figure 5.28 | Step 2 of test 3 — superimposed contour plot. | 5-28 |
| Figure 5.29 | Step 3 of test 3 — superimposed surface plot. | 5-29 |
| Figure 5.30 | Step 4 of test 3 — superimposed surface plot. | 5-29 |
| Figure 5.31 | Step 5 of test 3 — superimposed contour plot. | 5-30 |
| Figure 5.32 | Step 2 of test 4 — superimposed contour plot. | 5-31 |
| Figure 5.33 | Step 3 of test 4 — superimposed contour plot. | 5-32 |
| Figure 5.34 | Step 4 of test 4 — superimposed contour plot. | 5-32 |
| Figure 5.35 | Cave progression overview of strain contours — test 4. | 5-33 |
| Figure 5.36 | Test 3 (left) and test 4 (right) comparison at step 5. | 5-33 |
| Figure A.1 | Post fracture image of Brazilian disc test 3 (with subset mesh) | A-1 |
| Figure A.2 | Post fracture image of Brazilian disc test 4 (with subset mesh). | A-1 |
| Figure A.3 | Post fracture image of Brazilian disc test 5 (with subset mesh). | A-2 |
| Figure A.4 | Post fracture image of Brazilian disc test 7 (with subset mesh). | A-2 |
| Figure A.5 | Post fracture image of Brazilian disc test 11 (with subset mesh). | A-3 |

| | | |
|------------|--|-----|
| Figure A.6 | Post fracture image of Brazilian disc test 13 (with subset mesh). | A-3 |
| Figure B.1 | Dimensioned schematic of the test frame (front window) used in centrifuge testing. . . | B-1 |
| Figure B.2 | Dimensioned schematic of the actuators used in centrifuge testing. | B-2 |
| Figure B.3 | Dimensioned schematic of the complete test frame used in centrifuge testing. | B-3 |
| Figure C.1 | Geotechnical Centrifuge at the University of Pretoria | C-1 |
| Figure C.2 | Shear Mixer used to manufacture the artificial rock material. | C-1 |
| Figure D.1 | Superimposed Surface Overview of cave progression test 1 over steps 0–5. | D-1 |
| Figure D.2 | Superimposed Contour Overview of cave progression test 1 over steps 0–5. | D-2 |
| Figure D.3 | Superimposed Surface Overview of cave progression test 2 over steps 0–5. | D-3 |
| Figure D.4 | Superimposed Contour Overview of cave progression test 2 over steps 0–5. | D-4 |
| Figure D.5 | Superimposed Surface Overview of cave progression test 3 over steps 0–5. | D-5 |
| Figure D.6 | Superimposed Contour Overview of cave progression test 3 over steps 0–5. | D-6 |
| Figure D.7 | Superimposed Surface Overview of cave progression test 4 over steps 0–5. | D-7 |
| Figure D.8 | Superimposed Contour Overview of cave progression test 4 over steps 0–5. | D-8 |

Nomenclature

Roman Symbols

| | |
|---------------------|---|
| b | Y-axis intercept of the s and t regression line |
| B | Width of the cave back |
| c_{i0} | Cohesion intercept determined at low confining pressures |
| D, t | Diameter and thickness of the test specimen, respectively |
| D | Disturbance Factor |
| e | Magnitude of strain experienced by the rock mass |
| e_{3m} | Critical Extensional Strain of the model |
| e_{3p} | Critical Extensional Strain of the prototype |
| e_c or e_{3ult} | Critical extensional strain characteristic specific to the rock type |
| E | Young's Modulus |
| E_i | Intact deformation Modulus |
| E_m | Young's Modulus of the model |
| E_p | Young's Modulus of the prototype |
| E_{rm} | Rock mass Modulus |
| g_m | Gravitational acceleration of the model |
| g_p | Gravitational acceleration of the prototype |
| h or H | Height of the cave back |
| H_c or H_t | Height of the undercut to the surface |
| K | In-situ horizontal to vertical stress ratio |
| K_{bottom} | In-situ horizontal to vertical stress ratio at the base of the model |
| $K_{1/3}$ | In-situ horizontal to vertical stress ratio at 1 third the model height |
| L | Characteristic length dimensions. |
| L_m | Characteristic length dimension of the model |
| L_p | Characteristic length dimension of the prototype |
| m | Gradient of the s and t regression line |
| m_b, s and a | Hoek-Brown parameters |
| m_i | Hoek-Brown material constant |
| P | Load at failure |
| s, t | Centre and radius of the Mohr Circle, respectively |

Greek Symbols

| | |
|-----------------------------|--|
| α | Ratio of stresses at an equivalent point in the model |
| γ | Unit weight |
| η | Porosity |
| ν | Poisson's ratio |
| ρ_p | Relative density of the prototype material |
| ρ_m | Relative density of the model material |
| σ_1 | Major principal stress |
| σ_{1max} | The Major Principal Stress determined from the Hoek-Brown Equation |
| σ_2 | Intermediate principal stress |
| σ_3 or σ_{3n} | Minor principal stress |
| σ_{3max} | The upper bound of stress in the Mohr-Coulomb Model |
| σ_{ci} or σ_c | Unconfined Compressive Strength |
| σ_{htop} | Horizontal stress at the top surface of the model |
| $\sigma_{hbottom}$ | Horizontal stress at the base of the model |
| $\sigma_{h1/3}$ | Horizontal stress at 1 third the model height |
| σ_t | Tensile strength |
| σ_{vtop} | Vertical stress at the top surface of the model |
| $\sigma_{vbottom}$ | Vertical stress at the base of the model |
| $\sigma_{v1/3}$ | Vertical stress at 1 third the model height |
| τ | Mohr-Coulomb shear strength |
| ϕ | Internal angle of friction |
| ϕ_{i0} | Internal angle of friction determined at low confining pressures |

Acronyms and Abbreviations

| | |
|--------|--|
| ASTM | American Society for Testing and Materials |
| BDT | Brazilian Disc Test |
| BS | British Standards |
| CAD | Computer Aided Design |
| CPF | Cave Propagation Factor |
| DEM | Discrete Element Modelling |
| DIC | Digital Image Correlation |
| DSLR | Digital Single-Lens Reflex |
| FEM | Finite Element Method |
| GIMP | GNU Image Manipulation Program |
| GSI | Geological Strength Index |
| HBM | Hottinger Baldwin Messtechnik |
| HR | Hydraulic Radius |
| ISRM | International Society for Rock Mechanics |
| KFA | Kaolin Fly Ash |
| LVDT | Linear Variable Differential Transformer |
| MRMR | Mining Rock Mass Rating |
| OpenCV | Open-source Computer Vision |
| PFC | Particle Flow Code |
| PIV | Particle Image Velocimetry |
| PSD | Particle Size Distribution |
| RD | Relative Density |
| RG | Reliability Guided |
| RMR | Rock Mass Rating |
| RPM | Revolutions Per Minute |
| TDR | Time-Domain Reflectometry |
| TX | Triaxial |
| UCS | Uniaxial Compressive Strength |
| WSM | World Stress Map |

1 Introduction

1.1 Background

Cave mining involves the mass mining of an orebody through undercutting which entails blasting a horizontal section of in-situ rock and subsequently extracting this broken rock mass from draw points usually at an underground depth. At the point of reaching a large enough undercut area, a self-sustained propagating cave will advance as long as there is a removal of mined ore. An example block cave mining schematic is shown in Figure 1.1.

Cave mining is a cost effective method when compared to other mining operations, that allow for sustained high production rates of the ore body. Generally, rock with a uniform grade and strength is ideal for cave mining, ensuring maximum potential for ore deposits (Brady and Brown, 2006). The infrastructure required for a typical cave mine would include a decline or shaft to the level at which the undercut is performed. The level of extraction lies approximately 15–20 m below the undercut level and must be designed to be stable throughout the duration of mining. According to Sainsbury (2012): *“The three-dimensional nature of typical extraction level geometries, together with the complex stress-redistribution around a propagating cave makes it difficult to assess cave propagation and subsidence behaviour”*.

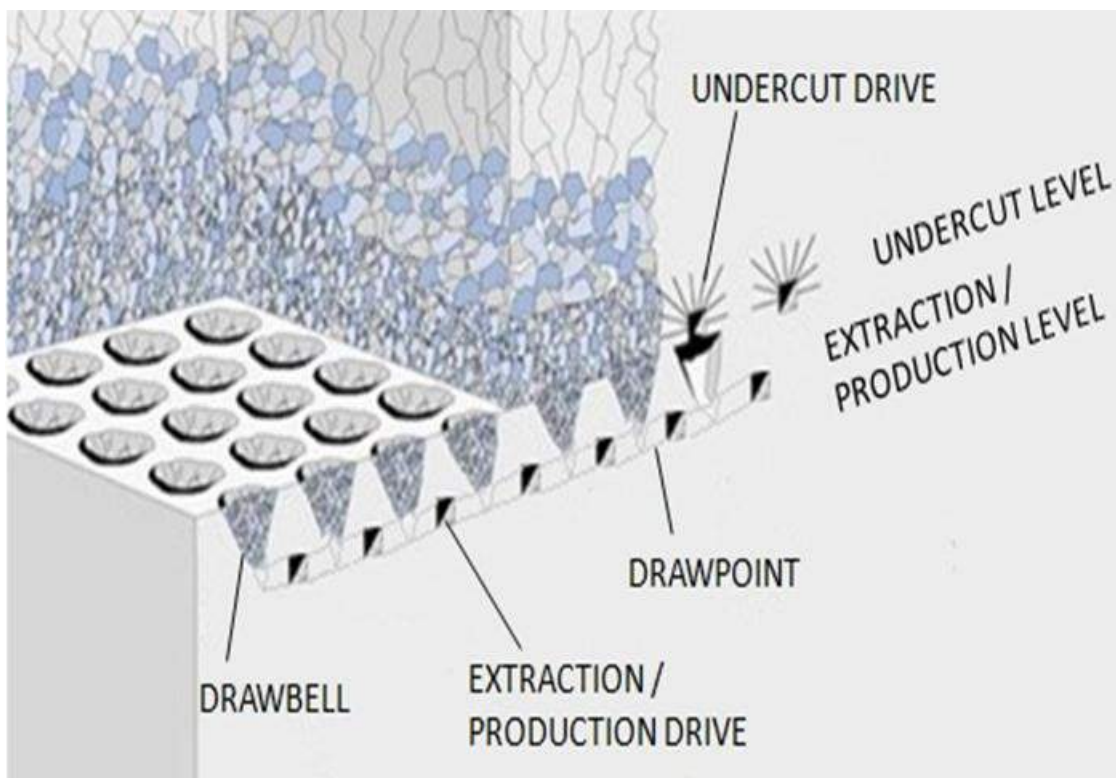


Figure 1.1: Schematic of a typical block cave mine (Sainsbury, 2012).

The cave mining method comprises several variations of cave mining. These are block-caving, panel-caving and sub-level caving. Block and panel cave mining methods involve ore being mined from an extraction point that is a single mining horizon where the intact rock mass is broken down into fragmented cave material without the activities of blasting and drilling after the material is initially undercut. This fragmentation is influenced by natural processes which include in-situ fracturing, stress redistribution and progression of crushed material downward resulting in autogenous grinding.

A distinction can be made between the types of cave mining. In block caving, the ore body is undercut completely prior to production of ore-withdrawal. Panel caving involves production mining before the entire ore body is undercut. In this manner, production commences earlier and mining laterally progresses across the body of ore. Sub-level caving, which is quite different to block and panel caving, makes use of a number of mining horizons at the same time. The progression of mining occurs downwards through the ore body and the ore is drilled and blasted in order to extract it in its mobile state. Similarly to block and panel caving, the material is still allowed to cave into the voids that were previously undercut and the material, as in caving, fails under its own weight.

This study investigates the conditions required for cave mining propagation to occur when the process of undercutting is performed. Cave propagation is simulated by the use of experimental models. The focus of this dissertation is to investigate the mechanism of cave propagation failure at various stress states.

1.2 Objectives of the Study

The main objective of this study was to investigate the behaviour of physical cave mining models subject to different degrees of horizontal and vertical stress conditions. The physical models themselves were made from a manufactured artificial rock material and the simulation of the cave mining process was performed in a geotechnical centrifuge. The caving propagation behaviour was analysed both qualitatively and quantitatively in terms of cave geometry and principal strains. A summary of the study objectives are to:

1. Manufacture and characterise a suitable artificial rock material capable of behaving in a manner representative of rock under increased acceleration in a geotechnical centrifuge.
2. Ascertain, from physical modelling, whether the resulting cave-formation geometry is dependent on stress state and orientation.
3. Determine the regions and mechanism of cave mining propagation failure through the use of a suitable mechanical model for brittle materials.

1.3 Scope of the Study

The scope of this investigation initially involved the manufacturing of one suitable artificial rock mass and thereafter determining the material properties of this specific material. This material (with its defined material properties) was then used in the rest of the investigation. It is noted that effect of material properties on caving propagation was not studied as part of this investigation.

Once the material was adequate to replicate a rock mass on a weaker scale, slabs were cast and used for centrifuge testing to simulate caving propagation at various horizontal to vertical stress ratios. This study was aimed at improving the understanding of caving propagation in brittle materials and the effect of lateral earth pressure on caving was investigated where the scope did not extend to studying the actual material properties required to enable caving propagation in mines. The effect of discontinuities (rock joints) and faults also falls outside the scope of this investigation.

Results from the physical models were obtained through photographs that were analysed using Particle Image Velocimetry (PIV) and other image analysis tools utilised by Python programming. As per the objectives, the study focused on cave geometry and principal strains during the attempt to simulate the cave mining process at different conditions of overburden and confining stress state. The simulations were conducted using a frame for trap-door centrifuge experiments.

Seismic data and fracture mechanics are excluded from this study.

1.4 Methodology

A literature review was conducted on previous studies of modelling rock, the stress states of mines, caving mechanics, scaling laws, physical modelling and numerical modelling. The components which comprise the methodology followed in the investigation include:

1. Manufacturing and characterisation of the artificial rock material

A trial and error method of Uniaxial Compressive Strength (UCS) testing of a range of materials was adopted to select the candidate cave mining material to represent rock. The following materials were used to replicate the brittleness of rock on a weaker scale. These included testing weakly cemented sands, slurry mixtures, Plaster of Paris and silica sand as well as mixtures of kaolin and fly ash. A characterisation of the chosen material was performed to determine its material properties. The geotechnical laboratory tests conducted included:

- Uniaxial compression testing for determining unconfined compressive strength.
- Triaxial testing for determining the effect of confinement on the compressive and shear strength of the material.
- Brazilian disc testing for indirect tensile strength (tests were photographed at regular time intervals to obtain image data).

2. Physical modelling through centrifuge testing

Physical modelling was conducted in the geotechnical centrifuge facility at the University of Pretoria. Four centrifuge tests were carried out with different initial states of stress brought about by vertical and horizontal loadings. The tests were conducted using a testing frame originally used for trap-door experiments and modified for cave mining undercutting processes. It is worth noting the ratio of horizontal to vertical pressure was kept constant in the applicable areas of the sample for a given test. Images were captured at regular time intervals throughout the duration of tests.

3. Image analysis and strain mapping

Material properties obtained from geotechnical laboratory tests and Brazilian disc test image data, which was analysed using PIV methods, aided in the selection of a suitable mechanical model for the chosen artificial rock material. PIV analysis was also applied to the image data from physical modelling results enabling the mapping of strains that generated over the duration centrifuge tests. Image-processing methods, described in Section 5.1.1, were performed through dedicated Python programming modules to track the cave-back formation geometry, as well as formation of fractures within centrifuge models over time.

1.5 Outline of the Dissertation

The report consists of the following chapters and appendices:

- Chapter 1 serves as the introduction to the dissertation, which defines the objectives, and outlines the scope. Herein, the methodology as well as the outline of the investigation are covered.
- Chapter 2 contains the literature review related to modelling rock, the stress states of mines, caving mechanics, scaling laws, physical modelling and concludes with approaches followed in numerical modelling.
- Chapter 3 provides the process by which the artificial rock material was manufactured. The chapter continues with defining the material properties of the specific material which is used in cave mining simulations. All geotechnical laboratory testing results are presented in this chapter.

- Chapter 4 describes the setup and model as well as relevant testing equipment used for the execution of centrifuge testing. Scaling relationships and laws are discussed and advised ranges applicable for the models are given herein. Theoretical stress calculations for each centrifuge test model are also provided in this chapter.
- Chapter 5 covers all discussions of results with regard to the physical modelling component of this investigation. The discussions facilitate the topics of cave geometry and position and magnitudes of strains experienced within the experimental models as identified previously.
- Chapter 6 summarises and concludes on the research objectives addressed. Recommendations and limitations of the research covered in cave mining propagation are presented.

2 Literature Review

This chapter presents previous cave mining research and discusses the process of cave mining. Efforts made thus far in literature to predict cave propagation as well as the material models used are contained in this chapter. Attempts from literature to replicate the cave mining process through physical and numerical modelling are also presented herein.

2.1 In-Situ and Induced Stresses

Deep underground, rock is subjected to stress from the vertical and lateral direction. The in-situ vertical stresses are due to overlying rock layering and overburden material above the rock while the in-situ horizontal stresses are present because of the movement of tectonic plates and factors such as over-consolidation over geological time. A newly induced set of stress conditions are caused locally when the in-situ stress state is disrupted by an opening in the rock (by earthquakes or excavations). The magnitude and directions of these stresses are particularly important for underground excavation design because the strength of the rock must not be exceeded during mining activities (i.e. excavations) as this could cause instability.

2.1.1 The Theory of Plate Tectonics

According to Mark and Gadde (2008), a dynamic earth is described by the theory of Plate Tectonics which is one that suggests that the earth's crust consists of a number of hard and brittle continental plates that move over the softer more ductile mantle which supports it. The contact of these plates and their relative movement to one another are responsible for the large forces experienced in the plate interiors. Over the last few decades, scientists have worked towards creating the World Stress Map (WSM) project in identifying regional stress fields across the world (Mark and Gadde, 2008).

2.1.2 World Stress Map Project

The World Stress Map (WSM) is a database for information about lithospheric stresses resulting from tectonic plate movement that make up the upper part (2–5 km thick from the surface) as well as the lower part (5–20 km) of the earth's crust. This upper part is essentially from where all of the well-bore breakout and hydraulic fracturing data is recorded while the lower part is where most of the earth's crustal earthquakes take place (Zoback and Zoback, 2002).

It is noted that the ‘near surface’ measurements are excluded from this database as the stresses recorded in these near surface layers (1–2 km from the surface) are influenced by effects of local topography or high degrees of surface fracturing. Zoback and Zoback (2002) claim that measurements of in-situ stresses at depths exceeding 100 m are caused purely by tectonic stress fields.

From the data collected by the WSM project, it was found that the stress state over large regions of plate interiors was relatively uniform. It was also noted that these stresses are caused by present day stresses and they are not residual stresses from past tectonic activity (Zoback and Zoback, 2007). Currently, there is a consensus within the community of geophysics about the efficacy of the trends described by the WSM (Mark and Gadde, 2008).

2.1.3 Stress Orientations of Cave Mines around the World

Figure 2.1 shows the mapped locations of the current and planned cave mines across the world including those that have closed down. There are about twenty currently operating cave mines worldwide.

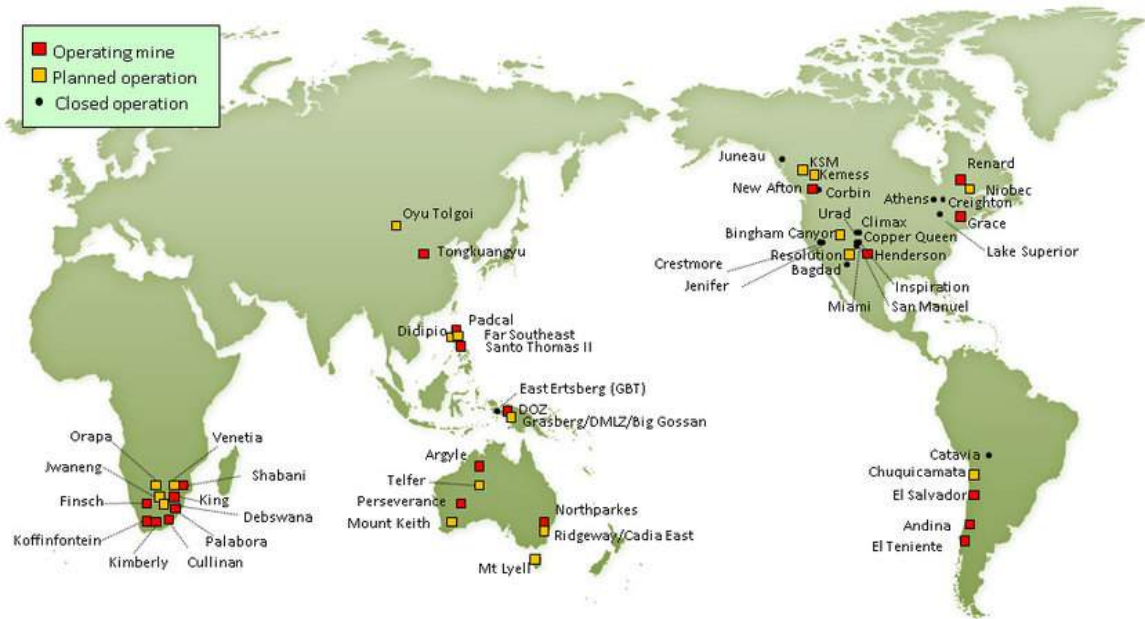


Figure 2.1: Distribution of both operating and planned block and panel cave mines, together with historic (closed) mines. Not included are sub-level caving operations (Brown, 2007). Note locations are not geographically accurate.

The stress orientations that are observed in coalfields around the world can be described from the data collected by the WSM project (Mark and Gadde, 2008). Note that there are three types of regions in that tectonic plates make contact with each other, which create their own different set of conditions with regard to stress state. These are namely normal

faulting, strike-slip faulting and reverse faulting. Figure 2.2 demonstrates the types of faulting contact.

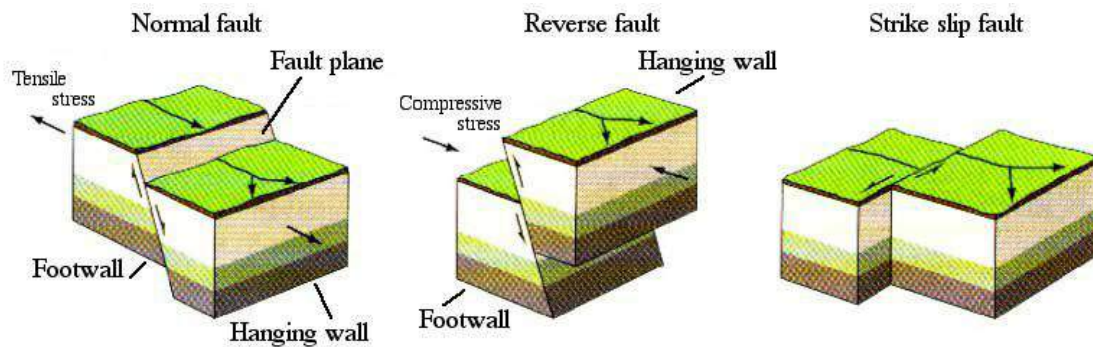


Figure 2.2: Various types of faulting at the boundaries of the tectonic plates (Van der Pluijm and Marshak, 2004).

The stress states that exist around the world include:

- **Western USA**

Normal faulting occurs in the coal fields of Utah, Colorado and Wyoming and New Mexico, suggesting that the vertical stress is predicted to be greater than either horizontal stress in most cases. Stress directions vary through this whole western mid-plate region.

- **Eastern USA**

The WSM describes the eastern part of North America as a stable mid-plate region with a consistent East North East horizontal stress orientation (Zoback and Zoback, 1989) with higher major horizontal stresses than in Western America.

- **Bowen Basin, Queensland, Australia**

Stress orientation in this continent varies substantially from region to region. This is owing to the plate boundary forces rather than the direction of absolute plate motion (Hillis and Reynolds, 1999). In coal fields of Queensland, the major horizontal stress is consistently orientated in a North North East direction while the vertical stress is either larger or smaller than the minor horizontal stress. It must be noted that the major horizontal stress almost always exceeded the vertical stress, with factors of up to 3 or more according to Nemcik et al. (2005).

- **Sydney Basin, New South Wales, Australia**

Stress orientations vary appreciably through this region. It should be noted that this basin in Australia is the most seismically active. It is suggested that plate boundary effects superimposed on the regional stress direction have resulted in major and minor horizontal stresses of similar magnitude.

- **South Africa**

According to Stacey and Wesseloo (1998), the horizontal secondary principal stresses are found to take on an approximate NW-SE orientation in most cases, with some NE-SW directions in less instances. The general trend found in South Africa's mines is that horizontal stress values are ranged between being equal to or greater than the vertical stresses. Stacey and Wesseloo (1998) pointed out that the approach of using a horizontal to vertical stress ratio of 0.5 for mining layout analyses, is normally invalid. With regard to mining areas in South Africa, it is commonly known that the Northern Cape is an area of high horizontal stress (Nieuwoudt and Rozendaal, 1990). At shallow depths, it is significant to note that horizontal stresses typically exceed the overburden stresses and this is particularly the case in regions of Carletonville, Klerksdorp and Rustenburg (a region near Cullinan Mine as shown on the map of Figure 2.1).

The WSM indicates that cave mining takes place in areas where the horizontal stresses in the rock mass vary from 60 % of the vertical stresses in normal faulting cases to 3 times as much as the vertical stresses in zones of reverse faulting. This is according to the assumptions of Townend and Zoback (2000) and evaluations made by Mark and Gadde (2008) with reference to Figure 2.2. It is postulated by Hillis and Reynolds (1999) that density differences, faults, or geological structures are the reasons for these stress rotations. It is hypothesised that this variation in stress ratio in the mines should affect the shape of cave propagation where larger ratios could lead to less steep caving and even cause cave stalling.

2.2 Rock Mass Modelling

This section of the literature review includes sub-sections that present research done on modelling rock mass, taking into account the effects of scaling. It follows with the current techniques implemented to represent the strength response of jointed rock masses that can be utilised for studying cave propagation behaviour.

2.2.1 Scale Effects

Generally, the strength and deformation behaviour of a jointed rock mass are dependent on two factors; namely the intact rock strength and presence of rock joints (Brown, 2003). The strength of underground rock usually stems from its intact rock strength established from laboratory testing; however, it can be observed that the uniaxial compressive strength of intact rock depends on sample size. This points towards 'scale effects' which is a term referring to the change in mechanical strength properties with size.

It has been shown that the size-dependency reduction may vary between 20–80 % of the intact strength from laboratory tested specimens (Hoek and Brown, 1980; Pratt et al., 1972). A comparison of the large scale in-situ testing and laboratory-scale testing of Pratt et al. (1972) is presented in Figure 2.3. It is shown by Bandis et al. (1983) that the deformation of pre-existing rock joints governs the behaviour of a rock mass. Laboratory testing was conducted on the deformation characteristics of rock joint masses involving high and low stress conditions under normal and shear loadings.

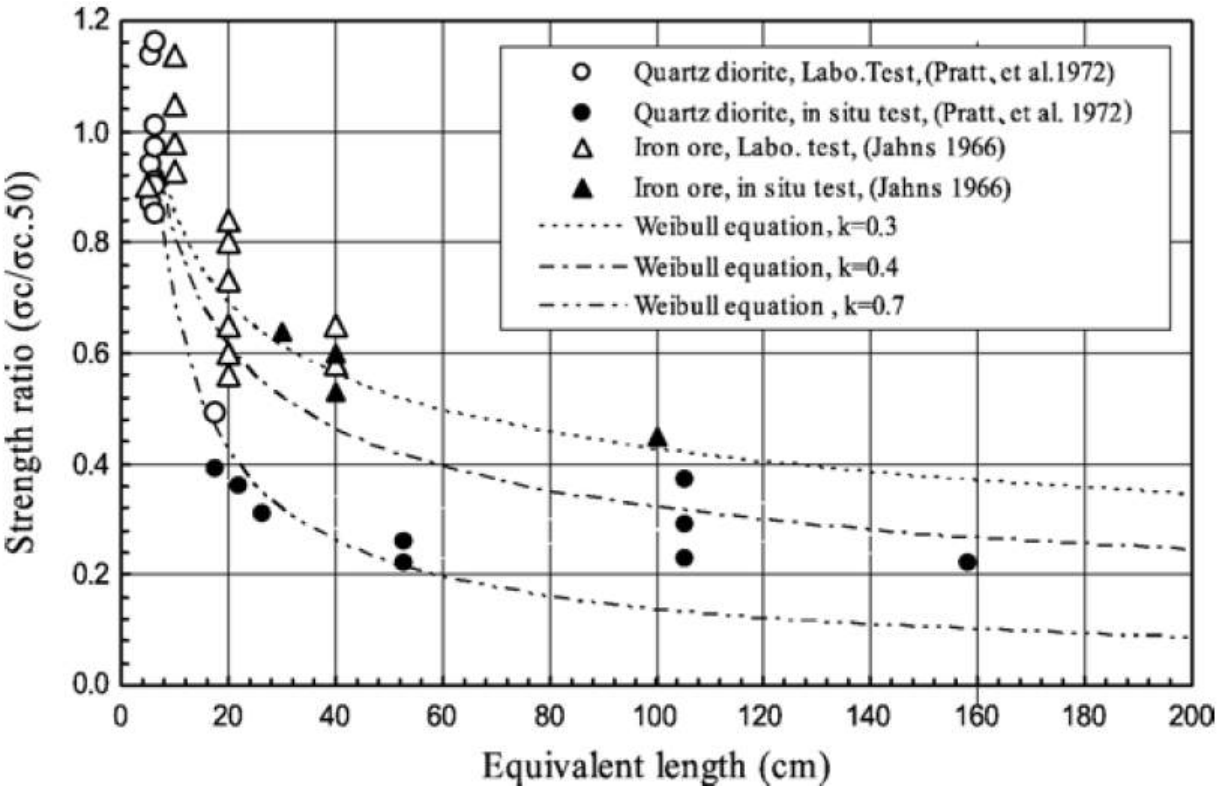


Figure 2.3: Measured rock strength-scale effect including large size specimens of in-situ test (Pratt et al., 1972).

It has also been shown that certain joint orientations have a noticeable effect on anisotropy in relation to the deformation modulus, strength and brittleness of the rock mass (Ivars et al., 2011). Furthermore, density of the joints must be considered relative to problem size which is shown in Figure 2.4 (Sainsbury, 2012).

Analytically, material properties of a rock mass currently cannot be derived based on laboratory testing data due to there being no sample scale (of ranged sizes) large enough to obtain repeatable strength results (Sainsbury, 2012). Similarly, the results obtained from field testing programs are considered crude estimates and are generally expensive to implement. Therefore current practice, resorts to characterising rock masses by empirical and numerical means.

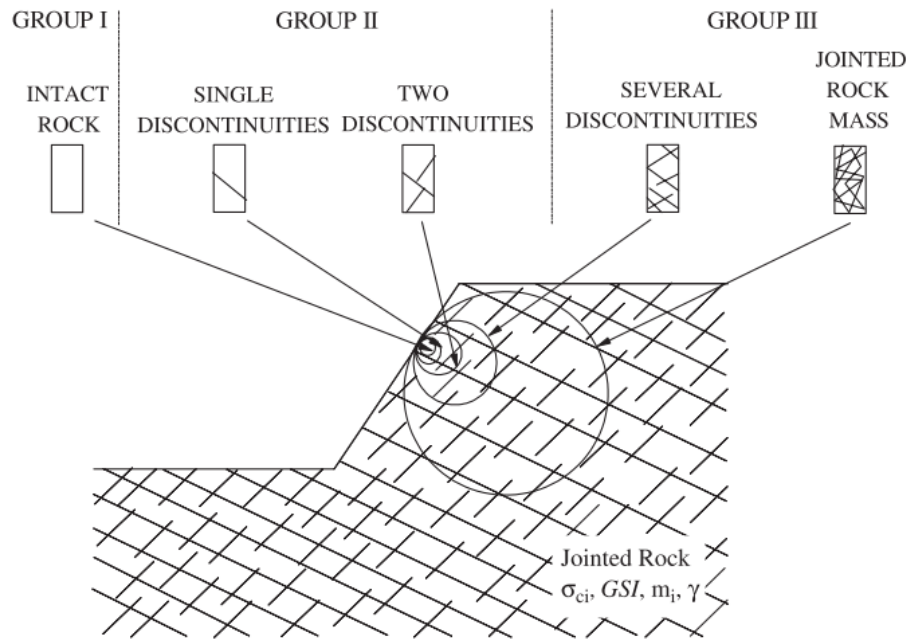


Figure 2.4: Applicability of the Hoek-Brown empirical rock mass strength criterion at different scales (Li et al., 2008).

2.2.2 Hoek-Brown Strength Criterion

The Hoek-Brown strength criterion established in the 1980s was based on the results of research conducted into the behaviour of brittle rock failure (Hoek, 1965a) and on modelling the behaviour of jointed rock masses (Brown and Trollope, 1970). It is extensively accepted throughout industry as the standard method of estimating rock mass strength. The criterion makes use of the specified intact rock properties and determines the large-scale peak strength response from applied reduction factors that are based on the rock mass fabric (faults and joints).

When numerical modelling codes were developed, they were generally written in terms of the Mohr-Coulomb criterion. A method of relating Hoek-Brown parameters to those of Mohr-Coulomb makes it possible to express Hoek-Brown strength in terms of cohesion and friction (Bray et al., 1983). Therefore, numerical modelling could be implemented for representative rock masses. The method originally used by Bray et al. (1983) involved fitting a least-square regression line to the Hoek-Brown Failure Envelope to obtain values representing cohesion and friction.

A more accurate solution entails fitting a bi-linear, Mohr-Coulomb line to the Hoek-Brown Failure Envelope which to some extent accounts for Hoek-Brown's non-linearity. The range of stresses for fitting the Mohr-Coulomb parameters can be bound to guarantee a better match over the range of stresses that are anticipated. The advantages of using the bi-linear fit over the linear fit along with the requisite estimation of the stress range is

demonstrated in Figure 2.5. It is recommended that friction angles and cohesive strength values derived, should not be utilised without a tension cut-off (Hoek and Brown, 2019).

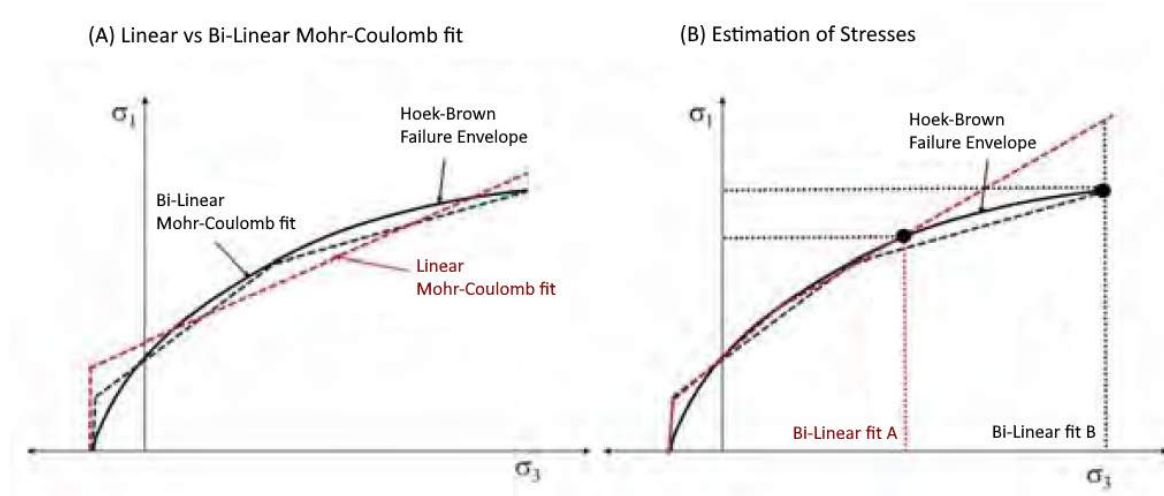


Figure 2.5: Development of equivalent Mohr-Coulomb property estimates from a fit to the Hoek-Brown curve (Sainsbury, 2012).

2.2.3 The Hoek-Brown Model

The Hoek-Brown strength criterion and the applicable Geological Strength Index (GSI) are widely accepted for the estimation of strength and deformation attributes of jointed rock masses. The reason it was accepted by the rock mechanics community was due to the lack of suitable alternatives (Hoek and Brown, 2019). The generalised Hoek-Brown criterion for the estimation of rock mass strength is given by Equation 2.1 followed by the Hoek-Brown parameters in Equations 2.2 to 2.4 (Hoek and Brown, 2019):

$$\sigma_1 = \sigma_3 + \sigma_{ci} \left(m_b \frac{\sigma_3}{\sigma_{ci}} + s \right)^a \quad (2.1)$$

With:

$$m_b = m_i \exp \left(\frac{GSI - 100}{28 - 14D} \right) \quad (2.2)$$

$$s = \exp \left(\frac{GSI - 100}{9 - 2D} \right) \quad (2.3)$$

$$a = \frac{1}{2} + \frac{1}{6} \left[\exp \left(\frac{-GSI}{15} \right) - \exp \left(\frac{-20}{3} \right) \right] \quad (2.4)$$

Where:

σ_1 = Major principal stress

σ_3 = Minor principal stress

σ_{ci} = Unconfined compressive strength

m_b , s and a = Hoek-Brown parameters

m_i = Hoek-Brown material constant

GSI = Geological Strength Index

D = Disturbance Factor

The Hoek-Brown parameters (m_b , s , a) determined from field estimates are indicative of rock material properties and contribute to the overall shape of the curved failure envelope. The unconfined compressive strength (σ_{ci}) and Hoek-Brown material constant (m_i) are determined by linear regression. It should be noted that for intact rock the Hoek-Brown parameters take on the following values: $s = 1$, $a = 0.5$ when the field estimates GSI and D are equal to 100 and 0, respectively.

The above equations are valid for rock masses in which failure is dominated by block sliding and rotation and with less consideration to the bulking of intact rock under conditions of low to moderate confining pressure. For higher confining stresses, modified forms of these equations are used which are provided by respective authors in literature. These modifications may take the form of altering the values of the constants or the form of the equations themselves. This is a completely understandable and acceptable approach as deemed by Hoek and Brown (2019).

2.2.3.1 Strength of Intact Rock

Equation 2.1 shows the unconfined compressive strength parameter, σ_{ci} , which heavily influences the scale of the rock mass strength failure envelope on a principal stress plot. The unconfined compressive strength is different to the uniaxial compressive strength (UCS) in that the latter is used to determine the former. The UCS of a material is generally obtained by testing a reasonable number of specimens managing to reach repeatable results.

The tests are performed with zero confinement ($\sigma_3 = 0$). Recognising that a series of UCS test results in a set of triaxial test results would create a bias of curve fitting, it is recommended by Hoek and Brown (2019) that the average UCS result represents the UCS data set. The triaxial data set, including the averaged obtained UCS results are then plotted with a regression analysis carried out to determine the unconfined compressive strength, σ_{ci} , as well as the Hoek-Brown constant, m_i . Regression Equations 2.5 and 2.6

are recommended by Hoek and Brown, where $x = \sigma_3$, $y = (\sigma_1 - \sigma_3)^2$ and n denotes the number of tests:

$$\sigma_{ci}^2 = \frac{\Sigma y}{n} - \left[\frac{\Sigma xy - \frac{\Sigma x \Sigma y}{n}}{\Sigma x^2 - \frac{(\Sigma x)^2}{n}} \right] \frac{\Sigma x}{n} \quad (2.5)$$

$$m_i = \frac{1}{\sigma_{ci}} \left[\frac{\Sigma xy - \frac{\Sigma x \Sigma y}{n}}{\Sigma x^2 - \frac{(\Sigma x)^2}{n}} \right] \frac{\Sigma x}{n} \quad (2.6)$$

The Hoek-Brown criterion was developed for shear failure in rock. The triaxial compression results were plotted for a wide range of rock types. This showed that the extent of applicability of the Hoek-Brown Model is perceived by the transition from shear to ductile failure. It was found that the average transition from shear to ductile failure (for a wide range of rock types) is defined by $\sigma_1 - \sigma_3 = 3.4\sigma_3$ (Mogi, 1966). This is a practical rule of thumb for the determining the extent of cell pressures for triaxial testing of intact rock specimens (Hoek and Brown, 2019).

2.2.3.2 Tensile Failure

Tensile failure is not accounted for by the Hoek-Brown criterion — nonetheless — it is considered a significant aspect in engineering problems (Hoek and Brown, 2019). Focusing on rock mechanics, the most valuable solution in accounting for tensile failure is Griffith's Theory, described by Fairhurst (1964). The solution is given in terms of the ratio of unconfined compressive strength (σ_{ci}) to tensile strength (σ_t), given in Equations 2.7 to 2.11:

If $w(w - 2)\sigma_3 + \sigma_1 \leq 0$, failure occurs when:

$$\sigma_3 = \sigma_t \quad (2.7)$$

If $w(w - 2)\sigma_3 + \sigma_1 > 0$, failure occurs when:

$$\sigma_1 = \frac{(2\sigma_3 - A\sigma_t) + \sqrt{(A\sigma_t - 2\sigma_3)^2 - 4(\sigma_3^2 + A\sigma_t\sigma_3 + 2AB\sigma_t^2)}}{2} \quad (2.8)$$

Where:

$$A = 2(w - 1)^2 \quad (2.9)$$

$$B = \left(\frac{w - 1}{2} \right)^2 \quad (2.10)$$

$$w = \sqrt{\frac{\sigma_{ci}}{|\sigma_t|} + 1} \quad (2.11)$$

Upon combining the two failure criteria, it was necessary to simplify the result to the preference of Hoek and Martin (2014). It was decided that a tensile cut-off based on Griffith's theory would implement an adequate solution. This is illustrated in Figure 2.6 particularly for the tensile results of Ros and Eichinger (1928) and Ramsey and Chester (2004).

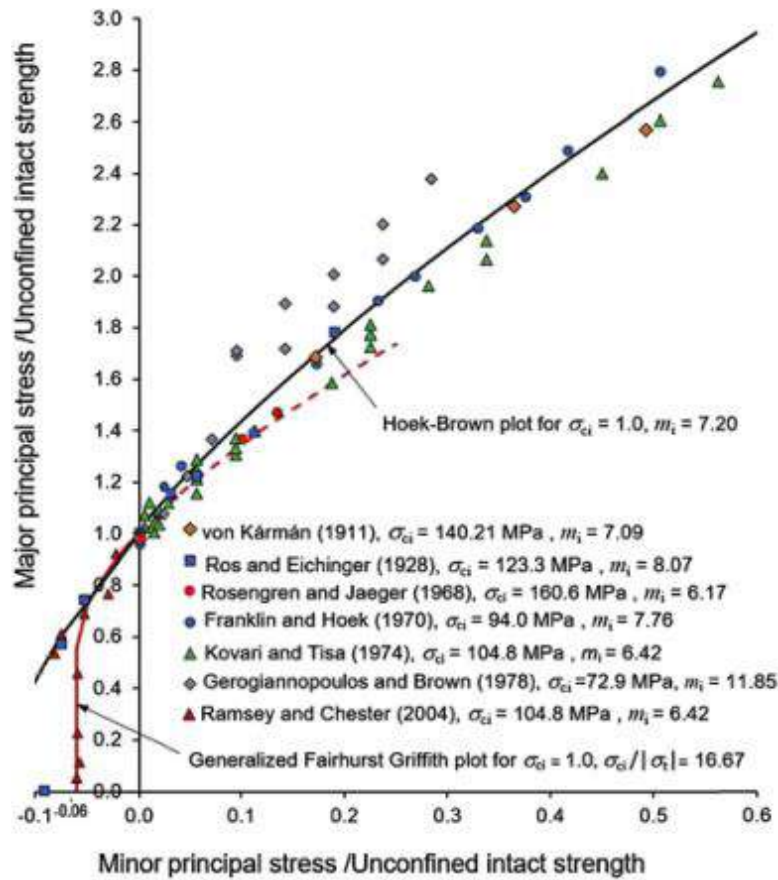


Figure 2.6: Dimensionless plot of triaxial test data for Carrara marble showing the use of the generalised Griffith theory for tensile failure and the Hoek-Brown criterion for shear failure (Hoek and Brown, 2019).

By applying the following interim approximate measure between the compressive to tensile strength ratio, $\frac{\sigma_{ci}}{|\sigma_t|}$, and the Hoek-Brown constant, m_i , a tension cut-off can be calculated. Figure 2.7 shows the relationship of the interim approximated measure of Equation 2.12.

$$\frac{\sigma_{ci}}{|\sigma_t|} = 0.81m_i + 7 \tag{2.12}$$

It is noted that only two parameters, for intact rock, are necessary for defining a Hoek-Brown failure envelope with a tension cut-off. These are the unconfined compressive strength (σ_{ci}) and material constant m_i (Hoek and Brown, 2019).

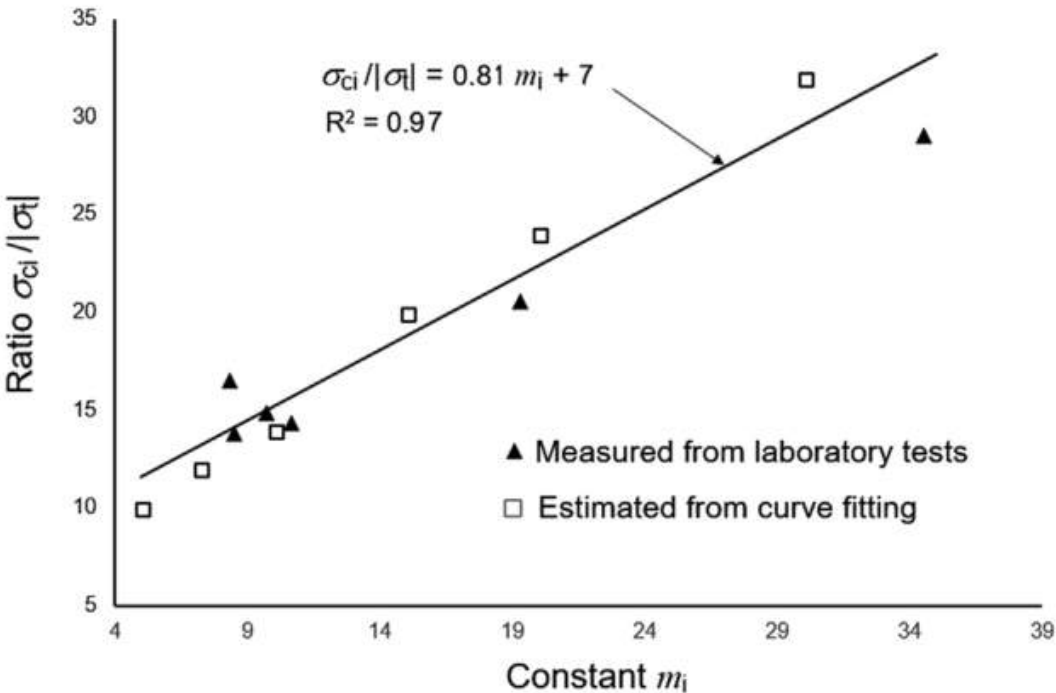


Figure 2.7: Relationship between the ratio of $\frac{\sigma_{ci}}{|\sigma_t|}$ and m_i (Hoek and Brown, 2019).

The Brazilian disc test, whereby a disc specimen is diametrically loaded until tensile failure is induced at the centre, is not accepted for inclusion in the analysis described previously. Due to the complex stress distribution and the effect of stress concentrations at the loading platens, the calculation of tensile strength requires significant correction (Perras and Diederichs, 2014). Hoek and Brown (2019) refer to the Brazilian disc test as an index test which must be calibrated against direct tensile tests for each type of rock.

2.2.3.3 The Geological Strength Index

Originally the Hoek-Brown GSI term in Equations 2.1 to 2.4 was based on the RMR (Rock Mass Rating) classification (Bieniawski, 1976). However, a subsequent replacement

of the rating method was made (Hoek et al., 1998). The GSI is a tool for estimating the Hoek-Brown parameters: m_b , s , a and material constant, m_i , in the criterion defined in Equations 2.1 to 2.4. This method of classification was established to account for two significant aspects reasoned to have an effect on mechanical properties of a rock masses which include its structure (i.e. blockiness) and the extent of discontinuities (joint conditions). The most recent revision of the GSI and its use in Equations 2.1 to 2.4 was made by Hoek et al. (2002). This is presented in Figure 2.8.

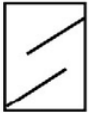
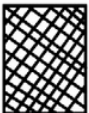

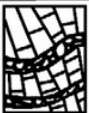


| GEOLOGICAL STRENGTH INDEX FOR JOINTED ROCKS From the lithology, structure and surface conditions of the discontinuities, estimate the average value of GSI. Do not try to be too precise. Quoting a range from 33 to 37 is more realistic than stating that GSI = 35. Note that the table does not apply to structurally controlled failures. Where weak planar structural planes are present in an unfavourable orientation with respect to the excavation face, these will dominate the rock mass behaviour. The shear strength of surfaces in rocks that are prone to deterioration as a result of changes in moisture content will be reduced if water is present. When working with rocks in the fair to very poor categories, a shift to the right may be made for wet conditions. Water pressure is dealt with by effective stress analysis | | SURFACE CONDITIONS DECREASING SURFACE QUALITY → | | | | |
|--|----------|--|---|--|--|---|
| STRUCTURE | | VERY GOOD Very rough, fresh, unweathered surfaces | GOOD Rough, slightly weathered, iron stained surfaces | FAIR Smooth, moderately weathered and altered surfaces | POOR Slickensided, highly weathered surfaces with compact coating or fillings of angular fragments | VERY POOR Slickensided, highly weathered surfaces with soft clay coatings or fillings |
|  INTACT OR MASSIVE - Intact rock specimens or massive in-situ rock with few widely spaced discontinuities | 90 80 | | | | N/A | N/A |
|  BLOCKY - Well interlocked undisturbed rock mass consisting of cubical blocks formed by three intersecting discontinuity sets | | 70 60 | | | | |
|  VERY BLOCKY - Interlocked, partially disturbed mass with multi-faceted angular blocks formed by 4 or more joint sets | | | 50 | | | |
|  BLOCKY/DISTURBED/SEAMY - Folded with angular blocks formed by many intersecting discontinuity sets. Persistence of bedding planes or schistosity | | | | 40 | | |
|  DISINTEGRATED - Poorly interlocked, heavily broken rock mass with mixture of angular and rounded rock pieces | | | | | 30 | |
|  LAMINATED/SHEARED - Lack of blockiness due to close spacing of the weak schistosity or shear planes | | | | | | 20 |
| | | | | | | 10 |
| | | N/A | N/A | | | |

Figure 2.8: Geological Strength Index (GSI) chart (Marinos et al., 2007).

The original intention of the GSI was to guide users in the initial estimation of rock mass properties with assumptions based on user discretion to improve the initial estimations by means of further detailed site investigations, numerical analyses and back-analyses to validate or modify these estimates.

2.2.3.4 Estimation of rock deformation modulus

In supplementation of the estimation of rock mass strength (intact and bulked), for the analysis of slope, foundation, and tunnel behaviour, the deformation modulus of the rock mass material is required. This poses a challenge and numerous suggestions for estimating the deformation modulus of a rock mass have been made in literature. A database of rock mass deformation modulus measurements was created from which the following empirical formula, shown in Equation 2.13, for estimating rock mass modulus was developed (Hoek and Diederichs, 2006):

$$E_{rm} = E_i \left[0.02 + \frac{1 - \frac{D}{2}}{1 + \exp\left(\frac{60+15D-GSI}{11}\right)} \right] \quad (2.13)$$

Where E_{rm} is the rock mass modulus and E_i the intact deformation modulus (in MPa). For the cases where laboratory testing is not an option to obtain measurable E_i values, it is recommended that reduction values (MR) are used for estimating the intact deformation modulus (Deere, 1968). Alternatively, when no information is available on the intact deformation modulus parameter, Equation 2.14 can be used for estimating rock mass modulus, E_{rm} (Hoek and Diederichs, 2006):

$$E_{rm} = 10^5 \left[\frac{1 - \frac{D}{2}}{1 + \exp\left(\frac{75+25D-GSI}{11}\right)} \right] \quad (2.14)$$

Figure 2.9 gives the comparison plot for the deformation modulus estimated using the equation which fits a variety of field measurements and predictions (Bieniawski, 1978; Serafim, 1983; Stephans and Banks, 1989; Read et al., 1999; and Barton, 2002). The general agreement between the results and the predictions (including those of Hoek and Diederichs, 2006) indicates that the predictions may be used with confidence for estimating parameters.

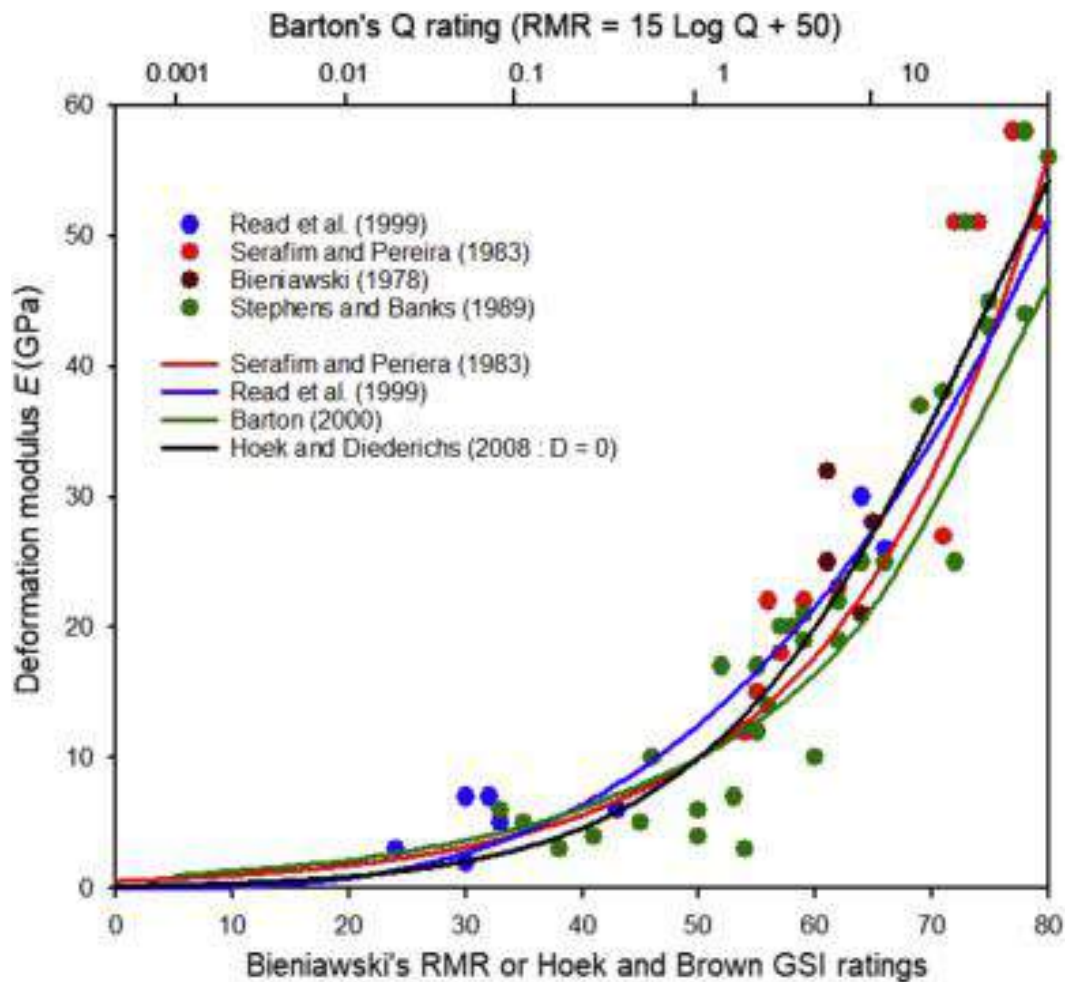


Figure 2.9: Comparison between field measurements and deformation modulus values predicted by several authors (Hoek and Brown, 2019).

2.2.3.5 The Disturbance factor

Excavations that occur in tunnels, slopes or foundations can result in stress relief and consequently cause the neighbouring rock to dilate. In Equations 2.2 and 2.3, the field estimate parameter, D , is a factor referring to the degree of disturbance with regard to blast damage and stress relaxation. It ranges from 0 for undisturbed rock masses to 1 for extremely disturbed rock masses. It is important to note that the factor D applies only to the blast damage zone and should not inherently be applied to the whole rock mass. For example, during tunnel excavation the blast damage is generally applicable to a depth of 1–2 m around the tunnel. This should be taken into account in numerical models by taking this material as weaker material than the adjoining rock mass. This could otherwise lead to inaccurate results. A plot of normalised in situ rock mass deformation modulus from China and Taiwan against Hoek and Diederichs' equation for a range of damage factors is shown in Figure 2.10 illustrating how the damage factor degrades the deformation modulus of the rock over a range of GSI values.

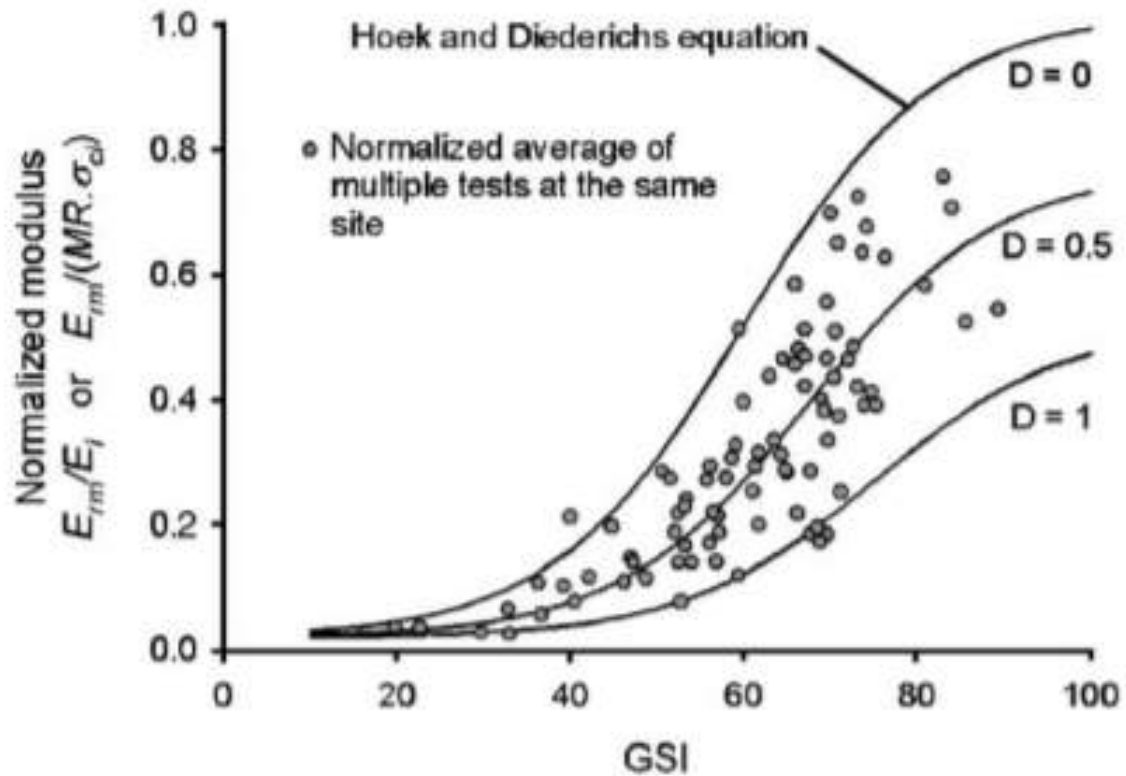


Figure 2.10: Plot of normalised in situ rock mass deformation modulus from China and Taiwan against Hoek and Diederich's Equation (2.13 and 2.14). Each data point represents the average of multiple tests at the same site in the same rock mass (Hoek and Diederichs, 2006).

2.2.4 Cohesion and Tension Softening

During failure, the rock yielding process is slow and moderate to achieve a caved state. The rate of change of this strain-softening behaviour is influenced by intact rock strength, joint network and confining pressure (Tiwari and Rao, 2006). Experimental stress-strain curves are presented in Figure 2.11 to demonstrate the idealised material behaviour in models typically used in numerical modelling.

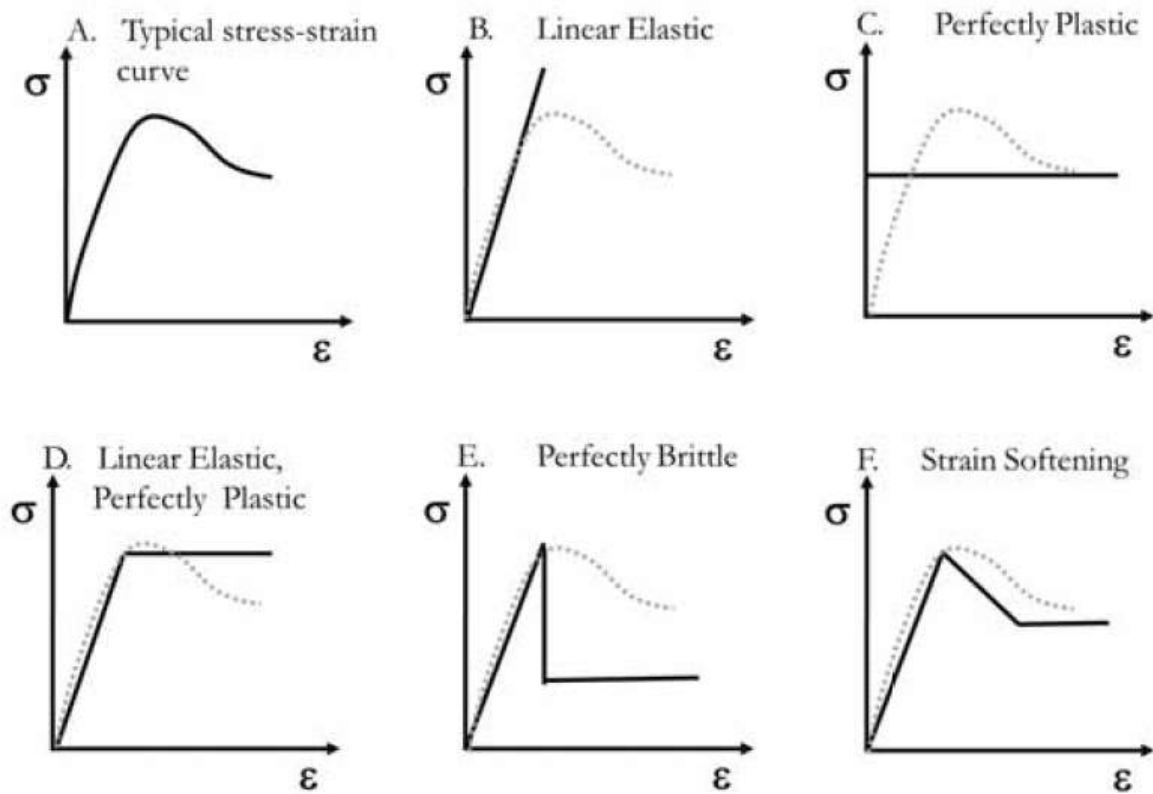


Figure 2.11: Idealised stress-strain curves representing different material behaviour used in numerical modelling (Sainsbury, 2012).

These idealised material models include the following behaviour:

- **Linear Elastic**

The simplest material behaviour assigned to a model is one that is linear elastic which is applicable for materials that are continuous, homogeneous and have no hysteresis upon unloading. Since infinite strength is given to the material using this model, it does not account for post-peak strength response. Rock only really exhibits linear elastic behaviour up to a certain point (the yield stress), which is followed by plastic deformation.

- **Perfectly Plastic**

When straining occurs in this model, it does so indefinitely at a constant stress value. The failure stress is represented by the yield stress which is related to the ratio of plastic strain. In this model, the main assumption is that the stress causing permanent strain must reach a specific value before any contraction or extension can occur. When a rock behaves as such, it is termed to ‘perfectly plastic’ because deformation occurs in-elastically at this yield stress.

- **Linear Elastic-Perfectly Plastic**

An elastic-perfectly plastic material represents its stress-strain response by two lines describing the initial elastic stiffness until the point that yield stress is reached.

Following the point of yield stress, plastic strain occurs constantly at this value as described previously. Rock tends to behave elastically before reaching a yield stress however does not deform in a ‘perfectly ductile’ manner as assumed in this model.

- **Perfectly Brittle**

Rocks that conform to stress-strain responses similar to Figure 2.11(E) are termed ‘perfectly brittle’ materials. In this case, the stress-strain curve is almost linear at all levels of stress up to the point of final fracture. Brittleness is observed in this stress-strain curve when the strength of the material drastically decreases, shown by the instant drop in stress. This drop in stress usually reaches a residual value at which plastic deformation occurs at a constant stress.

- **Strain-softening**

After the stress has surpassed the elastic range; the rock mass yields and continues to yield whilst the peak strength is reduced to a residual value. This model best describes the yielding of a rock mass in the process of caving as it considers the progression of strength reduction. A strain-softening model was used by Pierce et al. (2006) to simulate the process of gradual failure and rock disintegration of jointed intact rock to its bulked state during cave propagation. An example of this is displayed in Figure 2.12.

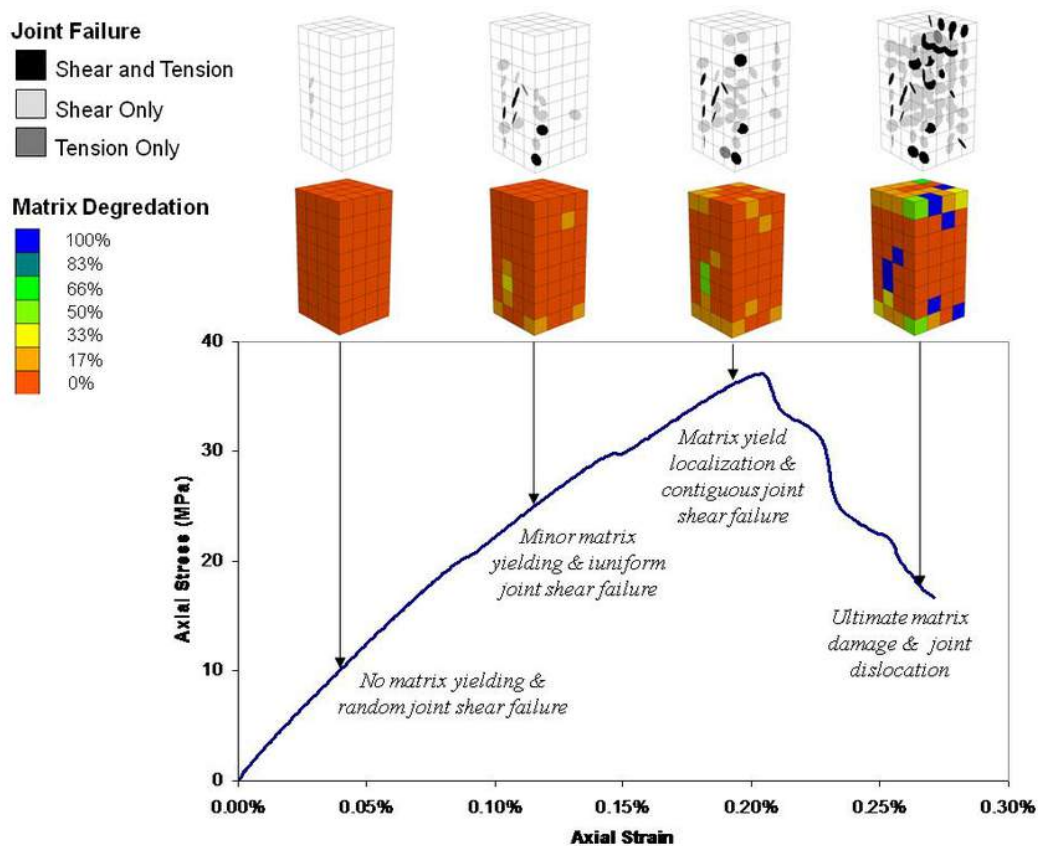


Figure 2.12: Damage stages of a three-dimensional, strain-softening specimen (Pierce et al., 2006).

2.2.5 The Mohr-Coulomb Model

If one was to plot linear fits of Mohr-Coulomb on a Hoek-Brown failure envelope in principal stress space (σ_1 vs σ_3), then it would clearly be shown that as confinement decreases, friction increases (along with an observed decrease in cohesion). This is shown in Figure 2.13. This graph indicates that there is an effect of the level of confinement on friction and cohesive strength.

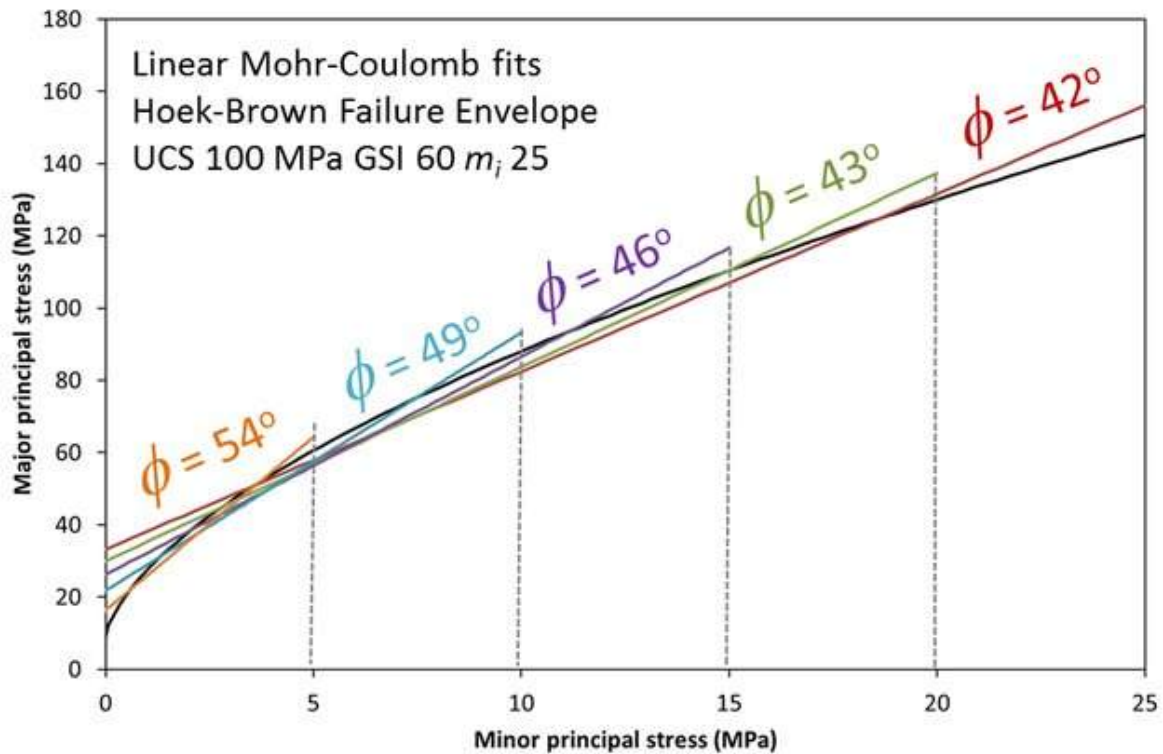


Figure 2.13: Development of equivalent linear Mohr-Coulomb strength parameters based on a fit to the Hoek-Brown strength envelope (Sainsbury, 2012).

From an investigation into the factors of cohesion and friction, it can be shown from laboratory testing that these two Mohr-Coulomb parameters are not necessarily mobilised at the same time during specimen testing when enduring strains. The cohesive strength is first mobilised (earlier in the test) followed by the mobilising onset of the frictional component which requires higher degrees of strain to maximise (Schmertmann and Osterburg, 1960). Additional research shows that the response of a rock mass yielding is due to a dominant tensile failure mechanism during the propagation of pre-existing joints. Subsequently, friction (and dilation) is inhibited only until a failure plane generates (Diederichs, 2007). Furthermore, this concept has been scrutinised with regard to failure in laboratory specimens and neighbouring rock masses in underground openings. A relationship exists between the mobilisation of cohesive strength and friction to plastic strain (Hajiabdolmajid et al., 2002). This model is displayed in Figure 2.14.

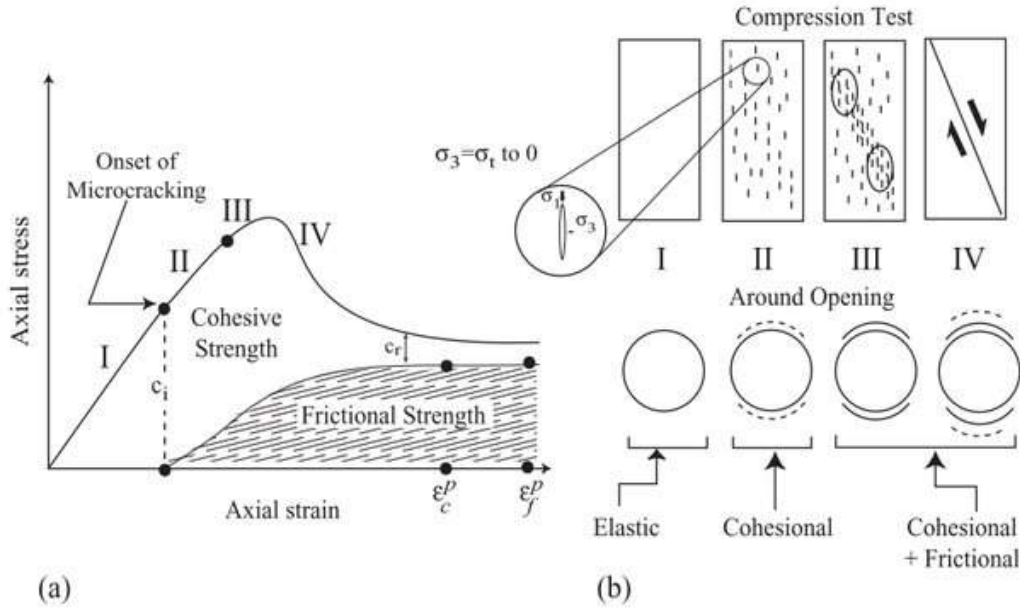


Figure 2.14: Schematic diagram of the mobilisation of the strength components cohesion and friction (a) in the laboratory (b) around an underground opening; c_i and c_r and ϵ_c^p and ϵ_f^p represent the plastic strain components when the friction and cohesion strength components have reached ultimate values (Hajiabdolmajid et al., 2002).

In order to obtain Mohr-Coulomb parameters as inputs for numerical modelling software programs, conversion equations can be used to obtain the friction angle and cohesive strength from Hoek-Brown parameters. These equations can be used over a specified stress range since the conversion is done by fitting an average linear relationship to the curve generated by solving the generalised Hoek-Brown equation (Equation 2.1) for this stress range of minor principal stresses. The approach used for curve fitting involves balancing the areas of stress above and below the Mohr-Coulomb line. When this is performed, the resulting equations for determining the respective angle of friction (ϕ) and cohesion (c) are as indicated in Equation 2.15 and Equation 2.16 for friction angle and cohesion, respectively. The range over which Equations 2.15 and 2.16 apply, is given in Equation 2.17:

$$\phi = \sin^{-1} \left[\frac{6am_b(s + m_b\sigma_{3n})^{a-1}}{2(1+a)(2+a) + 6am_b(s + m_b\sigma_{3n})^{a-1}} \right] \quad (2.15)$$

$$c = \frac{\sigma_{ci}[(1+2a)s + (1-a)m_b\sigma_{3n}](s + m_b\sigma_{3n})^{a-1}}{(1+a)(2+a)\sqrt{1 + \frac{(6am_b(s+m_b\sigma_{3n})^{a-1})}{(1+a)(2+a)}}} \quad (2.16)$$

Where:

$$\sigma_{3n} = \frac{\sigma_{3max}}{\sigma_{ci}} \quad (2.17)$$

It is important when making use of Equation 2.17 that σ_{3max} is the upper bound of stress whilst σ_{ci} is the lower bound over which the relationship between the Hoek-Brown and Mohr-Coulomb criteria is specified. The Mohr-Coulomb shear strength (τ) for a given normal stress (σ) is determined by the generic formula in Equation 2.18 and equivalently in terms of major and minor principal stresses in Equation 2.19:

$$\tau = c + \sigma \tan \phi \quad (2.18)$$

$$\sigma_1 = \frac{2c \cos \phi}{1 - \sin \phi} + \frac{1 + \sin \phi}{1 - \sin \phi} \sigma_3 \quad (2.19)$$

In the case studies used by Sainsbury (2012) in the validations of her models for cave propagation and subsidence, it was concluded that the utilisation of a bi-linear Mohr-Coulomb fit to the Hoek-Brown curve was capable of providing reasonable geomechanical property estimates of rock mass strength as well as softening responses.

2.2.6 Modified Mohr-Coulomb Characterisation

The traditional Mohr-Coulomb model is a popular strength criterion adopted in geomechanics but it suffers from two mentionable limitations. These include its inability to predict the non-linearity of rock mass strength and in its present form, it neglects the influence of the intermediate principal stress.

Considering the critical state concept for rocks by Barton (1976), it can be noted that when a rock is tested under confinement its strength increases with confining pressure. The rate of this increase; however, is highest at low confining pressure and decreases at higher confining pressures. Referring back to Mohr-Coulomb parameters, the instantaneous friction angle is, thus, highest at low confining pressure. This is owing to the dilatant and brittle behaviour of rocks at low confinements (Singh et al., 2011).

On a microscopic scale, the discontinuities in the rock open at the beginning of failure causing bulking. This increase in volume results in a higher friction angle at low confine-

ments. The opposite occurs at high confining pressures where the frictional angle is small due to inhibition of bulking (dilation). At higher confinements, the failure mechanism shifts from the brittle to the ductile mode. The mode of failure becomes entirely ductile at sufficient confining pressures and on further confinement, the rock enters critical state (Singh et al., 2011).

The failure envelope for rock in terms of shear and normal stresses is non-linear and concave downward. The slope of the envelope is steep near the shear stress axis and flattens for large normal stresses at which points it reaches a horizontal asymptote at a critical state stress.

Barton (1976) explains this phenomenon as the critical state of rocks: *“critical state for an initially intact rock is defined as the stress condition under which Mohr envelope of peak shear strength of the rocks reaches a point of zero gradient. This condition represents the maximum possible shear strength of the rock. For each rock, there will be a critical effective confining pressure above which the shear strength cannot be made to increase.”* This statement is also supported by Hoek (1983) who analysed triaxial results for Indiana limestone.

Figure 2.15 shows the flattened envelope of the Modified Mohr-Coulomb Failure criterion compared to the Mohr-Coulomb criterion. A conclusion to the studies conducted by Singh et al. (2011) is that response in strength at higher confinements causes deviation from the linear response of the original model. This non-linearity encountered by the modified version of the model holds importance when assessing rock strength at these higher confining pressures.

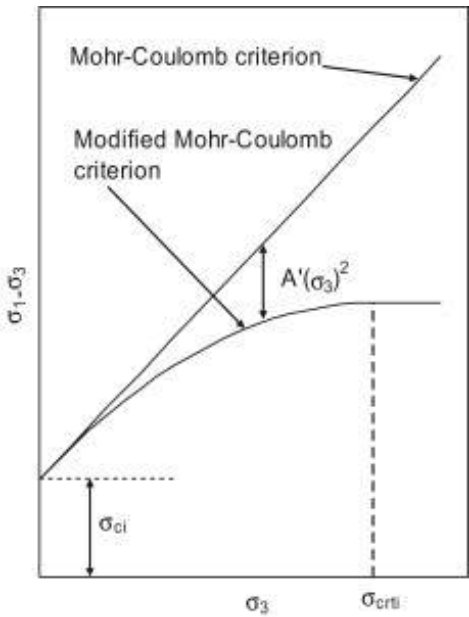


Figure 2.15: Modified Mohr–Coulomb criterion (Singh et al., 2011).

The general form of the modified Mohr-Coulomb criterion in principal stresses proposed by Singh et al. (2011) uses two parameters and can be given by the following Equations 2.20 and 2.21:

$$(\sigma_1 - \sigma_3) = \sigma_{ci} + \frac{2 \sin \phi_{i0}}{1 - \sin \phi_{i0}} \sigma_3 - \frac{1}{\sigma_{ci}} \frac{\sin \phi_{i0}}{1 - \sin \phi_{i0}} \sigma_3^2 \quad (2.20)$$

$$\sigma_{ci} = \frac{2c_{i0} \cos \phi_{i0}}{1 - \sin \phi_{i0}} \quad (2.21)$$

This equation is valid over a statistical range of $0 < \sigma_3 < \sigma_{ci}$ where $\sigma_{ci} \approx \sigma_{crit}$ (i.e. the critical confining pressure) and ϕ_{i0} is the internal angle of friction determined at low confining pressures. When utilising this modified Mohr-Coulomb criterion, the shear strength parameters are assumed to have been obtained from triaxial tests conducted at low confining pressures.

2.2.7 Extensional Strain Criterion

The Hoek-Brown and Mohr-Coulomb failure criteria and the various extensions and modifications made to their formulas are only concerned with the concept of stress. Moreover, the Hoek-Brown strength criterion was developed from the experiments of brittle rock failure conducted by Hoek (1968) and the use of parabolic Mohr-Coloumb envelopes which were derived from Griffith's crack theory (Griffith, 1920) to define the relationship between normal and shear stress at fracture.

From the work of Handin et al. (1967) on brittle materials tests performed in compression, torsion and tension, it should be noted that although these popular failure criteria are used extensively, neither were considered satisfactory in all cases. In an investigation involving stress-fracturing around a deep level bored-tunnel conducted by Stacey and De Jongh (1977), it was concluded that making use of Mohr-Coulomb and Griffith criterion resulted in the over-prediction of strength which did not account for fracturing at lower confinements. Instead, a network of fractures formed in the sidewalls and ahead of the rock face with their correct orientations and severity correctly predicted by the simple extension strain criterion which is a fracture initiation criterion developed by Stacey (1981).

In the work completed by Kirsten et al. (1979) regarding the control of fracturing in ore passes, it was reported that failure was not always anticipated by Mohr-Coulomb theory but, instead, by the extension strain criterion. Similarly, Waldeck (1979) found that in the design and support of large underground chambers, the potential fracture zones were more accurately predicted by elastic stress analysis and extension strain criterion over popular conventional methods when observations were made.

The research of Stacey (1981), which provides an alternative method for determining fracture initiation in brittle materials, has in some cases provided more satisfactory predictions over the stress-related failure criteria mentioned previously. It is important to note that the term ‘fracture’ used in the work of Stacey (1981) refers to the failure process whereby new surfaces are formed in a material or existing surfaces (cracks) are perpetuated. The extensional strain criterion is described as follows: initial fracturing of brittle rock will occur at the point where total extensional strain in the rock exceeds the critical value applicable for that particular rock-type (given in Equation 2.22). In other words fracture initiation simply begins when:

$$e \geq e_c \tag{2.22}$$

Where:

- e = strain applied/experienced by the rock mass
- e_c = value for critical extensional strain characteristic specific to the rock-type

Formation of fractures reported in planes perpendicular to the direction of extensional strain which correlates to the same direction of the minimal principal stress. Equation 2.23 relates the strain in this direction to all three principal stresses for linear-elastic materials:

$$e_3 = \frac{1}{E} [\sigma_3 - \nu(\sigma_1 + \sigma_2)] \tag{2.23}$$

Where:

- e_3 = Extensional strain
- σ_1, σ_2 and σ_3 = Major, intermediate and minor principal stresses, respectively
- ν and E = Poisson’s ratio and Elastic Modulus of the rock, respectively

From the expression of Equation 2.23, the term $v(\sigma_1 + \sigma_2)$ can be larger than the minor principal stress (σ_3). When this is true, extensional strain will occur, even in the case that all three principal stresses are compressive (i.e. when the net macro-stress is compressive). Equation 2.23 accounts for the intermediate principal stress (σ_2), which is not the case in Mohr-Coulomb-type and Griffith failure criteria.

In the research of Li and Wong (2013), Equation 2.23 was altered to neglect the effect the intermediate principal stress to allow for evaluating the critical extensional strain by means of the Brazilian disc test. At the centre of the Brazilian disc specimen surface, the major and minor principal stresses can be solved by Equations 2.24 and 2.25, respectively.

$$\sigma_1 = \sigma_r \approx \frac{-3P}{\pi Rt} \quad (2.24)$$

$$\sigma_3 = \sigma_\theta \approx \frac{+P}{\pi Rt} \quad (2.25)$$

Where:

σ_r = Radial stress (or major principal stress) in the Brazilian disc specimen

σ_θ = Circumferential stress (or minor principal stress) in the Brazilian disc specimen

P = Applied load

R = Disc specimen radius

t = Disc specimen thickness

Carrying out the method of Li and Wong (2013) by substituting these principal stresses into Equation 2.23, the extensional strain normal to compressed diameter can be evaluated for Brazilian disc specimens using Equation 2.26.

$$e_3 = \frac{1 + 3v}{E} \frac{P}{\pi Rt} = \frac{\sigma_\theta}{E} (1 + 3v) \quad (2.26)$$

Equation 2.26 shows that the extensional strain experienced at the centre of Brazilian disc specimens is larger than the value of σ_θ/E and is a function of the Poisson's ratio of the rock material. According to the critical extensional strain criterion of Stacey (1981), when $e_c \geq e_3$, an extension fracture will propagate in the disc specimen. The reason for the modification to Equation 2.23 as explained in Li and Wong (2013) is that the difference between the required tensile stress defined by the critical extensional strain criterion and

that which is measured conventionally (i.e. reported values for tensile stresses of rocks). This difference suggests that tensile cracks might have first initiated at the location where the tensile strain equals the critical extensional strain for rock specimens during Brazilian disk testing.

An example of such a difference can be shown in quartzite rock, where a Young's modulus and Poisson's ratio of 55 GPa and 0.10 can be assumed, respectively (Goodman, 1989; and Christen 1996). The critical extensional strain of quartzite is approximately 110×10^{-6} (Stacey, 1981). Using these values, a tensile circumferential stress (σ_θ) of 4.65 MPa can be back-calculated using Equation 2.26 which differs considerably from reported tensile stress values of quartzite that are above 10 MPa (Goodman, 1989).

In more recent literature, the studies of Benz et al. (2008), Sahouryeh et al. (2002), Colmenares and Zoback (2002) and Lee and Haimson (2011) concerning polyaxial rock failure for different rock types are similar in that they show a reduction in strength with increasing the intermediate stress under loading conditions where σ_1 and σ_2 have values that are of the same magnitude. From this observation, according to Wesseloo and Stacey (2016), it may be applicable to use the extension strain criterion as a failure criterion in some cases, particularly when the intermediate and major principal stresses are numerically similar.

An analysis was conducted by Wesseloo and Stacey (2016) to apply the extensional strain criterion to the published polyaxial data for different rock types in comparison to the Hoek-Brown model. It was observed that when the extension strain values were applied as a failure criterion to the rock types of the polyaxial data used in their study, the values were dependent on stress level. Lines for the extension strain criterion were superimposed on the polyaxial graphs of different rock types which resulted in constant e_3 values for discrete σ_3 values.

An example of this is shown in Figure 2.16 for polyaxial data for Shirahama Sandstone and KTB Amphibolite, respectively. This contrasts the original extension strain criterion used for fracture initiation. Upon plotting the ultimate strain values against the minor principal stresses (σ_3 vs. e_{3ult}), it was noted that relationship between them was linear. Further analysis indicated that the slope of these linear related parameters is directly proportional to the Poisson's ratio as well as to the rate of increase in strength with confinement. The intercepts of the σ_3 vs. e_{3ult} graph (which is the ultimate extension strain) linearly correlates to rock stiffness. More details can be found in Wesseloo and Stacey (2016).

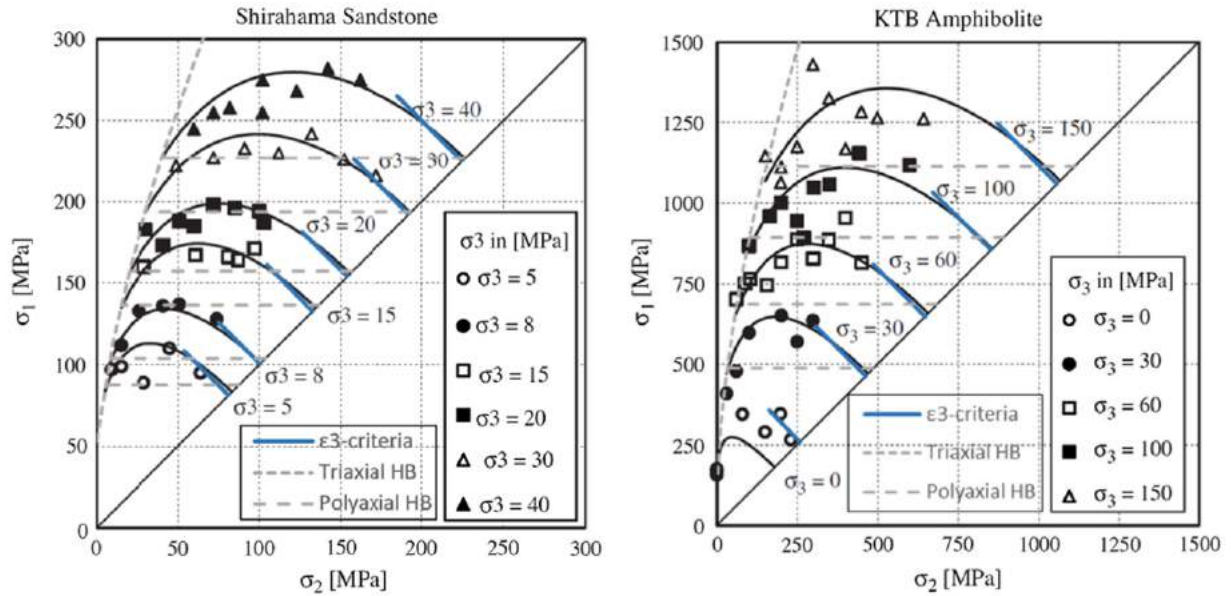


Figure 2.16: Polyaxial failure data for Shirahama Sandstone and KTB Amphibolite with the adaptation of Hoek-Brown strength criterion (Benz et al., 2008) and extension strain criterion (Wesseloo and Stacey, 2016).

From the conclusions of Wesseloo and Stacey (2016), the criterion is accurate in detecting fracture initiation in triaxial compression, specifically at low confinement levels where strength is over-predicted in conventional models and fracture orientation is not accounted for. The extension strain criterion is able to define the extent of potential zones of fracture as well as the orientations of these fractures. According to Wesseloo and Stacey (2016) this can be explained by the rock being ‘conditioned’ whereby converting the rock into a suitable condition for subsequent failure to occur by mechanisms usually other than extension.

An example given by Wesseloo and Stacey (2016) may be that the numerous orientated extensional fractures lead to the formation of pseudo-stratification in the rock, analogous to transverse anisotropy, which can cause the rock to fail in bending or buckling which was originally as a result of the ‘conditioned’ rock material. In other words, the extension fracturing (monitored by the criterion) can give rise to failure through various failure mechanisms and not only due to extension.

2.2.8 Hard Brittle Rock Failure

According to Bewick et al. (2011), the failure processes of hard brittle rock can be described by the various structural stages (or zones) given in Figure 2.17 which was previously investigated by Gramberg (1965).

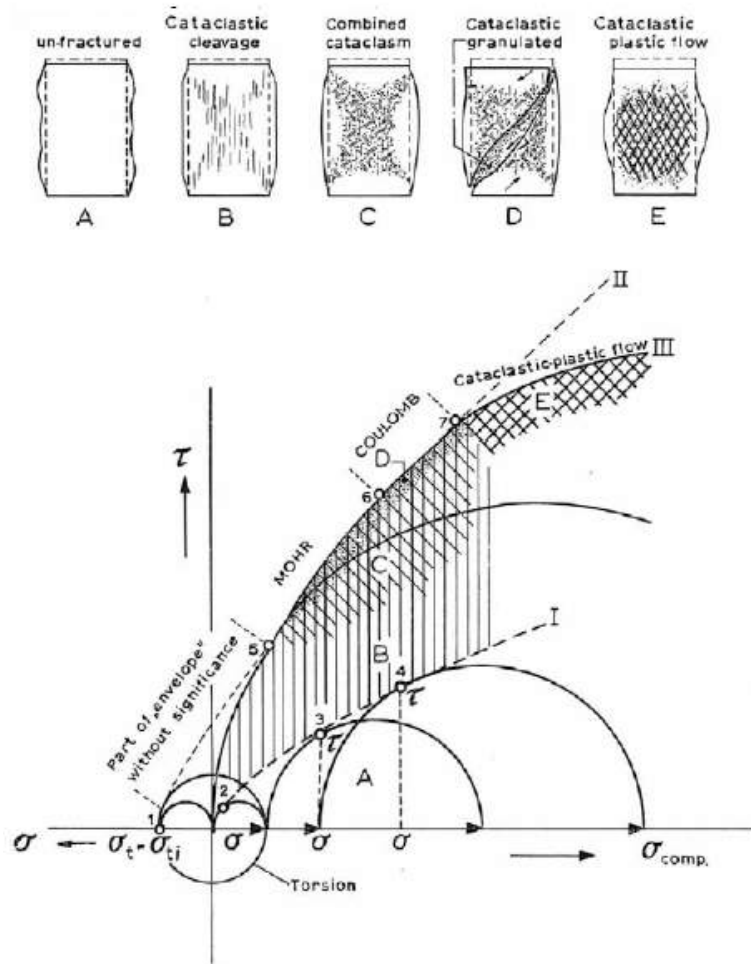


Figure 2.17: Mohr-circle representation of rock material passes through various structural stages when loaded in compression (Gramberg, 1965).

It is important to note that the term ‘cataclasm’ and ‘bulk cataclastic flow’ refer to a process whereby grain fracture leads to the collapse of local pores in the material (also called shear-enhanced compaction) which is typical at high confining pressures. Referring to Figure 2.17, the failure process for generalised hard brittle intact rock can be observed by linking it to stress state through distinct failure envelopes on the Mohr Diagram. The regions covered by these failure envelopes can be categorised by the following zones:

1. Zone A (un-fractured) consists of a region of un-fractured material which deforms either only elastically or plastically depending on whether the rock mass is intact or not. Stress distributions are almost always homogeneous and no change in structure occurs.

2. Zone B (cataclastic cleavage) tensile cracking occurs in the direction of loading which is referred to as cataclastic cleavage in Figure 2.17. At this point, permanent deformation causes the sample to become inhomogeneous as it expands laterally. Anisotropy commences from this zone.
3. Zone C (combined cataclasm) entails the combined effects of small cleavage fracturing and shearing zones which are consequent of tensile cracking and sliding movements. It should be noted that no cracks propagate in mode II or III of Figure 2.17 (Bewick et al. 2011). Cataclastic plastic flow is promoted following tensile cracking and sliding movements and is initiated from collapse in Zone D.
4. Zone D (cataclastic granulated) involves collapse by secondary shearing through generating a cataclastically granulated rupture caused by tensile fracturing.
5. Zone E (cataclastic plastic flow) progresses at high triaxial compressive loads that result in shearing failure equal to that of Zone D.

2.2.9 Typical Rock Properties

A general summary of typical mechanical properties for various igneous, sedimentary and metamorphic rocks is given in Table 2.1. According to Ulusay (2014), the following statement with regard to the utilisation of the UCS test can be made: *“It is most useful as a means for comparing rocks and classifying their likely behaviour as an index property.”* The stress-strain curves for these same rock types have been re-drawn using a data-extraction tool (Rohatgi, 2020) in Figures 2.18, 2.19 and 2.20 which were obtained from UCS data from various sources mentioned in Table 2.1.

From Table 2.1, it can be observed that the relative densities of rock, except anthracite, are somewhat constant throughout the three rock types. With regard to the Young’s modulus of the three rock types, igneous generally show the stiffest values with the exception of the metamorphic rock, slate. Sedimentary rocks are generally the least stiff rocks according to the data and show the largest amount of porosity. The compressive and tensile strengths of the rock types are also dominated by the igneous rock examples of the table.

Generally, igneous and metamorphic rocks are stronger than most sedimentary rocks which is as expected in the curves shown in the figures. In this case, Basalt is the strongest rock of all those presented. One important observation is that the failure strain of igneous rock at peak stress is between 0.37 % to 0.51 % strain. For sedimentary rock, this is in the region of 0.28 % to 0.53 % and metamorphic rock fails around a strain range of 0.23 % to 0.43 %.

In order to gain an indication as to the failure range in terms of axial strain for typical rock in conventional triaxial compression, Figure 2.21 was included which exhibits the stress-strain response of sandstone. The axial strain at failure was below 2 % in this case.

Table 2.1: A general summary various rock type properties (from various sources*)

| Rock Type | RD | E (GPa) | η (%) | σ_c (MPa) | σ_t (MPa) |
|-------------------------|-----------|------------|------------|------------------|------------------|
| Igneous Rock | | | | | |
| Granite | 2.60–2.70 | 10.0–70.0 | 0.50–1.50 | 75–300 | 10.0–25.0 |
| Andesite | 2.50–2.80 | 20.0–50.0 | 10.0–15.0 | 69–211 | 9.99–24.13 |
| Basalt | 2.85–3.00 | 82.1–93.6 | 0.10–1.0 | 100–300 | 10.0–30.0 |
| Sedimentary Rock | | | | | |
| Limestone | 2.30–2.80 | 15.0–55.0 | 5.0–20.0 | 50–300 | 5.0–30.0 |
| Shale | 2.30–2.80 | 1.0–70.0 | 10.0–30.0 | 5–125 | 1.0–10.0 |
| Sandstone | 2.20–2.80 | 1.0–40.0 | 5.0–25.0 | 20–200 | 4.0–25.0 |
| Metamorphic Rock | | | | | |
| Slate | 2.70–2.80 | 11.3–105.8 | 0.10–0.50 | 100–200 | 7.0–20.0 |
| Marble | 2.40–2.70 | 50.0–70.0 | 0.50–2.00 | 100–200 | 8.72–10.1 |
| Migmatite Gneiss | 2.60–3.00 | 50.0–80.0 | 0.50–1.50 | 50–225 | 6.0–20.0 |

*Sources include: Aghamelu et al. (2011), Rodriguez-Sastre and Calleja (2006), Chen et al. (2016), Chuanliang et al. (2015), Zhang et al. (2015), Sygala et al. (2013), Brace et al. (1982), Li and Wong (2013), Briševac et al. (2015), Malik et al. (2018), Okubo et al. (2006), Meng et al. (2015), Xu et al. (2016), Siratovich et al. (2012), Rahn (1996), Ljunggren et al. (1985), Farmer (2012), Attewell and Farmer (1988) and West (2010).

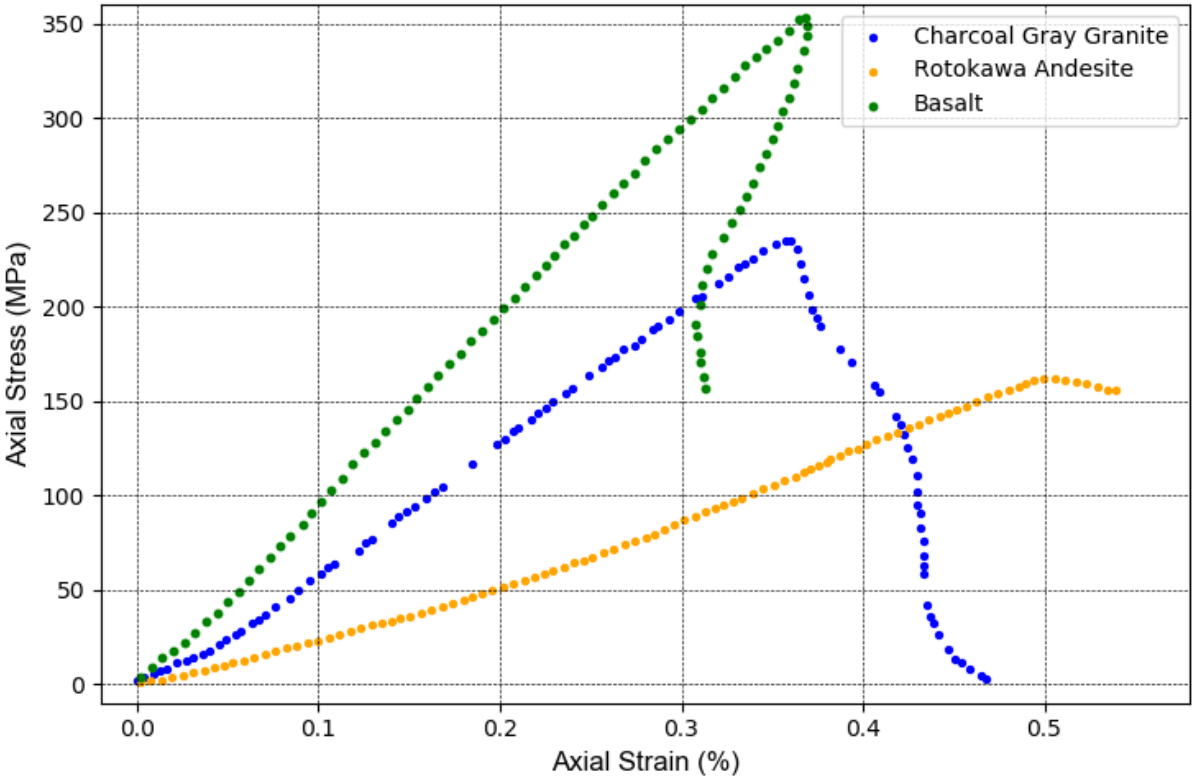


Figure 2.18: Typical UCS stress-strain curves for three igneous rocks (adapted from Wawersik and Fairhurst (1970) as well as Siratovich et al. (2012)).

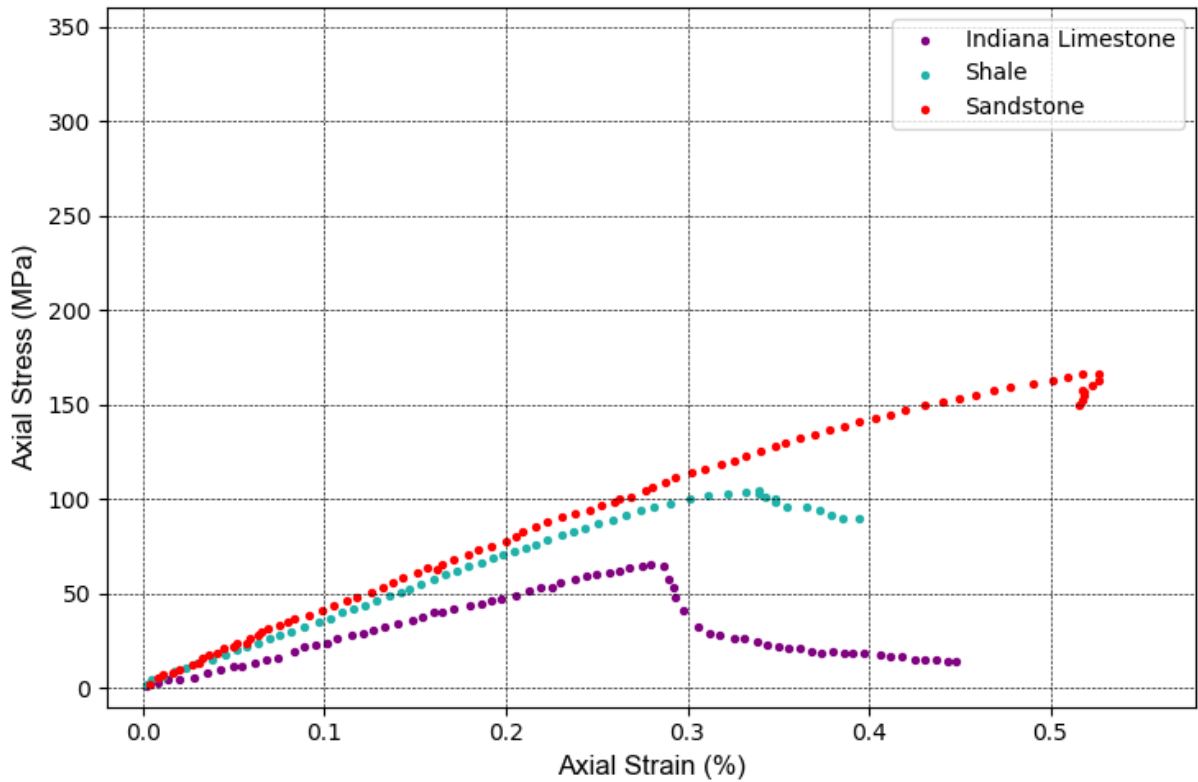


Figure 2.19: Typical UCS stress-strain curves for three sedimentary rocks (adapted from Wawersik and Fairhurst (1970), Chuanliang et al. (2015) and Sygala et al. 2013)).

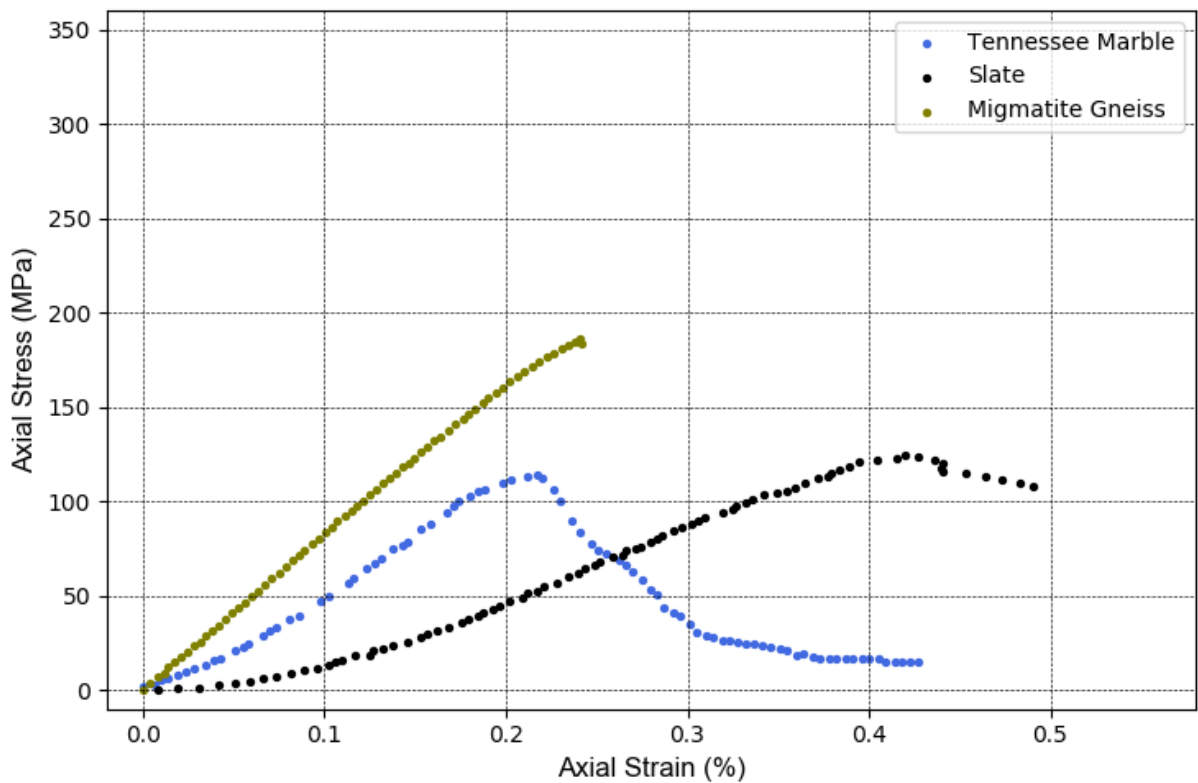


Figure 2.20: Typical UCS stress-strain curves for three metamorphic rocks (adapted from Wawersik and Fairhurst (1970), Chen et al. (2016) and Rao et al. (2011)).

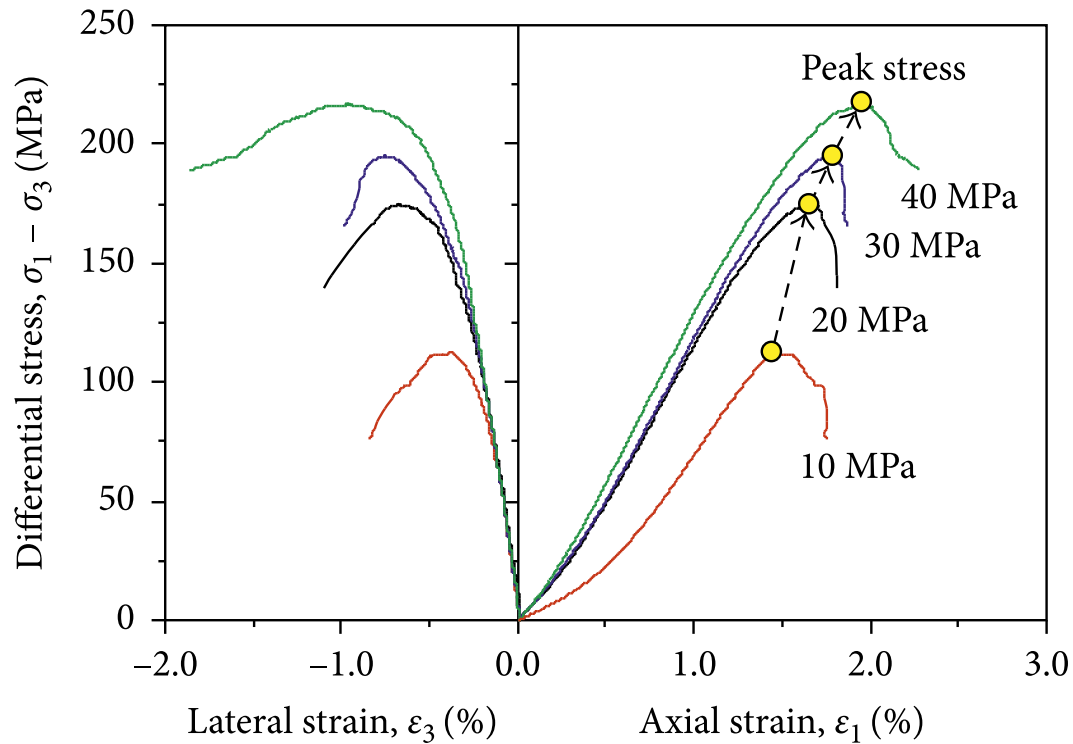


Figure 2.21: Typical triaxial compression test stress-strain curves for sandstone (Li et al., 2018).

Table 2.2 contains examples of rock types for which the critical extensional strain values are provided. Incidentally, these appear to be slightly less than the failure strains of the reported UCS tests which is to be expected. These were obtained from the laboratory tests of Stacey (1981), where the simple strain criterion was developed. Figure 2.22 provides the Poisson's ratio ranges for various rock types.

Table 2.2: Examples of critical extensional strain values for various rock types (Stacey, 1981).

| Rock Type | Core Size | Specimen Length/Diameter ratio | Extensional Strain (%) |
|---------------------|-----------|--------------------------------|------------------------|
| Quartzite A | BX | 2 | 0.0120 |
| Quartzite B | BX | 2 | 0.0109 |
| Quartzite C | AX | 2 | 0.0081 |
| Quartzite D | BX | 2 | 0.0107 |
| Quartzite E | BX | 2 | 0.0130 |
| Lava A | BX | 2 | 0.0152 |
| Lava B | BX | 2 | 0.0138 |
| Diabase | BX | 2 | 0.0175 |
| Norite | NX | 2.5 | 0.0173 |
| Conglomerate Reef A | BX | 2 | 0.0086 |
| Conglomerate Reef B | BX | 2 | 0.0073 |
| Conglomerate Reef C | BX | 2 | 0.0083 |
| Sandstone | BX | 2 | 0.0090 |
| Shale A | BX | 2 | 0.0116 |
| Shale B | BX | 2 | 0.0150 |
| Shale C | AX | 2 | 0.0095 |

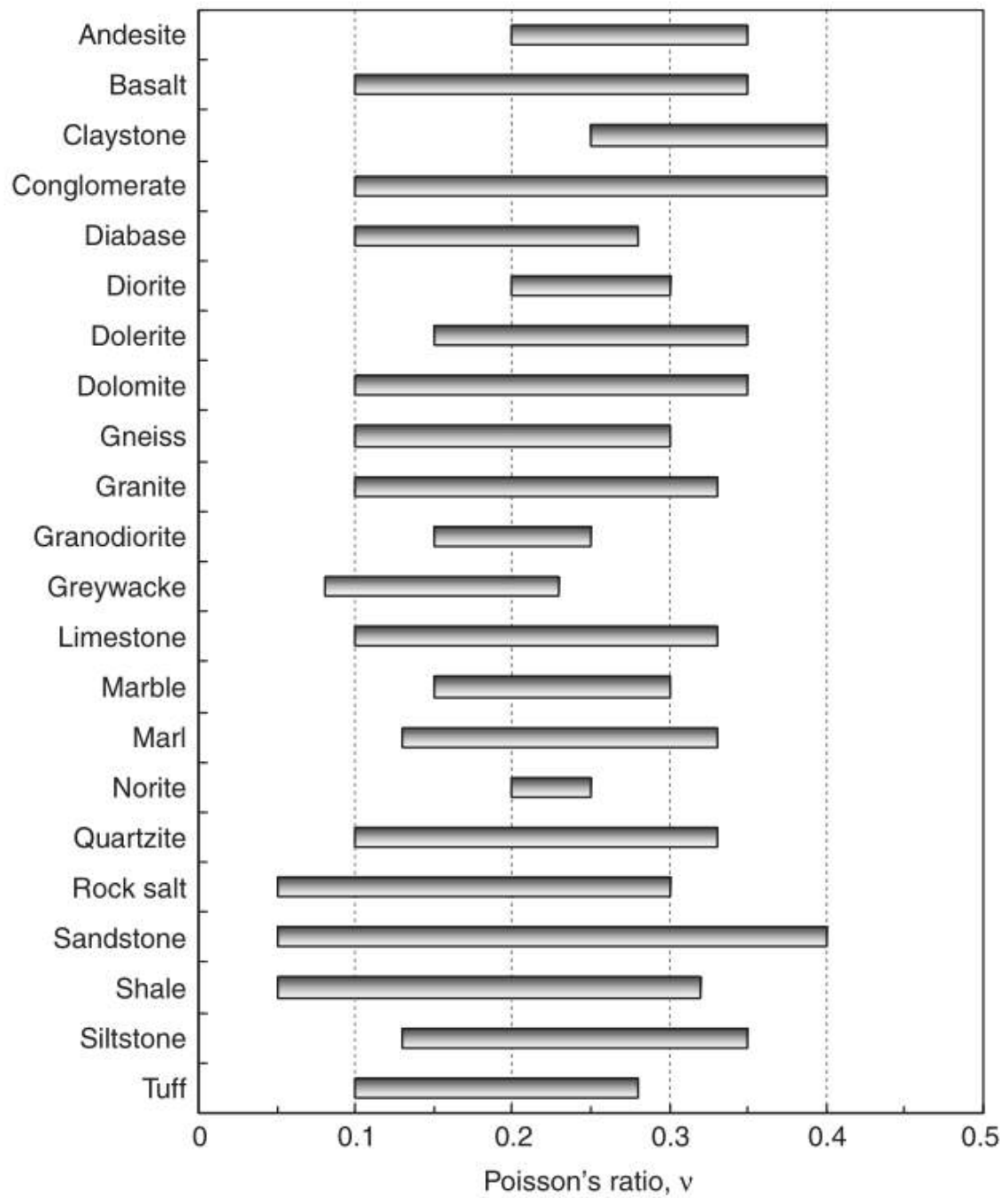


Figure 2.22: Typical ranges of values for Poisson's ratio of various rock types (Vutukuri et al. (1974), Hatheway and Kiersch (1986) and Gercek (2007)).

2.2.10 Synthetic Rock

In this section, the procedure of replicating rock on a weaker scale is discussed with regard to previously published literature. Table 2.3 shows various attempts in literature to model the brittleness and stiffness of rock for relevant applications using a variety of artificially manufactured materials (as reviewed by Stimpson, 1970).

Table 2.3: Summary of authors replicating rock-mass for various applications in literature

| Author(s) | Material | Application |
|-----------------------------------|---|---|
| Barton (1968) | Plaster of Paris / barytes, Plaster of Paris / red lead | Weak and dense materials investigated for proposed opencast mine model study simulation |
| Benito (1968) | Plaster of Paris and sodium citrate | Simulation of concrete for concrete model studies. Gives similar uniaxial compressive stress-strain curve to Brock's damp plaster |
| Brock (1959, 1960, 1964 and 1968) | Damp and Shellac sealed plaster | Simulation of concrete for models of reinforced shell concrete structures and bridges |
| Durelli and Jacobsen (1962) | Plaster / 200-mesh silica flour / sodium citrate | Brittle material for study of stress concentration factors in mechanical engineering components |
| Hobbs (1966) | Plaster of Paris / whitening, Plaster of Paris / Shellac, Plaster of Paris/mica | Materials investigated for simulation of rock for underground coal mine model study |
| Pancini (1961) | Plaster of Paris / barytes | Model study of dam and foundation of concrete arch dam |
| Patton (1966) | Plaster of Paris / kaolinite | Laboratory study of shear failure of idealised joints |
| Saucier (1961) | Plaster / pumice | Material studied for models proposed for study of effect of nuclear blasts on underground structures |
| Vorobjev (1963) | Plaster of Paris / lime | Simulation of rock for model studies of underground mines |

The following materials presented below are those used to replicate rock on a weaker scale:

- **Weakly Cemented Sands**

Cemented sands include an extensive range of materials; including those that are weak in nature comprising unconfined compressive strengths of below 100 kPa. They are the transitional zone between soil and rocks and often show characteristics of both extremes (Sitar and Clough 1983).

At the soil end of the spectrum, uncemented soils derive their strengths from particle interlock due to particle geometry (Dusseault and Morgenstern, 1979). At the rock end of the spectrum, the cementation between the carbonated sand particles provide strength (Sitar and Clough 1983).

It must be noted that cemented sands are capable of resisting stresses that are compressive and shear in nature in the same way as uncemented sands. Furthermore, in contrast, cemented sands can resist a minimum degree of tensile stress due to their cohesion (brought about by the degree of cementation or particle interlocking effects) — the latter of these playing an important role in the material's relative strength and slope stability (Martins et al., 2005).

Irrespective of where the cohesion originates from, the end effects are as follows: cemented sands can form steeper and higher slopes than uncemented sands with the failure of cemented sands being more brittle in nature (Collins and Sitar, 2009). According to Collins and Sitar (2009), linear Mohr-Coulomb strength envelopes are only applicable over certain ranges of stresses. Friction angles are the same for both cemented and uncemented soil whereas cohesion must be defined as a function of degree of cementation and particle interlock due to the shape and orientation of the particles that provide bonding surfaces. Brittle failure tends to occur at low confining stresses and at low strains (generally from 0.5–2 %) with higher confinements showing more ductility (Collins and Sitar, 2009). Tensile strengths are typically 10 % of the UCS from the analyses of Clough et al. (1981) and Das et al. (1995).

From the research and laboratory testing done by Collins and Sitar (2009), the contribution of strength parameters to slope stability in cliffs include the following: the UCS evaluates the cohesion of the soil which originates from the degree of cementation and particle interlock. Failure of cliffs containing weakly cemented sands (i.e. a low UCS); are more likely to be governed by their frictional component. Conversely, the behaviours of moderately cemented soils (i.e. high UCS) are more likely to be governed by their cohesion component (and potentially their tensile strength).

- **Plaster of Paris**

Plaster of Paris is a brittle solid substance made up of hydrated calcium sulphate and has fracture properties similar to that of cement, sandstone and porous ceramics. It allows for different formations to be achieved by being moulded and shaped. Once hardened, it can be used as a material to study brittle behaviour through macroscopic crack propagation.

According to Vekinis et al. (1993) the use of this material is applicable in simulating the spalling of rock material in boreholes which holds relevancy to the mining industry. When plaster of Paris is hydrated, water is absorbed generating the production of gypsum. The exothermic reaction initiates, causing an orderly formation of interconnected needle-shaped crystals. Approximately 18.6 % of water is needed for hydration; however, more water is needed to give the plaster of Paris the correct consistency for casting. Excess water in the mixture evaporates which allows for a significant amount of porosity upon setting. The arrangements of the gypsum crystals in their hardened state cause a 0.5 % expansion in volume.

Vekinis et al. (1993) conducted a study whereby the mechanical properties of plaster of Paris were evaluated using plain specimens and specimens containing cylindrical holes. The mechanical properties of plaster of Paris were determined through laboratory testing for specimens with various densities. Properties evaluated in the investigation conducted by Vekinis et al. (1993) included the following: Young's modulus (four-point bending and uniaxial compression conditions), the modulus of rupture, fracture toughness (by four-point straight-edge-notched beams), uniaxial tensile strength and unconfined compressive strength. The investigation also involved biaxial and hydrostatic compression testing. A summary of the properties of plaster of Paris is presented in Table 2.4. Figure 2.23 shows the variance in pore diameter with density which inherently affects the Young's modulus of the material.

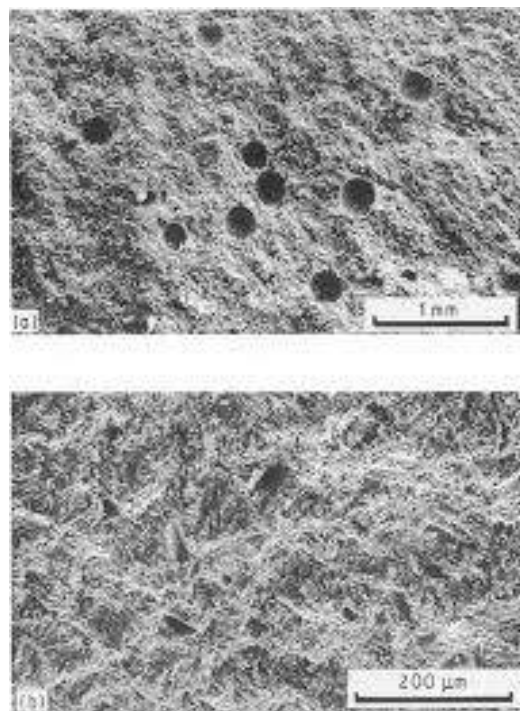


Figure 2.23: The structure of the plaster of Paris: (a) 50 % relative density and (b) 70 % relative density specimens (Vekinis et al., 1993).

Table 2.4: Material properties for plaster of Paris samples (cast with 62.5 % water).

| | Vekinis et al. (1993) | Dinsdale (1986) | Units |
|---|-----------------------|-----------------|----------------------|
| Physical Properties | | | |
| Theoretical density | 2350 | - | kg/m ³ |
| Density | 1170 ± 30 | 1060 | kg/m ³ |
| Total porosity content | 51 ± 2 | 50 | % |
| Mean diameter of spherical macropores | 212 ± 18 | - | µm |
| Mean grain size | 3 × 15 | - | µm |
| Mechanical properties | | | |
| Young's modulus (bending) | 4.5 ± 0.1 | - | GPa |
| Young's modulus (uniaxial compression) | 4.6 ± 0.3 | - | GPa |
| Modulus of rupture (four-point-bending) | 5.8 ± 0.6 | - | MPa |
| Weibull modulus | 6.2 | - | - |
| Fracture toughness | 0.14 ± 0.015 | - | MPa m ^{0.5} |
| Uniaxial compressive strength | 14.6 ± 0.9 | 12.8 | MPa |
| Hydrostatic compressive strength | 19.2 ± 1.4 | - | MPa |
| Uniaxial tensile strength | 3.2 ± 0.6 | - | MPa |

The investigation was extended by means of equibiaxial and hydrostatic testing of plaster of Paris. Cubed specimens were tested in equibiaxial compression using an Instron and SEM (scanning electron microscope) compression rig, while cylinders 10 mm high and 10 mm in diameter were tested under hydrostatic conditions in a Polytetrafluoroethylene (PTFE) capsule inside of a high pressure vessel. The schematic of this setup is shown in Figure 2.24. All specimens were characterised by a linear response up until fracture initiation which is indicative of the small steps in the curves given by Figure 2.25 (Vekinis et al., 1993).

The discussion of the results of the investigation can be summarised by Vekinis et al. (1993) in the following comments. When the specimens were removed from the pressure vessel at various pressures to be examined at stages during which they were tested, damage was observed to have initiated at the surface of pores and collapse tended to progress with the further fracturing of larger sections immediately beside pores. This fracture consisted of inward failure which filled the pores with crushed material. It was generally noticed throughout the study that pore collapse occurred before any material bulk fracturing.

Cylindrical holes of 0.5 mm were drilled into the centres of the 4.5 mm cubed specimens to closely study pore collapse during uniaxial and biaxial testing using an in-situ SEM compression machine. It can be noted that when these specimens are subject to biaxial compression, all principal stresses at and near the pores are zero or compressive.

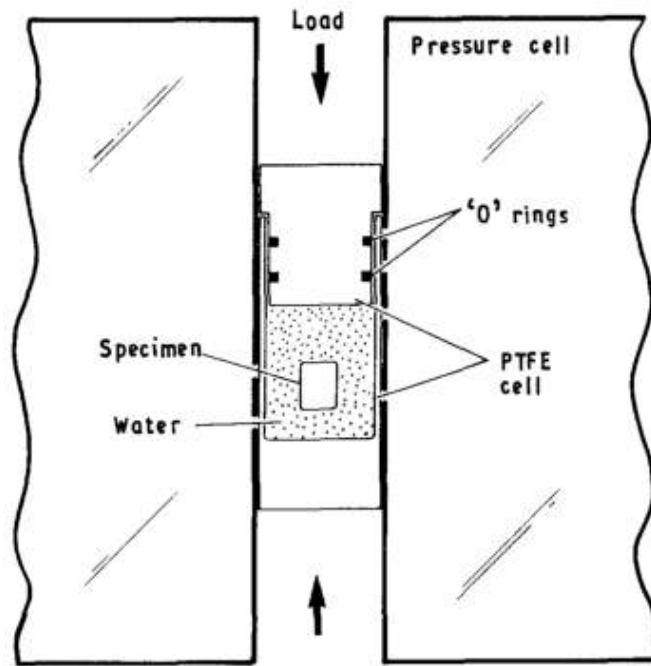


Figure 2.24: The PTFE cell used in the hydrostatic compression experiments (Vekinis et al., 1993).

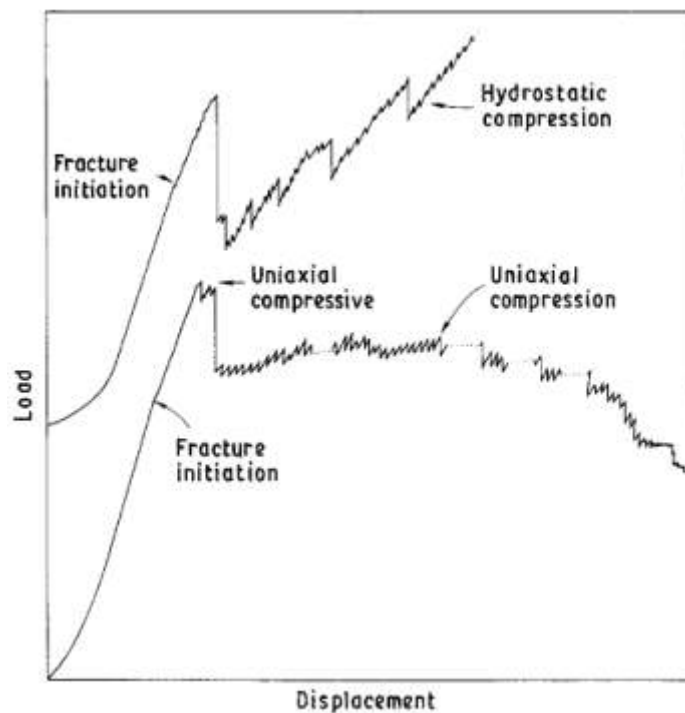


Figure 2.25: Load contraction curve for a specimen tested in uniaxial compression (lower curve) and in hydrostatic compression (upper curve) (Vekinis et al., 1993).

The testing was once again completed for a variety of densities (summarised by Figure 2.26) and aimed at studying the initiating and progression of cracking from holes and pores, under a multitude of stress states. Micro-graphs shown in Figure 2.27 (left) for the uniaxial compression specimens illustrate that some of the bulk fracture of specimens occurs prior to hole collapse. The hole then fails due to the rupture of the arc-shaped regions around the walls of the holes (indicated by Vekinis et al., 1993). The regions located specifically at the ‘equators’ of the hole are typically the highest in compressive stress. Vekinis et al. (1993) describes the collapse and fracture process as discontinuous in that the load required to continue failure lessens as with increasing strain (shown previously by Figure 2.25).

On the contrary, a small increase in lateral restraint — in biaxial testing — induces the combined effect of bulk fracture and hole collapse. Upon the commencing of equi-biaxial loading of the specimen, hole collapse was initiated before bulk fracturing occurred (this is shown in Figure 2.27 (right)). Vekinis et al. (1993) explains that as the specimen approaches an equi-biaxial state of stress, the collapse regions around the hole became more uniformly distributed. Finally, hole collapse occurs before the failure of the entire specimen which happened in a discontinuous manner. It can be reported that collapse observed in biaxial tests were more stable than those in uniaxial test cases. In other words, the magnitude of the load needed to sustain the collapse process either decreased very gradually or remained the same with increasing strain.

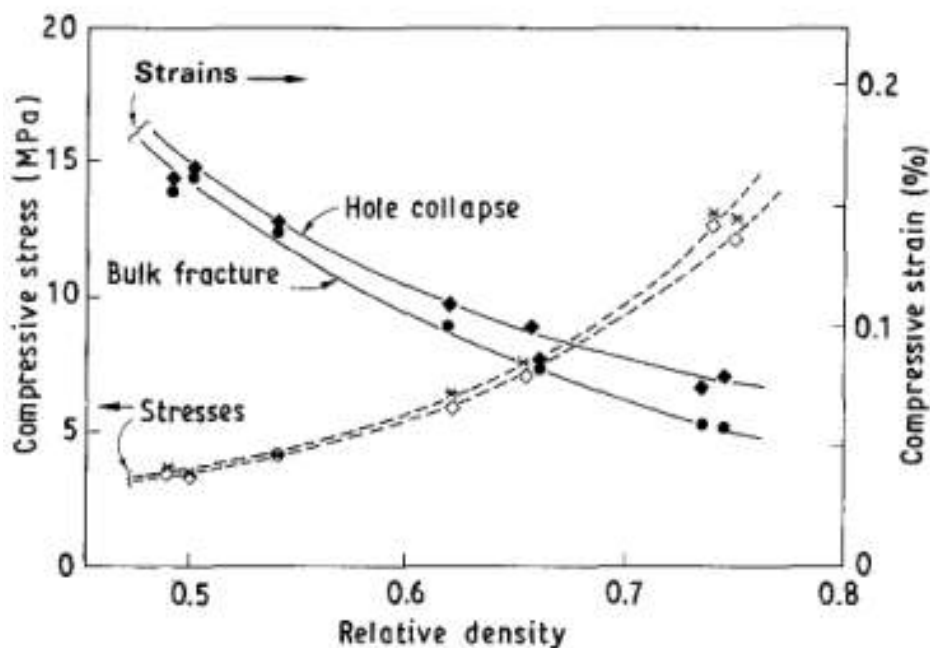


Figure 2.26: Fracture initiation and hole collapse initiation stress and strain as a function of relative density (Vekinis et al., 1993).

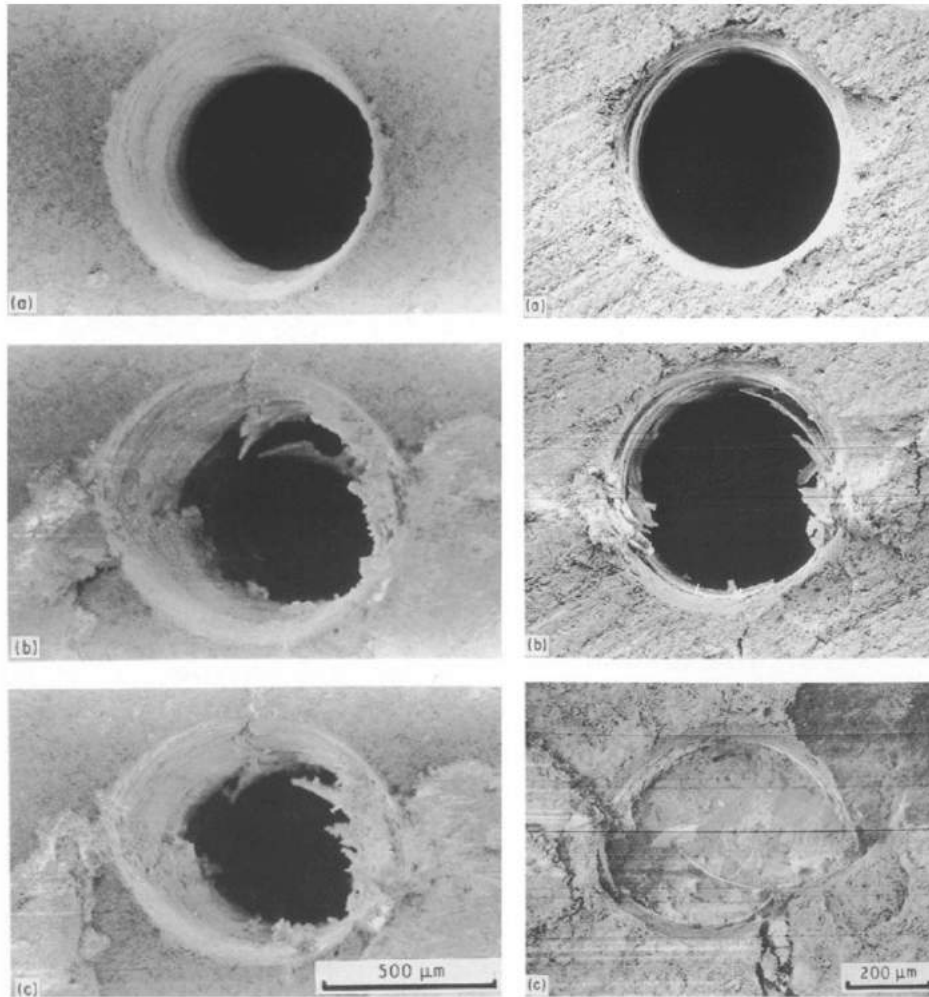


Figure 2.27: Micro-graphs for the uniaxial specimens (left) and biaxial specimens (right) (Vekinis et al., 1993).

Plots of the principal stresses (i.e. axial vs radial stresses) for typical plaster of Paris specimens in fracture initiation and final collapse are given in Figures 2.28 (a) and (b), respectively, for three relative densities. These plots illustrate the weak tensile strength of plaster of Paris and show a similar behaviour in comparison to rock-mass.

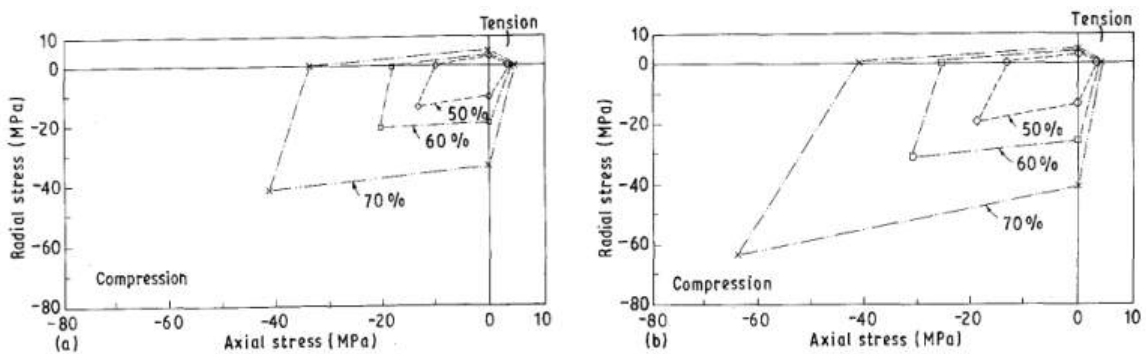


Figure 2.28: (a) Fracture initiation, and (b) final collapse surfaces for plaster of Paris, for three relative densities (Vekinis et al., 1993).

- **Geo-polymer Concrete: Kaolin and Fly Ash**

Geopolymers are alternative cementitious materials produced by the combination of source materials that primarily contain traces of the chemical compounds silica and alumina. Kaolin is a white clay powder made up of the mineral kaolinite which consists of layered silicates with one tetrahedral sheet of silica joined by oxygen atoms to a sheet of alumina octahedra (AlO_6). Under microscopic view, kaolinite is roughly hexagonal, composed of plate-like crystals that are approximately 0.1 μm to 10 μm in size. These crystals are characterised by a vermicular or book-like form as shown by the photo taken with an electron microscope in Figure 2.29 (left). Kaolin that naturally occurs in nature comprises certain amounts of other minerals including: muscovite, quartz, feldspar and anatase.

Fly ash is a grey fine powder which is a byproduct of burned, pulverised coal found in electricity generation power plants. It is a pozzolanic material (i.e. containing aluminous and siliceous material which is cementitious upon contact with water). When combined with lime and water, it becomes a compound similar to that of Portland cement. This well-known recyclable building material is readily used in concrete mix designs for replacing a certain percentage of the cement. Figure 2.29 shows the composition of the raw materials, kaolin and fly ash, under an electron microscope.

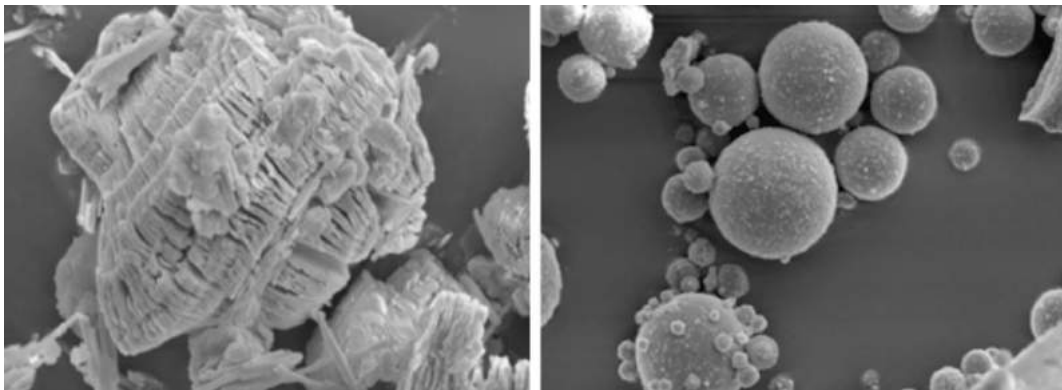


Figure 2.29: Microscopic images of Kaolin (left) and Fly Ash (right) side-by-side (Yahya et al., 2018). Scale not specified.

According to Razi et al. (2016) the driving force for research in geo-polymers was caused by the demand for more environmentally-friendly construction materials (mainly from coal-production processes and decomposition of natural resources). What makes geo-polymer materials so attractive are their properties of high compressive strength, fire, corrosion and thermal resistance and the fact that they can be sourced from waste materials in industrial processes.

Typical geo-polymer materials include fly ash, kaolin, slag, rice husk ash, palm ash and alkaline activators. In the last three decades, improvements to the quality of processing these materials particularly with regard to clay-based geo-polymers have occurred.

According to Heah et al. (2011), the use of kaolin as a geopolymer source material results in a weak structure owing to low reactivity where a certain period of time is required in order for strength-gain to be observed during geo-polymerisation process. This low reactivity of the kaolin is due to the shape of the particles themselves as the surface area thereof provides minimal dissolution of Si and Al with the usage of alkaline activator (Heah et al. 2012). The reaction always starts from the surfaces and edges and slowly penetrates inwards. Thus, it is not always able to reach all places within the structure due to the shape of the particles (Davidovits, 2008). It should be noted that this factor, along with the limited replacement of the other binder in the mixture during the reaction compromises the strength gain. Despite these limitations, kaolin does prove to have good volume stability when mixed with water and a compressive strength that increases gradually with ageing (Yahya et al., 2018).

Van Jaarsveld et al. (2002) indicated that when a high kaolin content (41 % by weight) was included in fly ash based geopolymer mix designs, the final product's strength was reduced. This was due to unused kaolin during the geo-polymerisation process for the reasons mentioned previously. However, in contrast, in the work conducted by Okoye et al. (2015), it was found that fly ash could be replaced by up to 50 % kaolin in fly ash based geo-polymer concrete to achieve a higher compressive strength. In the study, a replacement of fly ash with kaolin of less than 10 % caused a decrease in strength.

In an investigation conducted by Yahya et al. (2018), fly ash was replaced with different kaolin contents (from 0 % to 15 %) and the fly ash-kaolin geopolymer concrete was tested both destructively and non-destructively to identify the homogeneity of the two materials. The chemical composition of the two materials used in the study is given in Table 2.5. The geopolymer mixture used in the investigation consisted of an alkaline activator made of sodium silicate (Na_2SiO_3) and sodium hydroxide ($NaOH$) solution with a molar concentration of 12 M (i.e. mol/L). The ratio of the fly ash to activator was fixed at 1.5 to obtain a certain favourable consistency. The coarse aggregate and sand made up 70 % of the mass of the mixture. Fly ash was substituted by kaolin from 0 % to 15 % in 5 % intervals.

Table 2.5: Chemical composition of fly ash and kaolin by percentage mass (Yahya et al., 2018)

| Constituents | Fly ash (% mass) | Kaolin (% mass) |
|------------------------------------|------------------|-----------------|
| <i>SiO₂</i> | 55.9 | 54.0 |
| <i>Al₂O₃</i> | 27.8 | 31.7 |
| <i>CaO</i> | 3.95 | - |
| <i>Fe₂O₃</i> | 7.09 | 4.89 |
| <i>TiO₂</i> | 2.25 | 1.14 |
| <i>K₂O</i> | 1.55 | 6.05 |
| <i>SrO</i> | 0.37 | - |

The preparation of the mixture was as follows: fly ash was combined with kaolin and alkaline activator for approximately 3 minutes to ensure homogeneity. The coarse aggregate and sand was then inserted into the mix and cast after another 5 minutes of mixing. Concrete cubes of 100 mm x 100 mm x 100 mm in size were cast and vibrated for 5 minutes using a vibrating table to release entrapped air. Samples were left at room temperature (24 °C) for 7, 14 and 28 days to cure. The mix design of the geo-polymer concrete is given in Table 2.6. Note that KFA is an abbreviation for Kaolin-Fly-Ash with a number representing the percentage of fly ash replaced by kaolin (Yahya et al., 2018).

Table 2.6: Mix design of fly ash-based geo-polymer concrete (Yahya et al., 2018)

| Sample Name | Quantity of material (kg/m ³) | | | | | |
|----------------|---|--------|------|------------------|-------------|--------------------------------------|
| | Fly ash | Kaolin | Sand | Coarse Aggregate | <i>NaOH</i> | <i>Na₂SiO₃</i> |
| KFA0 (control) | 432 | 0 | 672 | 1008 | 82 | 206 |
| KFA5 | 410.4 | 21.6 | 672 | 1008 | 82 | 206 |
| KFA10 | 388.8 | 43.2 | 672 | 1008 | 82 | 206 |
| KFA15 | 367.2 | 64.8 | 672 | 1008 | 82 | 206 |

Three concrete cubes were tested in compression for each mix design as per the British Standards (BS. 1881: Part 166:1983) on days 7, 14 and 28. The rate of stress exerted on the sample in the hydraulic press machine was 0.3 MPa/s. Figure 2.30 shows the compressive strength of the various kaolin-flyash ratios for different ages. From the graph, it can be noted that the compressive strength increases progressively at 3 days for sample types KFA5 and KFA10, respectively. The compressive strength increases slightly with age as expected. The results conform to previous research in that early strength gain was observed and, significantly, at a more rapid rate than the control samples.

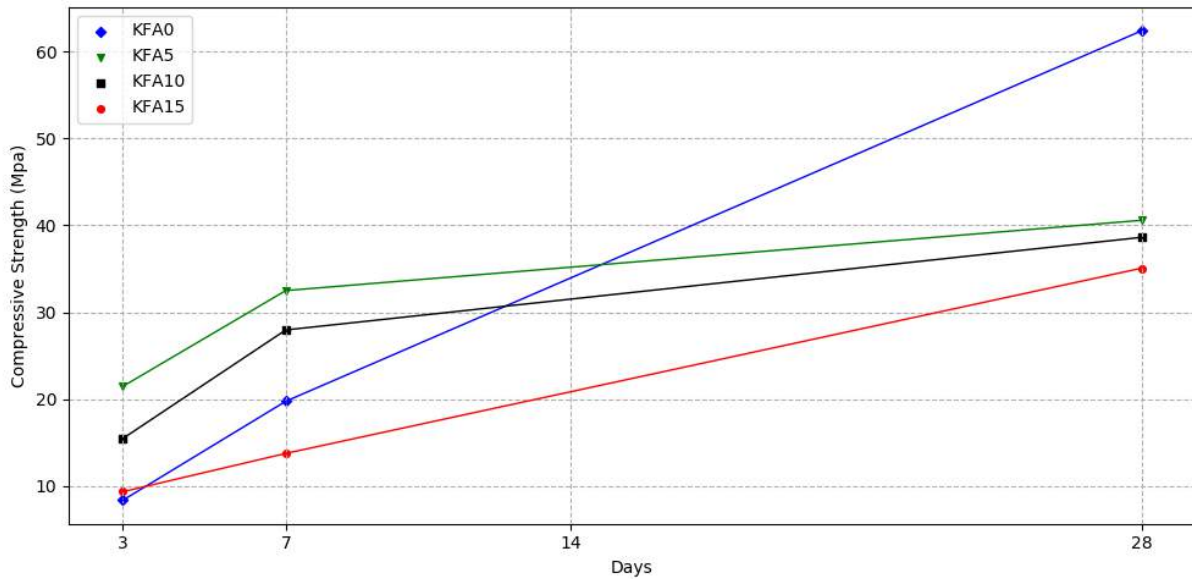


Figure 2.30: Compressive strength of geopolymer concrete with age (after Yahya et al., 2018).

The control sample (KFA0) displays an increase in compressive strength from 8.4 MPa at 3 days to 62.1 MPa at 28 days. At 3 days it is clear that the different amounts of kaolin affected the early age strength as all cases were higher than the control sample. It can be seen that the compressive strength is increased in the ageing of samples containing kaolin (especially at 7 days). Generally, the strength of the geopolymer samples increased only up to 5 % kaolin and decreased gradually past this point. In samples with higher kaolin contents, the mixture became stickier and the time for setting increased.

KFA5 yielded the highest compressive strength of 21.3 MPa and 32 MPa at 3 and 7 days, respectively. The control sample obtained the highest compressive strength after 28 days of 62.1 MPa and secondly KFA5 at 40.4 MPa after 28 days. The samples KFA10 and KFA15 showed greater compressive strengths than the control sample at 3 days (15.5 MPa and 9.2 MPa, respectively). This demonstrates that the inclusion of kaolin in fly ash-based geopolymer concrete can improve the early-age compressive strength up to a certain point and that the inclusion of more than 10 % retards the hardening of concrete and does not allow for added development in concrete compressive strength. In the same investigation, Yahya et al. (2018) claims that the quality of concrete in the geopolymer mixture declines as the percentage of kaolin is added because this contributes to increased porosity and anisotropy.

Weakly cemented soils seemed an ideal rock mass modelling material due to their significantly weaker strengths; however, samples were known to suffer from edge-effects which led to the pursuit of a suitable weaker geopolymer-based alternative.

2.3 Caving Mechanics

2.3.1 Fundamentals of Caving Mining Propagation

It is regularly understood that if a rock mass were to be undercut to a given extent, caving would be induced. The caving mechanism is influenced by the relationship between induced stresses, shape of the cave footprint as well as the strength and joint fabric of the rock mass (Brown, 2003). Thus, caving can exist as a result of two effects, described by Brown (2003), namely gravity and stress caving.

- **Stress Caving**

The phenomenon of stress caving occurs when the induced stresses in the cave back (roof of the cave) are greater than the strength of the material. Yielding and fragmentation of the rock mass into a caved state is the result of stress caving.

- **Gravity Caving**

Gravity caving is distinguishable by low mining induced stresses. Using the joint fabric of the rock and simple kinematics, gravity caving can be analysed. Gravity caving is usually dominant in the cave back as tensile failure mechanism during low stress conditions. Failure can take the form of slip along pre-existing rock discontinuities since the mass is unconfined underneath. Failure can also take place due to the deflection and bending of rock layers through Voussoir Beam Theory (Sainsbury, 2012).

Since gravity caving occurs in lower-end stress conditions, drawpoint fragmentation will be coarser due to the less damaged, less stressed rock mass during mobilisation. Figure 2.31 shows the stress paths followed for gravity and stress caving respectively. It can be noted that if mobilisation and the fragmentation of the rock mass resulted from yielding in the compression regime — which should be smaller and more numerous — then stress caving would have taken place. On the contrary, if the fragmentation is larger and blockier, then the resulted yielding rock mass would have been from failure of the tensile regime which points to gravity caving. The stress caving stress path touches the failure envelope on the compressive regime and the gravity caving stress path coincides with the failure envelope on the tensile region (not shown in this plot).

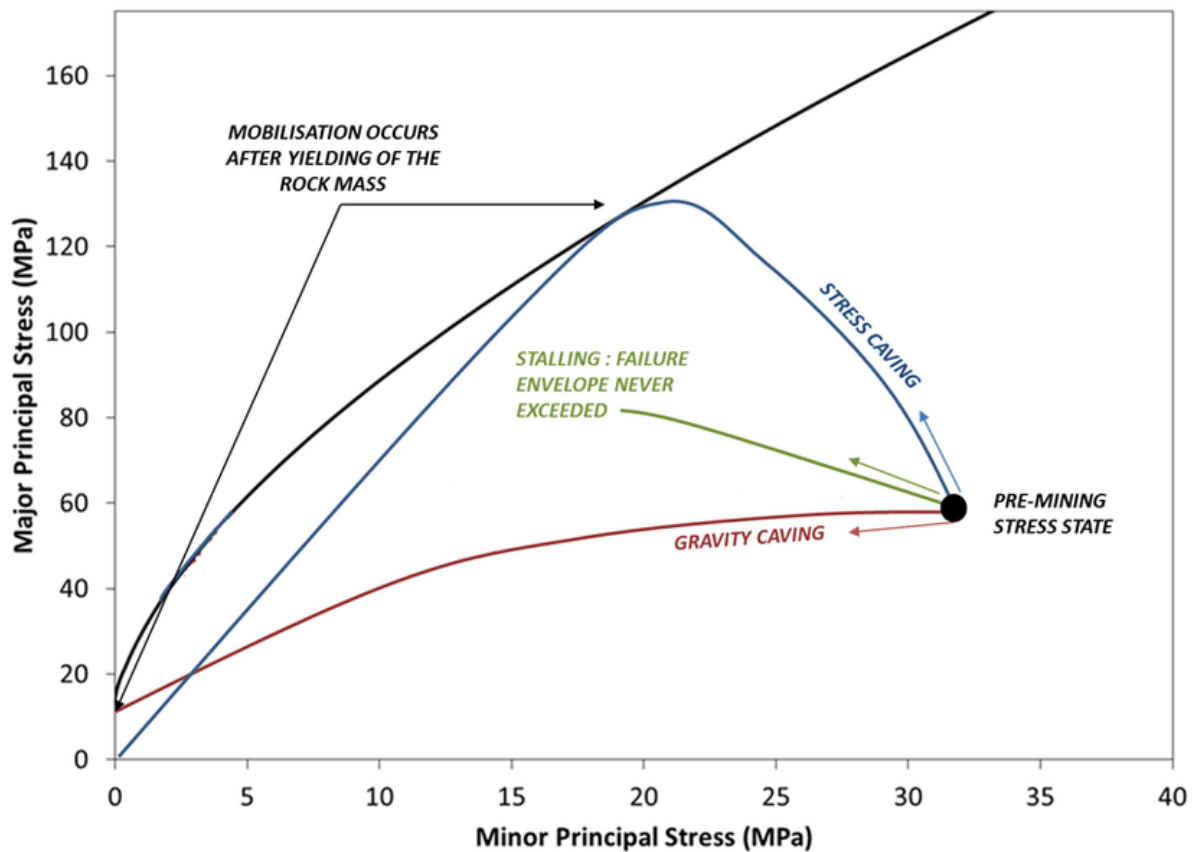


Figure 2.31: Typical caving stress-paths representing stress and gravity caving mechanisms (Sainsbury, 2012).

Self-sustaining cave propagation does not occur when a stable arch forms in the advancing cave back (cave stalling). In a case such as this, the induced stresses do not surpass the rock strength of the formed ‘rock bridges’ nor is it able to induce failure along the pre-existing fissures of the rock. Thus, stress corrosion, ground water ingress and other time-dependent processes will need to mobilise the cave stall that has developed. In most cases — to maintain production — artificial cave stimulation is necessary. Brown (2003) and Sainsbury (2012) have described a detailed concept of stress state that exists around the propagating cave (shown in Figure 2.32).

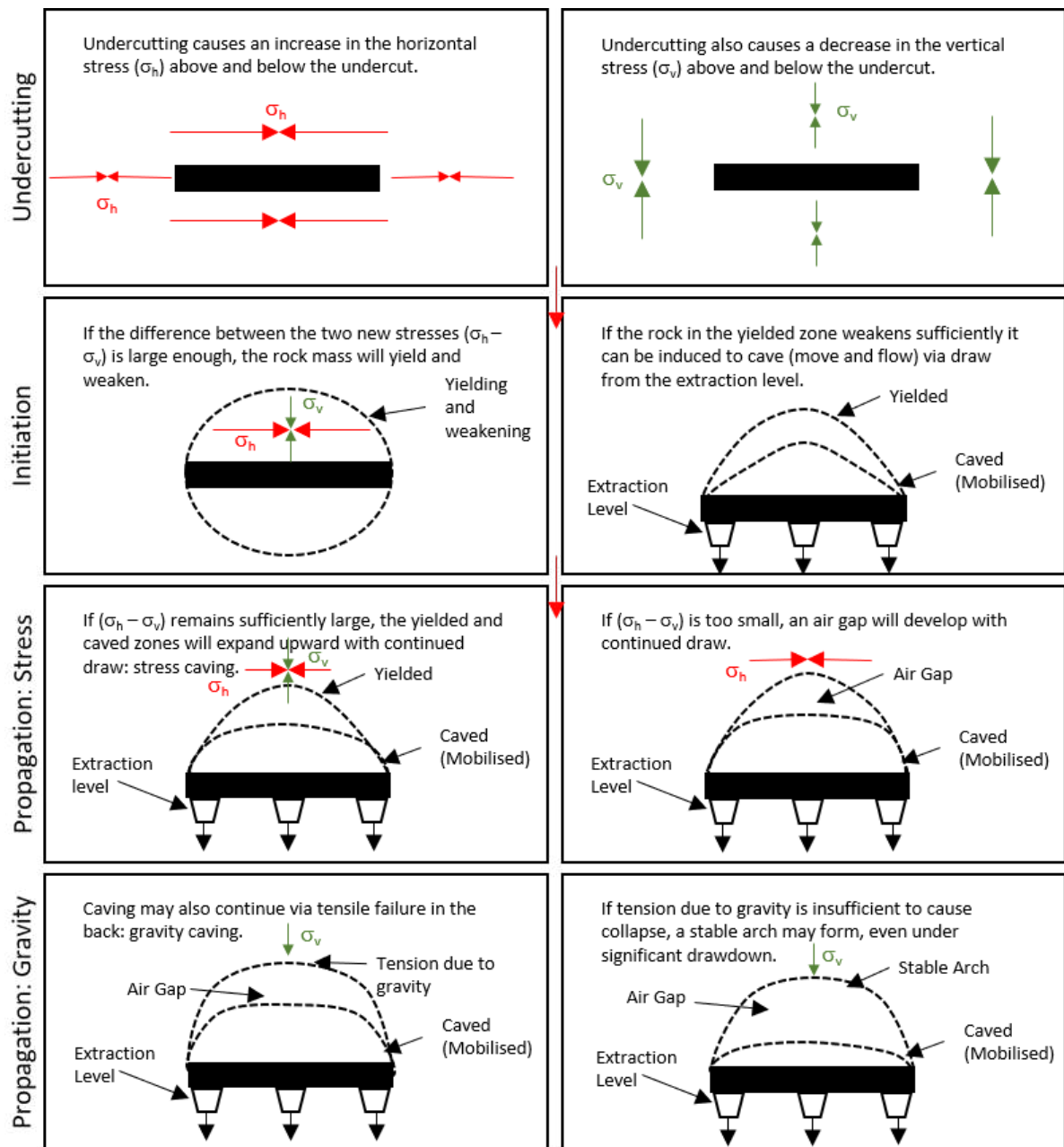


Figure 2.32: Conceptual stress-state development around a propagating cave (adapted from Sainsbury, 2012).

Focusing on Figure 2.32, stress and gravity caving mechanisms are impacted by seven critical factors with regard to cave propagation (Sainsbury, 2012). These are listed and elaborated upon below:

- **Cohesion and Weakening**

The peak in-situ rock mass strength is reduced during the occurrence of stress caving to its lower residual value. It is representative of the caved state of the material. This process is often referred to as strain softening and is the outcome of strain-dependent material properties.

- **Post Peak Brittleness**

Brittleness is the rate at which the peak strength of the material drops to its residual value within the rock mass. Rocks that retain their peak strength are considered to deform perfectly plastically (ductile failure). Furthermore, rock masses that have their peak strengths lowered to residual strengths are termed perfectly brittle. Generally, brittle rocks are more susceptible to caving than ductile ones.

- **Deformation Modulus**

Rock masses increase volumetrically during caving as intact rock fails, segregates and rotates when mobilised. This process can be referred to as bulking during which there is a cutback in deformation modulus. As bulking occurs the potential of the rock material for carrying stresses depletes.

- **Dilation Behaviour**

Dilation occurs when shear distortion takes place thereby changing the volume of the rock mass. When predicting the bulking behaviour and assessing the increase in volume of the air gap, it is imperative to accurately assess and model the dilation behaviour of the jointed rock mass at the start of and during cave propagation.

- **Rock Mass Jointing**

There is significance of geological structure on subsidence and cave propagation. If the rock mass has steeply orientated faults the angle of draw may be less than its normal value. Similarly, if the rock mass were to have shallower orientated faults which intersect the caving rock column, the lateral area of subsidence can spread outwards toward the fault that meets with the ground surface. It has been shown that despite rock joints and their geomechanical properties being inclined towards slipping — the presence of high horizontal confinement in-situ stresses can prevent the failure of rock and thus stall cave initiation and propagation (Brown and Trollope, 1970).

- **Production Draw Schedule**

There is a relationship between the rate of draw and the shape of the undercut for the behaviour of cave propagation (Laubscher, 1990). Furthermore, the caving propagation might be affected by the undercut footprint geometry (in its evolving state) relative to the principal stress direction. For example, if the undercut were to occur in a more centred position, cave back arching may be prominent. In this case, induced stresses will be larger; however, they will be limited to a minor portion of the cave back.

- **Other Excavations**

Other excavations that are present around the main cave being considered, may influence the induced stresses in the main cave. Caves adjacent to the main cave

tend to prevent the build up of mining induced stresses, whilst caves above (like an open pit) the main cave, might magnify the induced stresses and assist caving.

2.3.2 The Duplancic Conceptual Model

The failure mechanism that is most commonly accepted in industry is that of the Duplancic model. This model assumes that the damage ahead of the cave decreases upward from the point of the cave back and caving takes place mainly due to slip planes on pre-existing discontinuities. The manner of failure involves steps that lead to collapse of the material body. According to Duplancic (2001) a proposed model describing the zone of influence affected by cave mining is divided into the following five identifiable zones as shown in Figure 2.33:

- The *caved zone* which entails a zone of caved material that has collapsed from the cave back, providing some support to the walls.
- The *air gap* between the cave back and the caved zone.
- The *zone of loosening* which is made up of rock that is in a loosened state which does not provide support to the overlying rock mass. This is the zone of disintegration.
- The zone above this is the *stressed seismogenic zone* which is further up the cave back. Seismic fracture, as the name suggests, exists in the part of the rock mass which causes slip through pre-existing discontinuities.
- The last recognisable zone is that of the *pseudo-continuous domain*. This zone is above the seismogenic zone in which only elastic deformations take place.

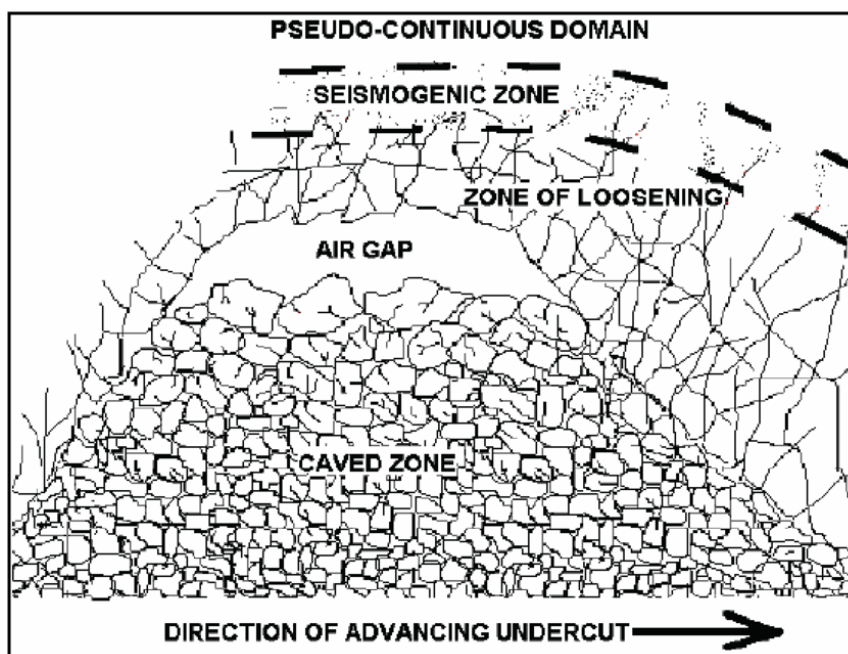


Figure 2.33: The influential zones of the Duplancic model (Duplancic and Brady, 1999)

Based on the inaccessibility of the caving zone in cave mines, direct observation of the process of cave propagation is not possible. As a result, this generally accepted model has not been thoroughly examined and confirmed (Cumming-Potvin et al., 2016a).

2.4 Empirical Cave Propagation Assessment

Empirical methods are still extensively used to predict cave propagation behaviour. The most common method of predicting cavability is based on a series of case studies - most forming part of the Kimberlitic (low strength) deposits in South Africa (Diering and Laubscher, 1986).

Laubscher's Stability Chart (shown in Figure 2.34) maps out three regions of possible outcomes; these include the 'stable' zone, a 'transitional' zone where cave initiation exists but with minimal propagation and a zone of 'caving' where self-sustained cave propagation takes place. Data points shown are labelled either by cave mining sites or types of rock mass.

The zones (or states) depend on the measure of rock mass strength using a parameter called the Mining Rock Mass Rating (MRMR) and the hydraulic radius of the undercut footprint. The MRMR is an in-situ rock mass rating (within 0–100) which is based from measurable geological parameters weighted according to significance. The Hydraulic Radius (HR) which can be defined as the ratio of the undercut footprint area to the cumulative undercut footprint perimeter length. The MRMR number was originally developed by Laubscher (1975), taking into account the intact rock strength, rock joint frequency as well as orientation, weathering, stress and blasting.

Laubscher's Stability Chart is still used to estimate the undercut dimensions required to induce self-sustained cave propagation which, in most cases, gives a good indication. There have been instances of conflicted reportings of significant differences between the actual and predicted cave behaviour (Lorig et al. (1995), van As and Jeffrey (2000), as well as De Nicola Escobar and Fishwick Tapia (2000)).

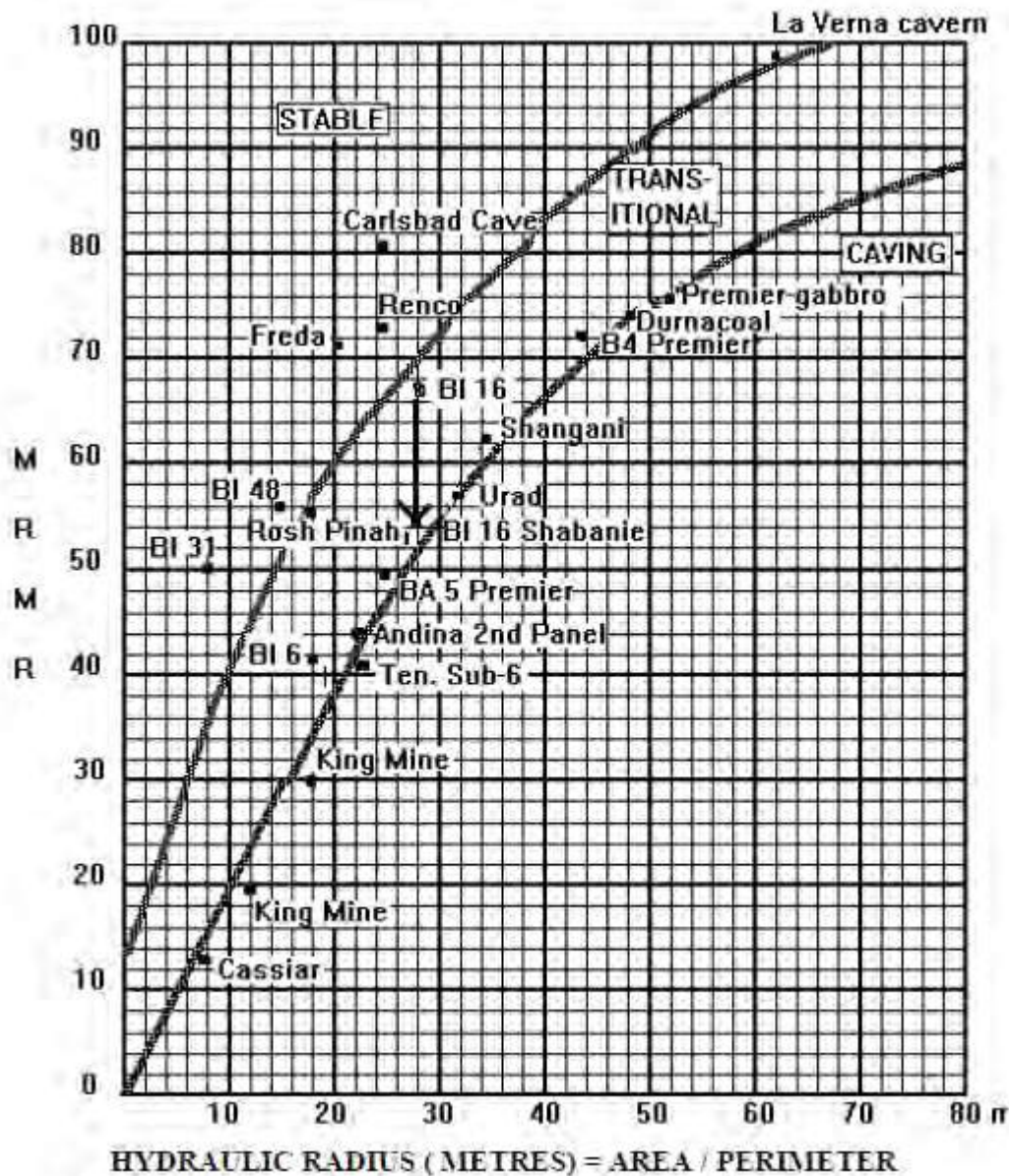


Figure 2.34: Empirical method for predicting caveability: Laubscher's Stability Chart (Laubscher, 1994).

Trueman and Mawdesley (2003) showed that the largest variance between actual and predicted cave behaviour was seen in the stronger rock masses (where the MRMR exceeded 50) and identified a misinterpretation of the application of adjustments in the MRMR rating. Subsequently they proposed an improvement for the prediction of self-sustained cave propagation by extending the empirical method to the Mathews slope stability chart (Mathews et al., 1981). This chart is shown in Figure 2.35. Two lines divide the zones which are analogous to those of the Laubscher's Stability Chart, namely: the 'stable' zone, 'failure and major failure' zone as well as the 'caving' zone.

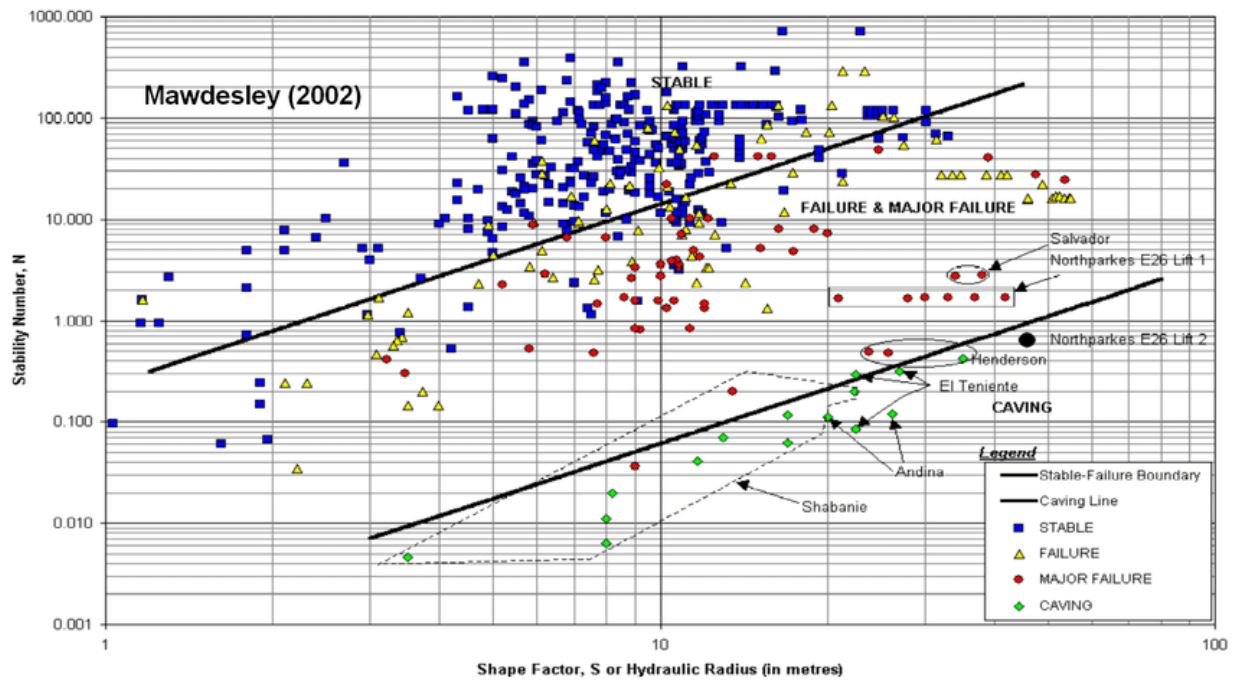


Figure 2.35: Empirical method for predicting caveability: Extended Mathews Stability Chart (Trueman and Mawdesley, 2003).

Despite this extension made to the method used for predicting cavability of stronger rock masses, the method is still limited by the nature of the data-set that it originated from. Furthermore, these methods developed by Laubscher as well as Trueman and Mawdesley (2003) were identified to have additional short-comings in that the approaches are only satisfactory for undercut footprints lengths to width ratios of three or less (Brown, 2003). Overall, this technique — suitable for initial estimations on cavability — cannot take into account three-dimensional stress redistribution around rectangular undercut footprints (Sainsbury, 2012). Further limitations include: only one joint set orientation can be evaluated and from experience, it is suggested that the critical joint set orientation varies around the undercut footprint due to the variation of principal stress direction during undercutting and cave propagation. Milne et al. (1998) indicate that the adjustment factors are misleading and could be subjective - which could lead to different caving behaviour predictions for the same data set.

The use of empirical methods, aside from the limitations listed previously, do not account for the rate at which caving occurs, nor the extent of caving behaviour in various regions. It can only be assumed that the extent to which a certain scenario falls into the caving zone is the measure of the amount caving that can take place. The actual timing, magnitude and impact made to underground infrastructure cannot be predicted since the bulking behaviour cannot be taken into consideration. Limited case study data restrict the application of empirical methods to scenarios in which large scale jointing, rock mass strength anisotropy, excavations and topographical relief or heterogeneous rock material domains do not exist (Sainsbury, 2012).

2.5 Physical Cave Propagation Assessment

2.5.1 Two-Dimensional Scaled Models

Physical modelling is a valuable tool for determining the failure mechanism of cave mining propagation in two dimensions which cannot otherwise (at least easily) be observed in the field (Cumming-Potvin, 2018). While this method of assessment is widely used for simulating earthquakes, tunnelling, foundations (shallow and deep), excavations, shafts as well as geomechanics involving gas and oil investigations (Gaudin et al., 2006; Randolph and Gourvenec, 2017), there have been attempts to physically model cave propagation and subsidence to simulate the mechanism of caving. It can be noted that past experimental studies have often had strong limitations which compromise their usefulness in understanding cave mechanics (Cumming-Potvin, 2018).

Little research has been done on the physical modelling of draw control, which is how the fractured material is removed from the caved zone to allow failure of the rock mass above it (Kvapil, 1965; Castro et al., 2007; Paredas and Pineda, 2014). The only previous research found in literature which includes the simulation of cave propagation is that of McNearny and Abel Jr. (1993), who used a two-dimensional model of layers of bricks (4.6 m in height) overlying a gravel base to investigate the effect of draw point spacing on cave propagation. The brick mass was then ‘undercut’ by drawing material from the bottom of the model. The bricks used in this experiment had a uniaxial compressive strength of 52.4 MPa which is notably higher than typical induced stresses. Thus, the model cannot be compared with the scale of block cave mines. Not only does the model inadequately represent environmental stress conditions found in cave mines (due to the absence of both horizontal confinement and overburden pressure), but cannot be used to predict the behaviour of intact rock failure because of the use of discrete bricks which do not represent the random nature of jointed rock (Duplancic, 2001).

The main purpose of the experiment conducted by McNearny and Abel (1993) was to study the effect of production draw and flow of undermined material. The observations were that as the bricks would 'peel off' the cave back and fall into the undermined material, deformation would occur deeper into the rock mass. This would take place at two to four brick depths from the cave back (McNearny and Abel Jr, 1993). The 'fractures' (analogous to separations of the bricks) occurred parallel to the caving void surface. This behaviour, which can be described as a discontinuous damage pattern, was also observed by Panek (1981) at San Manuel Mine.

Another model applicable to simulating cave propagation was that of Baumgartner and Stimpson (1979). This model took the form of a base frictional model aimed at observing the caving mechanism in a jointed rock mass. The material used to represent the rock mass was a mixture of flour and methanol. Once the synthetic rock material was set, joint sets were cut into the material at regular intervals. This could influence the model by causing a biased mode of failure (Cumming-Potvin, 2018). The experiment was conducted in a friction frame with only vertical pressure applied. The failure mechanism observed in the investigation was sliding, block-rotation, beam-column buckling and intact rock crushing within the model. An example of this is shown in Figure 2.36. It was noted that different failure mechanisms occurred simultaneously. Caving behaviour in this investigation was inconclusive.

The base friction model was improved when horizontal confinement stresses were included by using hydraulic jacks in the investigation done by Nishida et al. (1988). Although the focus of this study was the formation of sinkholes and related subsidence (or cave-ins) and not that of block cave mining propagation, the tests were representative of a shallow cave, where the material was not removed. The material had strengths of 4 MPa to 49 MPa with single jointed patterns that had different angles of dip. A hydraulic jack was used to pressurise the system which is not representative of cave mining conditions. Despite these differences, similarities could still be seen between this sinkhole experiment and cave propagation behaviour. Figure 2.37 displays an example of the typical subsidence behaviour in this study. This figure correlates well with the discontinuous damage pattern, including parallel fractures ahead of the cave back (Cumming-Potvin, 2018). These do not coincide with the boundaries between the layers of the sample. Nishida et al (1988) were less interested in the progressive damage profile and failure mechanism than the final shape of subsidence.

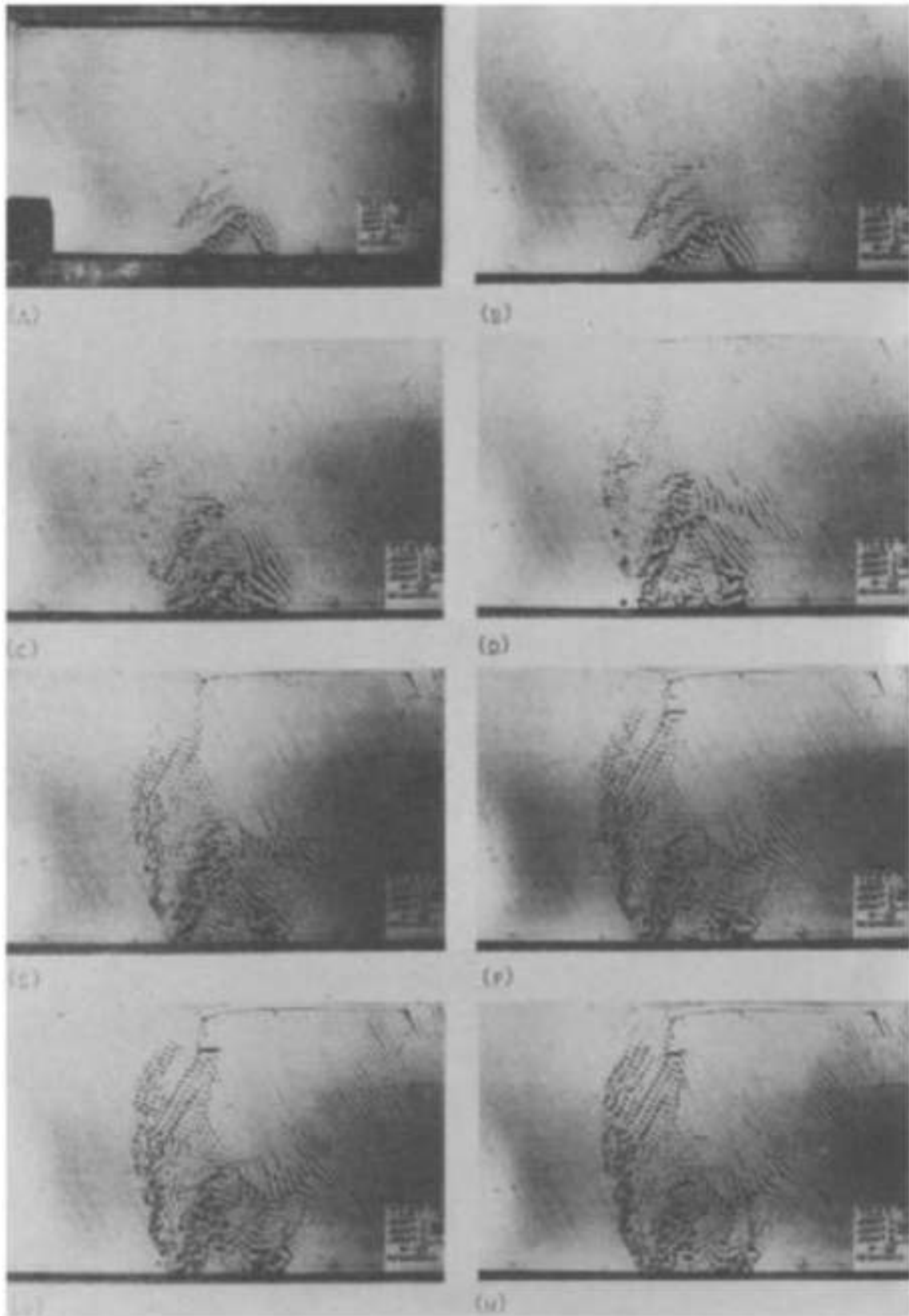


Figure 2.36: Model of caving simulated using the base friction technique (Baumgartner and Stimpson 1979).

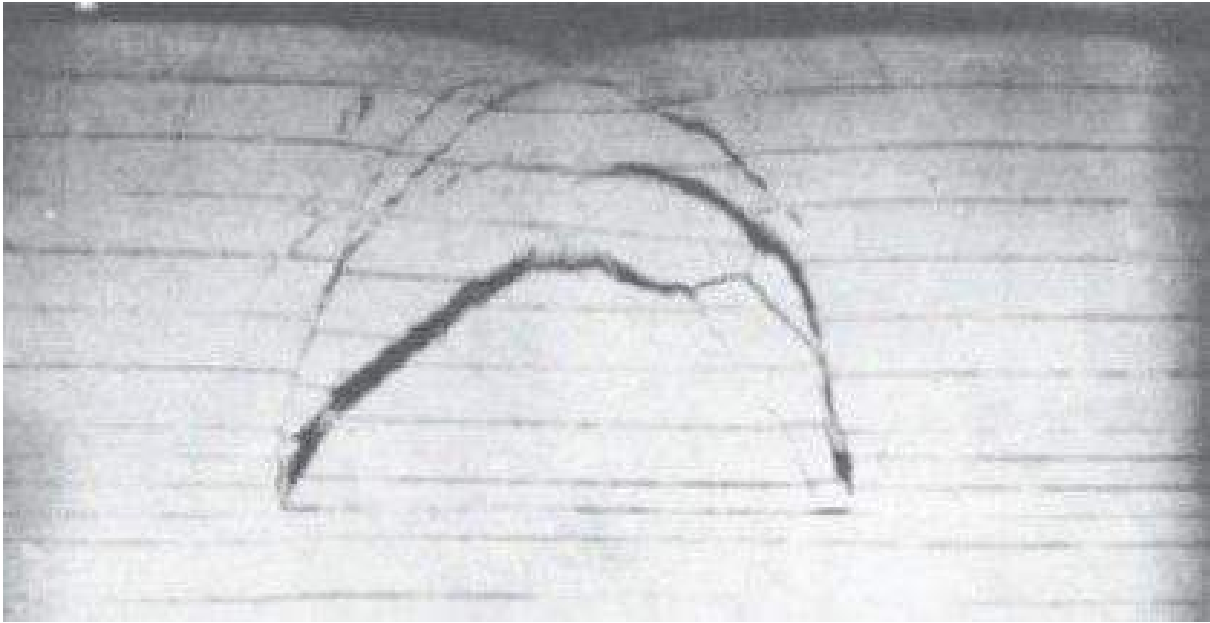


Figure 2.37: Typical subsidence (cave-in) test to model sinkhole development (Nishida et al., 1988).

2.5.2 Centrifuge Modelling

Early literature on centrifuge testing addressing mining problems comprise the work of Hoek (1965b). In the 1960s he was responsible for the design and supervision of construction of a 2.74 m diameter centrifuge. It was utilised for the simulation of gravitational force field in mine models (having a capacity of 45.4 g-ton). Hoek's mining models were typically made up of photo-elastic materials that were 'stress frozen' at high acceleration using heating elements so that the models could be easily analysed even after test completion (Hoek, 1965a). Hoek also provided scaling laws which assist the simulation of the block cave mining in a centrifuge.

A number of physical models were developed with the objective of recreating the cave mining process (Cumming-Potvin et al., 2016a). The physical modelling was conducted using a geotechnical centrifuge at the University of Pretoria (Jacobsz et al., 2014). The physical models were produced by casting weakly cemented sand and fly ash panels in which a series of random networks of pre-cut joints were made during the curing of the samples. The fly ash was included in the mixture for added brittleness to better represent the stress-strain behaviour of rock. Currently, no tests of brittleness have been performed and further research would be necessary to determine the influence of brittleness on the results of these centrifuge tests.

As a way of simulating the horizontal confining pressure in cave mines, water-filled bladders were utilised and positioned on the sides of the samples. The samples were tested in the centrifuge at 80 g and the cave mining undercut was simulated by five hydraulic-powered pistons (actuators). The tests were two-dimensional and performed under essentially plane strain conditions. This allowed for visual observations of the caving process to be photographed using digital single-lens reflex (DSLR) camera at a specific frequency.

The anticipated results of the physical modelling programme were favoured towards resembling and confirming the industry-accepted model of Duplancic (2001). On the contrary, the results did not compare well with this expected behaviour. What was observed in the study by Cumming-Potvin et al. (2016b) was an extensional failure mechanism that exhibited a succession of parallel fractures that formed sequentially from the cave back. The failure was characterised as extensional because of the direction of movement and the lack of damage to the edges of the ‘fracture bands’ as referred to by Cumming-Potvin et al. (2016a). The authors noted that their evidence is not definitive, but indicative that these fractures form in extension.

The test programme consisted of five samples that were tested, all of which resulted in the extensional type failure that was described above. Figure 2.38, Figure 2.39 and Figure 2.40 display the five tests where A is the original photograph and B is highlighted with the described fractures for easier clarification. In Figure 2.40 (right), the sequence of photographs taken are shown from the the beginning of the test to the time when the last undercutting was done by the withdrawal of the last piston. It can be noted that the red lines outline the parallel fractures and the dotted blue lines indicate pre-existing discontinuities or faults along which shearing has occurred. Figure 2.40 also shows the progressive formation of ‘fracture bands’.

In Figure 2.40 (right), the dashed green lines show the current cave outlines while the red lines show the previous caved outlines. According to Cumming-Potvin et al. (2016a) it was important to note that even though the spacings of fractures were not consistent from one test to another, they were consistent within each test. This suggests that spacing might be a function of material properties and stress state.

Figure 2.41 shows that some of the fractures discontinued at the the edges of the pistons, creating the impression that fracture banding is an artificial by-product of the undercutting performed with comparatively wide pistons. Upon careful analysis of the data it is shown that this is not the case. While the withdrawal of the pistons may have influenced the endpoint of fractures, numerous parallel fractures existed entirely independent to the positioning of the piston edges (shown by the dashed orange lines). According to Cumming-Potvin et al. (2016a), this is confirmation that the pistons had little effect on cave initiation and propagation of the fractures in the early stages.

Furthermore, redirecting the attention to Figure 2.38 (right) it can be observed that fracture banding occurred between the two discontinuities, at a distance from the undercut position. Fracture also occurred in a zone uninfluenced by the undercutting process. This renders the failure mode of fracture banding independent of the method used to undermine the material in this experiment. Assuming that the same theoretical stress distribution was applied across all tests in the models of Cumming-Potvin (2018), the variation of the in-situ horizontal to vertical stress ratio (K) can be estimated throughout the model (given in Figure 2.42). From this graph it can be estimated that K was approximately 2.90 and 1.05 at the top and the bottom of the sample, respectively, as well as 1.20 at a depth one third from the bottom of the sample.

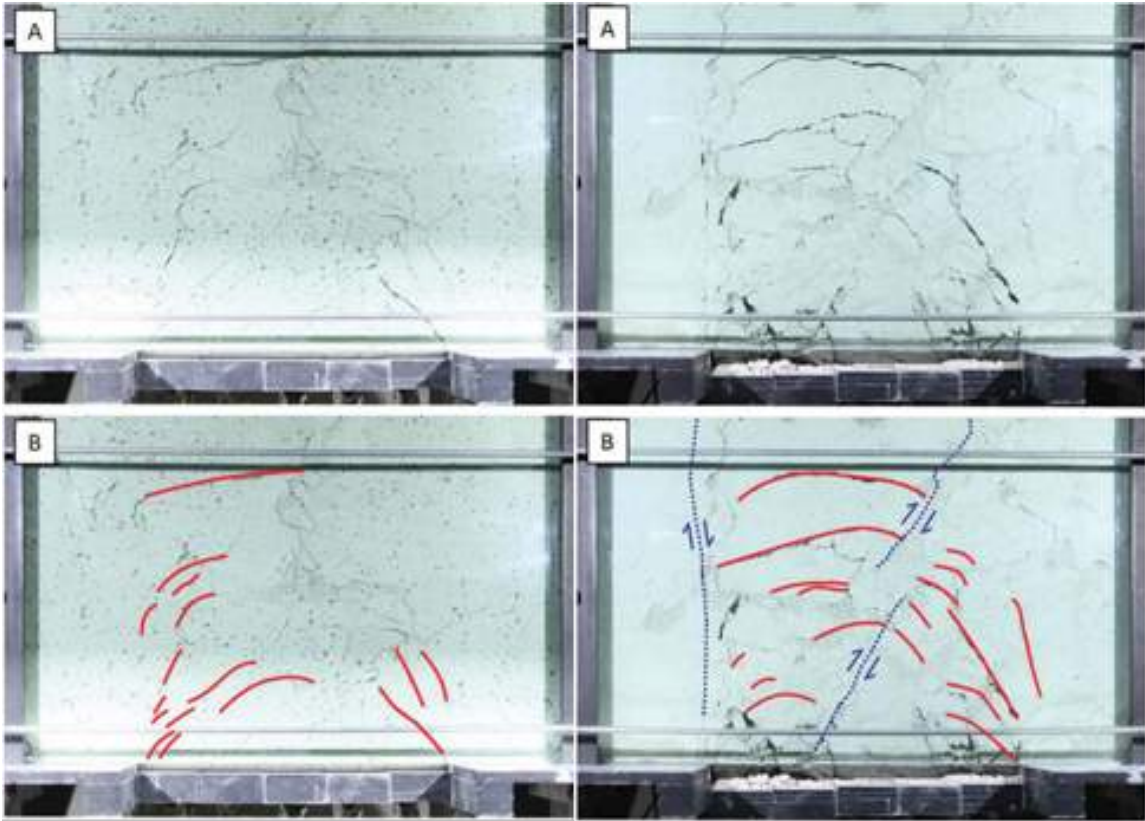


Figure 2.38: Parallel fractures ahead of the cave back and on the cave periphery — test 1 (left) and test 2 (right) (Cumming-Potvin et al., 2016a).

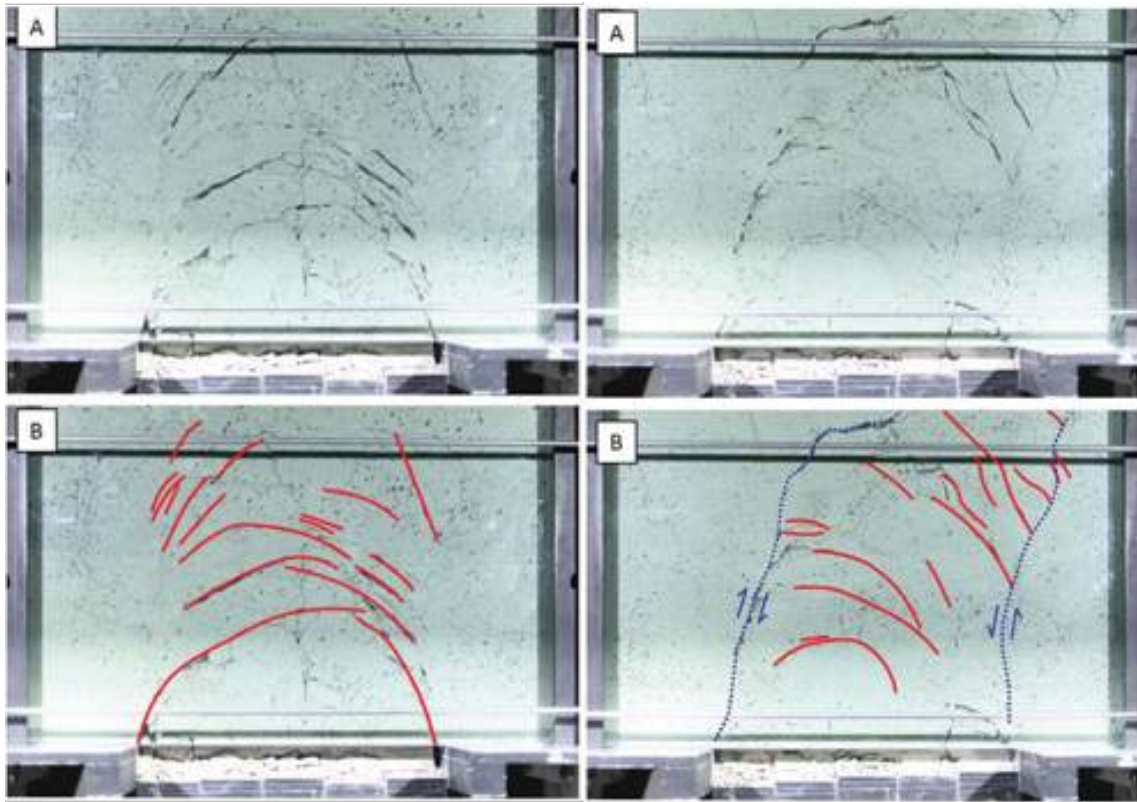


Figure 2.39: Parallel fractures ahead of the cave front and on the cave periphery — test 3 (left) and test 4 (right) (Cumming-Potvin et al., 2016a).

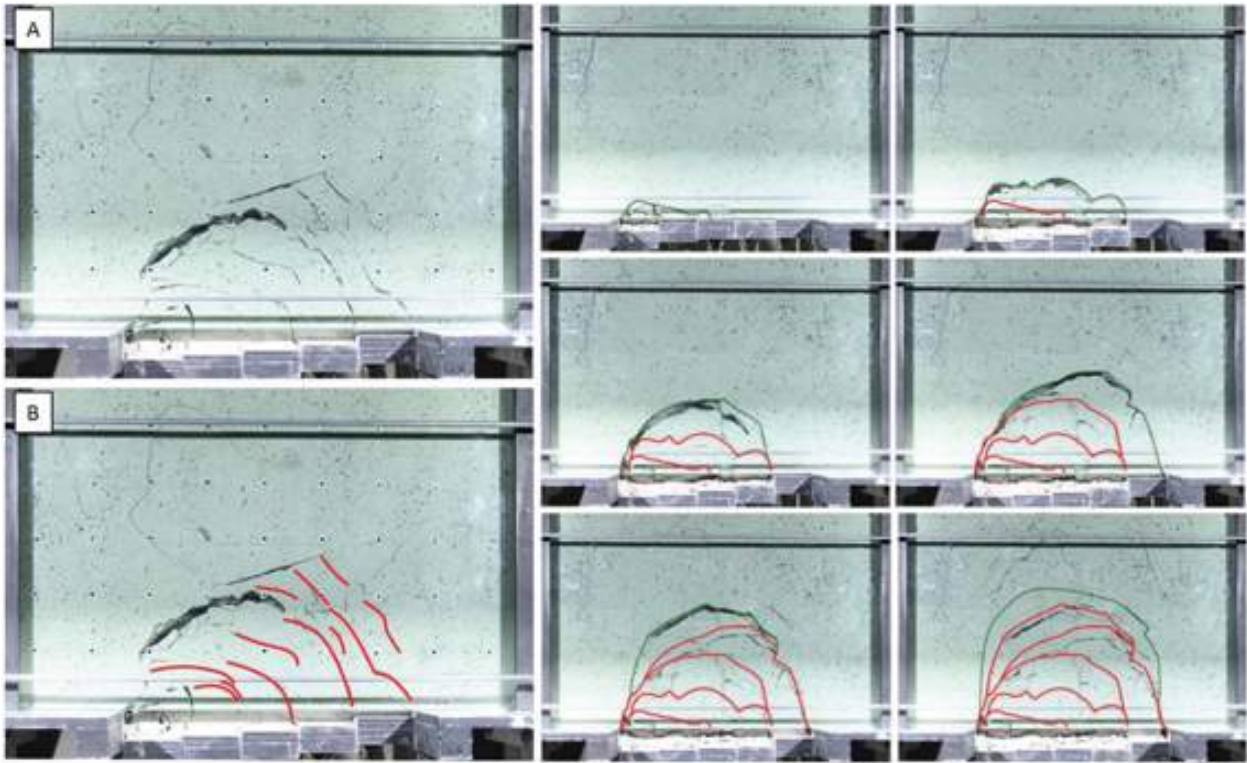


Figure 2.40: Parallel fractures ahead of the cave front and on the cave periphery — test 5 (left) and cave progression (test 3) (right) (Cumming-Potvin et al., 2016a).

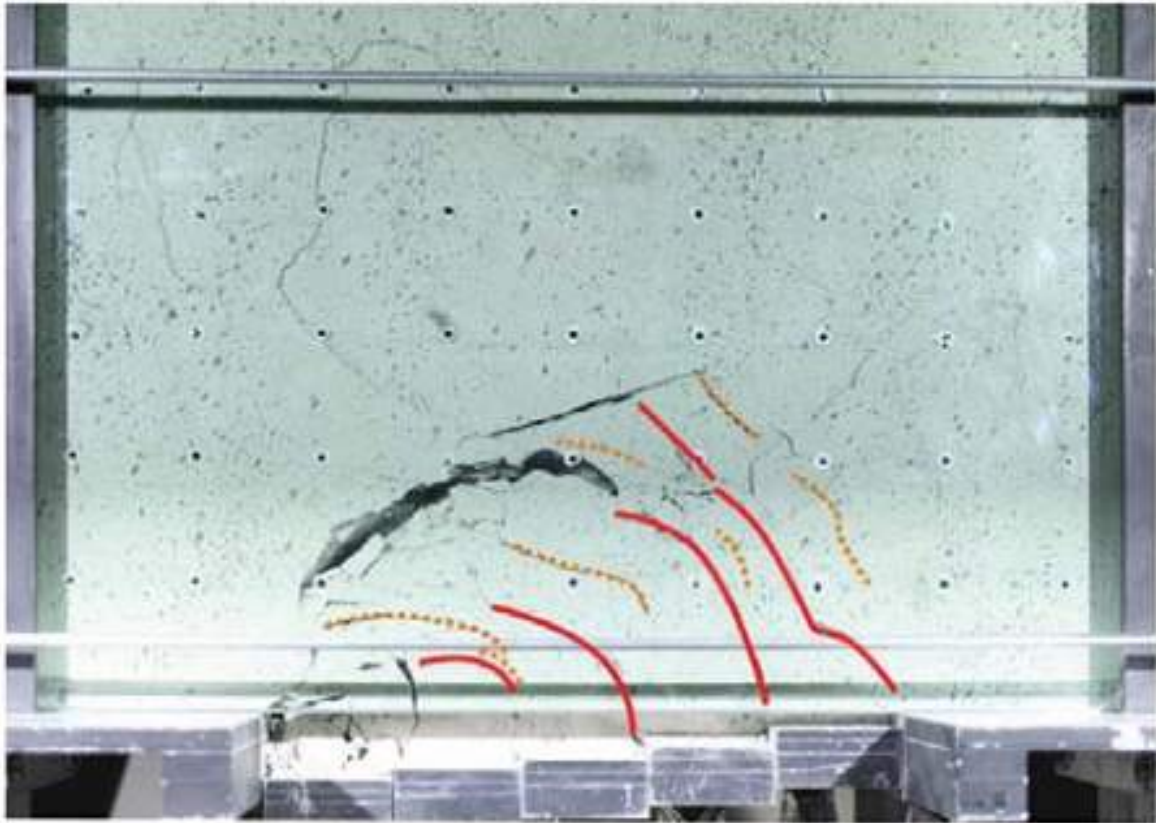


Figure 2.41: Fractures lining up with the edges of pistons (solid red lines) and those that do not (dashed orange lines) (Cumming-Potvin et al., 2016a).

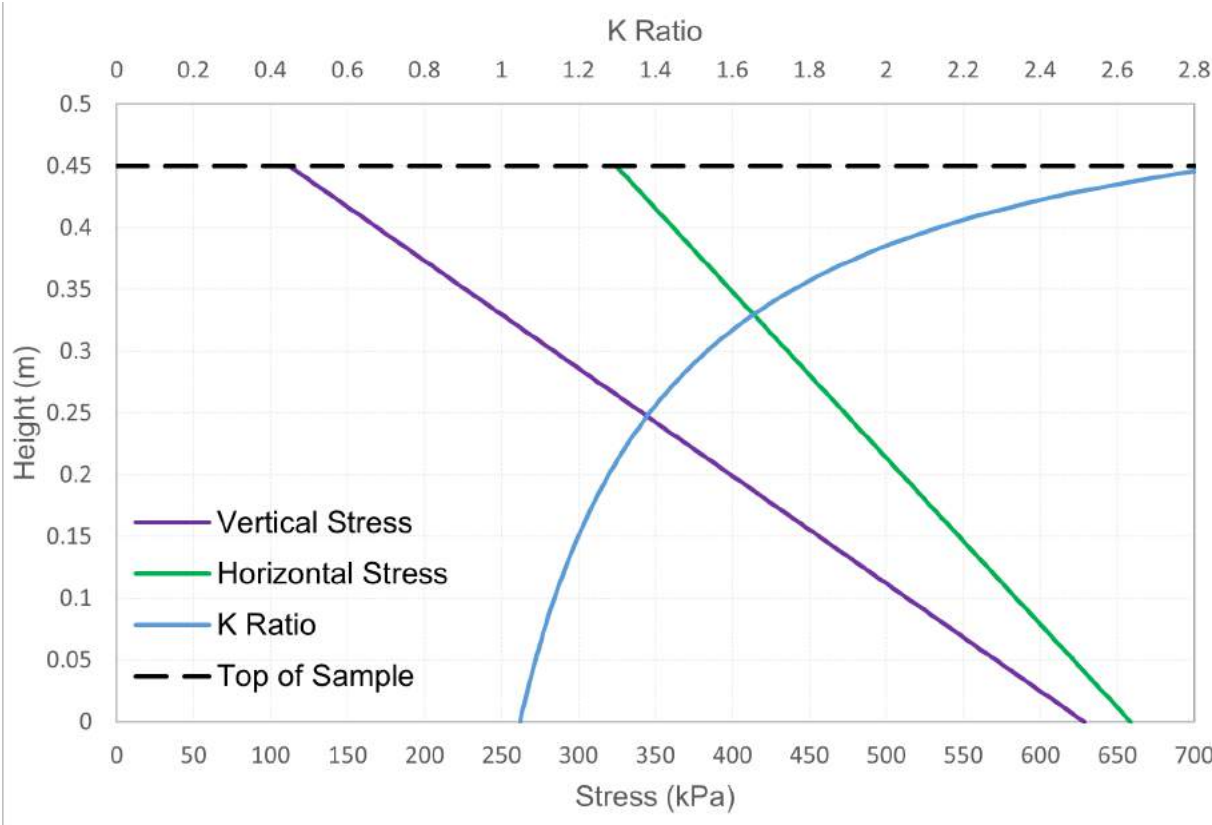


Figure 2.42: Centrifuge model stress distributions (adapted from Cumming-Potvin, 2018).

2.5.3 Cave Mine Site Observations

According to Heslop (1978), Panek (1981), Lorig et al. (1989), Sharrock et al. (2002) as well as Carlson and Golden Jr (2008) tensile fracturing has been reported in the crown and boundaries of block cave mines as well previously-caved open stopes. The reported tensile fractures were found by the use of extensometers, time-domain reflectometry (TDR) cables, borehole cameras and visual observations.

In a significant case of reported tensile fracturing in the block cave mine of San Manuel mine Panek (1981) concluded that a series of parallel extension fractures with strike angles tangential to the cave back formed “a roughly circular fractured zone of expansion about each active cave.” Figure 2.43 shows this postulation visually.



Figure 2.43: Parallel fractures in a circular zone around an active cave (Panek, 1981).

Panek (1981) also theoretically proposed that identical extensional fractures tangential to the cave back should be present below and above the caved block. No attempt was however made to instrument the cave block. A further postulation was made that this fracturing pattern can affect the potential for the rock mass to cave upwards and that this would play a large role in the viability of cave mining projects. No further attempts were made to confirm the hypotheses of Panek (1981). Nonetheless, Panek’s visual observations are a form of evidence which is a valuable contribution that seems to have been lost in the modern interpretations of caving mechanics.

2.6 Numerical Cave Propagation Assessment

Many methods are available for numerically modelling geomechanical problems. These include: Boundary Elements, Finite Elements, Finite Differences, Discrete Elements as well as Hybrid methods which are utilised to perform stress and deformation analyses. According to Brown (2003), numerical modelling is a more robust method for cave mining initiation and propagation behaviour assessment in comparison to empirical and analytical methods. Numerical models are relatively cheap and can be used to quantify the effect of variables to the extent that is not possible with physical models.

On the contrary, it should be noted that numerical models should not be relied upon for validation of the cave mining occurrences in reality. On this point, the following statement regarding numerical modelling by Cumming-Potvin (2018) should be taken into account: *“Numerical models cannot be used to determine the mechanism and progression of failure present in reality. The failure mechanisms of numerical models are determined by the constitutive model used, the boundary conditions imposed and the type of code used. Hence, the mechanisms present must be validated through other means. However, numerical models can be a useful tool in attempting to evaluate the stress regime leading to potential failure mechanisms.”* The following section highlights some numerical modelling undertaken in literature for two dimensional models simulating cave mining propagation.

2.6.1 Two-Dimensional Elastic Models

From the establishment of Finite Element Method (FEM) modelling for the evaluation of stresses and displacements in continuous structures (Clough et al., 1981) came the development of the first known two-dimensional, elastic finite element model to investigate caving behaviour at the El Teniente Mine in Chile (Palma and Agarwal, 1973). In the investigation, it was necessary to analyse the in-situ rock mass fracture network and the effect of principal stress direction in connection with the size of the undercut footprint on cave propagation behaviour.

In the model used by Palma and Agarwal (1973), the fracturing of the rock mass was taken into account by assigning zero tensile strength zones within the model. Limited details are provided in literature of this study; however, the clear observation here was that the rock mass overlying the undercut footprint was assumed to cave when a tensile stress component was identified within a zone of the model. The results of this undertaking are presented in Figure 2.44 where the cave back height is determined by in-situ stresses and the orientation of the undercut.

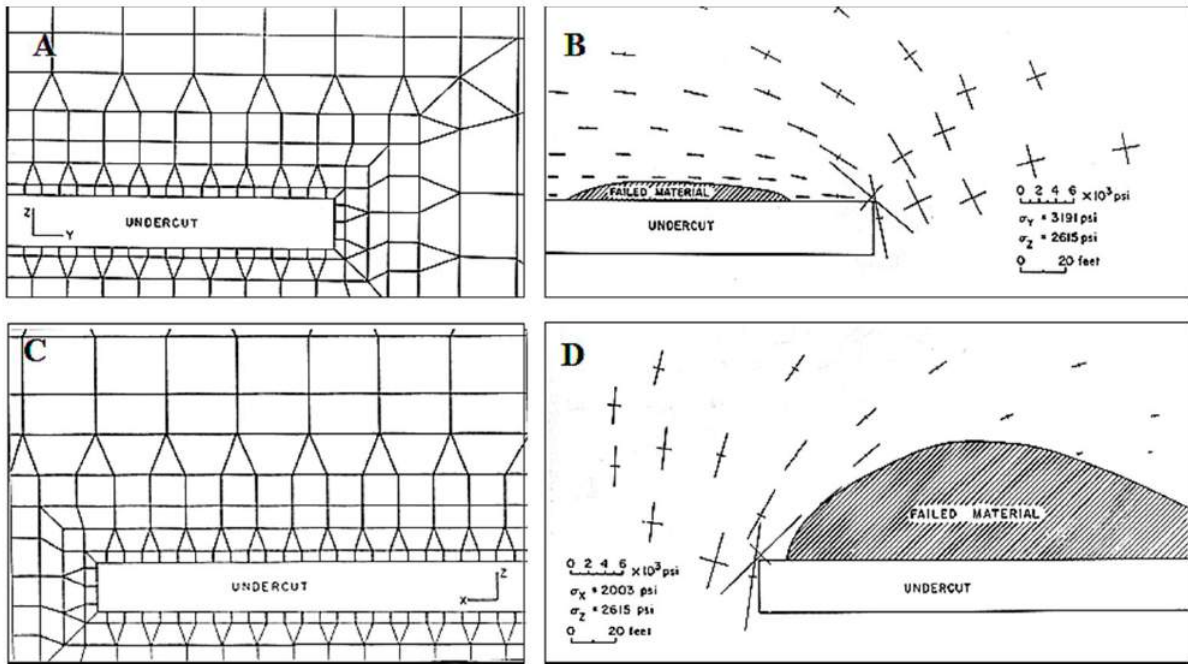


Figure 2.44: Impact of principal stress orientation in relation to an undercut as defined by two-dimensional numerical modelling (Palma and Agarwal, 1973).

The limitation of this model was that it assumed caving only took place through the mechanism of tensile failure; however, it was constructive in that it pointed to the factors of strength degradation and rock mass fabric influencing cave propagation behaviour. Particular value can be placed on this investigation because it revealed the directions of in-situ principal stresses during cave propagation. Furthermore, if the maximum principal stresses were to be projected parallel to the shorter side of the rectangular undercut footprint area, i.e. perpendicular to the undercut's largest dimension, larger stress concentrations would be induced thereby more likely to promote cave propagation. Alternatively, if the maximum principal stresses were to be acting perpendicularly to the smallest dimension of the undercut (i.e. the width), the stresses would need to overcome a larger obstacle to cave (Sainsbury, 2012). This analogy can be explained more easily through Figure 2.45.

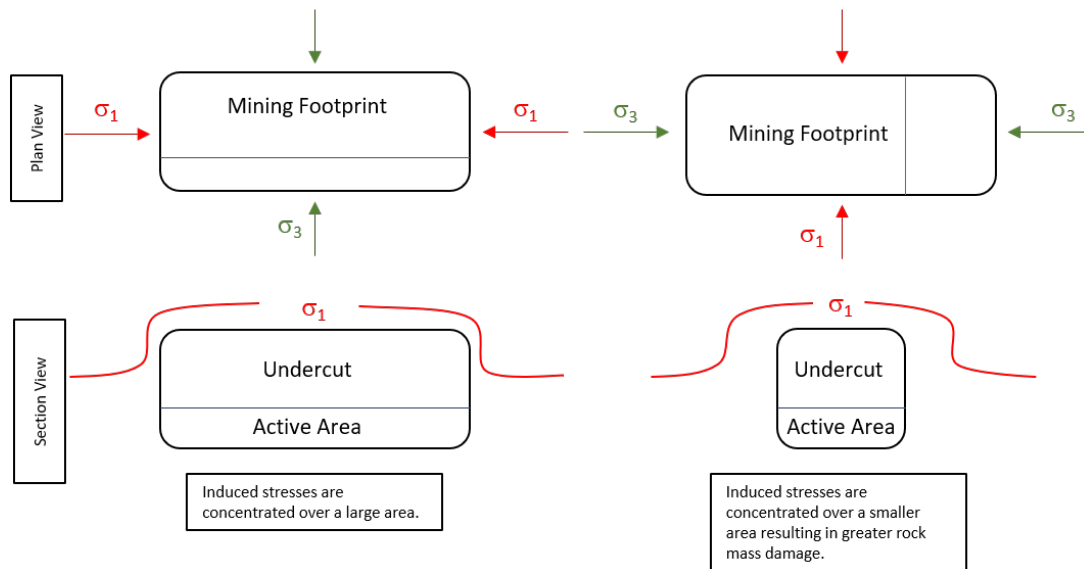


Figure 2.45: Conceptual diagram of effect of principal stress direction and undercut footprint dimensions on cavability (after Sainsbury, 2012).

From the work of Palma and Agarwal (1973), a basis is provided for a more meticulous analysis of the gravity caving mechanism of tensile failure. Furthermore, from their results, they outlined the influence of variation of stresses around the geometry of the undercut on the cave back height. Since an elastic material model was utilised, stress caving could not be accounted for since the material was essentially given infinite strength which points towards no failure that could have occurred. The implications of this are that the material in the cave back was allowed to deform and be stressed indefinitely without failing. The outcome of this could give misleading results especially in weaker rocks when there is a possibility for shear failure and redistribution of stresses within the rock mass (Sainsbury, 2012).

2.6.2 Two-Dimensional Plasticity Models

A softening material model was introduced to resemble the degradation of in-situ rock mass strength to a fully weakened and bulked state during cave propagation at Grace Mine, Pennsylvania, USA (Barla et al., 1980). The application of this softening material model was done in two dimensions and was deemed to be more realistic modelling than the elastic models of previous research at the time. With this model the mechanism of stress caving could be taken into account, alongside gravity caving as modelled before.

The softening behaviour in this model was evidently simulated through the review of failure states in the numerical mesh that were periodically made. When a zone (or element) failed in compression due to stress caving or in tension due to gravity caving, a residual value would be assigned to the strength, density and the stiffness at that specific zone. The simulation of production draw took the form of a force applied in the undercut roof.

The schematic of the model mesh, geometry of the mined section, undercutting process and contours of strength mobilised are provided in Figure 2.46.

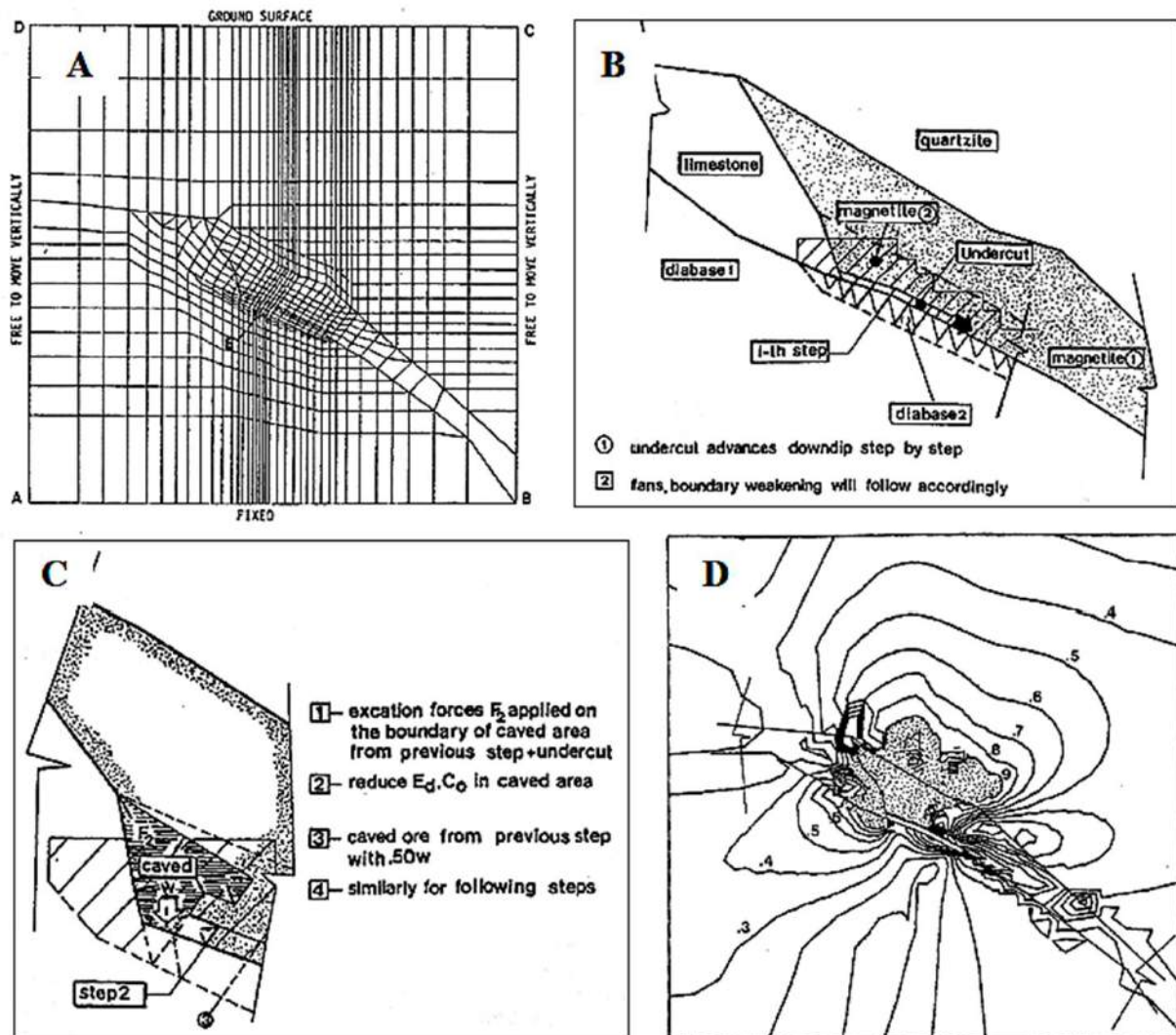


Figure 2.46: Development of two-dimensional numerical modelling approaches for cave propagation analysis (A) Model mesh (B) section through the mining geometry (C) simulated undercutting process (D) contours of resultant mobilized strength – the shaded area represents a fully softened or caved rock mass (Barla et al., 1980).

The results contributed by Barla et al. (1980) are deemed valuable as they accounted for plasticity through a softening material model. Considerations were made to represent deformation modulus and density during cave propagation. Furthermore, Barla et al. (1980) were able to highlight the significance of the ability to adequately represent the mining process within a numerical model that predicts realistically the response of rock masses. A limitation of this study was that literature did not indicate the amount of material undercut or withdrawn.

The first attempt to relate production draw to cave propagation was done by Rech and Lorig (1992) whereby they used a two-dimensional model, solved by finite difference analysis. This was used to not only reproduce existing caving conditions, but also predict future cave propagation behaviour at the Henderson Mine in Colorado, USA.

Caving was initiated in the model by undercuts made incrementally consistent with the history and planned production schedule. The bulking factor and vertical draw were assumed using volumetric equations from Panek (1984). At the failure specified in the model, stresses were set to zero values and rock mass properties were brought down to residual values of a bulked rock mass. These simulated residual values allowed for accurate representation of cave mining conditions in terms of stress state magnitude and direction. Using the method of manual cave initiation, it must be noted that the true and most natural initiation of caving could not be adequately ensured and thus predicted. The artificial reduction of stresses to their residual values does not allow for equilibrium, nor the conservation of mass and energy in the system. This jeopardised the exact amount of production draw simulated within the model. It could be that the actual damage done by caving induced stress may have been understated. The algorithm followed by Rech and Lorig (1992) used to undermine and predict cave propagation is shown in Figure 2.47.

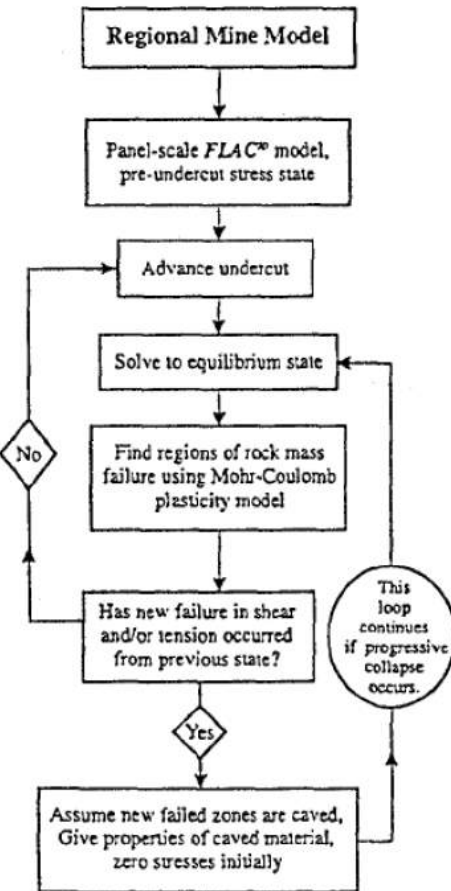


Figure 2.47: Methodology for the application of a continuum based numerical model for the prediction of onset of caving (Rech and Lorig, 1992)

Two-dimensional modelling, with the use of FEM code, was performed by Karzulovic and Flores (2003) in the International Caving Study (ICS 1997 - 2004). Their model took into account depth, stress, large-scale jointing, rock mass strength mass, as well as the effect of ground water on cavability which was conducted through a sensitivity study. The parameter is defined as the ratio of average deviatoric stress on the cave shape to the maximum deviatoric strength of the rock mass. Equation 2.27 can be used to estimate the Cave Propagation Factor (CPF) using the generic Hoek-Brown parameters:

$$CPF = \frac{\sigma_1 - \sigma_3}{\sigma_{1max} - \sigma_3} \quad (2.27)$$

Where:

σ_1 = is the Major Principal Stress

σ_3 = is the Minor Principal Stress

σ_{1max} = is the Major Principal Strength determined from the Hoek-Brown Equation 2.1

By adopting an analytical-type approach, the assumptions included vertical cave propagation and an estimate for potential cave growth was set to 10 % of the undermined length as shown in Figure 2.48 (A). The model and results of Karzulovic and Flores (2003) are presented in Figure 2.48. The area above the shaded region in Figure 2.48 (B) refers to self-sustained caving propagation (i.e. CPF is greater than the CPF_{min}). The shaded area itself is defined as the problematic caving propagation (where $CPF < 1$).

When the CPF is equal to unity, caving propagation is considered transitional. Having considered the stress redistribution near an imposed cave back, a Cave Propagation Factor calculated to assess whether the caving in the model is ‘Self-Sustained’, ‘Problematic’, or ‘Transitional’ which is analogous to the ‘zones’ of Laubscher’s Chart. It can be noted that H_c or H_t is the height of the undercut to the surface, h , the height of the cave back, B , the width of the cave back and, K , the in-situ stress ratio.

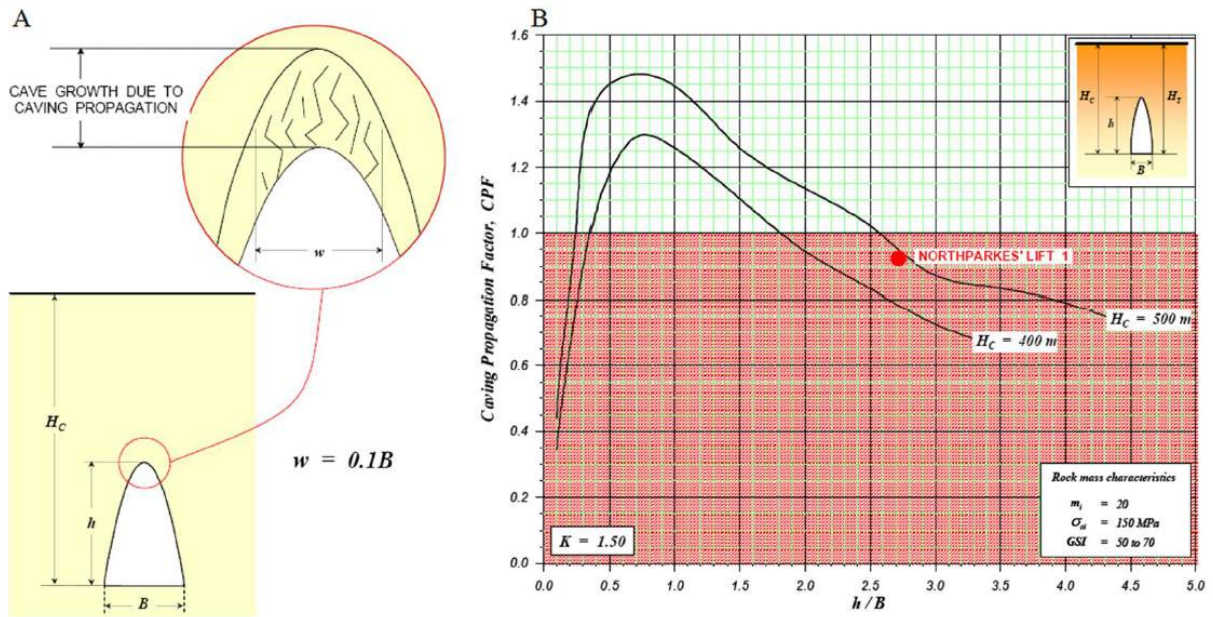


Figure 2.48: Cave Propagation Factor at Northparkes Lift 1 Mine (Kartzulovic and Flores 2003)

The figure shows the assessment of a 480 m block height rock mass of fair to good geotechnical quality (where $H_c = 480\text{ m}$, $B = 180\text{ m}$, $K = 1.50$). It is indicated in the chart that cave propagation will be inhibited through the 480 m block. In the case of Northparkes Lift 1 Mine, the Hoek-Brown parameters utilised were as follows: $m_i = 2$, $\sigma_{ci} = 150\text{ MPa}$ and $GSI = 50\text{ to }70$.

The value of this method lies in the simple assumptions made with regard to the characterisation of geometry, stress redistribution, post-peak rock mass behaviour, plasticity and assessment of the CPF. Considering the above, the model was able to reasonably correlate to the actual cave propagation occurrences at Northparkes Lift 1 Mine, predicting stalling of the cave in 1999 — shown by the red dot in Figure 2.48 (B).

Although the model was able to predict stalling of the cave back, it did not consider the stable arching aspect (which is time-dependent) or the apparent plug-failure. The assumption made about the cave back forming only 10 % of the size of the undermined length is, however, unreasonable since it is limited to predicting three-dimensional, self-sustained cave propagation and disregards the influence zones proposed by the Duplancic model (Figure 2.33). Furthermore, caving is limited to vertical propagation only and anisotropy is not considered.

2.7 Literature Review Summary

The information in this section provides summaries of the literature review as well as highlights the aspects which are aimed to improve on methods of physical modelling and rock mass modelling from Cumming-Potvin (2018).

From the formation and existence of the World Stress Map database it is evident that the state of stress around the world — and more importantly — around the cave mining sites of the world differ. These differences in stress orientations and conditions at various cave mines play a major role with regard to the type of faulting that occurs in a particular region. Having recognised that the faulting of certain areas can be categorised, each category translates to a set of horizontal and vertical stresses for a specific region. Thus, the way of comparing two regions for instance would be to utilise the lateral earth pressure which is the in-situ horizontal to vertical stress ratio (K) of that region. This ratio is also related to the depth at which cave mining is undertaken. It is important to summarise that South African mining sites have an approximated K value of 1 or slightly more. These cave mines would typically be limited to kimberlite rock surrounded by stiffer country rock. The implications of this is that theoretically there would be lower stresses in these areas when caving occurs (Wesseloo, 2019).

For the sake of adequate physical modelling, it is crucial that the behaviour of the artificial rock mass material be as comparable and representative of the rock mass in actual cave mines as possible. The inclusion of typical rock properties of igneous, sedimentary and metamorphic rock was done for this purpose. Following the section presenting the typical rock properties, numerous authors from literature were listed who have provided a surrogate means of representing rock mass. This section was necessary for the solution of an artificial rock mass to be developed which would contribute to adequately representing rock on a weaker scale of strength and, thus, providing the most rock-like attributes with regard to fragmentation, brittleness and porosity. The following can be summarised from this section: the failure strain of igneous rock at peak stress is between 0.37 % to 0.51 % strain. For sedimentary rock, this is in the region of 0.28 % to 0.53 % and metamorphic rock fails around a strain range of 0.23 % to 0.43 %.

The important difference in the failure mechanism of cave propagation must be highlighted when undercutting material during cave mining operations. It is vital that when cave mining simulations are conducted via the geotechnical centrifuge during the physical modelling component of this dissertation that when caving occurs, the cause thereof can be distinguished. These causes are, firstly, that caving is brought about by stress caving or gravity caving. The second significant observation to make whilst conducting physical

modelling is whether the caving failure mechanism itself conforms to the Duplancic model or takes on an ‘extensional failure’ mechanism as described by Cumming-Potvin (2018) in his study of an extended model of caving mechanics.

What can be deduced in terms of the use of numerical modelling is that it is a cost-effective method for quantifying the effect of variables one is unable to find in the field. It is also valuable in confirming what is observed with other analytical means. Moreover, what can be taken from the review of literature with regard to numerical modelling is that the work of Palma and Agarwal (1973) provided a basis for a more meticulous analysis of the gravity caving mechanism of tensile failure enabling the influence of variation of stresses to be outlined around the geometry of undercut on the cave back height. Barla et al. (1980) introduced the component of plasticity into numerical modelling and evidence of tension zones were reported linked to gravity caving. It is important to note that numerical modelling of caving suggests the presence of tensile stresses in the caving process.

The following conclusions were made by Cumming-Potvin et al. (2016a): *“To date, no specific tests of brittleness have been conducted and further research would be needed to determine the effect of brittleness on the results of the tests.”* Further more, in Cumming-Potvin et al. (2016b), the following was reported: *“It was concluded that further testing of physical models of caves using acoustic emissions should focus on improved system sensitivity and using a material with higher brittleness.”* Given these reported conclusions, this dissertation aims to extend on the physical modelling research and attempts to recreate the previously identified extensional-type failure mechanism in different pre-defined stress conditions. The current study also aims to improve the substrate material used in caving models with an alternative artificial rock material that attributes better rock-like features such as blockiness, fragmentation, overall brittleness and stiffness.

3 Rock Material Characterisation

This chapter outlines the experimental methodology undertaken to perform material testing before physical modelling is conducted in the study. Firstly, the development and manufacturing process of the artificial rock material is discussed and is followed by its characterisation through the calibration of representative Hoek-Brown and Mohr-Coulomb Models. It should be noted that the material is compared directly to underground sedimentary rock in this chapter since to the properties of the artificial material compare well with the likes of shale, sandstone and Indiana limestone sedimentary rocks better than other rock types presented in Section 2.2.9. According to Lye et al. (2006): “*All of the Northparkes deposits are cross cut by late faults/veins filled with quartz-carbonate, gypsum, anhydrite, pyrite, chalcopyrite, sphalerite and galena*”. This demonstrates an example of the existence of all underground rock type minerals in a single cave mining site. For the sake of this investigation, all models are limited to the material presented in this chapter which transpired to show bias towards sedimentary rocks mostly because samples needed to be weak but have manoeuvrability.

3.1 Development Process for the Artificial Rock Mass

A trial and error approach was adopted for the development of an ideal synthetic rock material. A material was needed that resembled the brittleness and stiffness of rock mass, yet was weak enough to fail under its own weight when subjected to the process of being ‘undercut’ during cave mining under high acceleration in a geotechnical centrifuge. It should be noted that despite the use of a centrifuge, the high stresses present in real mines could not be achieved which necessitated the use of an artificial rock mass. Experimentation with the different techniques of manufacturing the desired material was initially undertaken where the density, brittleness and stiffness were prioritised. This included methods of casting using concrete mixers, slurry infiltration and a method of saturating samples using only suction. Numerous candidate materials were manufactured in conjunction with carrying out laboratory tests on specimens to determine the desired characteristics. The specimens mainly took the form of weakly-cemented sands or ceramics.

The raw materials used to manufacture these included dolomitic and silica sands of varying sizes, fly ash, plaster of Paris, cement and kaolin. Samples cast were 50 mm in diameter and 100 mm in height. These were then tested in uniaxial compression once the samples were completely oven dried, from which point it was assumed negligible strength was gained. It is important to note that a uniaxial compressive strength of approximately 350–750 kPa was targeted to ensure the material would fail under its own weight when the under-cutting process was initialised in the physical modelling at high gravitational

acceleration. This was based on observations from Cumming-Potvin (2018). This target strength also ensured that samples were strong enough to be handled. The choice of the most suitable artificial rock mass material was not only based on the target strength required but on its friability. It was concluded that weakly-cemented sands would not provide a sufficient degree of friability as samples suffered severe damage when excess material causing edge-effects was removed. The focus was shifted to manufacture the required material by combining kaolin clay and fly ash to form a ‘weak ceramic’ when oven dried that is friable, brittle, can be handled and that met the target strength range. It was decided that this material was the ideal candidate for further consideration and since it is porous, it could contribute to another attribute representative of sedimentary rock.

3.2 Particle Size Distributions

The grading curves of the kaolin clay powder and fly ash are shown in Figure 3.1. The artificial rock material is also shown in this graph in its dry, powdered form having a relative density of 2.304. Table 3.1 lists the relative densities of the raw material used to manufacture the artificial rock material. From Figure 3.1, it can be observed that the more dense material contains the smallest particles as expected in comparison to the ash.

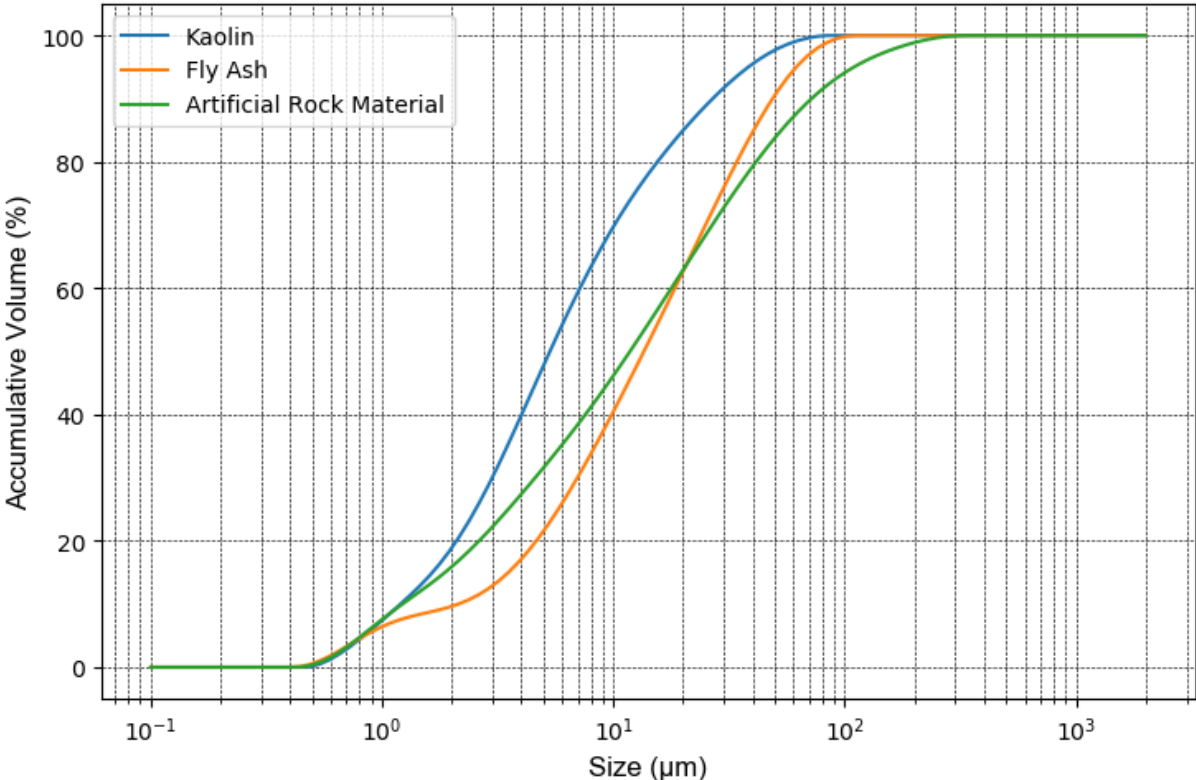


Figure 3.1: Particle size distributions for the raw material as well as artificial rock material.

Table 3.1: Final Mix Design of Kaolin-Fly Ash Artificial Rock Material

| Constituent | Relative Density | Proportion (kg/m ³) | Percentage Mass (%) |
|-------------|------------------|---------------------------------|---------------------|
| Kaolin | 2.70 | 269.62 | 16.40 |
| Fly Ash | 2.22 | 875.04 | 53.24 |
| Water | 1.00 | 499.04 | 30.36 |
| Total | - | 1643.70 | 100.00 |

3.3 Mixing and Curing Procedure

For the physical modelling that followed the characterisation of the artificial rock material it was necessary to cast panels that were scaled models representative of rock-mass sections in block cave mines. The following procedure was adopted for mixing and casting the artificial rock material using a high speed shear mixer in the geotechnical laboratory of University of Pretoria:

- Raw materials were proportioned according to values in Table 3.1
- Fly ash was inserted into the bowl of the shear mixer (shown in Appendix C) followed by water.
- The fly ash and water were mixed for 5 minutes on a moderate setting using the shear mixer (at approximately 855 RPM).
- One third of the kaolin was added to the shear mixing bowl and mixed for 5 minutes at a time. This method allowed for the fly ash and kaolin to be mixed thoroughly. This was performed at the same speed setting.
- The mixture was then poured into oiled slab and cylinder moulds and vibrated for approximately 7 minutes.
- The 500 mm by 450 mm by 55 mm sample panels were cured (uncovered) at approximately 24 °C for 13 days after which they could be handled.
- The slab and cylinder specimens were then oven dried at 70 °C for 48 hours and stored at room temperature thereafter.
- Similar to the cylinder specimens, it was assumed that negligible strength was gained after panels were fully oven dried.

The curing procedure was finalised by trial and error and careful monitoring. All panels were cast, cured and oven dried in a horizontal orientation which allowed for a thorough floating process to produce a smooth and uniform finish. This made it possible to insert

the fragile specimens into the centrifuge frame that had small working tolerances (which is further explained in Section 4.4). The densities of the panels were around the same as that of the cylinder specimens that had undergone materials testing. The average relative unit weight of the material is reported in Section 3.7; however, the range of unit weights for all panels cast was between 1392 and 1459 kg/m³.

3.4 Uniaxial Compressive Strength Testing

As mentioned previously, uniaxial testing was used as the basis for meeting the target strength for the artificial rock material. Figure 3.2 shows the testing apparatus and a specimen before a uniaxial compressive test, which was used to determine the stress-strain behaviour of the candidate rock materials.

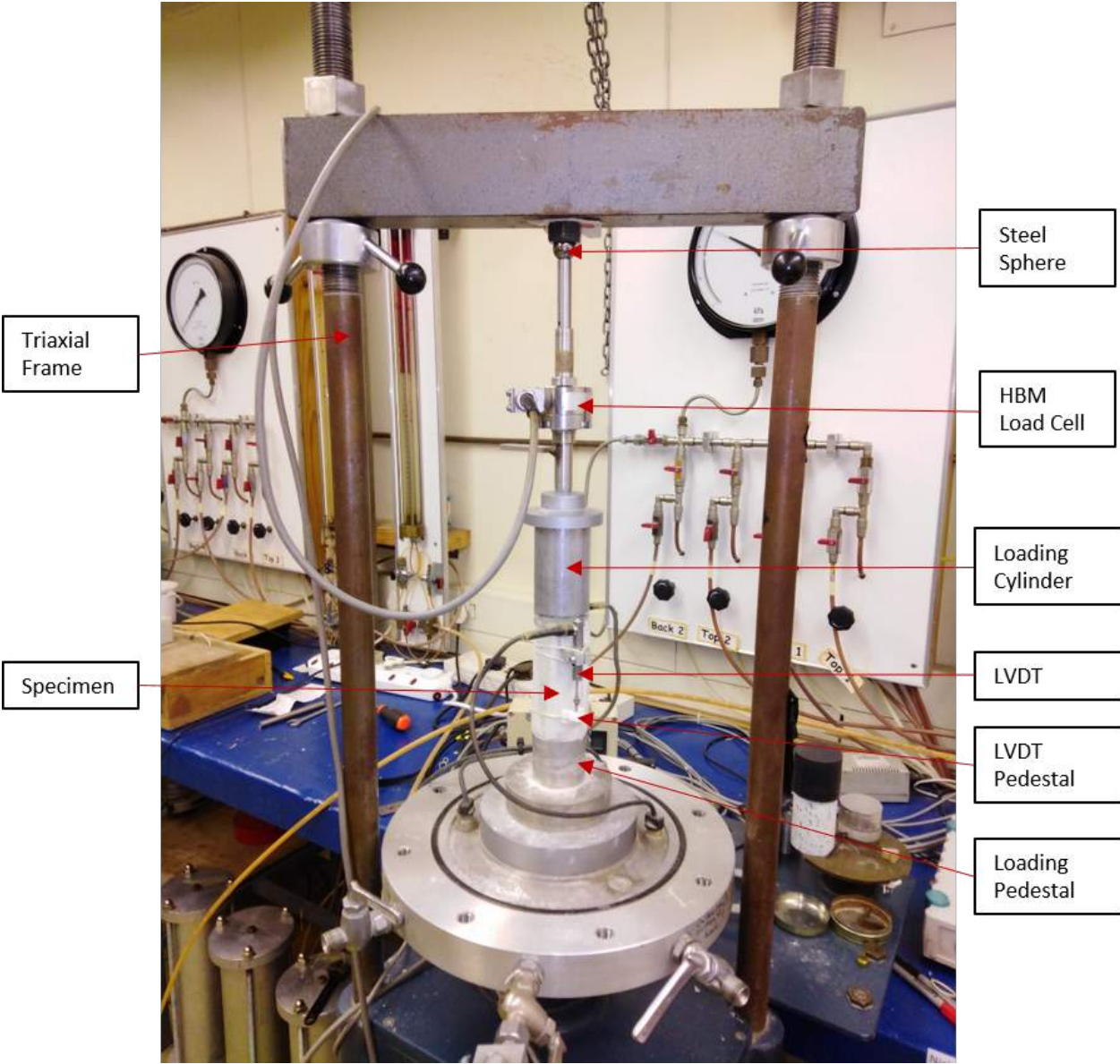


Figure 3.2: Experimental setup for uniaxial compressive strength testing.

The kaolin and fly ash cylinder specimens were capped to size for standard testing procedures (i.e. with an aspect ratio of 2) using a band saw. The top and bottom faces of specimens were then mounted to discs using Rockset — which is a rapid setting cementitious grout from Dupre Minerals — to limit edge effects and to ensure uniform loading during testing. The specimens were left for the fast anchoring cement to set. This allowed for sufficient repeatability. Two Linear Variable Differential Transducers (LVDTs) at opposite sides of the specimen (as shown in Figure 3.2) were used to measure vertical displacements and a clip-gauge LVDT was attached around the middle of the specimen to measure the lateral displacements (only used in triaxial tests). Data was logged at a frequency of 10 Hz and machine compression speeds for uniaxial and triaxial tests were set at 0.5 and 0.1 mm/min, respectively. Figure 3.3 exhibits the response of the uniaxial compressive strength of the artificial rock material against the truncated UCS curve of 48-hour cured material in Cumming-Potvin (2018). The average UCS from 5 tested specimens was 735.6 kPa which correlates to a strain as low as 0.25 %. The behaviour of the unconfined material seems to be near linear for strains below 500 microstrain (0.05 %) and stresses below 385 kPa. The artificial rock mass tends to behave in an elastic-plastic manner. The observed failure of these UCS specimens can be described as ‘abrupt’ and placed in the category of either perfectly brittle or strain softening idealised stress-strain behaviour. The shape the curves compares well with the observations of Pierce et al. (2006) in their numerical strain softening simulations (Figure 2.12) where the sample undergoes gradual local failure due to micro-cracking which is followed by complete disintegration to its bulked state. A similar process can be speculated for the artificial rock material.

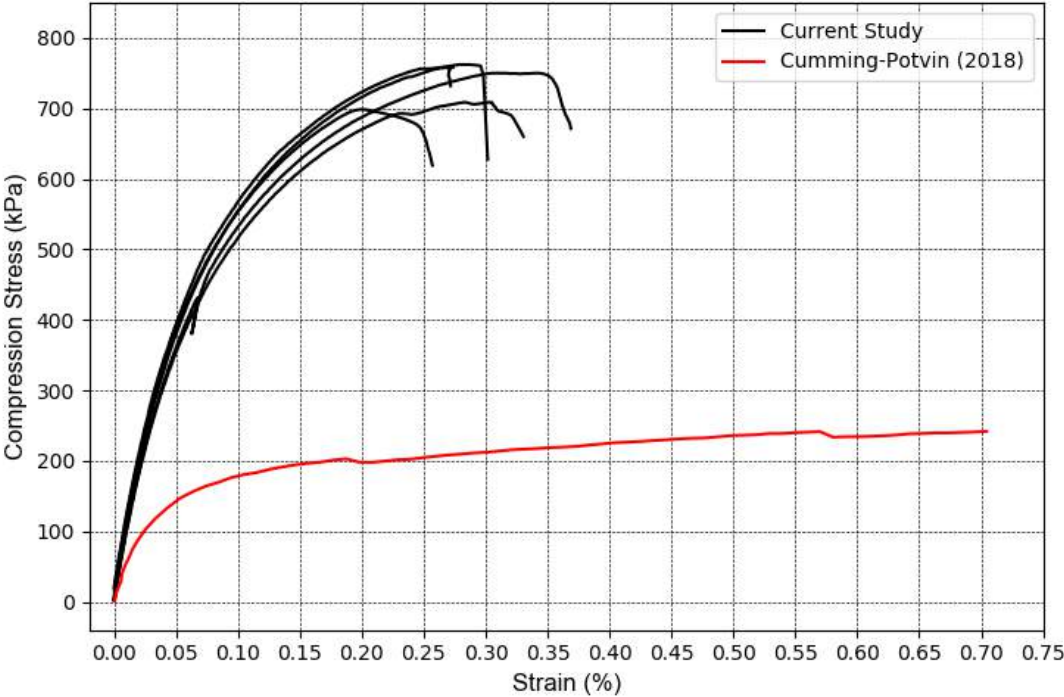


Figure 3.3: Uniaxial compressive strength repeatability tests for the artificial rock material.

3.5 Triaxial Testing

The Standard Triaxial Compression test is the most extensively used laboratory test for measuring the shearing behaviour of soil and is aptly used for artificially cemented sands as well as rock specimens. Cylindrical specimens, typically having an aspect ratio of 2, are set on a central pedestal supported by a circular base. A chamber which allows the specimen to be kept in a space of pressurised water fastens on to the circular base causing a water tight environment. The sample is stressed in the axial direction using a loading ram and is confined radially from the pressure exerted by the water. Triaxial compression comprises keeping the confining water pressure constant throughout testing while the loading ram incrementally exerts a compressive axial stress on the sample (Knappett and Craig, 2012). The apparatus used for a standard triaxial compression test is shown schematically in Figure 3.4 below.

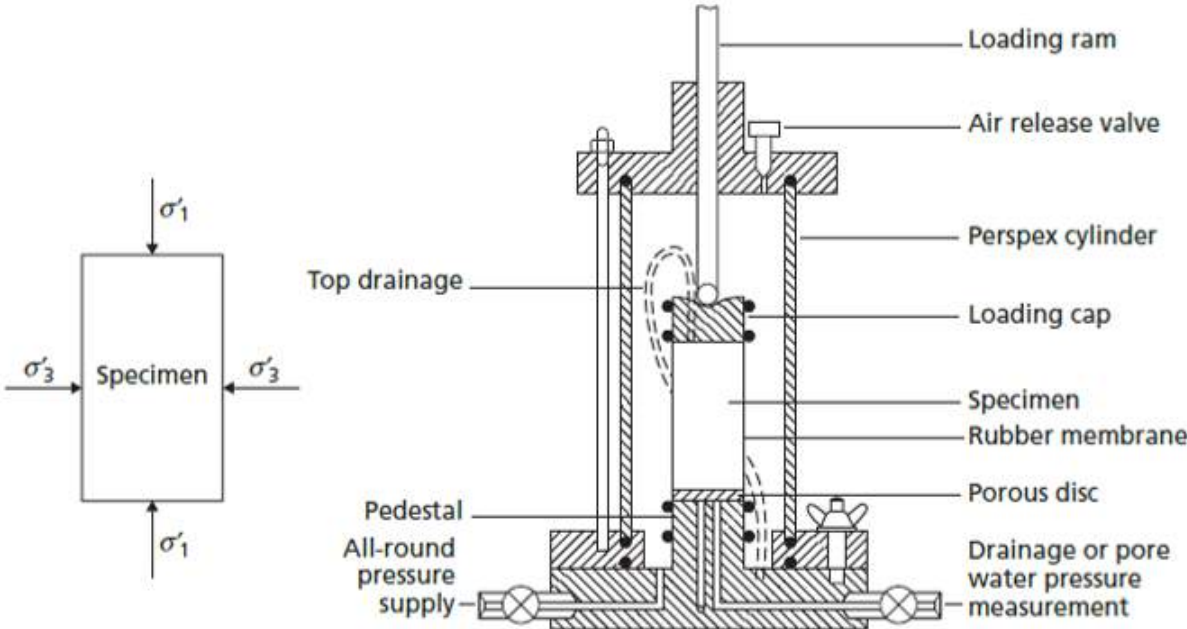


Figure 3.4: Typical setup of a triaxial cell (Knappett and Craig, 2012).

The triaxial testing performed in this investigation covers a stress range that would be deemed applicable and representative to what samples would experience during centrifuge testing. Six triaxial tests specimens were tested at constant cell pressures of 100, 200, 300, 400, 500 and 700 kPa. A variety of specimens from two batches of cast samples used for centrifuge testing were used in order to take into account the variability of the material, as well as to represent the material used in the physical modelling, which could be assumed to behave within the bounds of the two batches tested. Three triaxial tests were conducted on the batch which was left for longer periods after being oven dried (termed ‘Mature specimens’ herein) and the other three triaxials were conducted on the batch which was left for shorter periods after they were oven dried (termed ‘Young specimens’).

Figure 3.5 displays the stress-strain responses for all specimens under varying cell pressures. It can be observed from the figure that the material reaches a strength limit at confinement of around 500 kPa. The stress-strain behaviours indicate elastic-plastic behaviour for confined specimens with the stiffness reducing with an increase in axial stress. Regardless of confinement stress, the material reached maximum load at axial strains below 2 %, which suggests relatively brittle failure. The reason for this is that it is suspected that the material crushes into its pores. Table 3.3 contains the peak and residual principal stress values from the triaxials performed during laboratory testing of the artificial rock material.

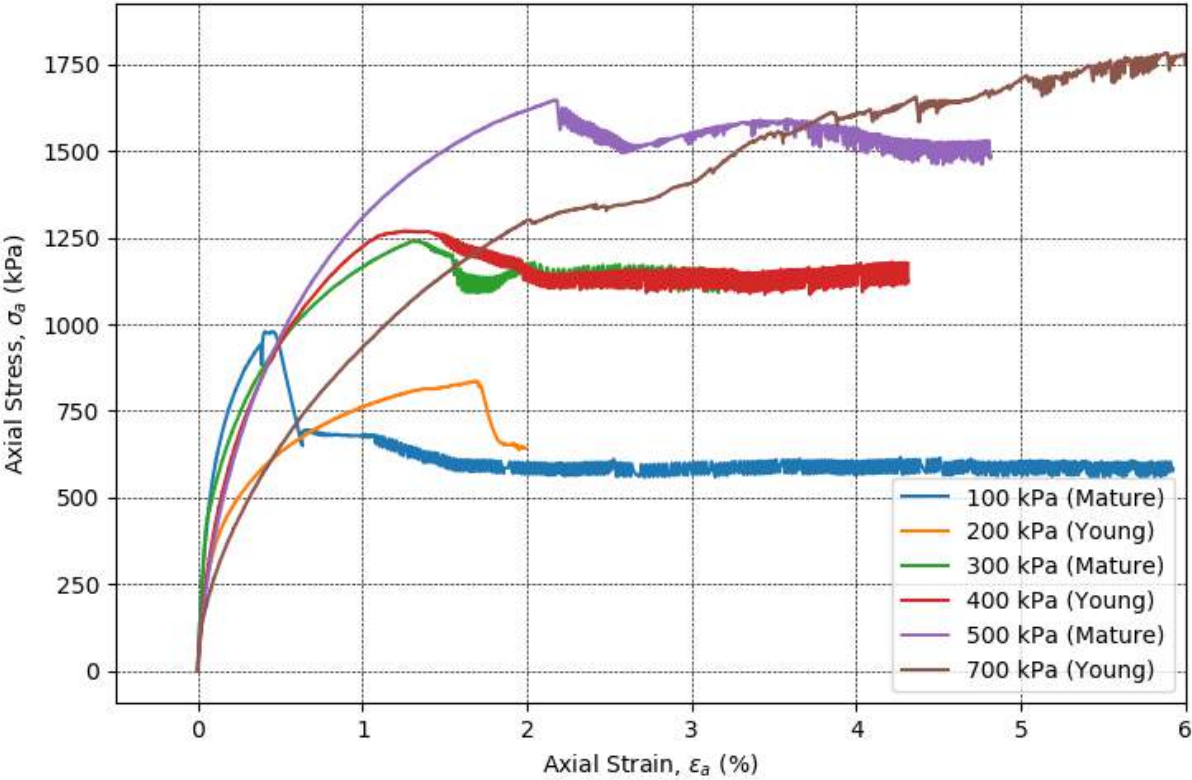


Figure 3.5: Axial stress-strain plot of the artificial rock material for various confining pressures.

The principal stresses are extracted from the triaxial results in order to characterise the artificial rock material. These are listed in Table 3.3. Due to the non-linearity of the curves, the Secant modulus was defined from the origin to the point where the coefficient of correlation exceeded 95 %. The Young’s modulus of the material was then evaluated by using the average Secant modulus of the stress strain curves of the six triaxial tests. A value for Young’s modulus of 778.4 MPa was determined, considering all laboratory tests. The material’s high porosity did not allowed for a clear Poisson’s ratio to be evaluated when using independent triaxial results. However, since the Poisson’s ratio of sandstone is approximately 0.2, it was expected that the artificial rock material would be similar. Upon using the triaxial result for the cell pressure of 100 kPa, the Poisson’s ratio was calculated as 0.22.

3.6 Brazilian Disc Tests

3.6.1 Indirect Tensile Strength

Although tensile strength is not accounted for when using the Mohr-Coulomb and Hoek-Brown criteria, it can still, however, be used as an estimation of the tensile cut-off, when these failure criteria are combined with Griffith's Theory. In this section, the measured tensile strengths obtained from indirect tensile tests (via the Brazilian disc test method) are compared to the calculated strengths that are obtained when combining Hoek-Brown criterion (in particular) with Griffith's Theory. The 5 kN Lloyds press machine at the University of Pretoria was used for the Brazilian disc testing at a testing compression speed of 0.5 mm/min. Disc specimens were prepared from cylinder specimens to the approximate dimensions of 50 mm in diameter and 25 mm in thickness. In total 13 Brazilian disc tests were conducted which resulted in brittle failure. The test setup (utilising curved loading strips) for splitting disc specimens is shown in Figure 3.13. The suggested formula from ASTM 2008 (and ISRM 1981) for the splitting tensile strength (σ_t) at the centre of disc specimen in a Brazilian disc test (BDT) is given by Equation 3.1:

$$\sigma_t = \frac{2P}{\pi Dt} \quad (3.1)$$

Where:

σ_t = Tensile strength (kPa).

P = Load at failure (kN).

D, t = Diameter and thickness of the test specimen, respectively (m).

Figure 3.6 clearly indicates that the tensile tests conducted on the material causes absolute brittle behaviour. The average indirect tensile strength for the artificial rock mass was calculated as 87.02 kPa. The average approximate measurement of vertical displacement at failure for these tests was between 0.4 and 0.85 mm. Of the 13 tests conducted, 6 (which are indicated in red) were reported to have split from the centre of the disc (i.e. visually deemed to have failed in tension) from captured photos. Upon presenting the tensile strength results in this section, Li and Wong (2013) have concluded that the Brazilian test has been found to overestimate the tensile strength of rocks. In their research, they have stated that despite this discrepancy the Brazilian test is deemed a popular means of determining the tensile strength of rocks due to its ease of specimen preparation and experimental procedure when compared with the methodology of the direct uniaxial tensile test.

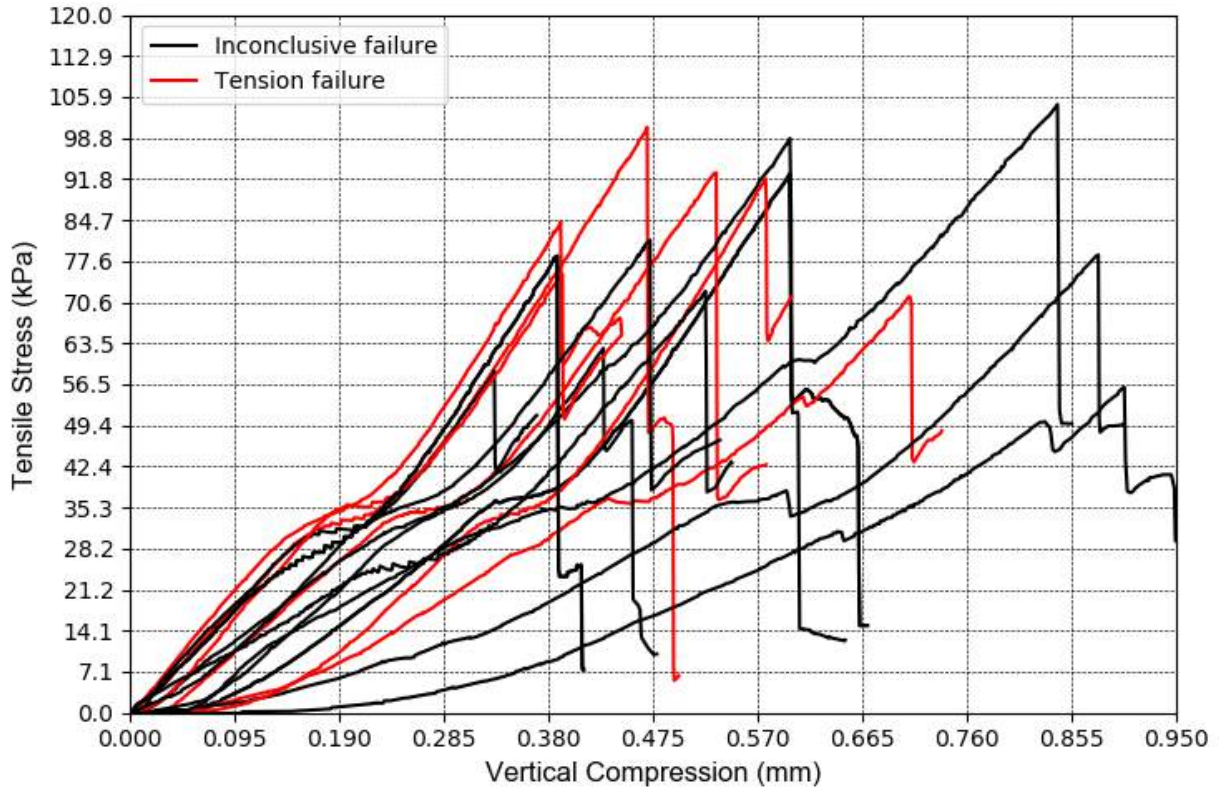


Figure 3.6: Tensile stress-displacements curves of the artificial rock material.

3.6.2 Particle Image Velocimetry

Particle Image Velocimetry (PIV) — also referred to as Digital Image Correlation (DIC) — is a method originally described by Adrian (1984) as well as Pickering and Halliwell (1984) in the field of fluid mechanics for flow visualisation. PIV is a two-dimensional photogrammetric measurement technique allowing for instantaneous spatial velocities and incremental displacements on surfaces of moving and deforming materials to be calculated.

A PIV analysis begins with the first image (termed the ‘reference’ image by the authors of the software) containing a region of interest (ROI) specified by the user. This region is then subdivided into a grid of patches (or subsets) for the software to track displacements in successive images. The tracking of displacements from one photograph to another is performed for all subsets defining a field of relative displacement.

This method allows the deformation of specimens to be captured and reported in terms of horizontal and vertical displacements as well as strains. A brief overview of the PIV process is shown in Figure 3.7. GeoPIV-RG software developed by Stanier et al. (2016) was used in this study.

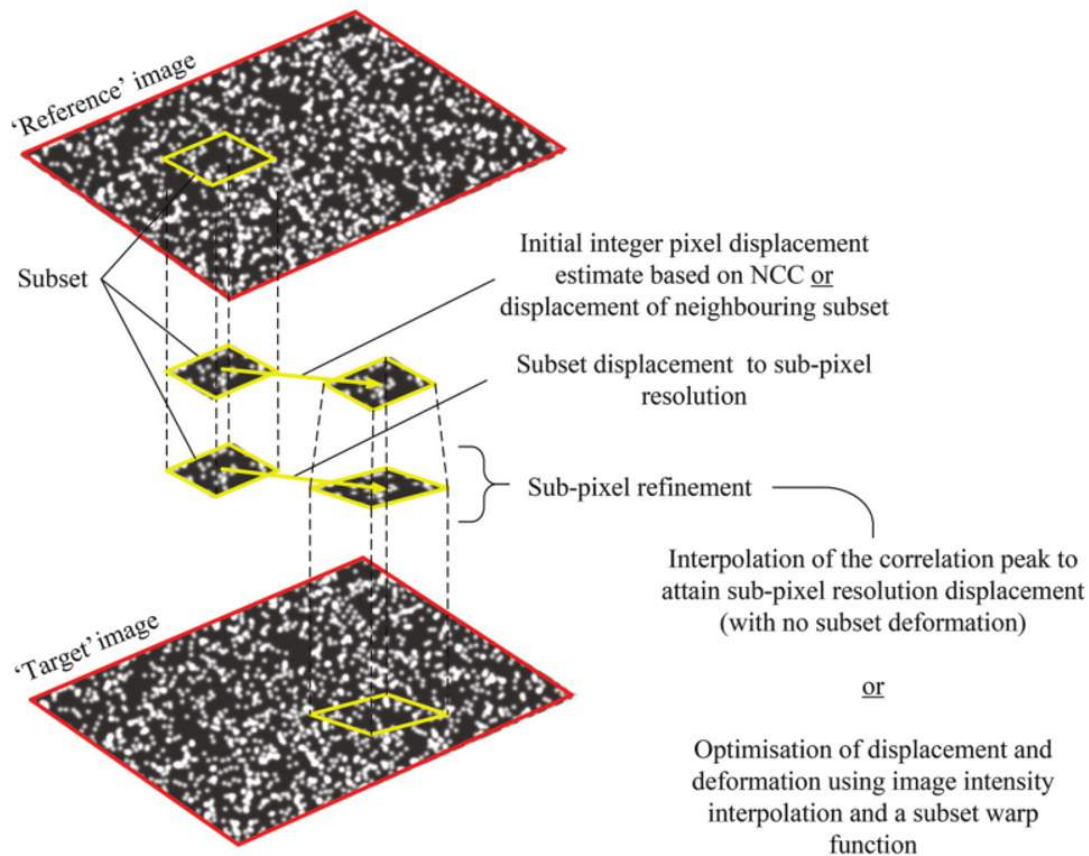


Figure 3.7: General overview of the PIV–DIC method (Stanier et al., 2016).

The PIV procedure was utilised to determine the horizontal (tensile) strains of the 6 Brazilian disc tests indicated in Figure 3.6 (distinguished in red). The method followed when conducting PIV analysis on the Brazilian disc tests included the use the GeoPIV-RG software package within the MATLAB toolbox environment. The test setup involved a pair of curved loading strips to accommodate the cylindrical disc specimens. The loading strips used had a radius slightly larger than that of the specimen radius which prevented specimens breaking under compression due to stress concentrations caused by the loading strip edges (Gaspar, 2017).

Figure 3.13 (left) illustrates the test-setup used in the investigation for conducting Brazilian disc tests. An image used in the analysis after failure is shown in Figure 3.13 (right) which contains subsets used in the PIV procedure by the program. It is vital to note is that the loading strips were aligned vertically in order for the specimen to be loaded uniformly. This can be illustrated by the red construction lines drawn over the photograph taken by the camera during the beginning of a test. The camera was setup via a tripod in a safe position less than 1 m away from the test specimen. The camera’s angle, when applicable, was corrected for fish-eye and perspective using GIMP (GNU Image Manipulation Program) before the images were processed in the PIV analysis.

3.6.3 Critical Extensional Strain

General steps are listed below with regard to procedures followed in conducting PIV analysis. PIV results and load data from Brazilian disc testing were subsequently used in a three-part approach for determining an adequate value for the critical extensional strain parameter.

- After configuring the MATLAB toolbox environment for the PIV analysis, a mesh to populate the subsets over the reference image was generated with a patch size of 50 px. Images used in the analysis had adequate texture to allow for particle tracking. The diameter of specimens was typically around 1250 px in image-based distance. The PIV procedure was then conducted using the ‘Leap Frog’ method.
- Once x and y displacements were computed and filtered for each subset, they were exported to Microsoft Excel to calculate image-based horizontal strains considering the bulging of the disc diameter. Strains were then correctly matched up with load cell data from the 5 kN Lloyds press machine using time stamps upon which the files were created. This was used for calculating the tensile stresses.
- Various approaches were adopted at this point when determining the value of critical extensional strain of the artificial rock material. These included the following:
 1. The first approach involved evaluating the elastic range for the artificial rock material from which the tensile limit was used as the lower bound for the critical extensional strain of the material. Simply dividing the calculated tensile stress by the material’s stiffness allowed for an initial under-estimation of the critical extensional strain. The compressive strain on the other extreme was calculated in a similar manner to obtain the full elastic range of the material which resulted in an expected linear response.
 2. The second approach necessitated the modification of Equation 2.23 with the substitution of Equation 3.1 as per Li and Wong (2013) and uses the added component of Poisson’s ratio to determine a more refined value for critical extensional strain over the first approach. Thus, utilising Equation 2.26 to calculate extensional strains using the circumferential stresses in Brazilian disc specimens anticipates an over-estimation of the value for critical extensional strain.
 3. The final approach aims to account for measured values thereby utilising the horizontal displacements from PIV analysis. Once horizontal displacements were exported, corresponding left and right subsets were chosen on either side of the ‘disc equator’ and used to calculate horizontal strains. The strains calculated from the chosen pairs of subsets were averaged and listed in a tabular

format. A plot of tensile strain in each image leading up to failure allowed for a certain range of estimates to be made for the critical extensional strain within the lower bound of Approach 1 and upper bound of Approach 2. Values of strains recorded outside the limits as defined by Approaches 1 and 2 were discarded in an attempt to select a conservative estimate of the critical extensional strain for the material.

Following each of the outlined approaches to determine a suitable value for the critical extensional strain of the artificial rock material, the findings of which are listed below:

1. Calculated Strains at the Elastic Thresholds

The compression strength of the material from Section 3.4, as well as the tensile strength from Section 3.6.1 were utilised in determining the set of extremes which are shown in Figure 3.8. This yielded a pair of strains corresponding to absolute values of 0.0111 % and 0.0495 % for the tensile and compressive extremes, respectively. In this case, a stiffness of 778.4 MPa was used with an average tensile strength of 86.09 kPa taken from the 6 Brazilian disc specimens that were reported to have split in their centres. This gave a coefficient of correlation of 1. A lower bound of 0.0111 % for the critical extensional strain was chosen from this approach.

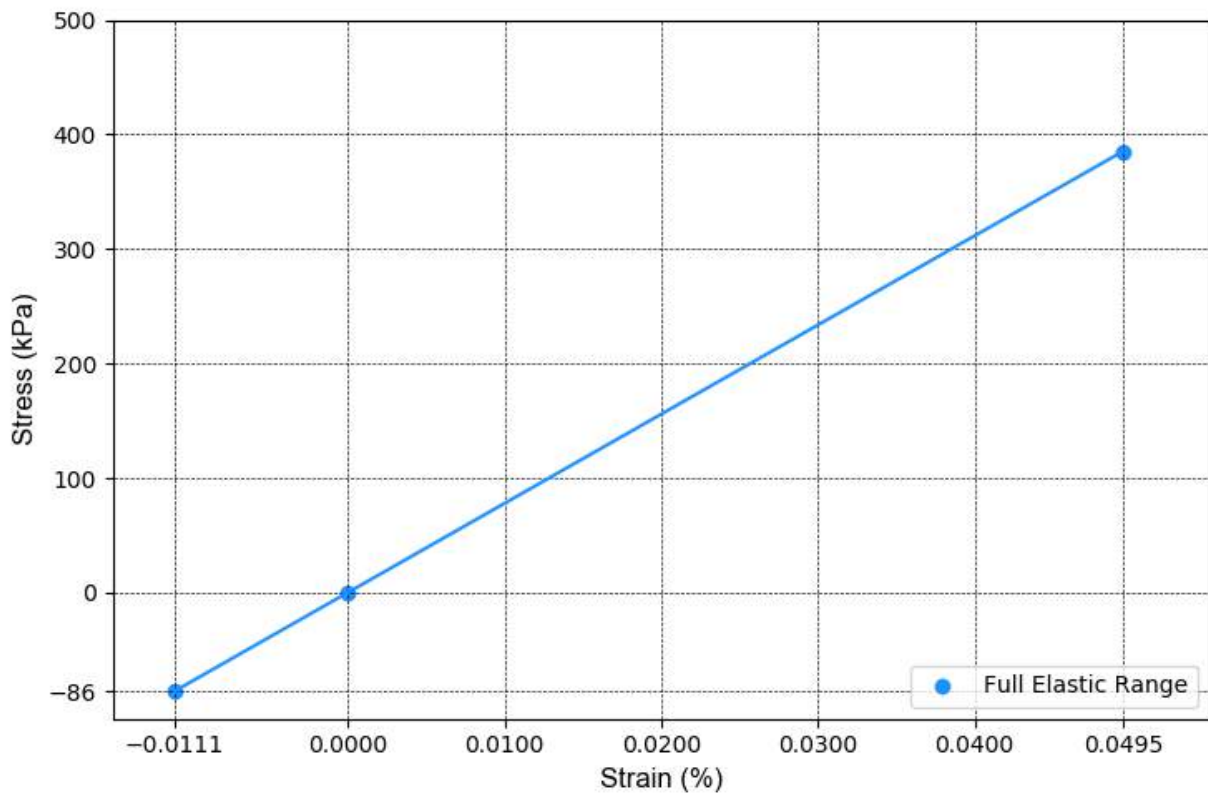


Figure 3.8: Linear elastic range of the artificial rock material.

2. Calculated Extensional Strains via Load Data

Making use of Equation 2.26 and the load data from the tests conducted in Section 3.6.1, the extensional strain (e_3) experienced normal to the cracks forming during Brazilian disc testing can be plotted against the vertical displacement. The extensional strain curves for the 6 tests which were reported to have split through their centres (in tension failure) are shown in Figure 3.9.

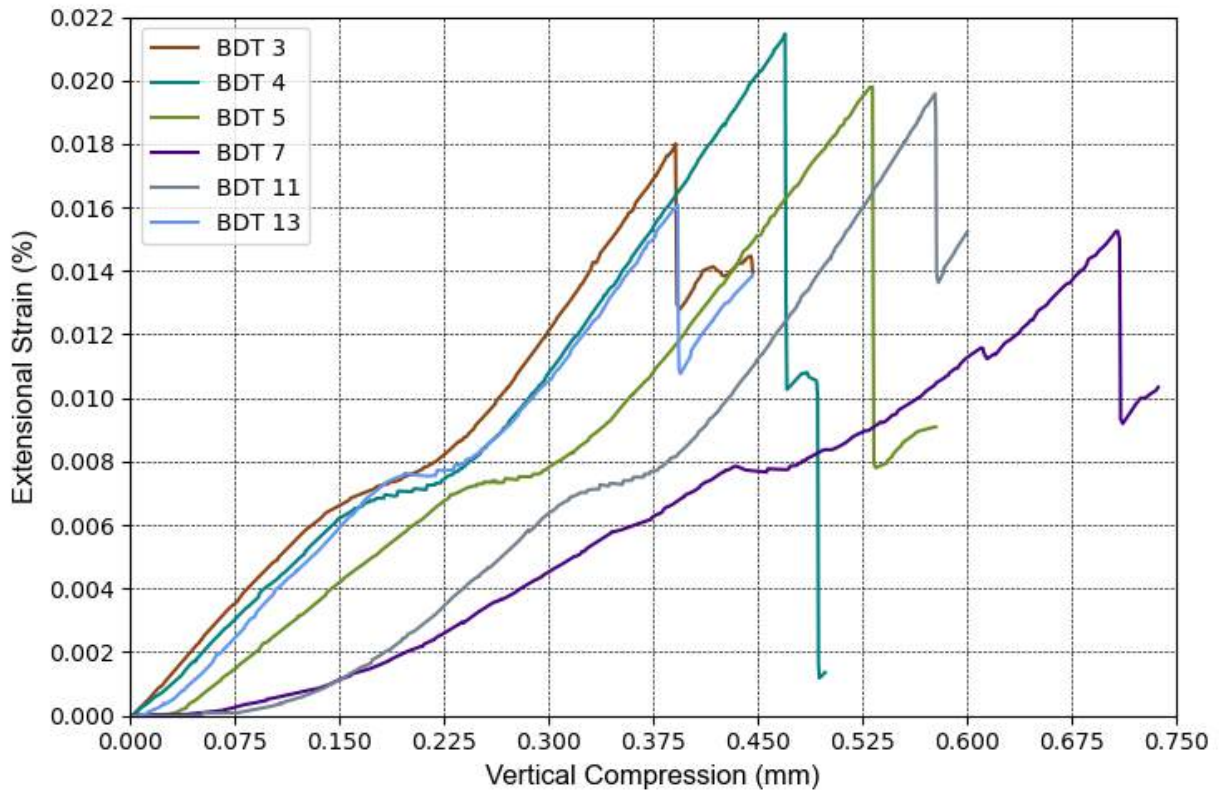


Figure 3.9: Tensile strain-displacements curves of the artificial rock material.

From Figure 3.9, the reported range of extensional strain values was 0.015 % to 0.021 % with an average of 0.018 %. Note that these values were taken from the peaks of the curves which correspond to the tensile strength of the material, and thus, if 0.018 % were regarded as a candidate value for critical extensional strain, it would be an over-estimation of the value when taking into account the discussion by Li and Wong (2013) in Section 2.2.7. For the purposes of including this approach in the determination of an adequate value for the critical extensional strain, an upper bound of 0.018 % was used in subsequent approaches.

3. Calculated Horizontal Strains from PIV Analysis Results

Considering the first and second approach as lower and upper-bound solutions, horizontal strains were analysed in the final approach to observe whether they would compare with magnitudes of what was previously observed. Again, significant tests shown in Figure 3.9 were only used for the analysis to exclude disc tests that might have resulted in inconclusive or compressive failure. Extensional strains are shown in Figures 3.10, 3.11 and 3.12.

Rows of subsets used for determining the horizontal strains in tests are listed in Table 3.2 and meshes of the subsets for each significant Brazilian disc test are shown in Appendix A. From all the tests, an average critical extensional strain using only plotted values within the lower and upper bounds was calculated as 0.014 %. The average extensional strain values that were recorded for each subset row are also shown in Table 3.2.

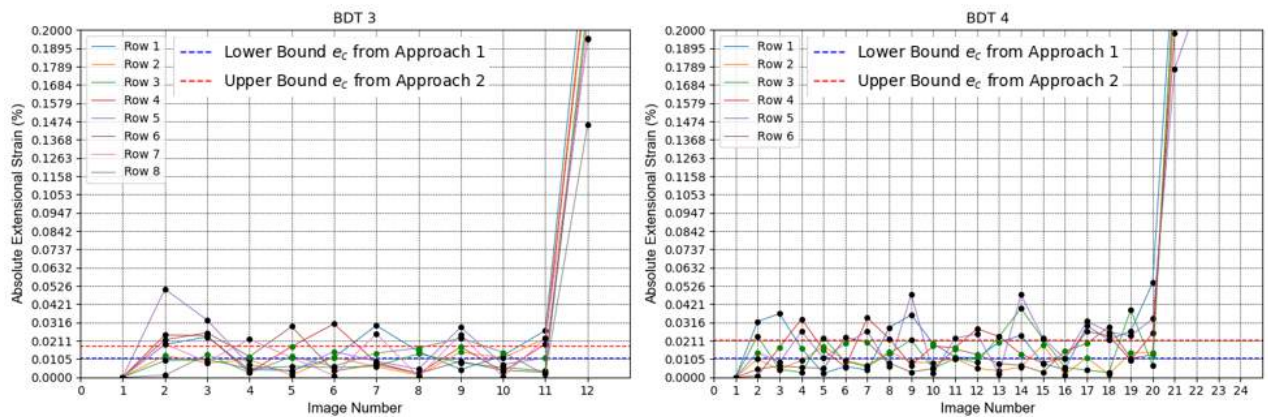


Figure 3.10: Extensional Strains plotted from PIV row data for Brazilian disc tests 3 and 4.

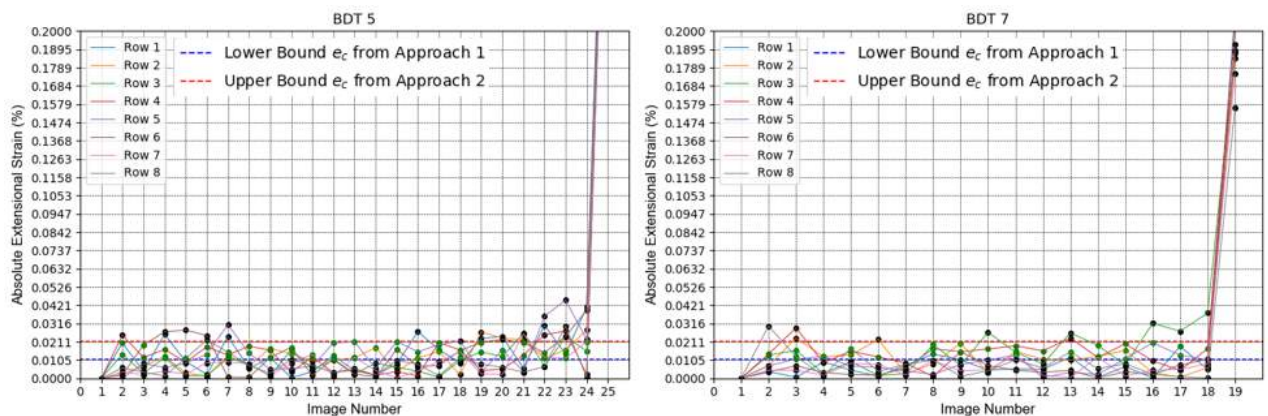


Figure 3.11: Extensional Strains plotted from PIV row data for Brazilian disc tests 5 and 7.

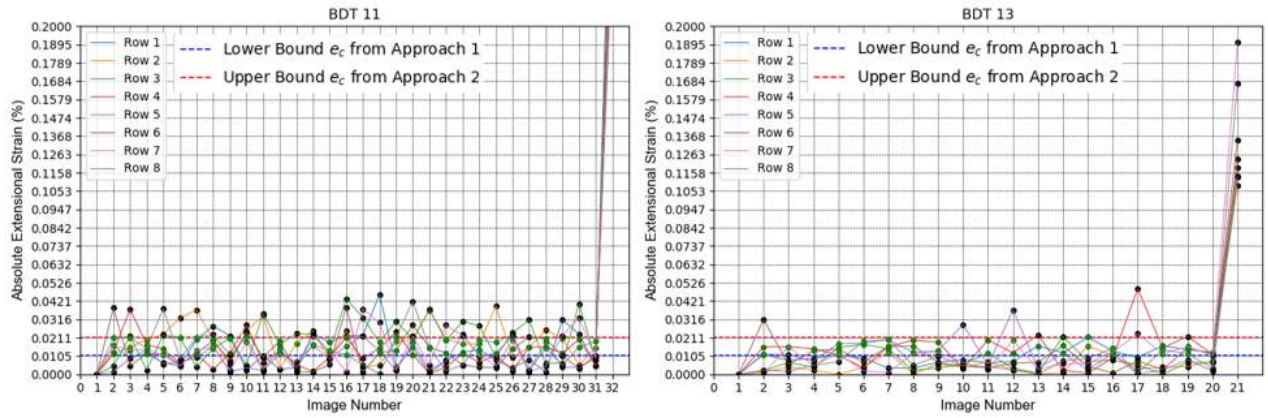


Figure 3.12: Extensional Strains plotted from PIV row data for Brazilian disc tests 11 and 13.

Figures 3.10, 3.11 and 3.12 show that in the cases of all tests, there is at least one row which shows a value within the upper and lower extensional strain bounds in the frame before the curve takes off upward at which point suggests the disc has exceeded its ultimate tensile strain limit.

Strain values experienced in Brazilian disc tests 5 and 13 conform particularly well to the bounds designated by Approaches 1 and 2. Values plotted above the upper bound, as seen in the curves, suggest the existence of minor cracking before the ultimate failure of the discs.

Figure 3.13 (left) displays the dimensions of a typical Brazilian disc test set-up (with the example of BDT 5); while in Figure 3.13 (right), the yellow highlighted subsets of BDT 4 are shown. The latter illustrates an example of where strips of subsets were selected to work out horizontal strains for BDT specimens. The subsets, chosen as such, ensured that regardless of where cracks has formed during tests, horizontal strains were adequately captured through monitoring the changes in the horizontal diameter of specimens.

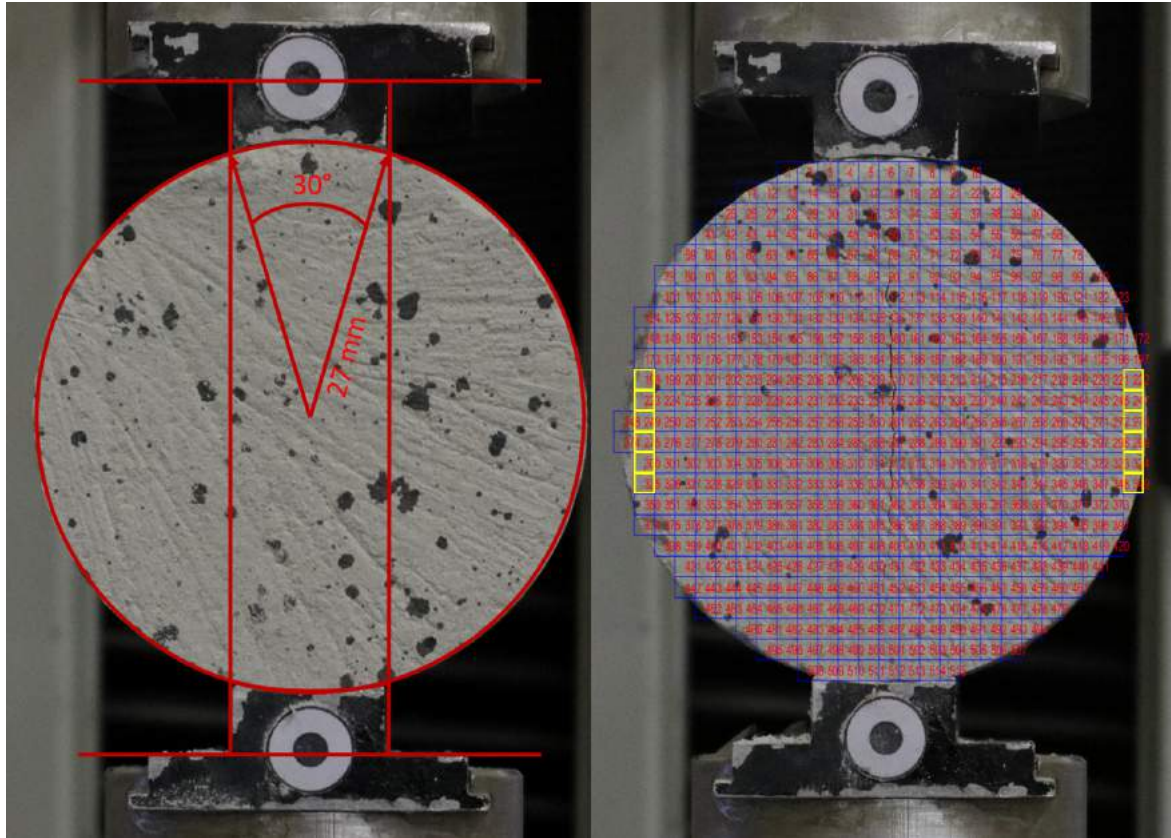


Figure 3.13: BDT Test setup (left) and failed specimen indicating subsets (right).

Table 3.2: Average Extensional Strain values for subset rows in Brazilian disc tests

| Brazilian Disc Test 3 | | | | | | | | |
|------------------------|--------|--------|--------|--------|--------|--------|--------|--------|
| Row Number | 1 | 2 | 3 | 4 | 5 | 6 | 7 | 8 |
| Left Subset | 151 | 176 | 201 | 226 | 251 | 276 | 301 | 326 |
| Right Subset | 175 | 200 | 225 | 250 | 275 | 300 | 325 | 350 |
| Extensional Strain (%) | 0.0129 | 0.0129 | 0.0135 | 0.0176 | 0.0130 | 0.0119 | 0.0113 | 0.0141 |
| Brazilian Disc Test 4 | | | | | | | | |
| Left Subset | 198 | 223 | 249 | 275 | 300 | 325 | - | - |
| Right Subset | 222 | 247 | 273 | 299 | 324 | 349 | - | - |
| Extensional Strain (%) | 0.0132 | 0.0145 | 0.0136 | 0.0154 | 0.0144 | 0.0144 | - | - |
| Brazilian Disc Test 5 | | | | | | | | |
| Left Subset | 155 | 180 | 205 | 230 | 255 | 280 | 305 | 330 |
| Right Subset | 179 | 204 | 229 | 254 | 279 | 304 | 229 | 354 |
| Extensional Strain (%) | 0.0139 | 0.0142 | 0.0139 | 0.0148 | 0.0150 | 0.0148 | 0.0131 | 0.0129 |
| Brazilian Disc Test 7 | | | | | | | | |
| Left Subset | 152 | 177 | 202 | 227 | 252 | 277 | 302 | 327 |
| Right Subset | 176 | 201 | 226 | 251 | 276 | 301 | 326 | 351 |
| Extensional Strain (%) | 0.0132 | 0.014 | 0.0148 | 0.0149 | 0.0124 | 0.0162 | 0.0129 | 0.0151 |
| Brazilian Disc Test 11 | | | | | | | | |
| Left Subset | 147 | 172 | 197 | 223 | 249 | 275 | 301 | 327 |
| Right Subset | 170 | 195 | 220 | 246 | 272 | 298 | 324 | 350 |
| Extensional Strain (%) | 0.0142 | 0.0158 | 0.0150 | 0.0136 | 0.0148 | 0.0130 | 0.0136 | 0.0147 |
| Brazilian Disc Test 13 | | | | | | | | |
| Left Subset | 170 | 195 | 221 | 247 | 273 | 299 | 324 | 349 |
| Right Subset | 194 | 219 | 245 | 271 | 297 | 232 | 348 | 373 |
| Extensional Strain (%) | 0.0138 | 0.0145 | 0.0149 | 0.0141 | 0.0139 | 0.0148 | 0.0133 | 0.0136 |

3.7 Summary of Material Properties

From the laboratory tests conducted, all results in terms of principal and residual stresses are listed in Table 3.3. The values presented are those used to determine the Mohr-Coulomb and Hoek-Brown parameters for the calibration of numerical models in the subsequent chapters.

Table 3.3: Principal Stress values from triaxial testing results of the artificial rock material

| Laboratory Test | Confinement, σ_3 (kPa) | Principal, σ_1 (kPa) | Residual, σ_1 (kPa) |
|-----------------------------|-------------------------------|-----------------------------|----------------------------|
| Uniaxial tests | | | |
| UCS1 | 0 | 758 | 732 |
| UCS2 | 0 | 709 | 660 |
| UCS3 | 0 | 699 | 619 |
| UCS4 | 0 | 750 | 672 |
| UCS5 | 0 | 762 | 628 |
| Triaxial tests | | | |
| TX1 | 100 | 979 | 584 |
| TX2 | 200 | 835 | 643 |
| TX3 | 300 | 1241 | 1101 |
| TX4 | 400 | 1269 | 1176 |
| TX5 | 500 | 1646 | 1488 |
| TX6 | 700 | 1833 | 1785 |
| Brazilian disc tests | | | |
| BDT1 | -93 | 0 | - |
| BDT2 | -93 | 0 | - |
| BDT3 | -93 | 0 | - |
| BDT4 | -84 | 0 | - |
| BDT5 | -101 | 0 | - |
| BDT6 | -99 | 0 | - |
| BDT7 | -79 | 0 | - |
| BDT8 | -75 | 0 | - |
| BDT9 | -81 | 0 | - |
| BDT10 | -79 | 0 | - |
| BDT11 | -79 | 0 | - |
| BDT12 | -72 | 0 | - |
| BDT13 | -105 | 0 | - |

The results can be summarised and the following material properties were deemed to be representative of the material tested:

- The relative unit weight of the material is 1.453 based on laboratory specimens. An average porosity of 37.3 % was calculated when taking into account laboratory specimens and panels used in the investigation.
- The Young's modulus and Shear modulus was taken as an average of 778 MPa and 365 MPa, respectively, with a Poisson's ratio estimation of 0.22.

- The UCS and BDT strengths were assumed to be 736 kPa and 87 kPa, respectively. The critical extensional strain, deduced by the various approaches used, was approximated to 0.014 %.

3.8 Mohr-Coulomb Characterisation

With reference to Table 3.3, it is necessary to make use of the correct set of stresses in the stress-strain curve that adequately represent the current stress conditions of the material. These are the peak response (the maximum principal stresses) and the residual response (post peak principal stresses). The cohesive component of the Mohr-Coulomb material model is mobilised first, while the frictional component is only mobilised at higher stages of strain, once the pre-existing joints propagate (Sainsbury, 2012). The failure envelope for peak and residual response can be defined using the stress parameters s and t (Parry, 2004) given by Equations 3.2 and 3.3. These parameters are plotted against each other (in s and t stress space) which are in turn used to calculate the Mohr-Coulomb parameters ϕ and c by making use of Equations 3.4 and 3.5:

$$s = \frac{\sigma_1 + \sigma_3}{2} \quad (3.2)$$

$$t = \frac{\sigma_1 - \sigma_3}{2} \quad (3.3)$$

$$m = \sin \phi \quad (3.4)$$

$$b = c \cos \phi \quad (3.5)$$

Where:

s, t = The centre and radius of the Mohr Circle, respectively (kPa)

m = The gradient of the s and t regression line (kPa/kPa)

b = The y intercept of the s and t regression line (kPa)

c = The cohesive strength due to curing (kPa)

ϕ = The angle of internal friction (°)

Plotting the peak triaxial results in s and t stress space and performing linear regression, allows for the necessary constants and gradients to be obtained for the calculations of the angles of internal friction and cohesion intercepts. Figure 3.14 shows the s and t plot for peak strength of mature, young triaxial specimens as well as for combining the specimens. Similarly, Figure 3.15 shows the s and t plot for the residual strengths. Mature specimens are indicated in blue and young specimens in red. As listed in Table 3.4, all the values of the regression constants were used to calculate the Mohr-Coulomb parameters. The Mohr-Coulomb failure envelopes for peak and residual strengths with their tension cut-offs are plotted in Mohr-circle stress space and shown in Figures 3.16 and 3.17, respectively. Solid lines indicate mature specimens and dashed lines indicate young specimens.

Table 3.4: Upper and lower bound Mohr-Coulomb parameters of the artificial rock material.

| Parameter | m (kPa/kPa) | b (kPa) | ϕ ($^\circ$) | c (kPa) |
|--------------------------|---------------|-----------|---------------------|-----------|
| Mature Peak Strength | 0.255 | 291.8 | 14.77 | 301.8 |
| Young Peak Strength | 0.331 | 150.7 | 19.33 | 159.7 |
| All Peak Strength | 0.284 | 230.2 | 16.50 | 240.1 |
| Mature Residual Strength | 0.388 | 115.2 | 22.85 | 125.0 |
| Young Residual Strength | 0.389 | 66.1 | 22.89 | 71.7 |
| All Residual Strength | 0.371 | 103.6 | 21.80 | 111.6 |

From the peak strength properties in Table 3.4, the values for ϕ (and m as related by Equation 3.4) are lower than those of the residual strength values. This is due to the frictional component of strength only being mobilised in the latter stages of triaxial testing as postulated by Schmertmann and Osterburg (1960) which is made known in the investigations of Sainsbury (2012). Conversely, the cohesive component of strength is mobilised first during a triaxial test which can be observed by the larger values of c (and b by Equation 3.5) in Table 3.4 for peak strengths compared to residual strengths. This demonstrates that peak strengths are primarily defined by the cohesive component of the material and residual strengths, by the frictional component of the material.

From Table 3.4 and Figures 3.14 and 3.15, it can also be observed that mature specimens yield slightly more strength than young specimens with the radii of the Mohr-circle (i.e. parameter t) being larger for mature specimens as expected. This shows that the ageing of specimens has negligible effects on the slope of the lines, but does affect cohesion. Thus, the degree of cohesion of artificial rock specimens is related to its curing time. It should also be noted that failure would inherently occur later on in triaxial tests for older specimens since the line drawn in s and t stress space would be higher than that of a younger specimen.

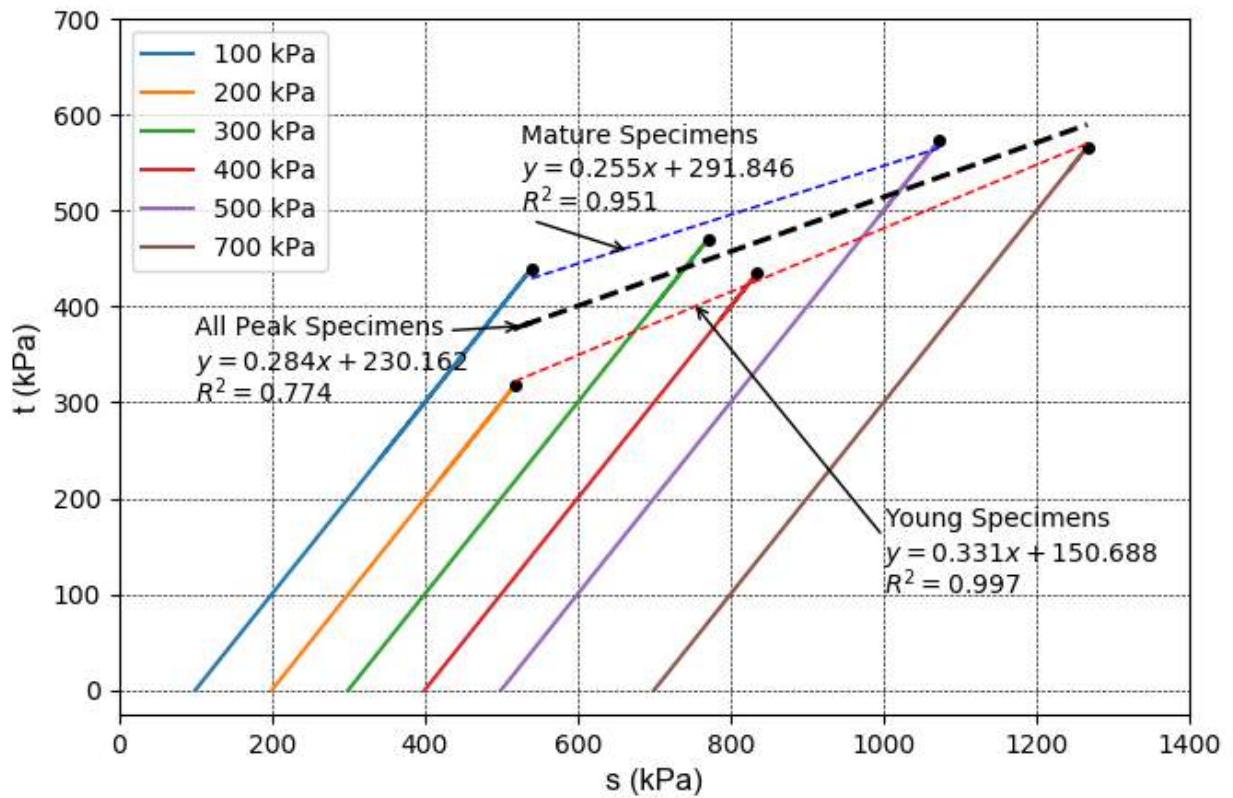


Figure 3.14: Plot of peak strengths in s and t stress space for all triaxial tests.

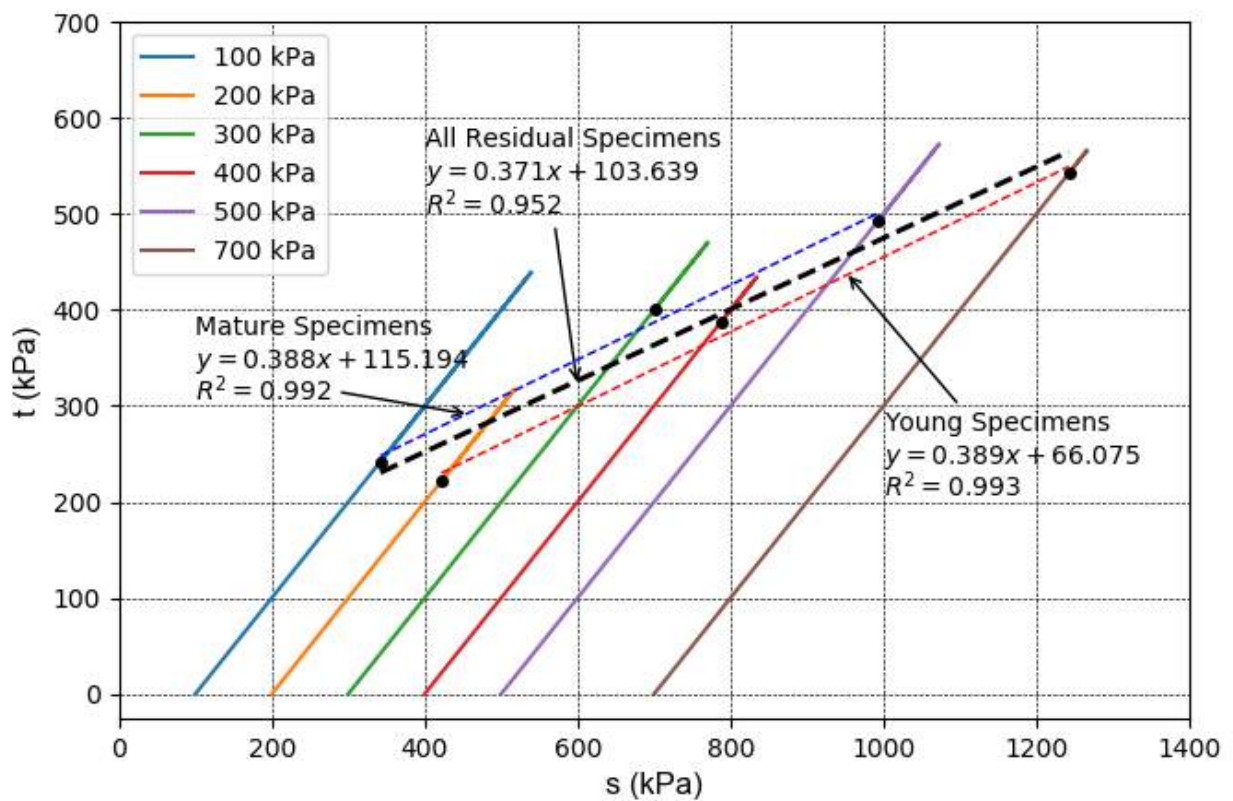


Figure 3.15: Plot of residual strengths in s and t stress space for all triaxial tests.

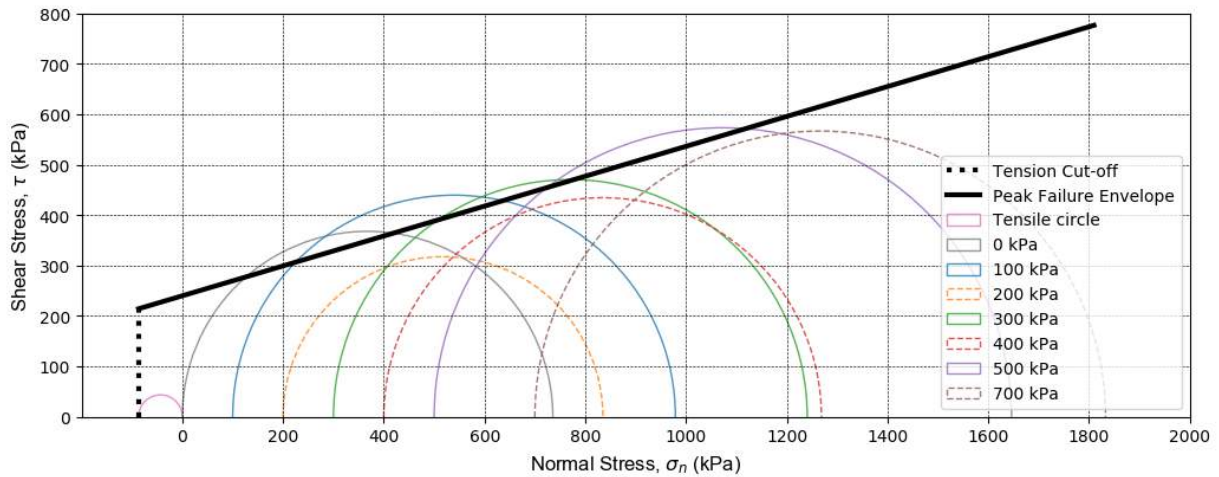


Figure 3.16: Plot of peak strength Mohr circles with defined failure envelope.

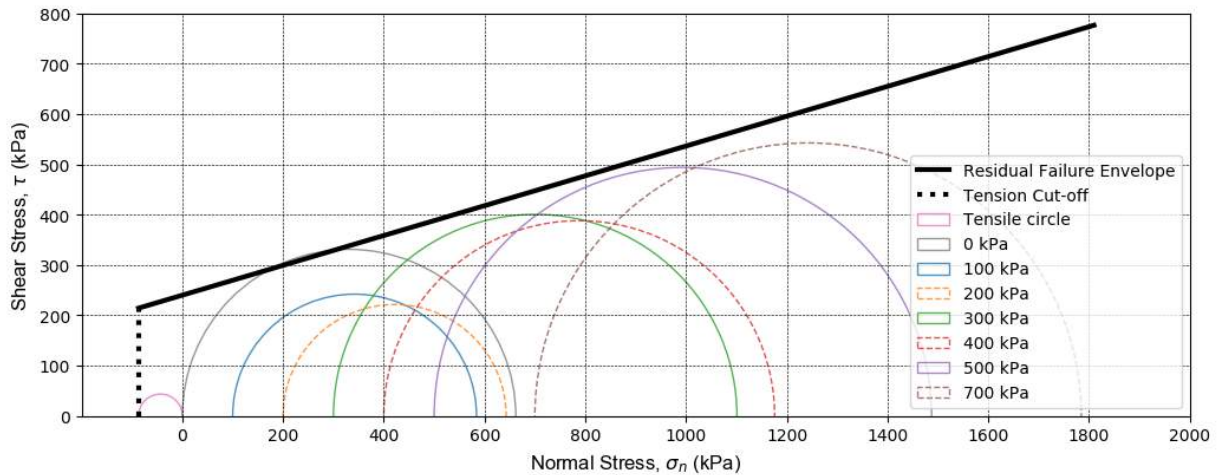


Figure 3.17: Plot of residual strength Mohr circles with defined failure envelope.

When plotting the Mohr-circles in the order of increasing confinement, one can note from Figure 3.16, that the difference between shear stresses of successive Mohr-circles decreases. This is observed by the flattening in radii of the Mohr-circles along the normal stress axis. This can be explained on a microscopic scale where the discontinuities initiate a state of bulking at low confinements, where the increased size of the material (in its bulked state) results in a higher friction angle. This is evident from the large Mohr-circles of the unconfined test and 100 kPa triaxial test. On the other hand, at high confinements, the opposite occurs where the friction angle is small due to the hindrance of high confinement on the bulking of the sample. This causes a ductile response at high confinements and hence the flattening of Mohr-circles. At a high enough confinement failure becomes entirely ductile (critical state). The phenomenon of critical state in rock, described by Barton (1976) and Singh et al. (2011) (see Section 2.2.6), seems to apply to the artificial rock material at the range of confinements 500 to 700 kPa. It must be noted that the conventional Mohr Coulomb model does not accommodate for this response of the material at high confinements, and is better suited for the residual strength case.

3.9 Hoek-Brown Characterisation

The single linear Mohr-Coulomb envelope does not account for the flattening off of the curve at higher confinements since there is a change in failure mechanism at high confinement stress. The Hoek-Brown model, although empirical, allows for a better characterisation of the artificial rock mass material using the laboratory results obtained. The procedure for characterising the artificial rock material in its peak and residual strength state is outlined below.

Following the method used in Hoek and Brown (2019), the Hoek-Brown parameters σ_{ci} and m_i were determined through the preferred method of uniaxial and triaxial testing. It must be noted that the GSI was not used to determine these parameters since all laboratory testing was conducted on intact rock specimens; thus, the GSI was inherently set to 100 with the damage factor, D set to 0 (as recommended in Section 2.2.3).

For characterising the residual values for laboratory tests, it was assumed that one joint was present in the mobilisation of friction during compression tests. The laboratory results used in the regression analysis to determine σ_{ci} and m_i were seven sets of peak and residual principal stresses taken from Table 3.3 which included the six triaxial test results and the average UCS result. It must be noted that the residual UCS average was taken as 622 kPa. From the regression analysis for the peak strength values, σ_{ci} and m_i were calculated as 694 kPa and 1.694 respectively. For the residual strength values, $\sigma_{ci} = 434$ kPa and $m_i = 3.091$.

The Hoek-Brown parameters used in producing the peak and residual strength failure envelopes are summarised in Table 3.5. The upper limit to the confining stress range chosen in this experiment was determined based on the maximum possible confined stresses condition of the samples that had undergone centrifuge tests. It was noted by the inventors of the Hoek-Brown model that there is no theoretically correct method for determining this confining stress range and so a trial and error procedure based on practical compromise is permitted.

For this case, the following σ_3 stress range was chosen for the peak and residual strength envelopes respectively: $-228 \text{ kPa} < \sigma_3 < 1300 \text{ kPa}$ and $-117 \text{ kPa} < \sigma_3 < 1300 \text{ kPa}$. The stress ranges were chosen to accommodate a tension cut-off at the tensile strength of -87.20 kPa . The tension cut-off was decided upon over using a function from Griffith's theory as it more comparable to the Mohr-Coulomb model. While the upper limit of the defined confining stress range is less critical and can depend on the user's discretion, the lower limit can be calculated using Hoek-Brown methods. Checks were made for the lower limit of confining stress by using the Hoek-Brown equation to calculate tensile strength, as shown in Equation 3.6:

$$\sigma_t = \frac{-s\sigma_{ci}}{m_b} \tag{3.6}$$

Using Equation 3.6 that includes Hoek-Brown parameters, the lower limit was calculated as -410 kPa for peak strengths and -140 kPa for residual strengths. It can be seen that these values were reduced accordingly to accommodate for the tension cut-off.

Table 3.5: Summary of Hoek-Brown Parameters for peak and residual failure envelopes

| Parameter | σ_{ci} (kPa) | m_i | s | a | m_b |
|-------------------|---------------------|-------|-------|-----|-------|
| Peak Strength | 694 | 1.694 | 1.000 | 0.5 | 1.694 |
| Residual Strength | 434 | 3.091 | 1.000 | 0.5 | 3.091 |

Figure 3.18 shows the comparison of the peak and residual Hoek-Brown failure envelopes in principal stress space. Transforming these failure envelopes into normal and shear stress space and plotting the Mohr circles for results obtained from laboratory testing, the artificial rock material can be fully characterised for the confining stress range needed. Figure 3.19 and 3.20 show the Hoek-Brown Criterion for the material for peak and residual values in terms of shear and normal stresses.

From Stacey (1981), the critical extensional strain criterion is applicable for especially predicting fracture initiation in low confinements of stress — which can be noted as an area in which the Mohr-Coulomb and Hoek-Brown models do not function well as these criteria tend to overpredict strength in this area of confinement.

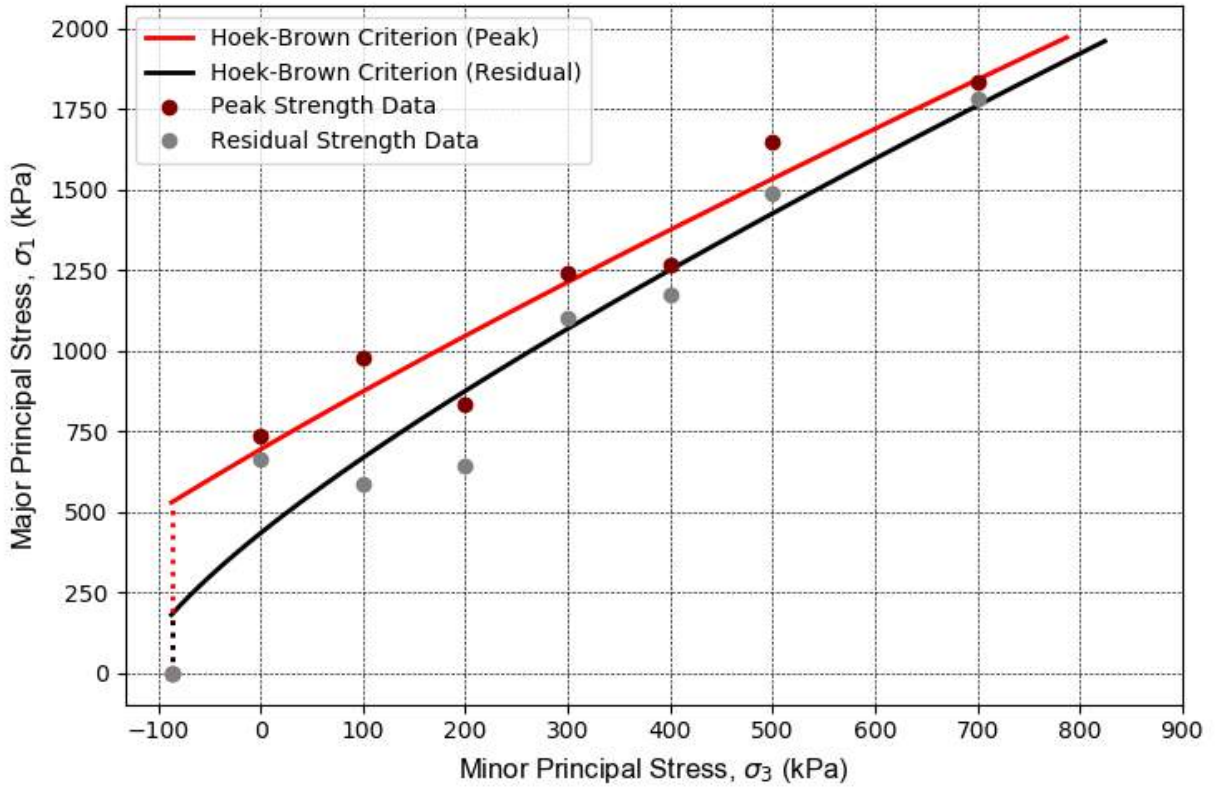


Figure 3.18: Hoek-Brown failure envelope in principal stress space.

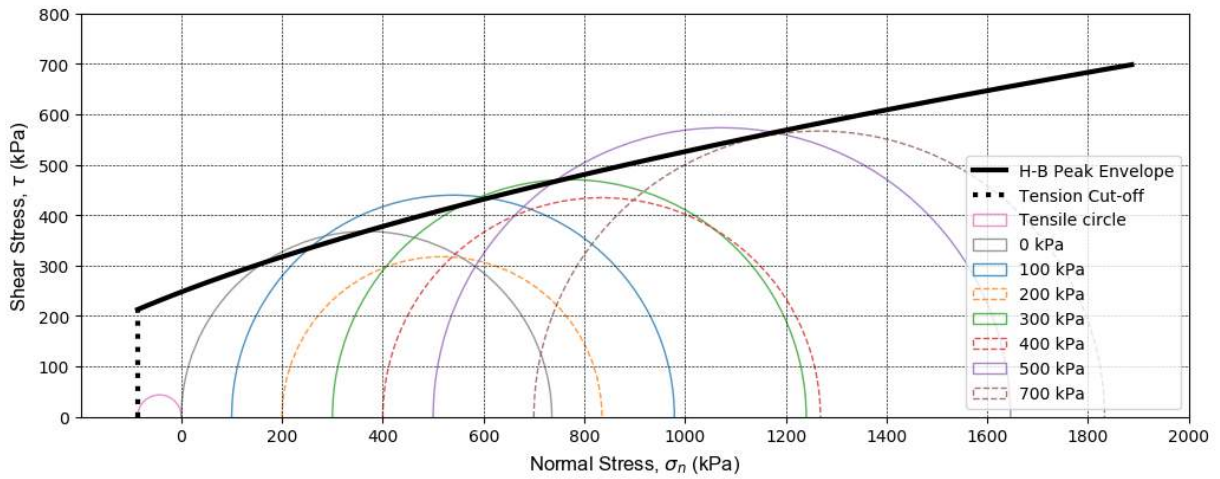


Figure 3.19: Hoek-Brown failure envelope for peak strength values in $\sigma_n - \tau$ stress space.

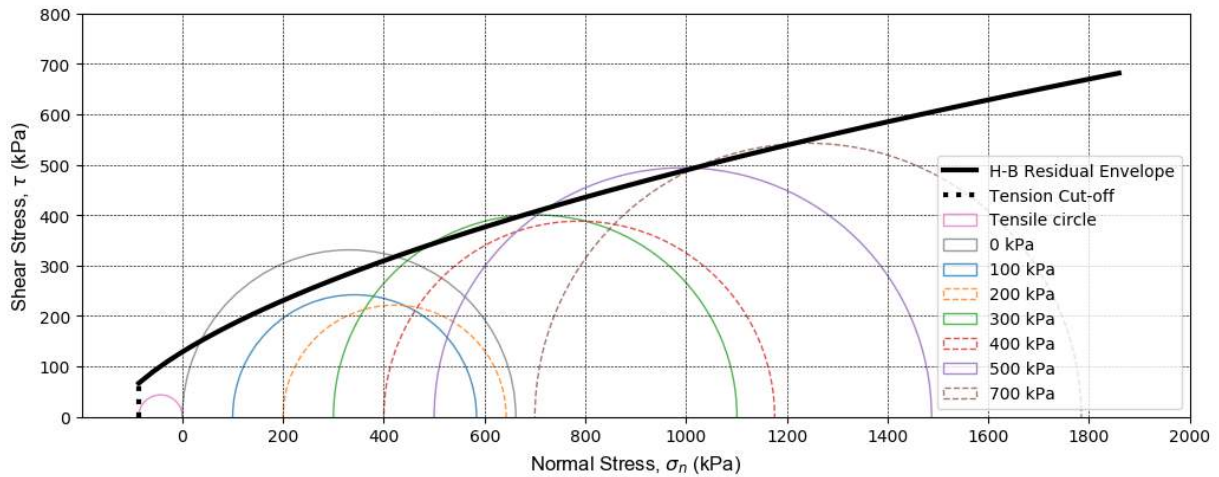


Figure 3.20: Hoek-Brown failure envelope for residual strength values in $\sigma_n - \tau$ stress space.

3.10 Artificial and Actual Rock-Mass Comparison

This section presents the final comparing and contrasting of characteristics between the manufactured artificial rock-mass and underground rock. The argument for using an artificial rock material that is representative of actual underground rock mass is based on the mechanical properties, brittleness and qualitative fragmentation of the artificial rock material. The mechanical properties of underground rock presented for three rock types in Section 2.2.8 are referred to when regarding the applicability of the artificially manufactured rock material.

Apart from the elastic-plastic behaviour exhibited by the artificial rock material in UCS testing, which compares well with the shape of the stress-strain plots of Section 2.2.8, the failure strain range of 0.25 % to 0.36 % (in Figure 3.3) is similar to the ranges of underground rock (furthermore with Indiana limestone and shale in particular). In addition, the material compares well with the failure strain of concrete which ranges from 0.30 % to 0.35 %. For this reason, the artificial rock material is able to facilitate brittleness in a way similar to that in which underground rock behaves. One contrast that can be made is the strength of the material. Most underground rocks are above two orders of magnitude larger in UCS strength than the artificial rock material characterised in this section. The same can be said in some cases for the Young's modulus between the material and underground rock. Incidentally, the high porosity of the manufactured material compares well with that of shale, when referring back to Table 2.1.

According to the data set utilised by Sheorey (1997), the compressive to tensile strength ratio covers a range of 2.7 to 39 for different rock types. Since Griffith's theory was based

on a ratio of 8.0 for brittle materials, the average ratio of compressive strength to tensile strength for the artificial rock material in this investigation was calculated as 8.46.

It can be noted qualitatively that the artificial rock material takes on rock-like features similar to that of sedimentary rock which displays fragmentation upon failure. The sedimentary rock shale, in its intact and fragmented form, can be visually comparable to the artificial rock material of this investigation. From Figure 3.21, a similar ‘blockiness’ is perceived between shale and the artificial rock material. In its intact form, shale is a clastic rock which means it is composed of broken pieces of old rocks (constituents of mud and flakes of clay) which forms layering during the sedimentation process. This same process can be compared to the artificial rock material since during curing the specimens become densified resulting in layering analogous to shale. Both specimens have fine-grained compositions as well.



Figure 3.21: Visual comparison between the artificial rock material and shale in their intact and fragmented forms.

It is concluded herein that the artificial rock material cannot be fully representative of rock; however, it shows signs and mechanical properties similar to that of certain rock. It is noted that the manufactured material does not resemble an exact type or family of rock; however, it is assumed that it functions in the same way rock does on a weaker scale when laboratory testing is conducted on the material which follows in this investigation. It should be noted that the ranges of failure strain in typical rock favourably correspond with the data of the artificial rock material which is valuable in determining a suitable failure criterion for the material when evaluating centrifuge test results.

4 Physical Modelling

The physical modelling conducted in this investigation was done using the artificial rock material characterised in Chapter 3. The aim of this chapter is to describe the experimental methodology followed to replicate the cave mining process in a geotechnical centrifuge. Firstly, the background to centrifuge testing is briefly introduced following the range of scaling laws used to satisfy similitude in the study. Discussions concerning the equipment and instrumentation used in carrying out physical modelling are given and the test procedure is presented. The two-dimensional experimental models which were subjected to different stress conditions are outlined with the provision of theoretical stress calculations for each. Lastly, the chapter is concluded with the methodology adopted for image analysis using OpenCV-Python (Computer Vision) as well as investigating strain development through Particle Image Velocimetry.

4.1 Background on the Geotechnical Centrifuge

According to Hoek (1965a), when designing physical models for excavations that are small relative to the depth of the model it is adequate to substitute the forces that are generated as a result of self weight by externally applied loads. However, when the size of the excavation that is modelled exceeds a significant depth, this substitution is no longer valid and centrifugal loading must be used. For large excavations relative to the model size in this study, it was necessary to utilise centrifugal loadings which would bring the stresses of models closer to the reality of the cave mining situation thereby scaling the forces applicable in actual cave mines. The physical modelling was conducted in the Geotechnical Centrifuge Laboratory at the Department of Civil Engineering of the University of Pretoria. The geotechnical centrifuge (also shown in Appendix C) at the university is a fourth generation C67 model built by the French manufacturing company, Actidyn, and is able to reach accelerations of up to 130 g, i.e. 130 times the earth's gravitational acceleration. The specifications of the machine are fully described by Jacobsz et al. (2014).

4.2 Scaling Relationships

For the physical modelling in this investigation to be representative of the conditions applicable in the field it was necessary to satisfy the requirements of similitude. Buckingham (1914) postulated that the similitude of systems is based on dimensional analysis used extensively in the Buckingham π theorem. This theorem makes use of independent parameters that characterise a system and uses them to determine equations that must be

satisfied for achieving similitude between the scale model and the prototype. The traditional scaling relation can be given by the Equation 4.1 which assumes that the material properties of the prototype and model are the same (Jacobsz et al., 2018). Note that subscripts m and p refer to the model and prototype, respectively:

$$\frac{g_m}{g_p} = \frac{L_p}{L_m} \quad (4.1)$$

Making use of Equation 4.1 would imply that the 500 mm by 450 mm by 55 mm sample panels would represent a 40 m by 36 m by 4.4 m volume of rock at 80 g provided the model material was identical to that of the prototype. According to Jacobsz et al. (2018), using the same material for both the prototype and modelling material to simulate deep mining problems is not feasible due to the limitations of most centrifuges. Hence it was necessary to manufacture an artificial rock material that would represent the brittleness rock at a much weaker strength scale. Through the use of the Buckingham π theorem, Hoek (1965a) outlined the governing equation needed for satisfying similitude when studying underground mining scale models, which is given in Equation 4.2:

$$\frac{L_p}{L_m} = \alpha \times \frac{E_p}{E_m} \times \frac{\rho_m}{\rho_p} \times \frac{g_m}{g_p} \quad (4.2)$$

Where:

α = The ratio of stresses at an equivalent point in the model. (i.e. $\alpha = \frac{\sigma_p}{\sigma_m}$)

L = A characteristic length dimensions.

ρ = The relative density of the material.

E = The Young's modulus.

Scaling relationships in Equation 4.2 were derived on the basis of various assumptions. They are listed as follows: firstly, the deformation preceding the point of fracture will be purely elastic. Secondly, the fracture strength of rock can be characterised by a Mohr-Coulomb-type failure criterion which consists of a frictional and a cohesive strength component. Lastly, it was assumed that the unconfined compressive strength of the material is competently represented by the cohesive strength component of the Mohr-Coulomb-type model used.

In the analyses conducted by Hoek (1965a), it was considered that fracturing resulted in the reduction of the strength component, leaving the remaining strength of the material

merely characterised by the frictional component. In the case of Mohr-Coulomb, this was equivalent to moving the failure envelope to pass through the origin in a graphical context. For Equation 4.2, it implies that the value of α can be taken as the ratio of UCS between the prototype and the modelling material. Further, upon accounting for the fact that material strength is affected by sample size, a modification was made by Hoek (1965a) resulting in Equation 4.3:

$$\left(\frac{L_p}{L_m}\right)^{\frac{3}{2}} = \alpha \times \frac{E_p}{E_m} \times \frac{\rho_m}{\rho_p} \times \frac{g_m}{g_p} \quad (4.3)$$

Raising the ratio of characteristic length dimensions of the prototype and model to the power of $\frac{3}{2}$ implies that a higher gravitational acceleration is required for fracturing a smaller sample compared to when scale effects are negligible. In addition, it was stated by Hoek (1965a) that investigating mining problems in a centrifuge should be performed at the highest practical acceleration to represent the high stresses present in deep mines. In this investigation, it was decided that an acceleration of 80 g would be used due to the limitations of the centrifuge camera at higher accelerations.

According to Hoek (1965b), for similitude to be satisfied between the prototype and modelling material, the Poisson's ratios of the two materials need to be equal. This allows for the stress response in the horizontal direction, caused by an increment in vertical stress, to be proportional and comparable in instances where the lateral deformation is constrained. In other words, the proportion of vertical to horizontal deformation would not match up if the Poisson's ratios of the two materials were different, and therefore the comparison would be void. From Figure 2.22, the Poisson's ratios for common rocks vary in the range of 0.05 to 0.4. The artificial rock material with a reported Poisson's ratio of 0.22 falls within the specified range which is generally similar to most rock types. Following the methodology of Jacobsz et al. (2018) and replacing the ratio of compressive strengths of the prototype and modelling material (α) with a critical extensional strain criterion developed by Stacey (1981), further modifications can be applied to the scaling relationship, given by Equation 4.4. Note that e_{3p} and e_{3m} are the critical extensional strains of the prototype and modelling material, respectively.

$$\left(\frac{L_p}{L_m}\right)^{\frac{3}{2}} = \frac{e_{3p}}{e_{3m}} \times \left(\frac{E_p}{E_m}\right)^2 \times \frac{\rho_m}{\rho_p} \times \frac{g_m}{g_p} \quad (4.4)$$

Using typical ranges for the rock properties presented in Table 2.1 allowed for the parameters of the all scaling relationships to be evaluated. Once these properties for the

relevant rocks discussed in Section 2.2.9 were obtained, along with those of the artificial rock material, they were used to back-calculate the scale factors for the centrifuge tests conducted in this investigation. The ranges of scaling law parameters are presented in Table 4.1 and the calculated scaling factors for the corresponding relationships are given in Table 4.2 where scaling factors are rounded up to their nearest whole numbers. Note L_p is calculated from setting L_m as a constant, which in this case was the width of the trapdoor used in the centrifuge model to achieve undermining of the model rock mass (see Section 4.3.4). The ratio of these properties is equal to the scale factor.

Table 4.1: Scaling law parameters for the prototype and model

| Prototype Property | Value Range | Unit | Model Property | Constant Value | Unit |
|--------------------|---------------|-------------------|----------------|----------------|-------------------|
| σ_p | 5.00–300 | MPa | σ_m | 0.736 | MPa |
| L_p | * x | m | L_m | 0.250 | m |
| ρ_p | 2.30–3.00 | kN/m ³ | ρ_m | 1.45 | kN/m ³ |
| E_p | 1.00–106 | GPa | E_m | 0.778 | GPa |
| e_{3p} | 0.0073–0.0175 | % | e_{3m} | **0.014 | % |

* x is calculated using Equations 4.2 through 4.4.

**Critical Extensional Strain value calculated in Chapter 3.

It should be noted for clarity that the artificial rock material, and hence the physical models, were not specifically representative of a certain type of rock (or of a certain block cave mine); however, the material and models of this study were aimed at satisfying the scaling laws for a range of rock types and therefore catering for cave mining in multiple rock types. Typically σ_m is taken at the base of models since the artificial rock material would first fail in this position when undercut.

Table 4.2: Comparison for the range of scale factors for various scaling relationships

| Equation | Scaling Relationship | Reference | Scale Factor |
|--------------|--|-----------------------|---------------|
| Equation 4.2 | $\frac{L_p}{L_m} = \alpha \times \frac{E_p}{E_m} \times \frac{\rho_m}{\rho_p} \times \frac{g_m}{g_p}$ | Hoek (1965) | 441–2 147 750 |
| Equation 4.3 | $\left(\frac{L_p}{L_m}\right)^{\frac{3}{2}} = \alpha \times \frac{E_p}{E_m} \times \frac{\rho_m}{\rho_p} \times \frac{g_m}{g_p}$ | Hoek (1965a) | 58–16 646 |
| Equation 4.4 | $\left(\frac{L_p}{L_m}\right)^{\frac{3}{2}} = \frac{e_{3p}}{e_{3m}} \times \left(\frac{E_p}{E_m}\right)^2 \times \frac{\rho_m}{\rho_p} \times \frac{g_m}{g_p}$ | Jacobsz et al. (2018) | 12–9 291 |

From Table 4.2, it is worth noting that by utilising the modifications to Equation 4.2 made by Hoek (1965a) the upper bound scale factor decreased by two orders of magnitude. Further differences in these factors were observed when the ratio of compressive strengths (α) was replaced by the ratio of critical extensional strains of the prototype and modelling materials as per the refinement made by Jacobsz et al. (2018).

4.3 Centrifuge Test Setup and Equipment

A typical physically modelled test involved the use of artificial rock panels which were in the range of young and mature strength values presented in Chapter 3. Before conducting centrifuge testing, samples were placed in the testing frame which supported the bottom base of the sample. Due to large shrinkage and settlement during the curing process, sample dimensions decreased significantly. After samples were scarified and prepared for being transported into the test frame, they were approximately 475 mm in width, 430 mm in height and 47 mm in thickness. Photographs of the test frame itself as well as the sample residing within the test frame before the window is fastened are presented in Figures 4.1 and 4.2, respectively. A schematic of the test frame schematic in which sample panels were contained is shown in Figure 4.3.

Physical modelling of the cave mining process using the geotechnical centrifuge was performed at a gravitational acceleration of 80 g whereby the five 50 mm wide platforms positioned adjacent to each other supported a sample panel of artificial rock material. These platforms (or trapdoors) were controlled using linear actuators driven by a 24 Volt DC motor and gearbox. The linear actuators in turn were controlled using a high current motor driver with a variable duty cycle. A closed-loop controller was developed specifically for centrifuge applications, termed Fly-by-Pi (Broekman et al., 2020).

Fly-by-Pi is based on a Raspberry Pi solid-state microcomputer. The user can remotely execute time-based, load control or displacement control scripts using pre-programmed Python scripts. For this experiment, the duty cycle was set to a low value which allowed for precision control of the linear actuator's velocity. Thus, the electric actuators were able to be withdrawn at a required rate causing the support of the trapdoor to be removed which simulated the undermining of an ore body in the cave mining process.

There are various components integrated within the test frame which were required for simulating external loads representing different cave mining conditions underground. The most important of these were the water bladders and brass weights, which allowed for a certain combination of horizontal and vertical stresses to be applied, respectively, and in turn a certain stress state to be achieved. These components, amongst other equipment and systems, are described in detail in the following paragraphs.

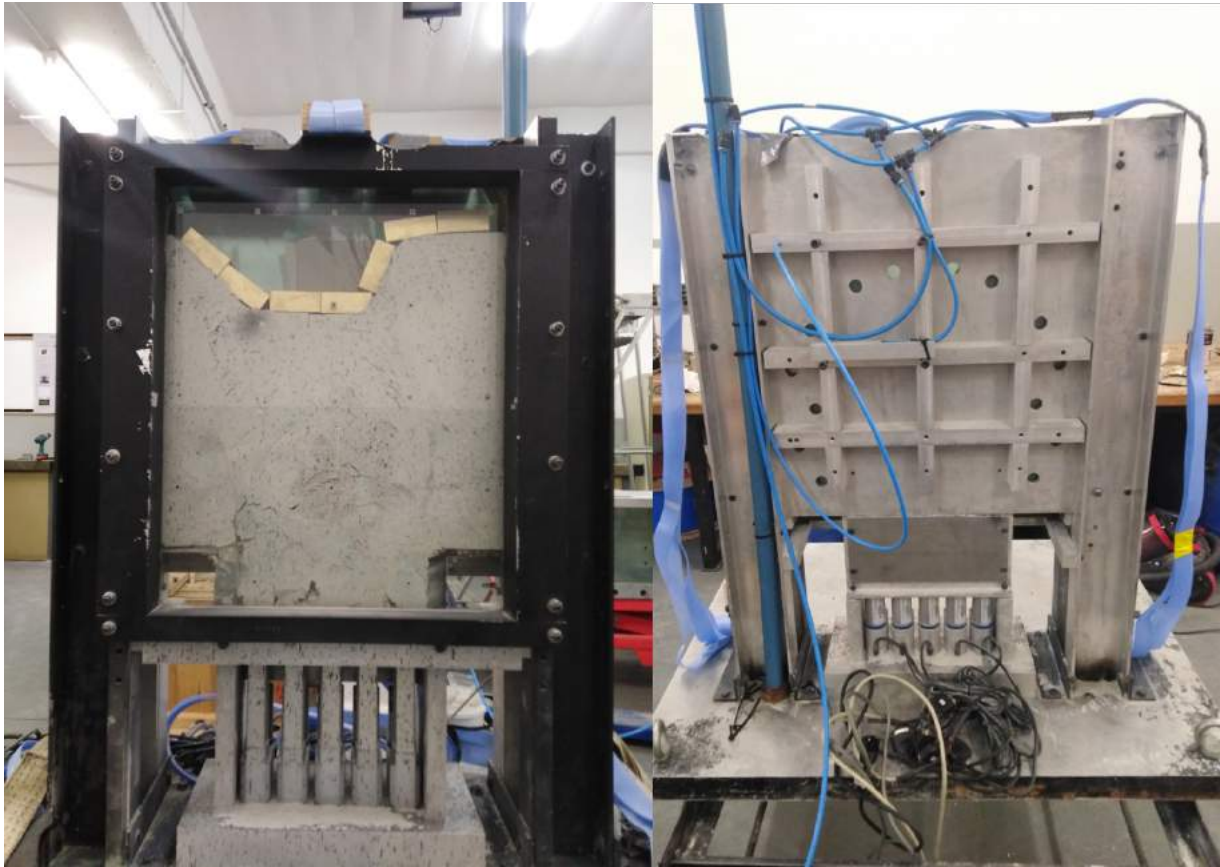


Figure 4.1: The front of the test frame (left) and the back of the test frame (right).

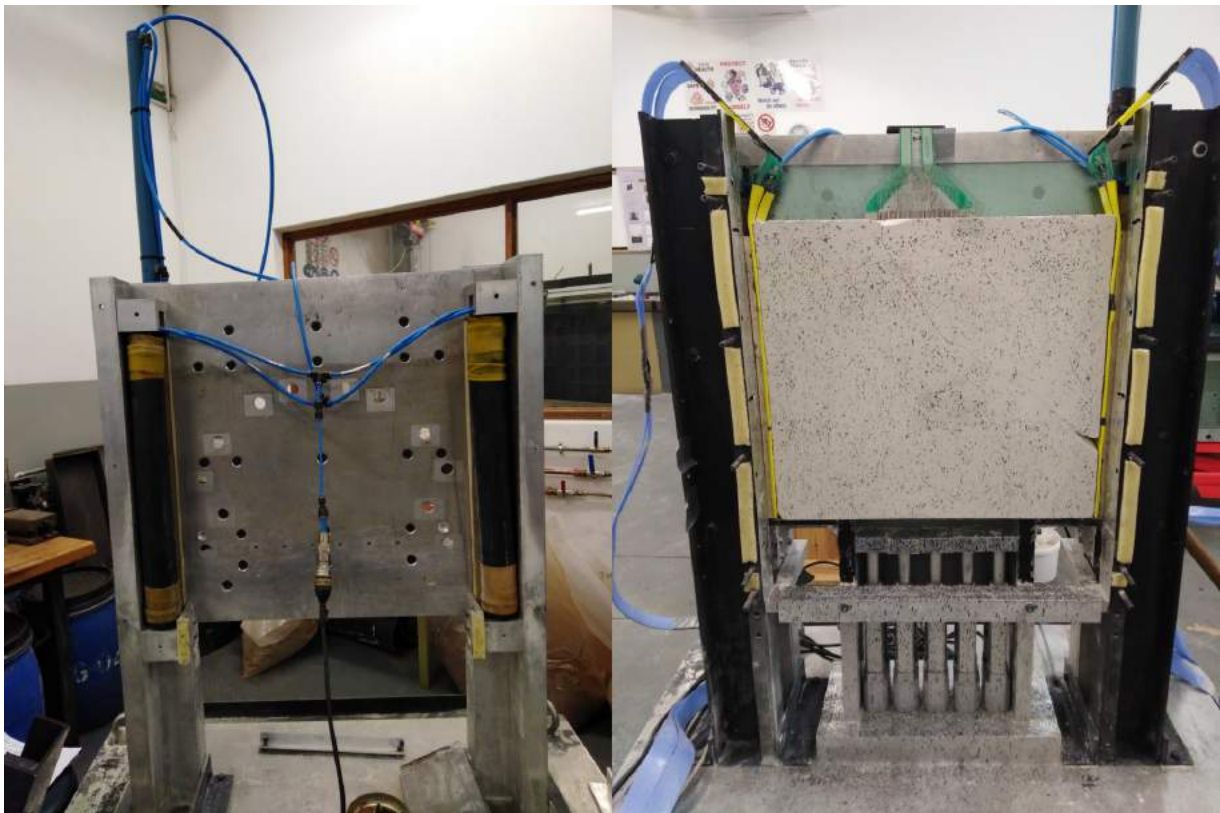


Figure 4.2: Water bladders housed within the test frame (left) and the test frame positioned on the centrifuge swing (right).

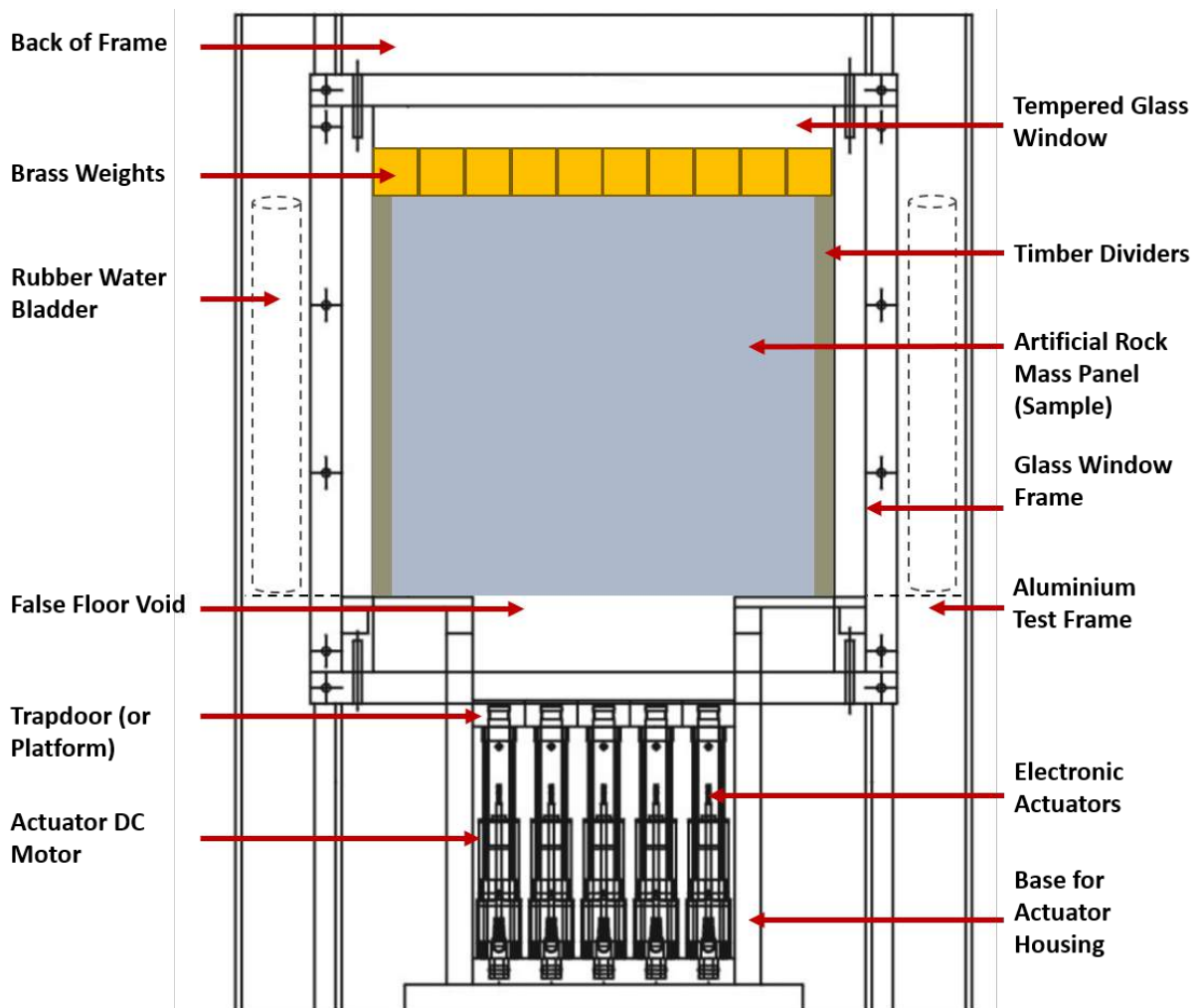


Figure 4.3: Labelled schematic of the test frame used during centrifuge testing.

4.3.1 Test Frame

As labelled in Figure 4.3, the frame incorporated five electric actuators attached to aluminium blocks, referred to as platforms or trapdoors which, supported the sample. The test frame contained two channel sections fastened to a thick aluminium base of about 50 mm. The back-plate of the frame was reinforced with a network of aluminium ribs which helped to torsionally brace the test frame at high accelerations and contributed to overall rigidity. The aluminium ribs are shown in the back of the frame Figure 4.1 (right) and the back-plate of the frame can be seen in Figure 4.2 (left).

The front glass window was attached to the frame using a strong silicon adhesive and consisted of three laminated layers of tempered glass panes. The actuators were seated into a separate base which fitted into the bottom of the frame. The base was not directly bolted to the frame but instead kept in position between the frame's back-plate and the front window.

Another small aluminium plate at the back of this base as well as an aluminium angle section allowed for the actuators be housed and kept in position during the undercutting process of tests (Figure 4.1 - left). The angle section also provided a rest for the window pane thereby reducing the shear stresses on the silicon joints. All aluminium components which made contact with the glass pane were lined with rubber strips to relieve any stress concentrations that could have built up during centrifuge tests and in doing so prevented the glass window from cracking.

Another three glass layers of 10 mm each as well as a 5 mm perspex sheet were positioned between the back-plate of the frame and the sample panel. This ensured that when samples were externally loaded on their top and side faces during centrifuge testing, sample deformation was inhibited in the third dimension. This allowed for near plane strain conditions to be achieved. The dimensioned Auto-CAD drawings of the test frame itself and the actuators can be observed in Appendix B. All components of the frame were made from aluminium and the total payload including all equipment and instrumentation on the frame was approximately 218 kg.

4.3.2 Water Bladders

The horizontal confinement applied to samples was implemented using water pressure in rubber bladders. The relative pressure magnitude was controlled by the use of a static head of water in a stand pipe attached to the bladders. The water pressure was also measured using a pressure transducer which was connected to the system supplying water to the bladders.

During centrifuge test preparation, the water bladders (shown on the left in Figure 4.2) were initially filled to 75 % of their capacity and inserted into the sides of the frame. Two long rectangular timber pieces were used to separate the bladders from the sides of the specimen to provide a medium for uniform pressure distribution of the confinement stress from the bladders to the sample. Figure 4.4 shows the piping and water flow diagram for the experimental test setup in Figure 4.5.

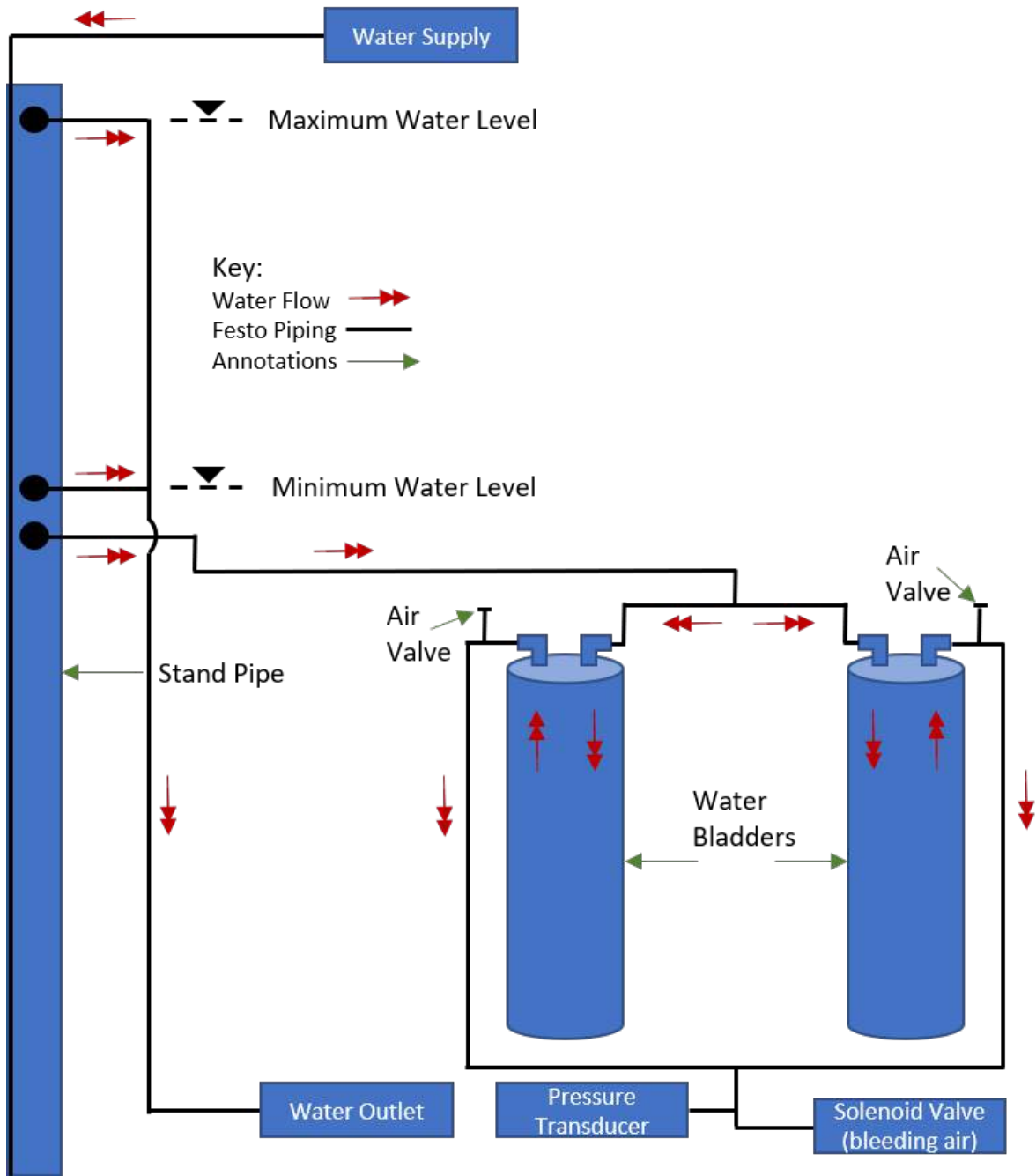


Figure 4.4: The piping and water flow diagram for the test setup.

A constant water flow was supplied with its entry point at the bottom of the 1330 mm tall stand pipe. A minimum or maximum water level, depending on the state of stress required, was used to allow a static water head to be maintained throughout the duration of testing. The water bladders were ‘bled’ for trapped air individually at the air valves. A pressure transducer was attached to the end of the water supply line and was fixed at a constant height at the back of the test frame.

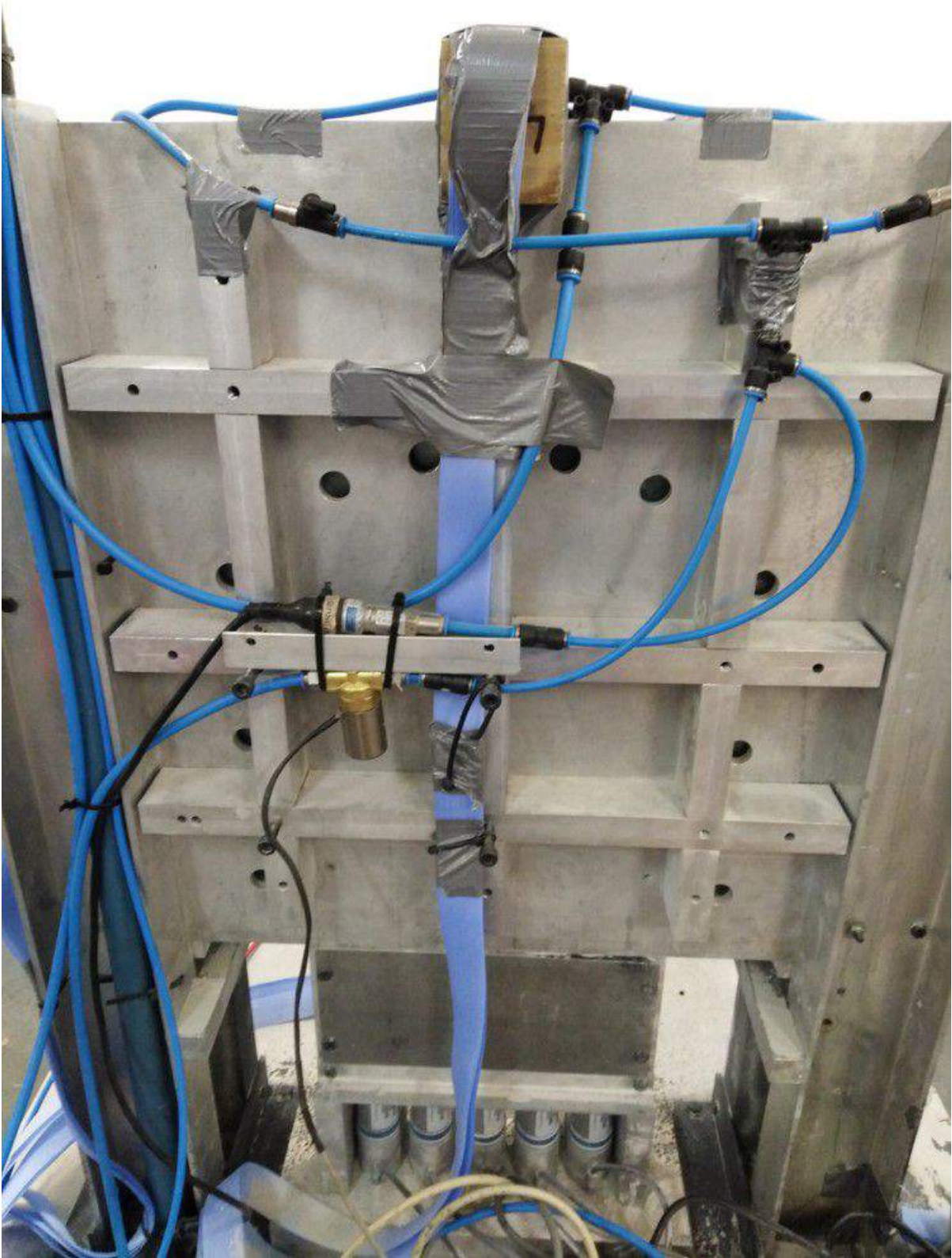


Figure 4.5: Water piping system for supplying a static head to experimental models.

4.3.3 Brass Weights

Vertical overburden pressure was applied to the sample during centrifuge tests using brass weights. The brass weights were manufactured to fit the top exposed surface of the sample as illustrated in Figure 4.3. A photograph of the experimental model after a centrifuge test is given in Figure 4.1 (left) which shows the movement of brass weights once cave propagation has taken place.

It should be noted that in this investigation three types of overburden pressures were used. These are cases of ‘zero’ surcharge (i.e. without the use of brass weights), ‘minimal’ surcharge (i.e. one row of brass weights applied to the top surface of the sample) and ‘maximum’ surcharge (i.e. 2 rows of stacked brass and steel plate weights to apply load to the top surface of the sample). The pressures for the ‘minimal’ and ‘maximum’ surcharge cases are equivalent to 186 kPa and 606 kPa, respectively.

4.3.4 Electric Actuators

Five linear electric actuators were used in this study to perform the undercutting procedure. As previously described, the lowering of actuator heads simulated the undermining of material in a cave mining environment. The undercutting procedure followed in this investigation was adopted from the physical modelling done by Cumming-Potvin (2018). The pattern followed took the form of withdrawing each platform (E to A) from right to left in step-wise manner. This procedure is illustrated in Figure 4.6. It is important to note that after each withdrawal step of the actuator platforms, the total increment of vertical displacement simulating the undercutting procedure was approximately 5 mm (indicated in Figure 4.6).

The Fly-by-Pi controls both the effective power delivered to actuators and the direction of movement. In this investigation a low duty cycle (controlling the power level) was applied to ensure precise control over the displacement. The multiplexer, consisting of a bank of relay switches, of the centrifuge system is used to direct the conditioned power to the appropriate actuator. Thus only one Fly-by-Pi is required for the control of multiple actuators. A compact Python script was programmed to supply the motor driver with a continuous 10 % duty cycle. The Fly-by-Pi controller is managed through a secure shell (SSH) connection over Ethernet.

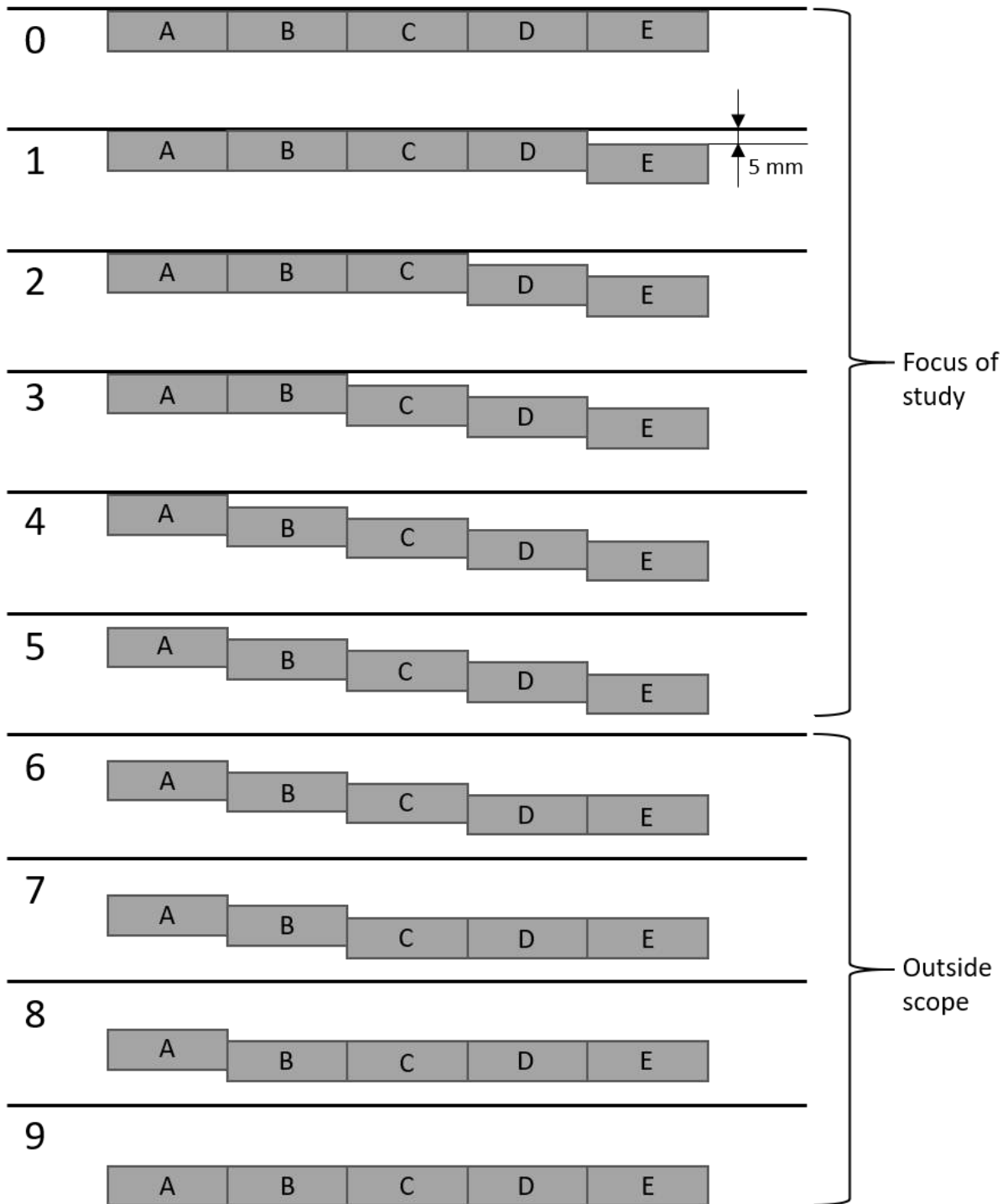


Figure 4.6: The undercutting procedure of material removal.

4.3.5 Data Capturing Instrumentation

The data obtained in this investigation was mainly in the form of visual data through photographs taken at particular time intervals. From the images taken using the combined effort of a Canon DSLR (digital single-lens reflex) camera at a rate of 0.2 Hz (5 second intervals) and a Basler high speed camera at over 100 Hz, events of caving propagation were captured in a progressive and detailed manner.

The Canon DLSR camera was used to capture images for Particle Image Velocimetry (PIV) analysis in this investigation. Videos were also taken to record caving events using the centrifuge webcam for general sample observation during centrifuge tests. The webcam, high speed Basler and Canon DLSR cameras were fixed to an aluminium and steel frame inside the centrifuge swing approximately 700 mm from the front window containing the sample. The cameras were connected using a USB 3.0 high-speed interface to computers in the centrifuge control room from where they were operated.

Potentiometers were used to measure the displacement of the actuator heads (and hence the platforms) during the undercutting process of the cave mining simulation in the centrifuge. Results recorded for typical actuator head displacements during a centrifuge test is observed in Figure 4.7 where the pattern exhibited in Figure 4.6 is repeated until the actuator heads have been withdrawn almost completely. It is worth noting that the focal interval of study lies within the first 5 steps of the centrifuge test (shown in Figure 4.6) only makes up short period indicated by the approximated dotted lines of Figure 4.7. A DigiDAQ data acquisition system was used to log the displacements of the actuators and water pressure, via the pressure transducer, throughout the tests.

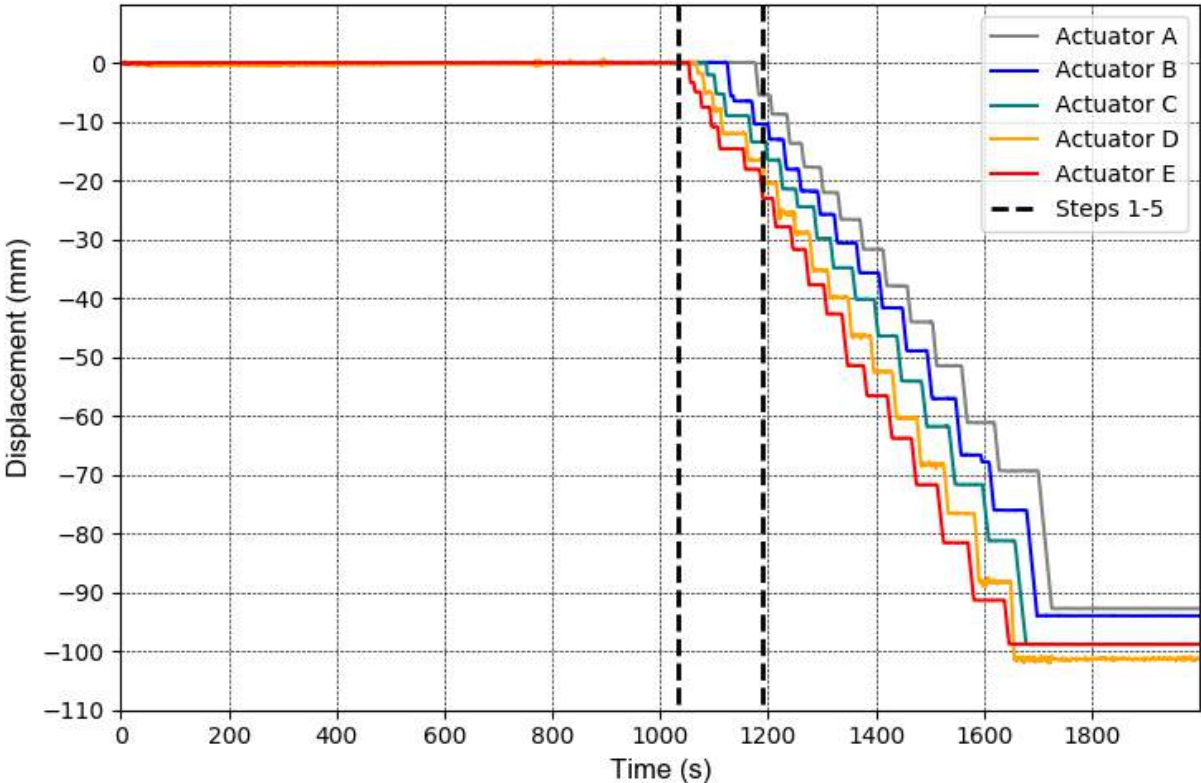


Figure 4.7: Actuator head displacements during a typical centrifuge test.

4.4 Centrifuge Test Procedure

The following procedure was implemented when conducting centrifuge testing:

With the exception of the first centrifuge test where the sample was only confined by sand, water filled bladders were placed into the side pockets of the frame between the channel sections followed by the standpipe tied to the frame. A panel that had undergone the mixing, casting and curing procedure outlined in Section 3.3 was abraded to the correct tolerance in order to eliminate any lack of fit. The panel was then carefully placed in the frame where the actuator heads were positioned below the sample. The back of the sample was pushed up against the three laminated glass panes and a perspex pane on the outermost side of the panel.

The actuator heads (platforms) were carefully extended to their maximum limit using a 24 V power supply to ensure that the panel rested on all the platforms. Once the panel had been centred over the five actuator platforms (leaving equal spaces on the sides of the panel) timber sections were positioned on the sides of the sample to allow for an equal distribution of pressure to be applied to the sample from the water bladders or sand. The panel was marked with black spray paint to give it definition or texture in the photos captured for PIV analysis.

The frame window was bolted on with care to avoid the sample cracking due to local stress concentrations. Brass weights were added to the top surface of the sample (as required). The centrifuge model was positioned on the centrifuge swing. The centrifuge lights were switched on, actuators connected, cameras configured and the data acquisition systems (DigiDAQ) calibrated. The water bladders were ‘bled’ to purge the system of any air. The model was examined to ensure that all pipes, cables and components were securely fastened and tied down. Data acquisition commenced once the model was accelerated to 80 g.

Image capturing using the DSLR Canon Camera and high-speed Basler camera was started before the actuators were withdrawn from right to left, adhering to the pattern shown in Figure 4.6 to initiate wave propagation. This was continued until all the actuators were fully withdrawn. Data acquisition was stopped and saved and the water supply was switched off before the model was decelerated to 1 g. The centrifuge chamber doors were opened and all instrumentation and equipment was disconnected and cleaned. After the centrifuge model was removed from the swing and parts of the test frame were dismantled, the model was then inspected for fragmentation.

4.5 Experimental Models

Four cave mining simulations were conducted in the geotechnical centrifuge under different stress conditions. In this section, the experimental models are presented, with theoretical calculations made with regard to their vertical and horizontal stress state.

4.5.1 Centrifuge Model 1

The first test consisted of a sample that was given insignificant horizontal confinement using a fine sand compacted into the sides of the frame contained within a plastic sleeve. The top surface of the model was left unloaded in this test. Figure 4.8 shows the schematic for the first centrifuge test and the theoretical vertical and horizontal stresses that are exerted on the model at 80 g. It can be noted that the coefficient of lateral earth pressure (i.e. the ratio of horizontal to vertical stress) is maintained at 0.50 throughout the depth of the sample model. The horizontal and vertical stresses at the bottom of the sample were calculated at 156.6 kPa and 488.0 kPa, respectively. When calculating the horizontal stresses exerted by the sand on the sample in this centrifuge test, the angle of internal friction and cohesion intercept of the sand were assumed to be 30° and 0 kPa, respectively. The unit weight (γ) was calculated as 13.65 kN/m^3 from the volume and mass of the sand that was inserted. Using the well-known expression of calculating the coefficient of earth pressure at rest from Jaky (1944), an horizontal in-situ pressure of 2.935 kPa was calculated at the bottom of the sample at 1 g with an active earth pressure of 0.50 using Equation 4.5. The first centrifuge test was deemed to represent cave mining at a shallow underground level where low horizontal stresses and minimal overburden stresses are present.

$$K_0 = 1 - \sin \phi \quad (4.5)$$

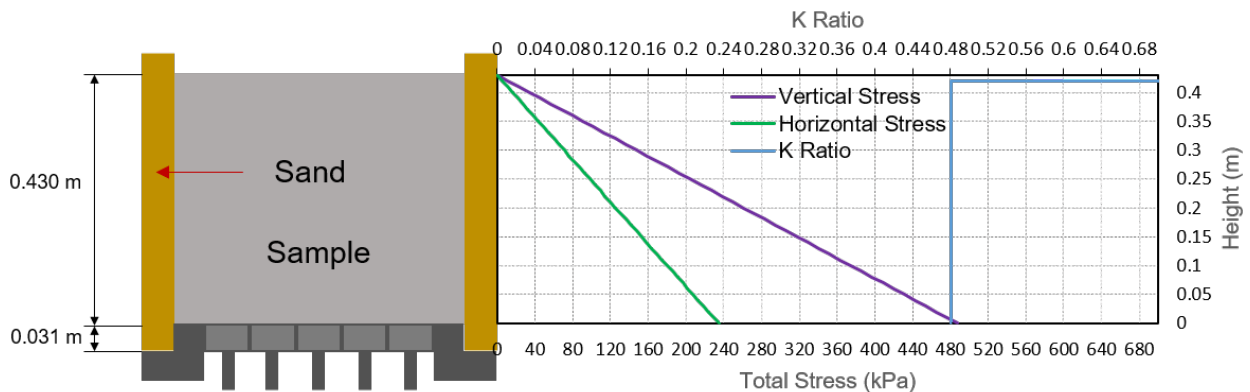


Figure 4.8: Distribution of stresses and K ratio of the sample in centrifuge test 1 at 80 g.

4.5.2 Centrifuge Model 2

The second centrifuge test consisted of a sample that was given relatively minimal confining pressure exerted by water-filled rubber bladders. Once again no overburden stress was applied to the top surface of the model. Figure 4.9 shows the test schematic and the stress distributions of the sample with depth at 80 g. The height of the water column above the top surface of the sample was recorded at 154 mm and this is termed the ‘minimum water level’ in this dissertation. The water was maintained at this level throughout the duration of the centrifuge test as mentioned previously. At 80 g, the horizontal and vertical stresses at the bottom of the sample were calculated as 458.3 kPa and 488.0 kPa, respectively.

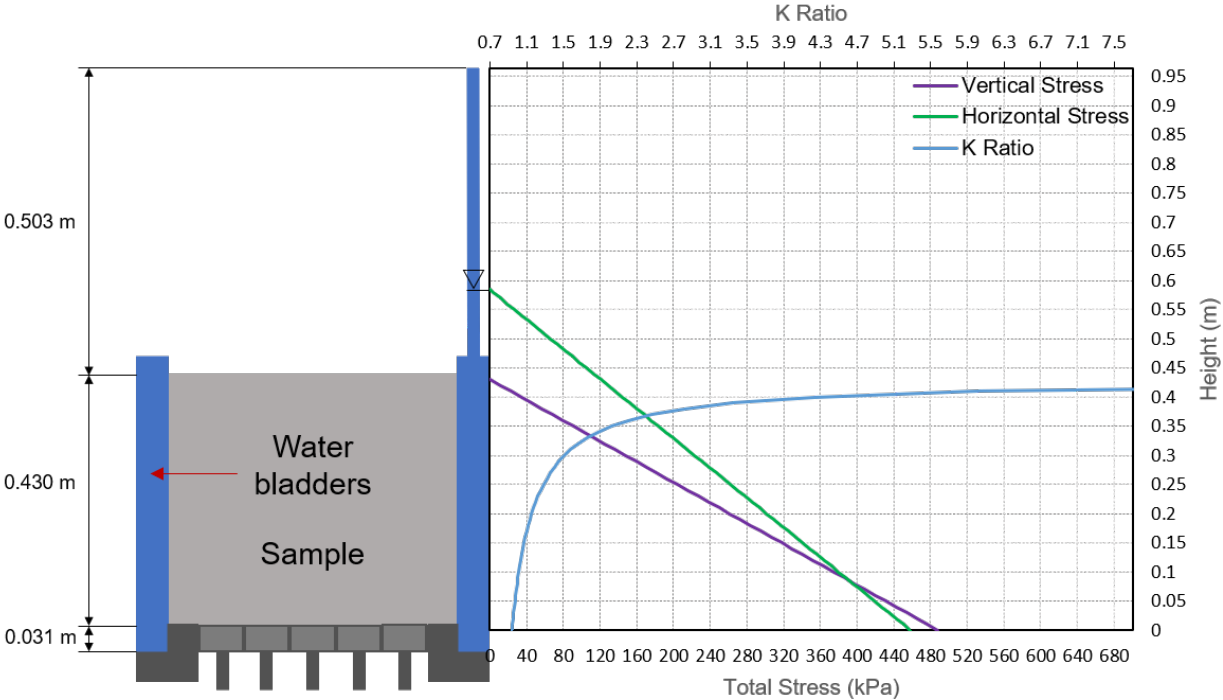


Figure 4.9: Distribution of stress state and K ratio in sample of centrifuge test 2 at 80 g.

From Centrifuge Test 1 it is observed that the horizontal to vertical stress ratio is constant throughout the sample depth. This is significant since the K ratio should be kept constant in each test thereby enabling a comparison in terms the stress-states to be drawn between the experimental models. From Figure 4.9 it can be noted that the K ratio seems to be extremely variable towards the top third of the sample (i.e. between values 1.401 and 11.34) and in the bottom two thirds of the sample the K ratio is relatively constant as it only varies between 0.939 to 1.401. This variation in K in the top third of the sample can be regarded as negligible since the bottom part of the sample will primarily be the area of focus for undermining from where cave mining propagation is expected to grow. Furthermore, at approximately a third of the sample height from the base of the frame, it should be noted that the centrifuge model stress coincides with the prototype stress,

leaving the stress to be underestimated above this point and progressively over-estimated below this point. Centrifuge test 2 was aimed at representing conditions where cave mining could occur where there are large horizontal stresses but in areas that are not deep underground.

4.5.3 Centrifuge Model 3

Centrifuge test 3 was similar to the previous test as the minimum water level was used to confine the sample; however, one row of brass weights was placed on the top surface which yielded a minimal surcharge of 186 kPa (at 80 g). The mass of the brass blocks was 5.10 kg in total and the blocks were spread evenly over the top of the sample to maintain uniform vertical loading on the sample. The weights were arranged in a fashion similar to what is conveyed in Figure 4.10. Thus they were fitted tightly against each other leaving no gaps in the shortest dimension of the frame and covered the entire area of the top section of the sample. Besides providing vertical surcharge, another reason for the utilising brass weights was to maintain the constant K ratio throughout the sample's depth as observed in the stress distribution alongside the schematic. Including the weights, which had a height of 27 mm, allowed for the intercepts of the total vertical and horizontal stress to coincide, which ensured that the K ratio is constant from the minimum water level to the bottom of the sample as if the vertical stress started from the above the sample height. This is indicated by the dotted purple line termed 'Apparent Vertical Stress'. The third centrifuge test was aimed to portray cave mines that are moderately deep underground, subject to both substantial horizontal and vertical stresses.

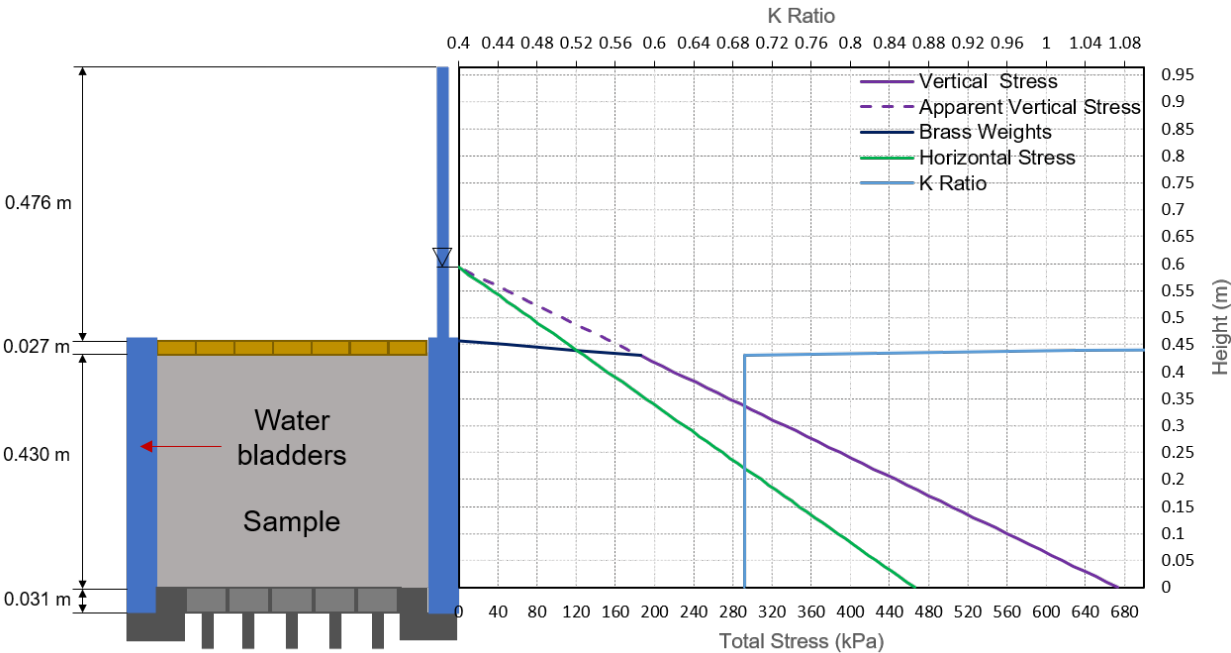


Figure 4.10: Distribution of stress state and K ratio in sample of centrifuge test 3 at 80 g.

4.5.4 Centrifuge Model 4

Finally, centrifuge test 4 was conducted with the maximum surcharge of 16.5 kg (exerting 606 kPa on top of the sample at 80 g) and the largest horizontal confining pressure with a static head at the ‘maximum water level’ of 534 mm above the top surface of the sample. The fourth centrifuge test can be considered an extension to test 3 since the magnitudes of the horizontal confinement and vertical overburden loads were increased in equal proportions, such that the K ratio was maintained at 0.69 for centrifuge tests 3 and 4.

The test schematic and theoretical stress distributions for the final test are shown in Figure 4.11. From the figure, it is easily observed that by increasing the brass weights and maintaining a higher column of water in the stand-pipe, larger stress conditions can be exerted on the sample. What is interesting to note is that stresses of 756.5 kPa and 1094 kPa for the respective horizontal and vertical total stresses, recorded at the bottom of the sample, surpass the UCS of the artificial rock material. Due to the lower values in total stresses of centrifuge test 3, which are 465.7 kPa and 673.4 kPa for horizontal and vertical stresses, respectively, the results (and failure mechanisms) are expected to contrast significantly. Centrifuge test 4 was aimed at simulating the cave mining process at a deep underground level.

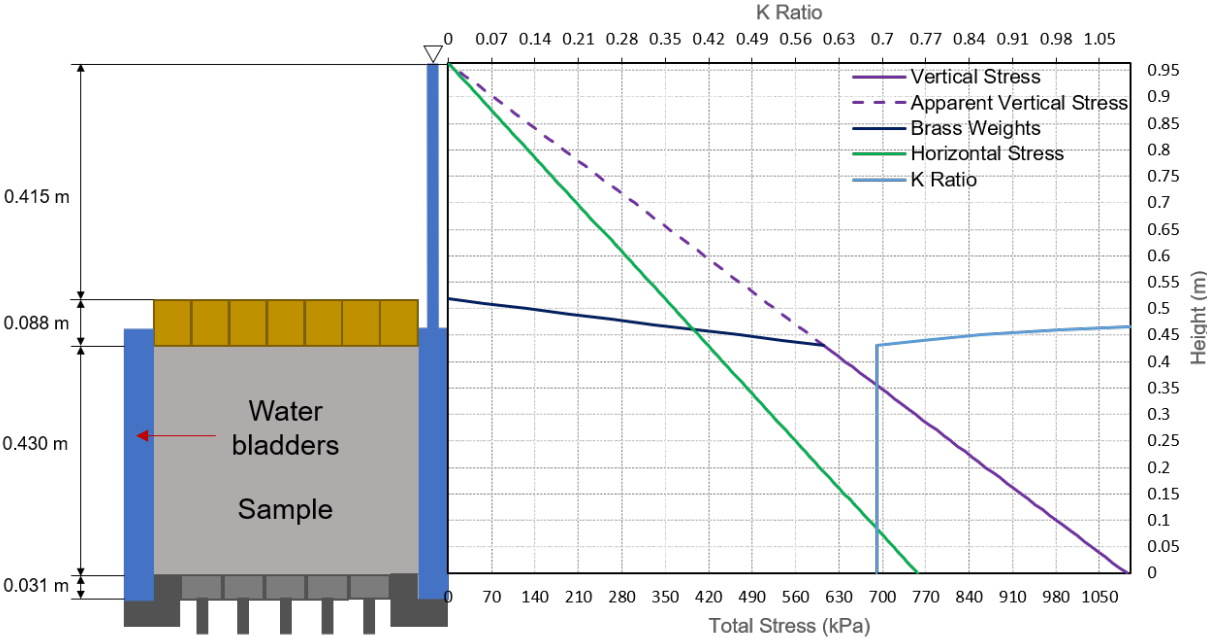


Figure 4.11: Distribution of stress state and K ratio in sample of centrifuge test 4 at 80 g.

4.6 Centrifuge Model Summary

This section summarises the experimental models presented in the chapter which comprises the physical modelling methodology of the investigation. Table 4.3 gives a summary of the models in terms of theoretical values for horizontal, vertical stresses and in-situ stress ratios at extreme and significant positions within the model. Included in Table 4.3, are the assumed values from the centrifuge experiments conducted by Cumming-Potvin (2018). Stress values are given in kPa and K values are ratios of the horizontal to vertical stress at a particular depth.

Table 4.3: Summary of horizontal, vertical stresses and K ratios for centrifuge models

| Parameter | Position | Model 1 | Model 2 | Model 3 | Model 4 | Cumming-Potvin (2018) |
|--------------------|------------|---------|---------|---------|---------|-----------------------|
| σ_{htop} | Top | 0 | 120.86 | 128.26 | 419.08 | 324.44 |
| $\sigma_{hbottom}$ | Bottom | 234.78 | 458.32 | 465.72 | 756.55 | 658.63 |
| $\sigma_{h1/3}$ | 1/3 Height | 158.34 | 348.45 | 355.85 | 646.68 | 546.68 |
| σ_{vtop} | Top | 0 | 0 | 185.46 | 606.00 | 112.00 |
| $\sigma_{vbottom}$ | Bottom | 487.98 | 487.98 | 673.44 | 1093.98 | 628.44 |
| $\sigma_{v1/3}$ | 1/3 Height | 329.10 | 329.10 | 514.56 | 935.10 | 455.43 |
| K_{bottom} | Bottom | 0.50 | 0.94 | 0.69 | 0.69 | 1.05 |
| $K_{1/3}$ | 1/3 Height | 0.50 | 1.06 | 0.69 | 0.69 | 1.20 |

From Table 4.3, the distinction to make between the models of the current study and those of Cumming-Potvin (2018) is that the models of this study allow for a constant in-situ stress ratio (K) to be achieved (with the exception of model 2 having slight variation) and so can be compared to each other. Since the tests of Cumming-Potvin (2018) assumed to have used the same initial theoretical stress-states in all tests, it would be difficult to compare this test with those of the current study. However, if a comparison was to be made in terms of K ratios, model 2 would be best candidate, and in so doing, the caving events observed in Cumming-Potvin (2018), could be regarded as an extreme case (where high K ratios are present) with reference to the models of the current study.

5 Experimental Results and Discussion

Experimental results are presented by image analysis covering cave geometry and strain contour mapping. The results are then interpreted in the latter part of the chapter which aims to quantify which visually observed cracks were the effects of strains mapped within the model through Particle Image Velocimetry and adopting the Critical Extensional Strain model by Stacey (1981).

5.1 Data Capturing Procedure

The findings of the centrifuge cave progression tests are presented via two techniques in this chapter which consist of qualitative and quantitative analyses of image results. A combination of the techniques is performed by superposition of measured strain contours (quantitative results) on the processed images of the experimental models (qualitative results). The aim of performing this exercise was to attempt to identify which cracks were generated in qualitative images by the measured magnitude of strain given by strain surface plots from PIV analysis. Since strain is a tensor quantity, its orientation can be used to identify whether the strain is compressive or tensile which ideally is used to quantify the mechanism of caving failure.

5.1.1 Qualitative Image Analysis

From the physical modelling performed in this investigation, images captured by the DSLR camera positioned inside the centrifuge swing were used to identify the cave back progression. This section describes the process followed in analysing images. The captured images from the tests of this investigation were analysed using the Canny-Edge Detection method (Canny, 1986) in order to accurately determine cracks which outlined cave back geometry in terms of cave height, cavity width as well as caved area, caved perimeter and hydraulic radius (defined as the geometric ratio of caved area to caved perimeter). The reason for identifying cracks using a program-based approach seems logical in limiting errors when carrying out manual tasks with regard to calculating the cave geometry from images thereby allowing resolution of one pixel. In brevity, the Canny-Edge Detection algorithm consists of a Gaussian function which smooths the image and calculates the image gradient magnitude and direction to apply noise reduction. The calculation of non-maximum suppression from the image gradient direction is done to obtain the unilateral edge response. Lastly, a double threshold is applied and edge tracking by hysteresis is implemented to detect and connect edges of the image (Biswas and Sil, 2012). The procedure of identifying cracks and discontinuities for image data using the ‘OpenCV’ (Open-source Computer Vision) Python programming module is outlined below:

- The image is loaded by using the ‘`imread()`’ (image-read) function which stores pixel data to an array.
- The image is resized for the purposes of viewing it on-screen.
- The image is converted to grayscale and histograms are calculated to quantify its distribution of intensities.
- Utilising the ‘`equalizeHist()`’ function within Python’s ‘OpenCV’ module, the image’s contrast can be brought to the same intensity thereby normalising the brightness (and improving gamma-correction) which resulted in higher-contrast images.
- Images were slightly blurred using a Gaussian filter at an appropriate constant setting.
- The image is parsed through a user-defined Canny-Edge Detection function where the median of the single channel pixel intensities is computed and used as a basis for detection-intensity.
- The resulting image is a binary-image containing all edges in high-contrast which allows for cracks to be clearly identified. An example of this is shown in Figure 5.2 in the next section.
- Cracks were then coloured to help visual-identification of discontinuities on images.

5.1.2 Quantitative Image Analysis

Images that were used in conducting the PIV analysis were initially corrected for over-exposure through the procedure outlined in Section 5.1.1. Subsequently, images were corrected for lens distortion using the open-source GIMP software (GNU Image Manipulation Program). When conducting the PIV analysis, a subset size of 50 pixels was chosen without control points. The analysis mode ‘Leap Frog’ was adopted with appropriate levels of seed correlation coefficient tolerance and minimum correlation coefficient tolerance which allowed the program to run successfully. When removing wild displacement vectors in the analysis, the manual method was seen to provide more realistic output data than applying automatic filtering via a specified tolerance through the GeoPIV-RG program (refer to Stanier et al., 2016).

Subsequent to plotting the displacements using GeoPIV-RG’s built-in functions, it was decided that advantage was taken through the software to calculate and export minor principal strains directly. The x and y coordinates of the subsets used in the analyses were exported and matched up with the minor principal strain data. Using a dedicated function in the Python programming module ‘Matplotlib’, an implementation of the

Delaunay triangulation algorithm allowed the minor principal strain data to be plotted through interpolated data points. The strain contours/surfaces produced were then used to identify regions where strains exceeded the critical extensional strain for the material, which in turn, allowed for the determination of expected cracking.

5.2 Image Analysis Results

The results are presented for all centrifuge tests in the form of flow diagrams which show the progression of caving events in selected images. The images that were selected for presenting these results are specifically similar through all the centrifuge tests in that they were images which were taken straight after the moment of actuator withdrawal. Images presented in this section are aimed at creating an overview, capturing the caving progression. These images correspond to steps 0 to 5 of actuator withdrawal of Figure 4.6.

It was observed in some cases that fractures were present in experimental models prior to reaching an acceleration of 80 g. These fractures were either due to loading of samples in the centrifuge test frame or due to centrifuge loadings sustained by the model during swing-up. These ‘pre-existing fractures’ influenced cave mining propagation; however, the distinction in caving progression of one experimental test under different confinement conditions to another could still easily be made. Pre-existing fractures were regarded analogous to rock-faults which are applicable in mines prior to cave propagation. Thus, the experiments were not compromised by these discontinuities caused by pre-existing fractures.

In the upcoming sections, the approach used can be described as follows: grayscale images are presented first, which correspond to the images whose intensities have been normalised. The steps of cave mining propagation can clearly be articulated in these high-contrasted images. The binary images obtained from using the Canny-Edge-Detection Method outlined previously are presented next, highlighting all pre-existing fractures (in cyan) and fractures caused by caving progression (in red). Lastly, surface plots are presented in a similar manner to the qualitative results.

Surface plots of tensile strain within the model for each test are shown (for steps 0 to 5) with a single colour-bar indicating the degree of minor principal strain (ε_3). It should be noted that the colour-bar reaches a minimum negative (tensile) value of -0.014 % strain which indicates the critical extensional strain for the artificial rock material. Values equal to and less than this limit are indicated in red. This allows easy identification of the zones of the material that have exceeded the specified tensile strain criterion. This can be shown in the example of Figure 5.3.

5.2.1 Cave Progression Test 1

The sample panel used in cave progression test 1 had one pre-existing fracture across the panel from the top right corner to two thirds the height of the panel on the left-hand side. The caving progression can be observed in the series of grayscale images of Figure 5.1. It can be shown that caving progression was initiated in step 2, only after the second actuator platform had been withdrawn. In step 3, cave progression expanded significantly which quickly connected to pre-existing fractures forming irregular cave-backs when reached.

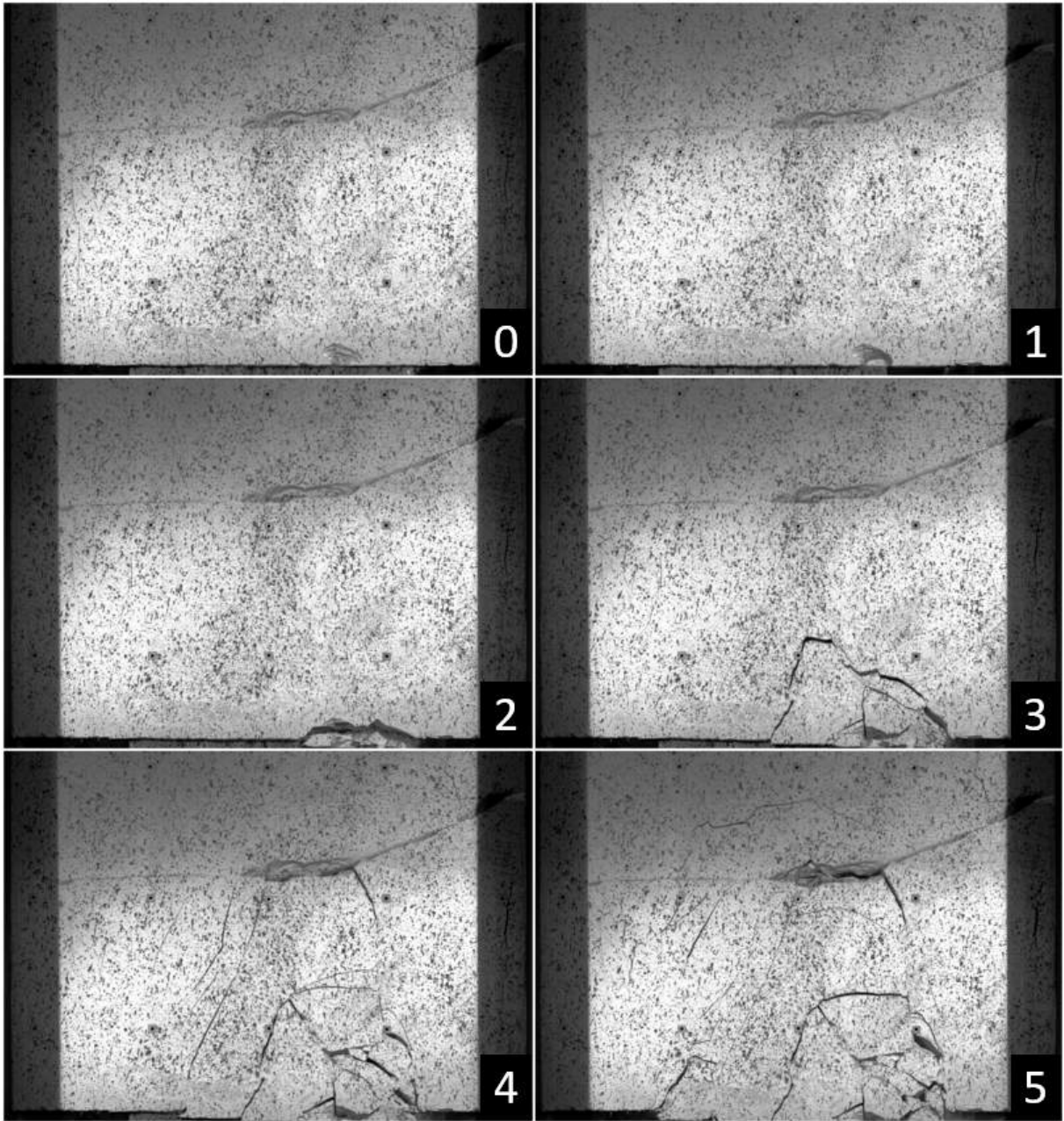


Figure 5.1: Overview of cave progression test 1 over steps 0–5 (zero confinement).

It is important to note that the caves formed in the same manner as described by Cumming-Potvin (2018), in that there were a series of successive fractures forming above

one another — especially in steps subsequent to step 5. The fractures within steps 0–5 were not exactly parallel to each other but seemed to form successively after each other. It is possible and likely that the pre-existing fractures hindered the formation of parallel successive fractures. The fracturing; however, became more parallel to each other in step 5 when the caving progression reached the top of the sample causing a ‘chimney’ to form where the fracturing ruptured the top surface of the sample. Figure 5.2 displays binary-image versions of the cave progression test photographs which enables the cracks to be highlighted to illustrate the development of crack propagation and determine at what point it is linked to pre-existing fractures during the cave mining simulation.

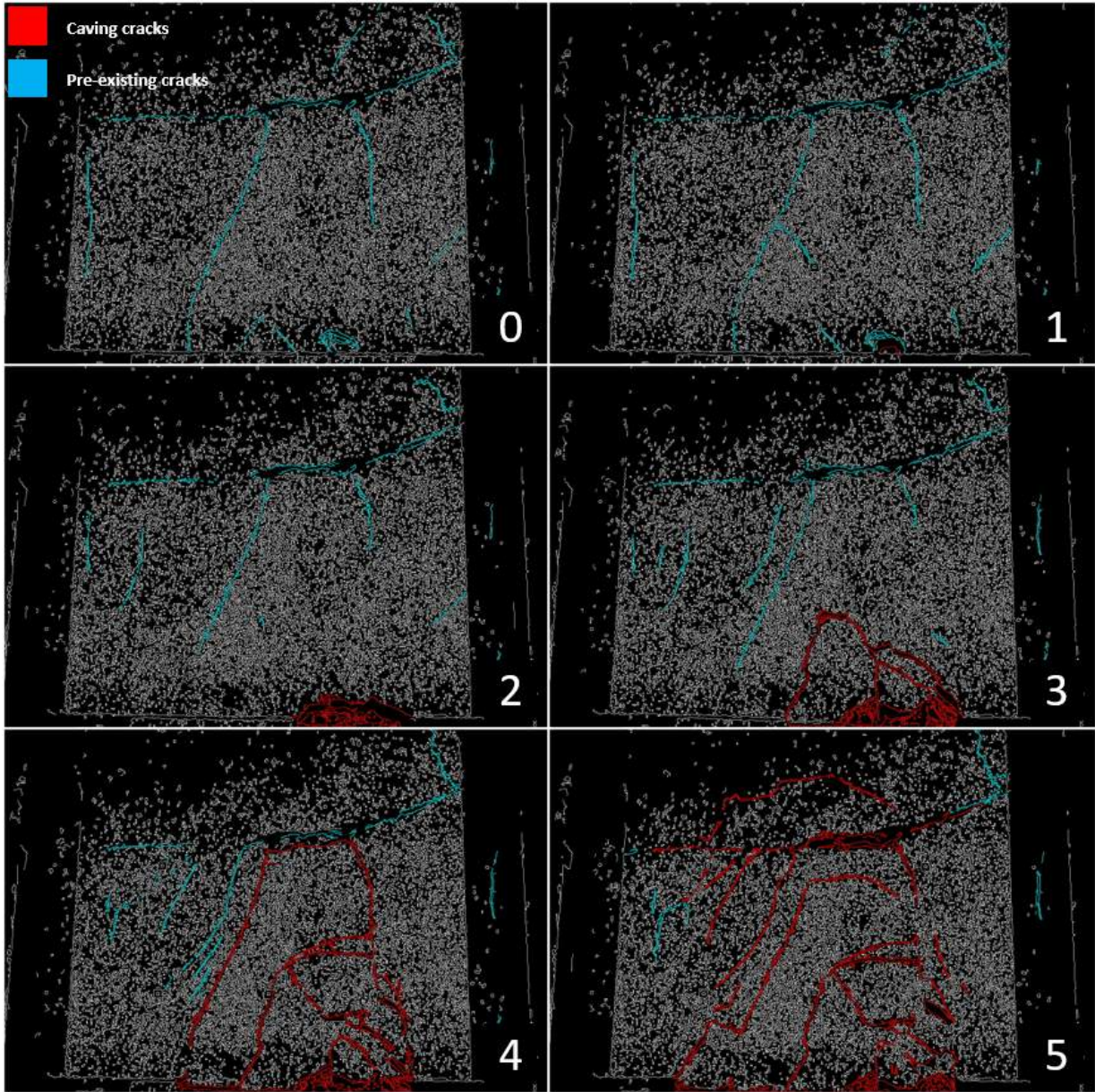


Figure 5.2: Binary Image of cave progression test 1 highlighting cracks over steps 0–5.

Revisiting step 0, more pre-existing fractures seem to exist than noticeably visible in the grayscale images. It should be noted that the cyan lines are present at stages where

cracks are ‘open’ and easily observed in the binary images. There might be cases where there are pre-existing fractures un-highlighted since the cracks have ‘closed’ and were not easily observed. An example of this is seen from step 1 to 2, where the pre-existing cracks reaching the bottom of the sample in step 1, ‘close’ in step 2. When a significant cave back forms in step 3, it connects to the pre-existing fractures in step 4 which explains the irregular shape of the cave geometry. Less obvious fractures higher up the sample in step 5 are easily identified in the binary images as opposed to the the grayscale images. Also, in step 5, fractures seem to be more parallel to each other which was not easily observed in the case of grayscale images. Surface plots of the steps in Figure 5.3 show the distribution of minor principal strains within the model which allow a visual comparison to be identified against the material’s critical extensional strain.

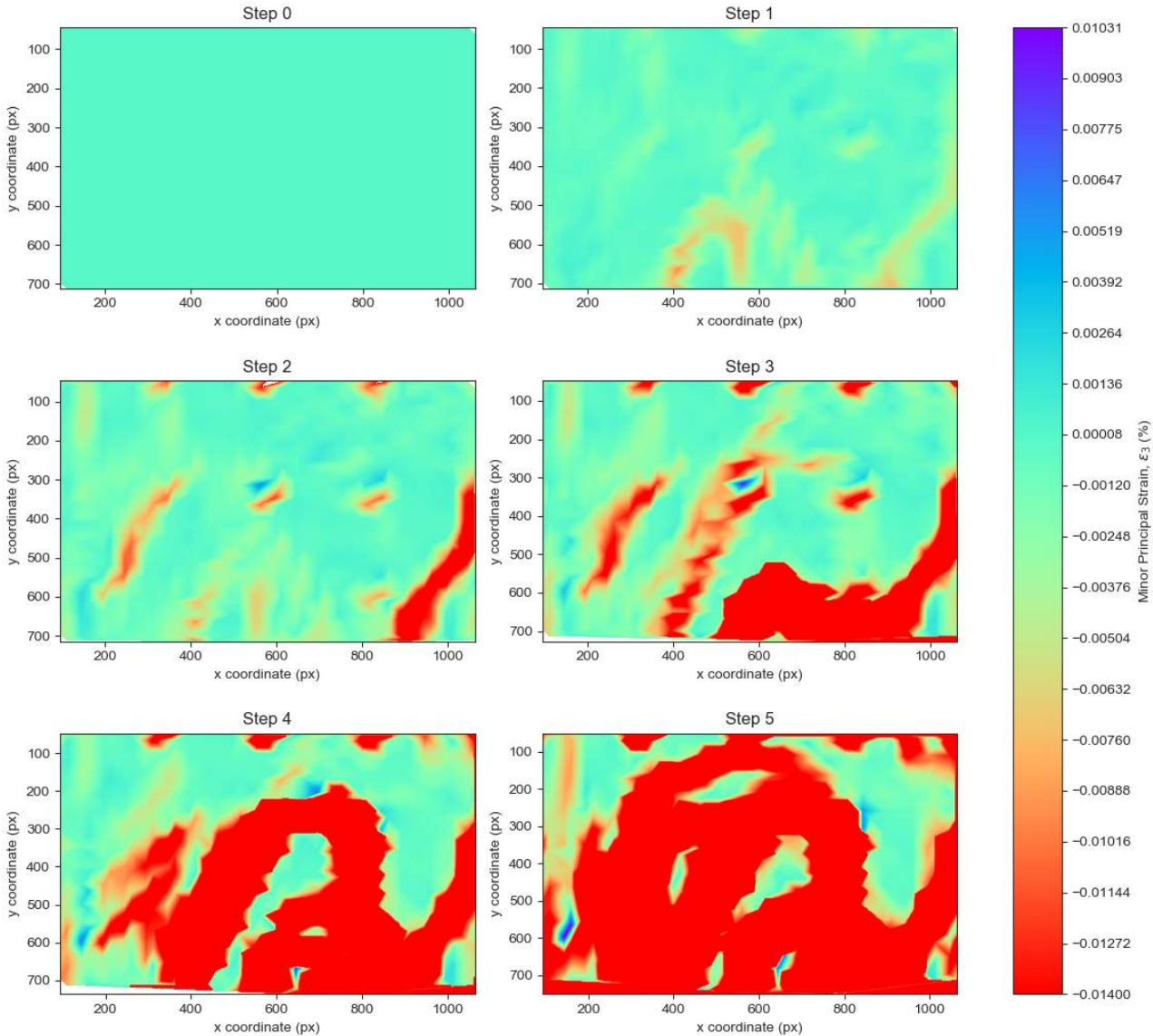


Figure 5.3: Minor principal strain surface plots during cave mining propagation over steps 0–5.

From step 0 and 1 of Figure 5.3, strains in the model did not exceed the critical extensional strain; however, some strains reaching a minimum of -0.010 % did occur in regions that

were in close proximity to pre-existing fractures. In step 2, where cave initiation occurred, strains that exceeded the critical value were observed along the right side of the model from where the trapdoors were lowered and spread in a left direction in step 3. As expected, step 4 and 5 show the regions of strain that have exceeded the critical value around the cave where crack propagation reached the pre-existing fractures. It is observed in step 5, that critical values were reached at the top of the model, above the cave back.

5.2.2 Cave Progression Test 2

Caving progression test 2 can be observed in Figure 5.4, where the pre-existing fractures can be identified using the binary images provided in Figure 5.5.

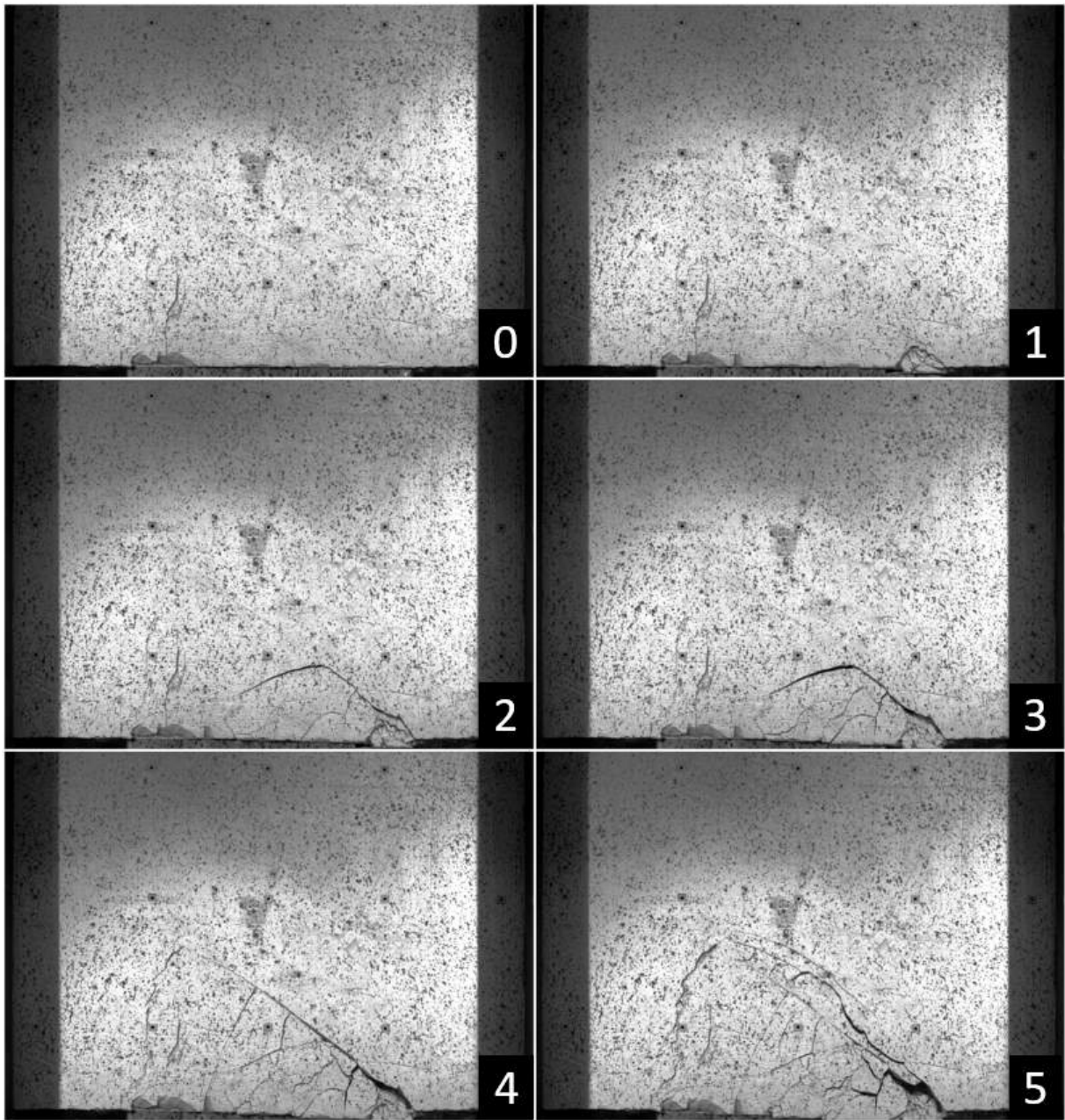


Figure 5.4: Overview of cave progression test 2 over steps 0–5 (minimum confinement).

The sample panel of test 2 had only small pre-existing fractures in the lower bottom and mid-sample regions, indicated in steps 0 and 1 of Figure 5.5. Cave progression commenced immediately with a shallow profile cave forming upon the withdrawal of the first actuator. Due to the horizontal confining pressure applicable to test 2, cave propagation continued to widen at a shallow cave back height. In step 4, the cave back reached the pre-existing fractures and formed a cave of the width of the 5 actuators.

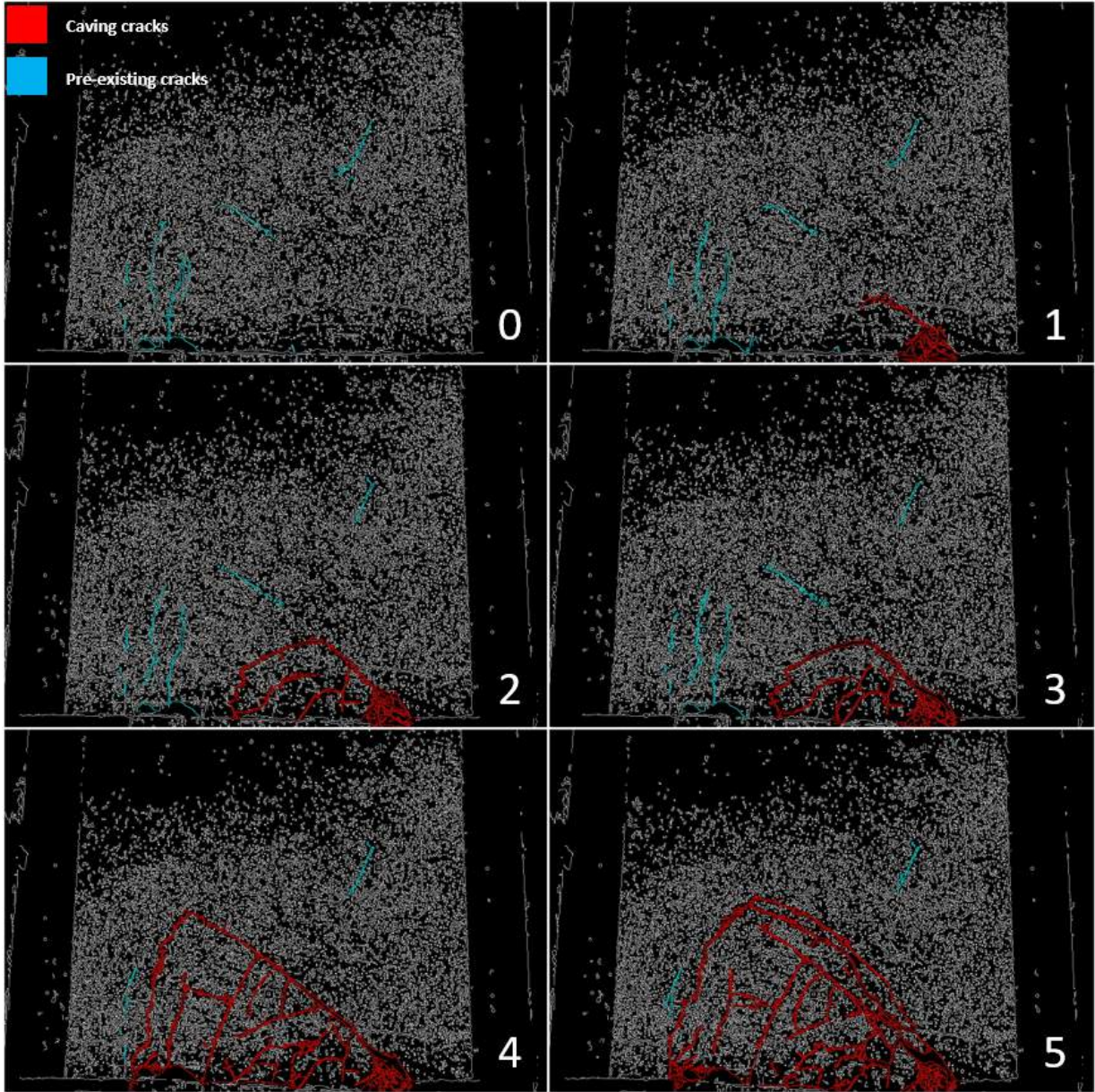


Figure 5.5: Binary Image of cave progression test 2 highlighting cracks over steps 0–5.

It should be noted that during the advancement of the shallow cave back in the second test, the caved material took the form of small, blocky pieces which correlates with what is described by the Duplancic model. Focusing the attention on steps 4 to 5, one can carefully discern that a jump occurred in the fracturing of the cave back, where in step 4 it took the form of a near-straight line and subsequently was succeeded by a parallel fracture

only a few millimetres above it, causing the straight cave back to become more rounded. With regard to the surface plot of tensile strain, it was clearly observed that critical strain values were exceeded in locations where cracks had formed as caving progressed. Zones of red minor principal strains compared well with the location and shape taken on by the cave back even throughout steps 4 and 5. Thus, the cracks of Figure 5.5 correlate well with the magnitude and position of tensile strains in Figure 5.6.

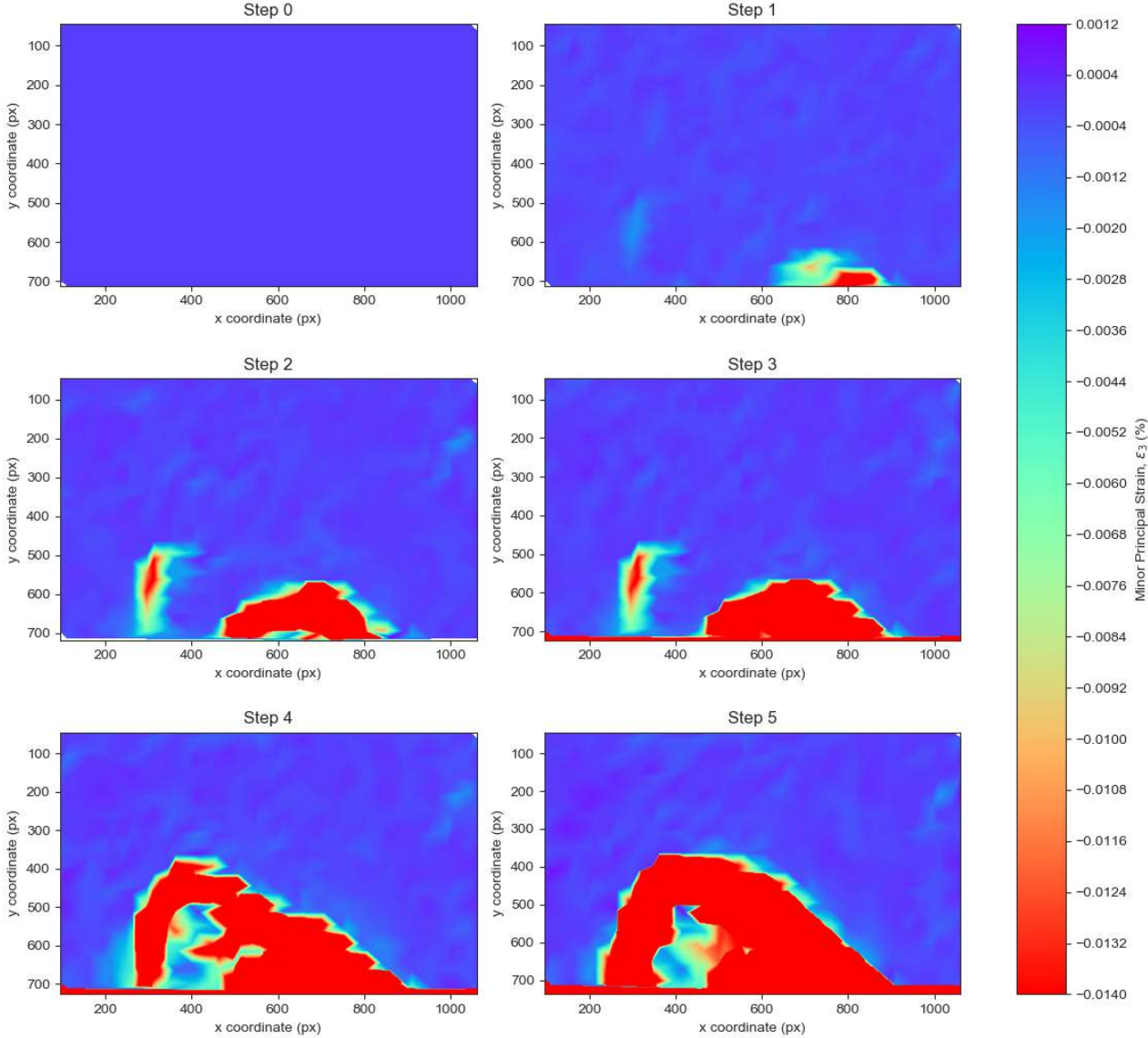


Figure 5.6: Minor principal strain surface plots during cave mining propagation over steps 0–5.

As for the strain distributions themselves, steps 2 and 3 of the model showed pre-existing fractures were clearly detected as critical due to red strains on the left of the cave back. Test 2 notably demonstrated that the material surrounding the cave back of tension was in a state of compression due to the preconditioned horizontal stresses within the model. Although critical extensional strain values were surpassed and a dome-shaped cave back had gradually formed, the state of the surrounding arched material in compression caused the cave to stall.

5.2.3 Cave Progression Test 3

Caving progression test 3 involved a model that was subject to minimal horizontal confinement and overburden. Figure 5.7 displays the overview of caving progression in grayscale, whilst the pre-existing fractures can be identified using the binary images shown in Figure 5.8.

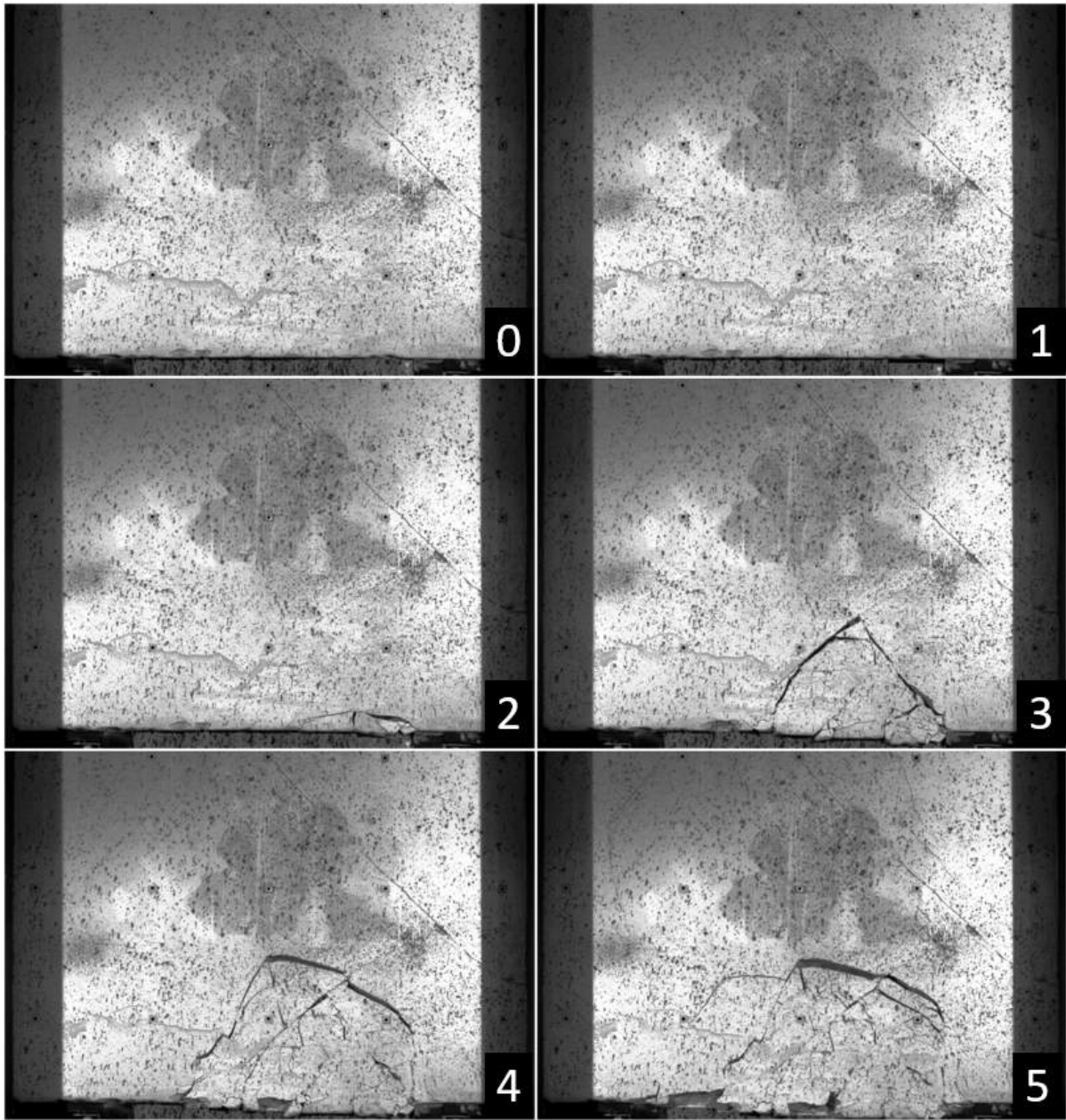


Figure 5.7: Overview of cave progression test 3 over steps 0–5 (minimum confinement and overburden).

The sample panel of test 3 contained one definite pre-existing fracture located diagonally across the top right corner of the panel and one speculated fracture across the middle of the panel (possibly connected to the definite pre-existing fracture) which might have formed during swing-up. Caving progression only commenced in step 2 with a shallow

cave back profile and rapidly advanced into a steep round, triangular shaped cave back. Successive parallel fracturing occurred from step 3 to step 4 where the width of the cave widened by one actuator head. The height of the cave at this point only grew slightly; however, when step 5 was reached the cave back flattened off and a transition zone was created allowing the cave to propagate to the top of the specimen (i.e. resulting in the formation of a ‘chimney’). The transition zone can be identified by the green lines in step 5 of Figure 5.8.

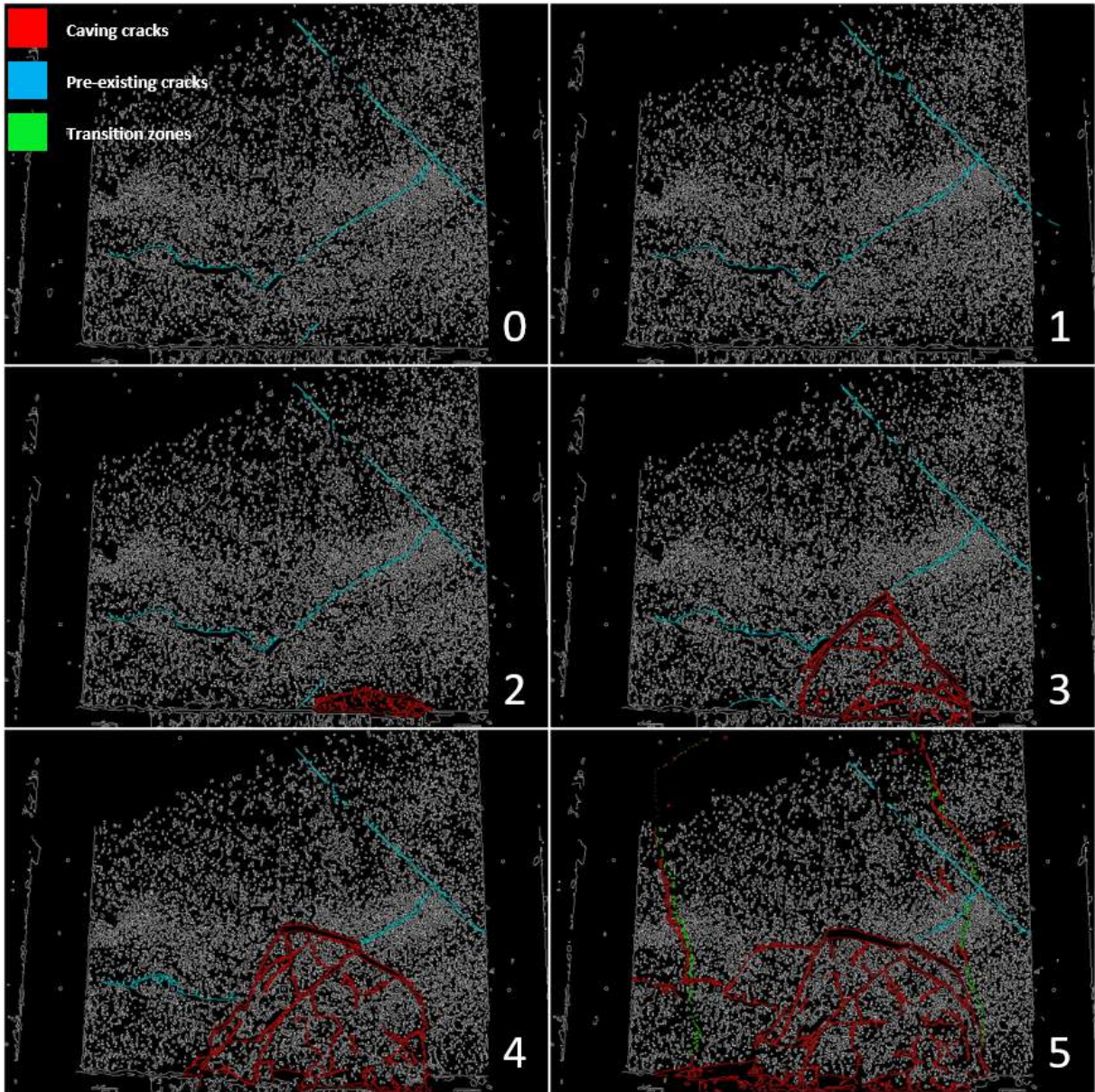


Figure 5.8: Binary Image of cave progression test 3 highlighting cracks over 6 steps.

From what is observed, it seems that the connection of the cave back with the pre-existing fractures was made only in step 5. What can be noted as well is the cave back itself remained shallow until the point of cave propagation reached the surface in step 5. It could be speculated that was due to the overburden weights which caused the material

just above the cave back to remain static and downward pressure allowing a shear failure to result on either side of the cave back.

Similarly to test 2, the critical extensional strain was exceeded in the same step as cave propagation was initiated (but this case in step 2) as shown in Figure 5.9. No movement was recorded in either of the first two frames of steps 0 and 1 of Test 3 as seen in from the strain surfaces.

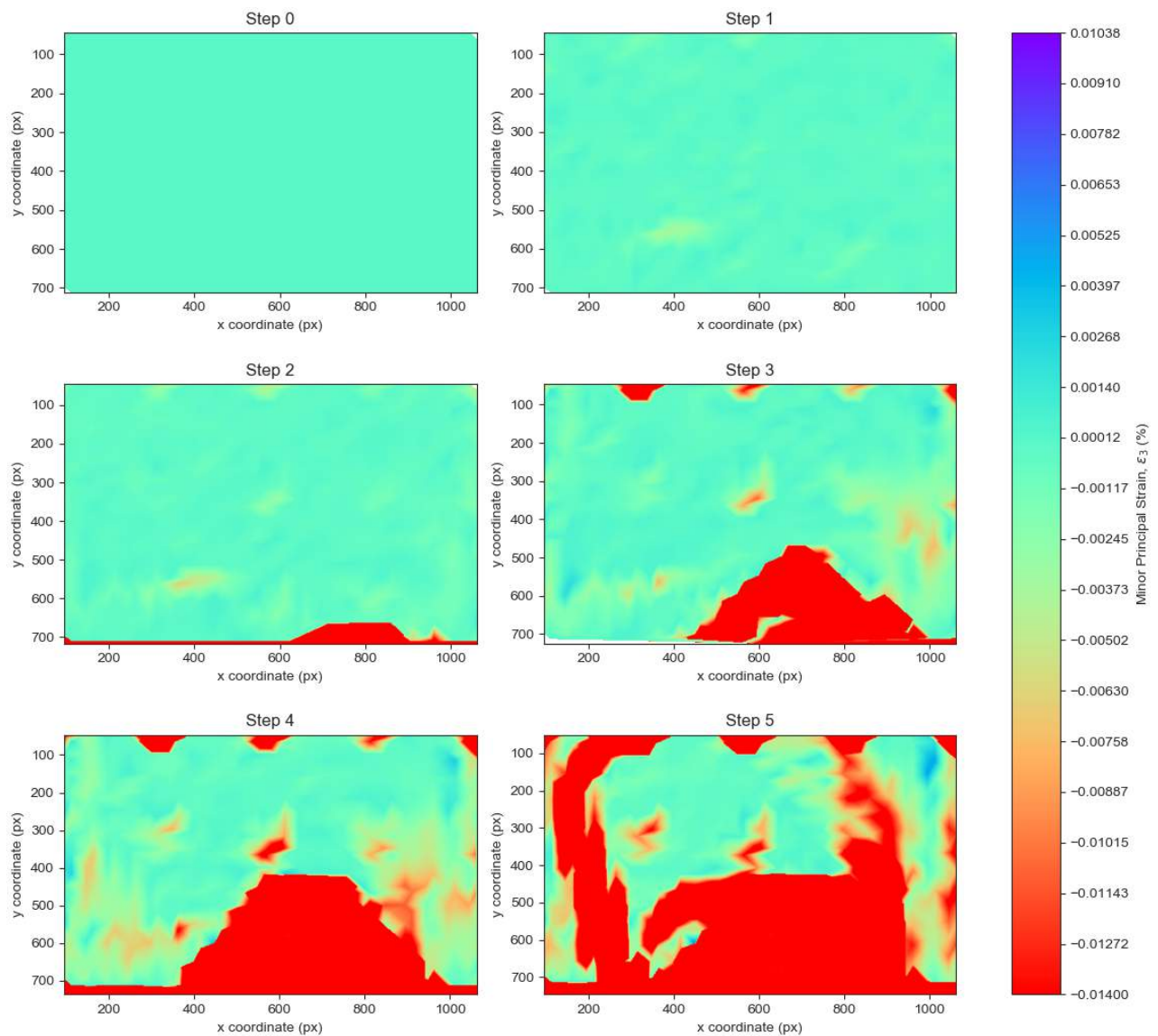


Figure 5.9: Minor principal strain surface plots during cave mining propagation over 6 steps.

Step 3 correlates well with the triangular shape of the cave back in the grayscale and binary images. Step 4 displays that the material's tensile limit had been further exceeded and had widened the same way as the cave back did in the images. Finally, step 5 shows that cave back had reached the top surface of the sample through transition zones on either side of the cave (indicated by the red vertical extensions to the cave back).

5.2.4 Cave Progression Test 4

Caving progression test 4 involved a model that was subject to maximum horizontal confinement and overburden. Figure 5.10 displays the overview of caving progression in grayscale. Once again the binary images are provided in Figure 5.11 for clarification of the pre-existing fractures and the strain surfaces are presented in Figure 5.12.

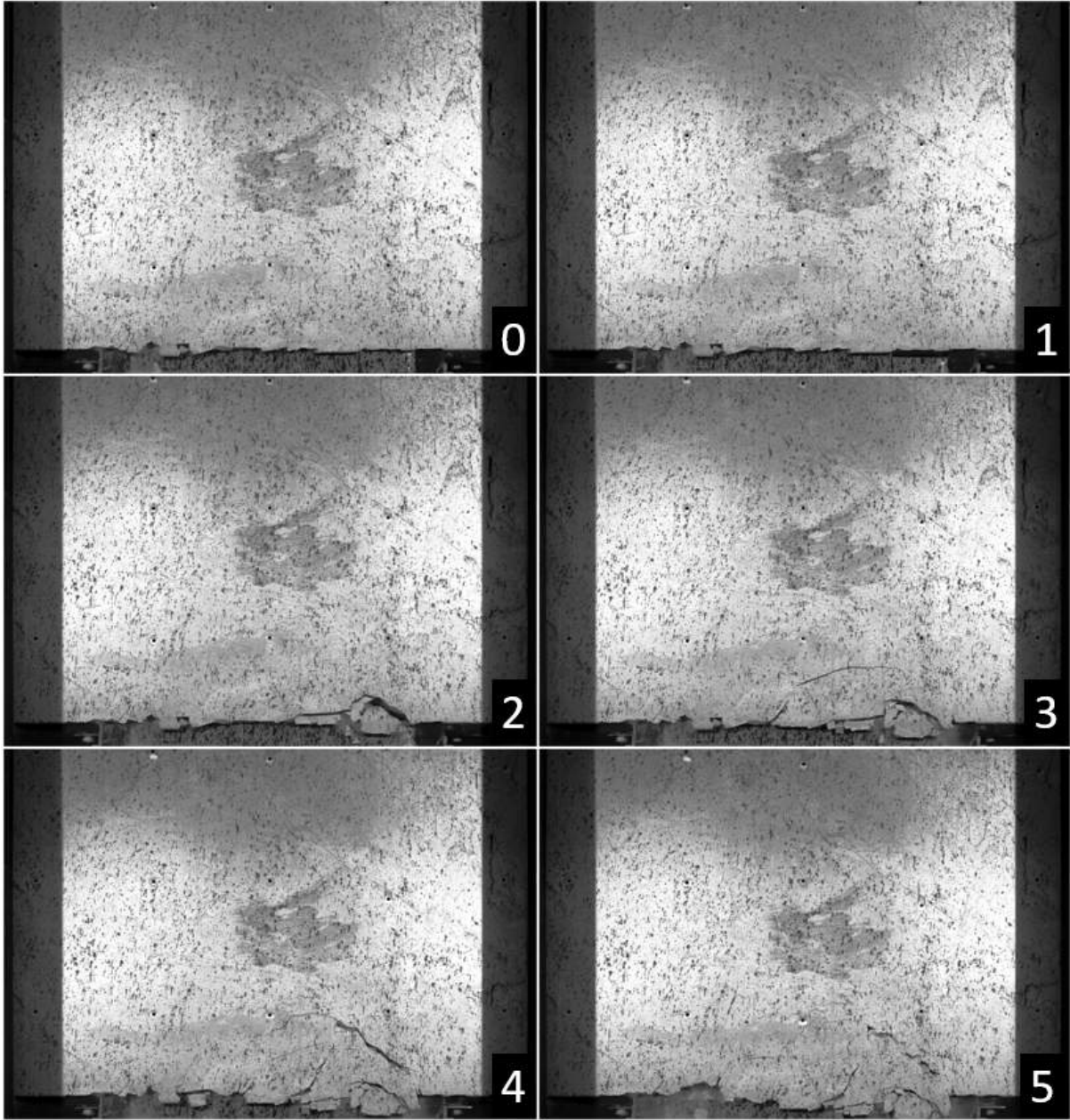


Figure 5.10: Overview of cave progression test 4 over steps 0–5 (maximum confinement and overburden).

The sample panel used in test 4, sustained many small pre-existing fractures from the time swing-up commenced to reaching an acceleration of 80 g. Amongst these less obvious discontinuities identified in Figure 5.11, it is noticed from steps 0 and 1 of the grayscale images that there are pre-existing fractures present on both sides of the sample within

the shadows formed by the test frame. A crack which travelled from the right side (mid-height) of the sample towards the top of the sample was identified and also forming before reaching 80 g conditions.

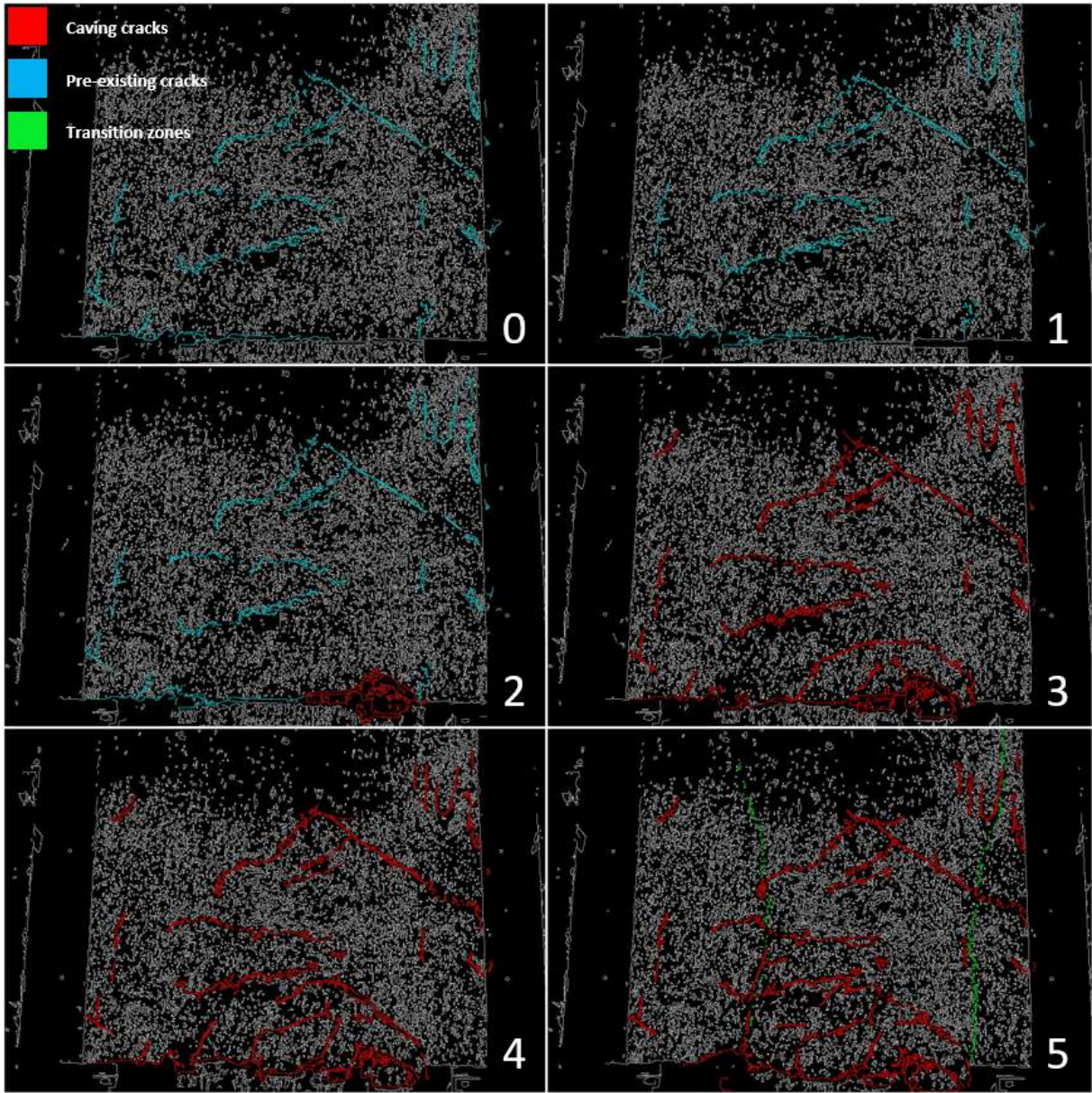


Figure 5.11: Binary Image of cave progression test 4 highlighting cracks over 6 steps.

Cave propagation began from the lowering of the second actuator head in step 2, which followed typical parallel fracturing as in most tests of this investigation. However, step 3 saw the weight of the overburden exceed the material strength and caused the sample to fail under the weight of the vertical pressure from the brass weights. This caused an immediate transition zone from this step onwards where material gradually moved downwards as actuators were withdrawn. The area affected by the mobilising of material can be measured by width of the undercut. Although this is difficult to visualise in the overview of Figure 5.10, it is indicated by the binary images changing from pre-existing

fractures in step 2 by cyan lines to cave propagation failure indicated by the red lines in step 3 and 4. Once again, the transition zone is given in step 5 by the green lines. Visual fracturing and cave back definition are not easily seen from Figure 5.10 since fractures are constantly filled with the caved material that is gradually moving downward.

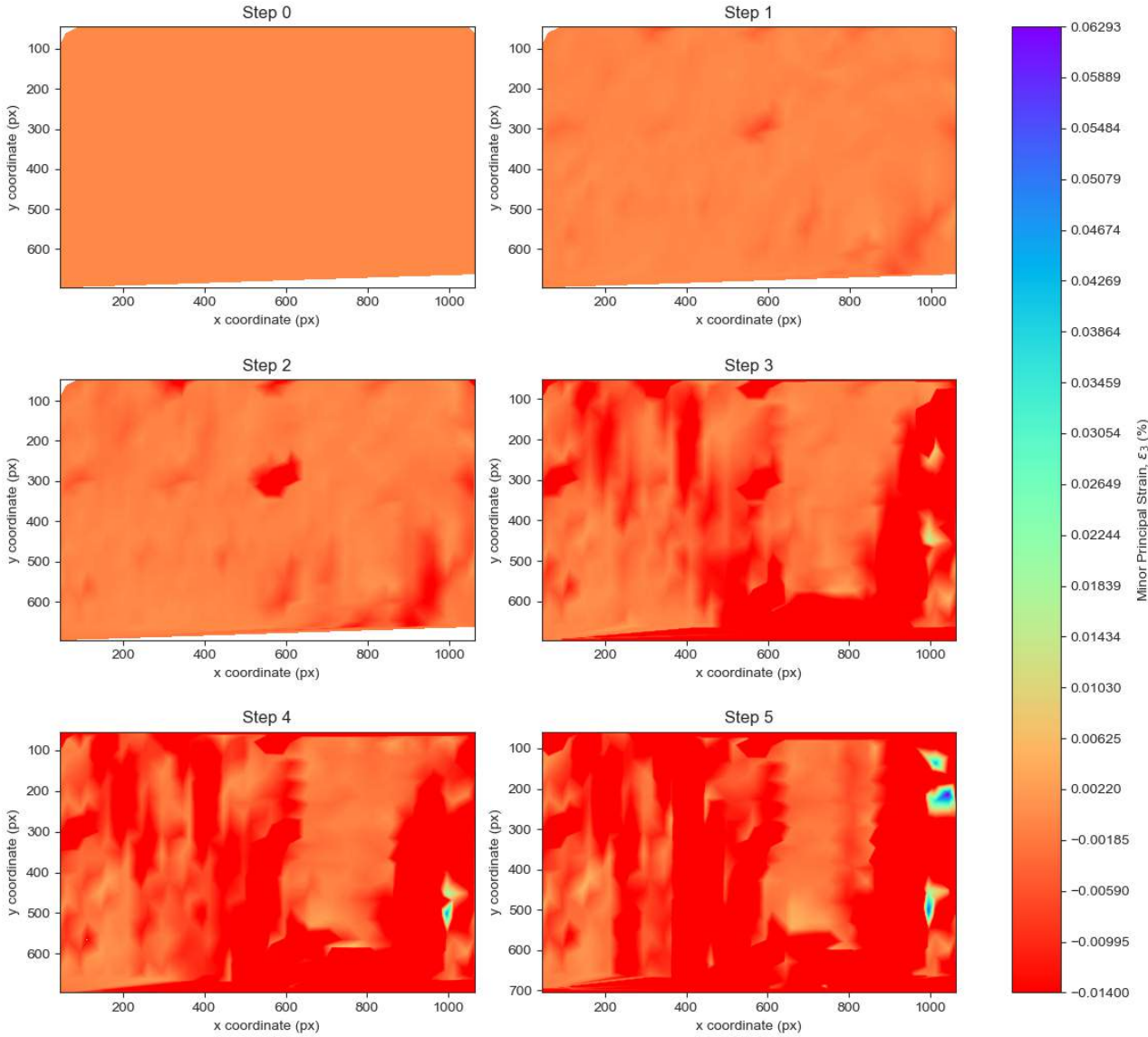


Figure 5.12: Minor principal strain surface plots during cave mining propagation over 6 steps.

Drawing attention to the contour mapping of minor principal strains through test 4, step 0 contained only compressive strains from the beginning of the test, following a near-critical increase of tension in the middle and throughout the right-hand side of the sample in step 1. The tensile strains grew in step 3 with clear indication of the strains exceeding the critical value when compared to cave propagation that had taken place in step 2 of Figure 5.11. Subsidence, which was applicable in step 3, was indicated by most of the panel material being in the red zone throughout the height of the model. In other words, caving of the sample centre (as well as the top right hand side of the sample) took place as failed material shifted downward, displacing the cave back that immediately formed

once the third actuator head was withdrawn. It should be noted that at this point the top section of material close to the top surface of the sample was crushed as the cave back only reached two thirds the height of the sample whilst the sample subsided towards the undercut. The transition zone is shown by the red columns of strains in step 4 and 5 of Figure 5.12.

5.3 Discussion of Results

The discussion of results begins with the comparison of the cave-back geometries in caving progression tests 1 to 4. The geometry of caves formed in the different tests is suggested to be influenced by the set of conditions (states of stress) within the experimental models described in Chapter 4. Furthermore, the exposition of critical extensional strain on cave mining propagation through superposition of qualitative and quantitative image results is considered. Lastly, the failure mechanisms of the experiments are identified and described, with reference made to results herein as well as previous physical modelling research.

5.3.1 Cave Progression Geometry

Geometric parameters mentioned in Section 5.1.1 were calculated using the measuring tools from Microsoft Paint.net. An example of a caved area is defined in this investigation as the area encapsulated by dotted lines in Figure 5.13 whilst distance covered by the red lines is taken as the perimeter of the cave. The resulting ratio corresponds to the hydraulic radius. Before the geometric parameters were plotted for each of the steps of undercutting procedure in Figure 4.6, the area and perimeters of caves used to calculate the hydraulic radii were plotted for cave progression steps, initially. Like the hydraulic radius, these parameters give an indication of cave progression and crack propagation within the model. The increase in cave perimeter and cave area for the first five steps of all four tests are shown in Figure 5.14 and Figure 5.15, respectively. The calculated hydraulic radius for the first five steps of all four experiments can be seen in Figure 5.16.

From the withdrawal of the first actuator in step 1 of Figure 5.14 and Figure 5.16, it is indicative that the cave perimeter and hydraulic radius were highest in test 2. This could be explained by the lateral-earth pressure being the highest for this particular test which could have possibly caused the cave growth to occur faster for smaller undercut areas. Since the caves have formed due to tension — the tension build up in test 2 could have easily been the highest. When comparing test 2 with test 1, 3 and 4, which show no caves at step 1, test 2, because of its high confinement stresses, (largest K value) could have caused material to be pushed vertically more than the other tests. It is observed in subsequent steps that due to the high horizontal stresses being maintained and arching of

the material taking place, a low profile cave resulted in test 2 unlike other tests, where the cave height steepened causing larger cave perimeters and areas to be defined, respectively, which is evident in Figure 5.14 and Figure 5.15 by the steepening in gradients of test 1 and 3 in steps 3 to 5 as well as test 4 earlier on in steps 2 to 3. Overall, test 2 maintained the most flat curve throughout steps 1 to 5.

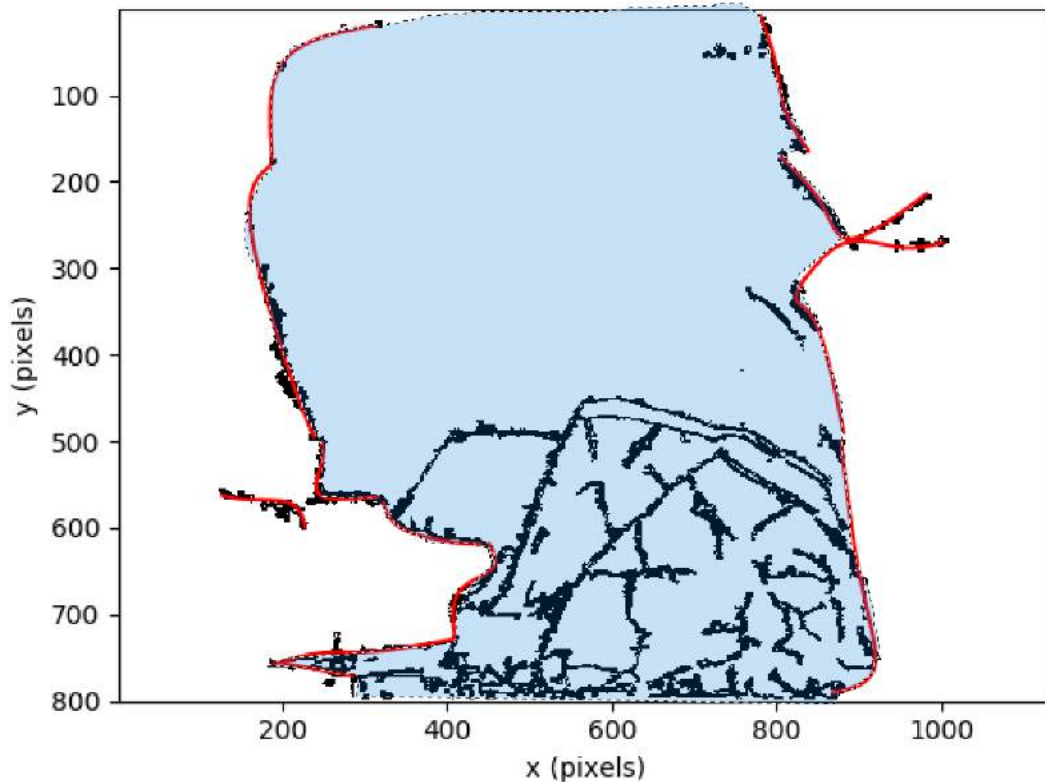


Figure 5.13: Derivation of geometry parameters used in the investigation (Step 5 of test 3).

It should be noted that the model in test 1 yielded the most linear response with respect to caving perimeter as well as in its hydraulic radius response over the cave progression steps. This observation perhaps could be owing to the lack of confinement and overburden which promoted the most-likely environment for gravity caving to occur. Since the cave progression of all tests showed failure in tension, all failures could be proposed as gravity caving failures. Subsidence could clearly be shown in step 4 for test 3 and step 2 for test 4 with the curves taking off at those respective steps in the tests. Lastly, it can be discussed that full failure of test sample 4 was observed as the cave perimeter and area remained constant after the bulk cave propagation occurred from step 2 to 3. At this point subsidence was reached where subsidence is only reached by test 3 in step 4 to 5.

Figure 5.16 containing the plot of hydraulic radii for the caves of test 1 to 4 seems to mask the change in gradient of the curves in Figures 5.14 and 5.15 since the curves conform with a certain linearity apart from having different lateral-earth pressures. Once again, test 4 stands out in this graph, revealing the early failure/subsidence in the test.

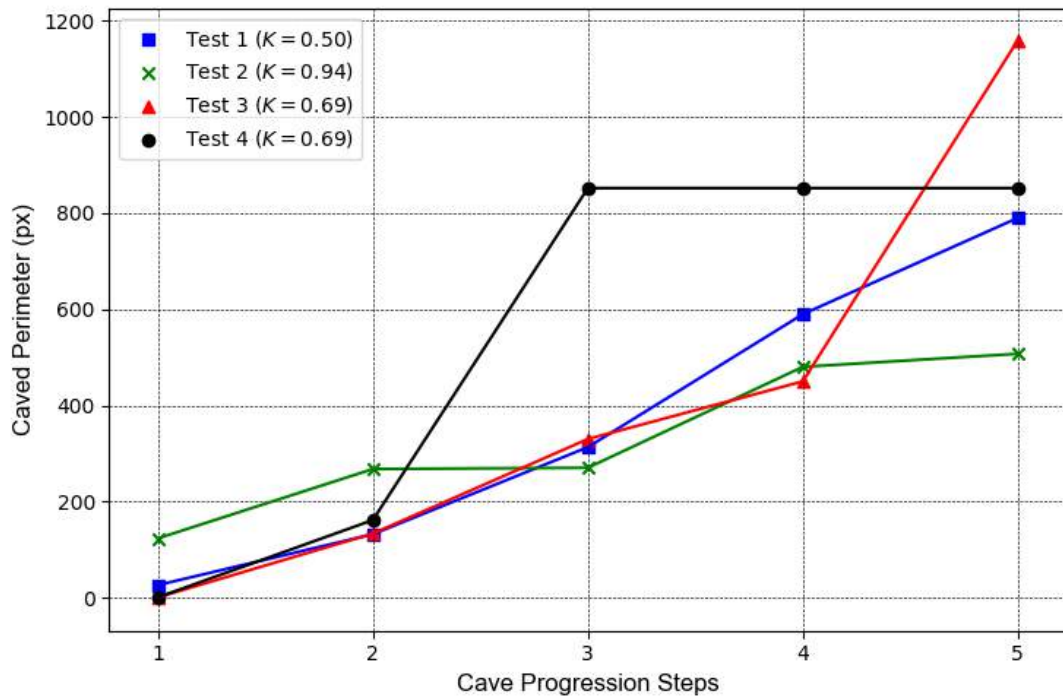


Figure 5.14: Caved perimeter during cave mining propagation over steps 1–5.

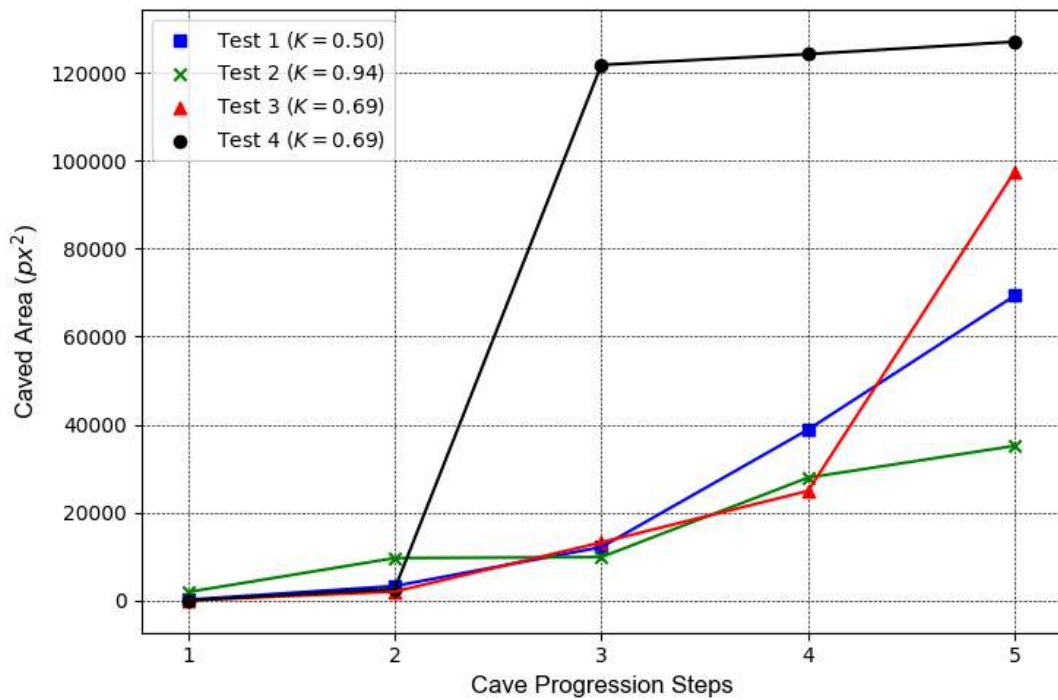


Figure 5.15: Caved area during cave mining propagation over steps 1–5.

Some material above the undercut was already crushed due to the weight on the sample at 80 g, which exceeded its UCS strength. The dimensions of the cave-back can be monitored over cave progression steps in Figure 5.17. Points for cave height and width are plotted similarly to previous figures in this section where a point represents values for the step where an actuator head has been lowered, but just before its successor actuator is lowered.

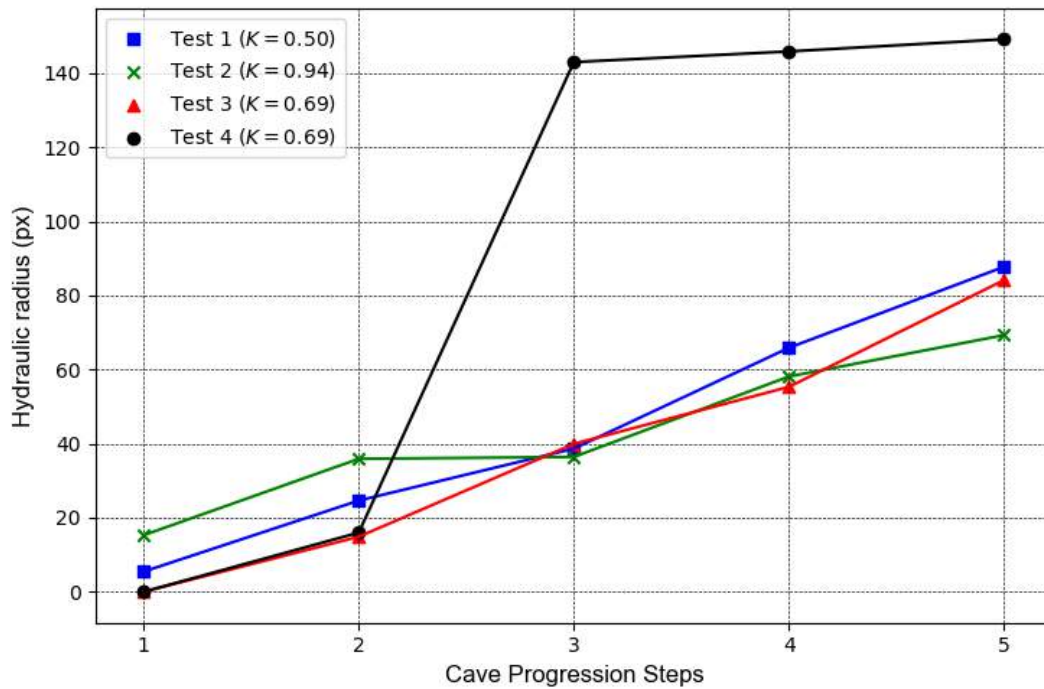


Figure 5.16: Caved hydraulic radius during cave mining propagation over steps 1–5.

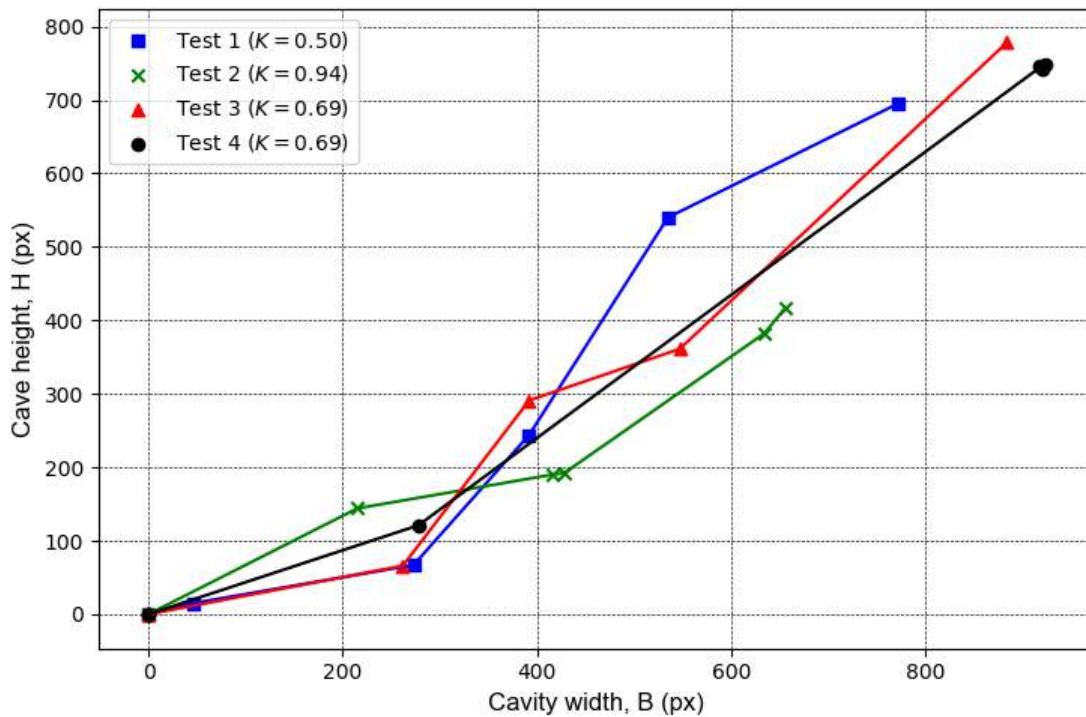


Figure 5.17: Cave height vs. cavity width plot during cave mining propagation over steps 1–5.

Test 1 shows a gradual cave growth where the height of the cave exceeded the width in step 2, but the cave slowly flattening off between steps 2 to 4, and growing in height again in subsequent steps until subsidence was reached. The monitored dimensions in cave-growth can be described as prominent in the beginning of test 2 with the cave-back having a larger height than width, but the height of the cave only reaching a maximum

of 417 pixels after step 5. test 3, like test 1, progressed laterally when the first actuator was withdrawn, and then propagated at a shallower cave height due to the confinement pressure placed upon the sample before subsidence was observed in step 5. Finally, in test 4, the last three data points are positioned at the height and width maximum, showing caving occurred rapidly in this test.

5.3.2 Lateral Earth Pressure

From a viewpoint of incorporating lateral earth pressure, it can be deduced from Figure 5.17 that higher lateral earth pressure ratios take on caving slopes which are steep initially and tend to flatten off when the cave-back progresses. On the other hand, smaller K values result in slopes that are initially flat due to the lack of horizontal confining pressure, but steepen once the width of the cave-back has reached a certain magnitude during cave progression (exhibited by tests 1 and 3, respectively). Furthermore, a plot of the K values of the applicable tests against the H/B ratios of each cave progression step is presented in Figure 5.18. Corresponding steps in the tests were joined through line graphs to make the comparison between the H/B ratios of caves that formed under the respective stress state conditions (i.e. K). From Figure 5.18, larger K values result in H/B ratios that are initially higher, given by test 2's data points plotted higher than those of test 1 and 3 initially (i.e in steps 1 and 2); however, being exceeded in step 3 to 5. Smaller K values are observed to result in H/B ratios that are initially low, but grow rapidly in subsequent steps compared to those subjected to higher K values (i.e. more horizontal confinement). Note the symbols of data points remain the same for each test.

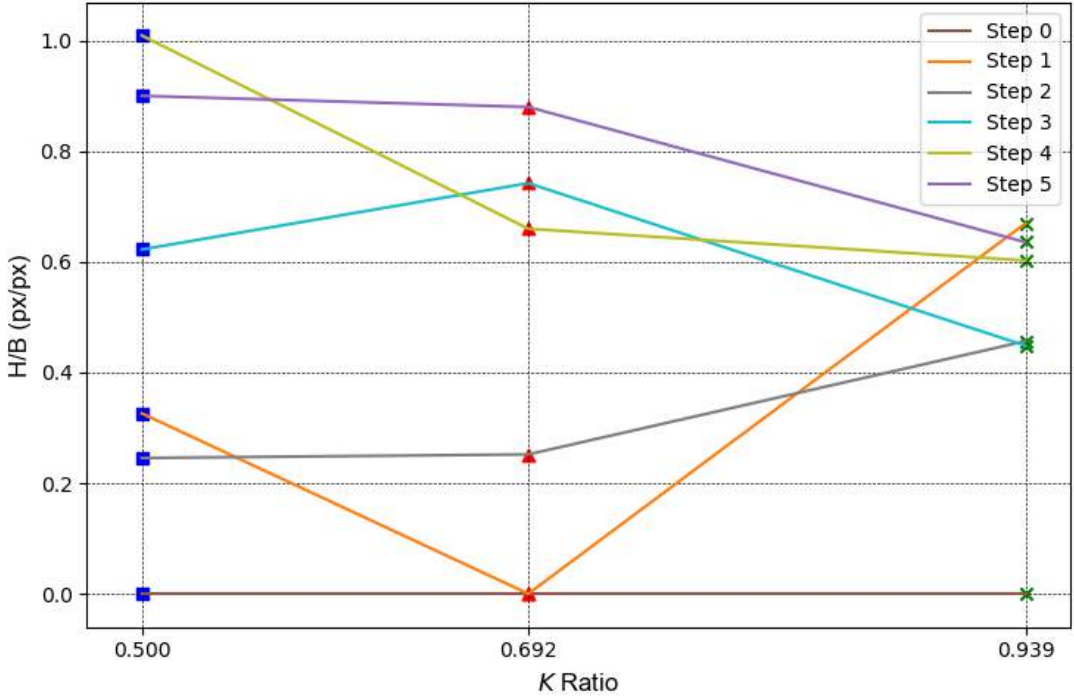


Figure 5.18: Plot of K values against H/B ratios for tests 1, 2 and 3.

5.3.3 Critical Extensional Strain in Caving Mechanics

This section focuses on the applicability of Stacey's Critical Extensional Strain model on cave mining propagation failure. Reference is made to the observations of Cumming-Potvin (2018) which concern extensional failure in physical testing of cave mining models.

A full overview of superimposed image results used within this sub-chapter can be found in Appendix D. Only what is deemed necessary is presented herein to draw attention to certain events in the cave progression results of tests. Two types of superposition are implemented, which are used interchangeably, intended to ease the purpose of matching up the positions of strains to fractures and vice versa. These two types comprise overlaying strain surface plots (such as Figure 5.3) on binary Canny-edge images (such as Figure 5.2) and are termed 'superimposed surface plots'. Similarly, overlaying strain contours on high-contrast images are termed 'superimposed contour plots'.

Figure 5.19 and Figure 5.20 show the two types of superimposed plots for step 3 of test 1, where cave progression has initiated. It should be noted that the magnitudes for the contours and surfaces plotted are taken from the original colour-bar (legend) for their respective test in Section 5.2 and that red contours/surfaces represent strains that are greater or equal to the critical value. The superimposed surface plot is helpful in locating regions of minor principal strain relative to where detected cracks are present given from Canny edge-detection. Superimposed contour plots are helpful in discerning whether strains and fractures coincide with each other. In step 3 of test 1, the region enclosed by the red surfaces span across the red (caving-caused) cracks of the binary image which are located on the bottom right-hand side of the cave-back. Also shown in Figure 5.19 (and Figure 5.20) are two elongated regions of critical strain contours which have already circumscribed the pre-existing fractures on the left-hand side of the sample in step 3.

The exceeded critical strains are also present underneath the peak of the cave-back, which is expected since material above the cave-back would still be intact and only that which is below would have exceeded the critical value. Since cave propagation originated from the bottom right-hand side (due to the right-most actuator being lowered first), most of the strain in red (i.e. values larger than critical) appear to the right of the cave in this step. When the third actuator platform was lowered, the crack merely propagated from its previous opening of the right and top of the cave to the bottom where the movement of the actuator took place. What is important to note is that the strains indicate the flow of the crack propagation which at any point does not originate from the side of the third actuator but from the top of the cave-back downwards, which was previously formed by actuators E and D (reference made to Figure 4.6).

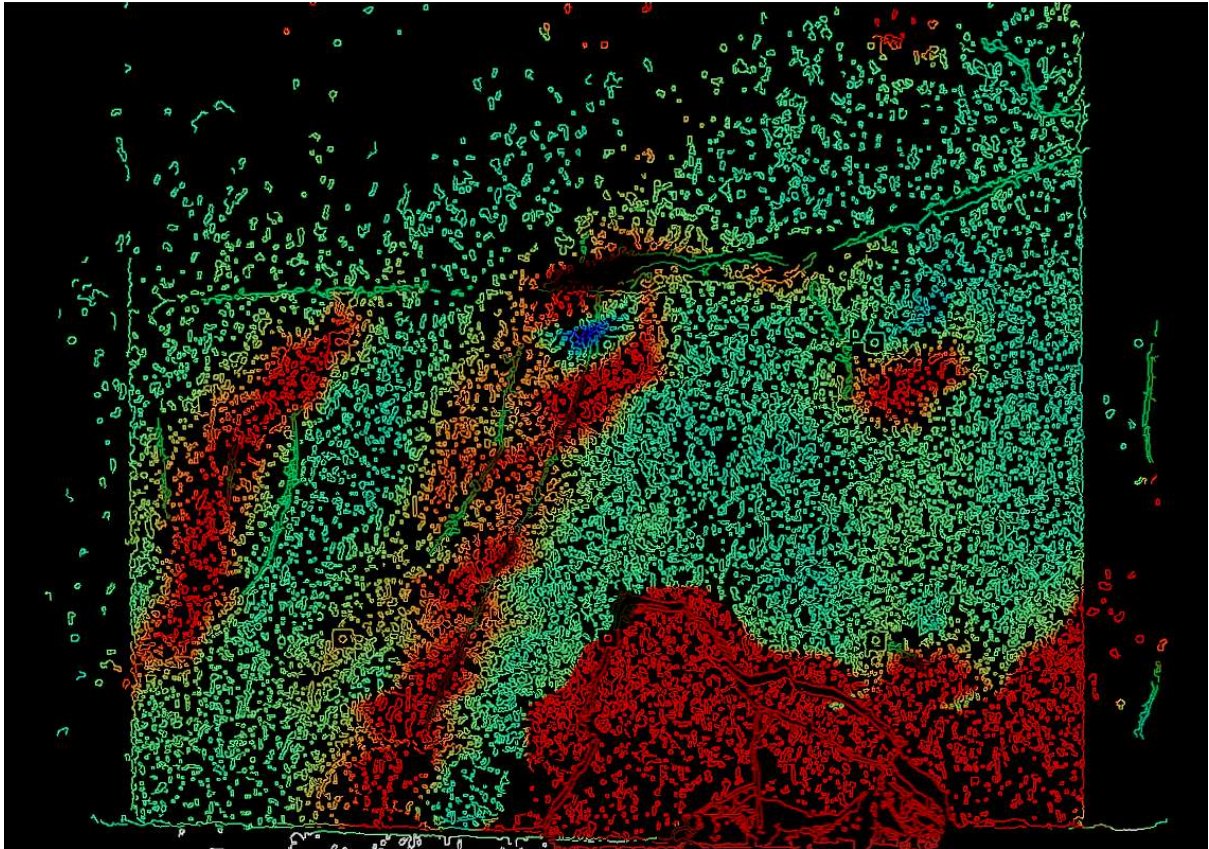


Figure 5.19: Step 3 of test 1 — superimposed surface plot.

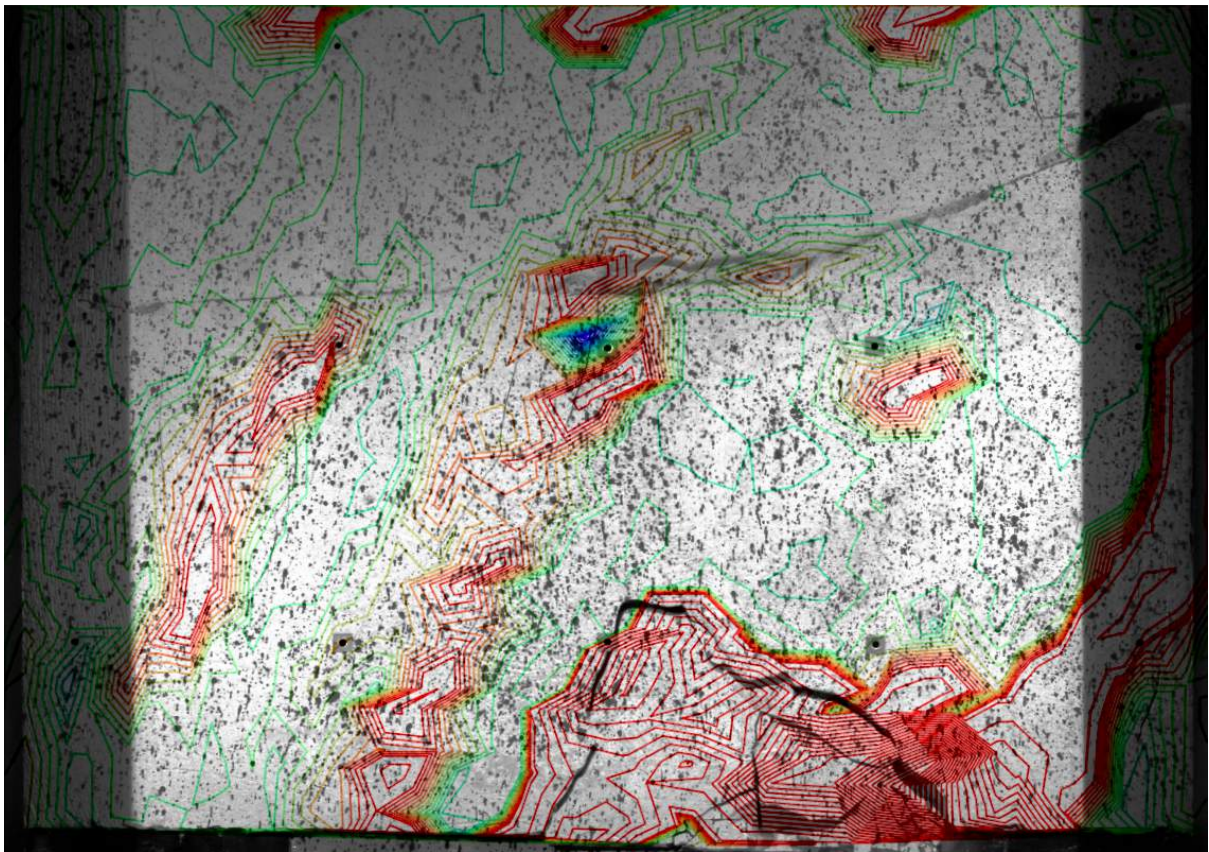


Figure 5.20: Step 3 of test 1 — superimposed contour plot.

Considering Figure 5.20, one can more distinctly observe the regions of strain contours that are affected in the model which are below the critical value. These areas include the top right-hand side of the sample where pre-existing cracks are present diagonally. This cannot otherwise fully be seen in the binary images as these pre-existing cracks were not detected in Canny-edge images.

Other places where non-critical strain contours are present are on the top surface of the sample, where strains in the order of -0.0012% strain are recorded, with the exception of three small adjacent regions. As expected, the outermost critical strain contours in Figure 5.20 approximately coincide with the largest crack. Subsequently in step 4 (shown in Figure 5.21), strains are observed to further exceed critical at wider distances to where pre-existing fractures had taken place and the formation of new cracks around these positions were highlighted — which provides evidence that the critical value does provide pertinence in determining the tensile failure of the artificial rock material.

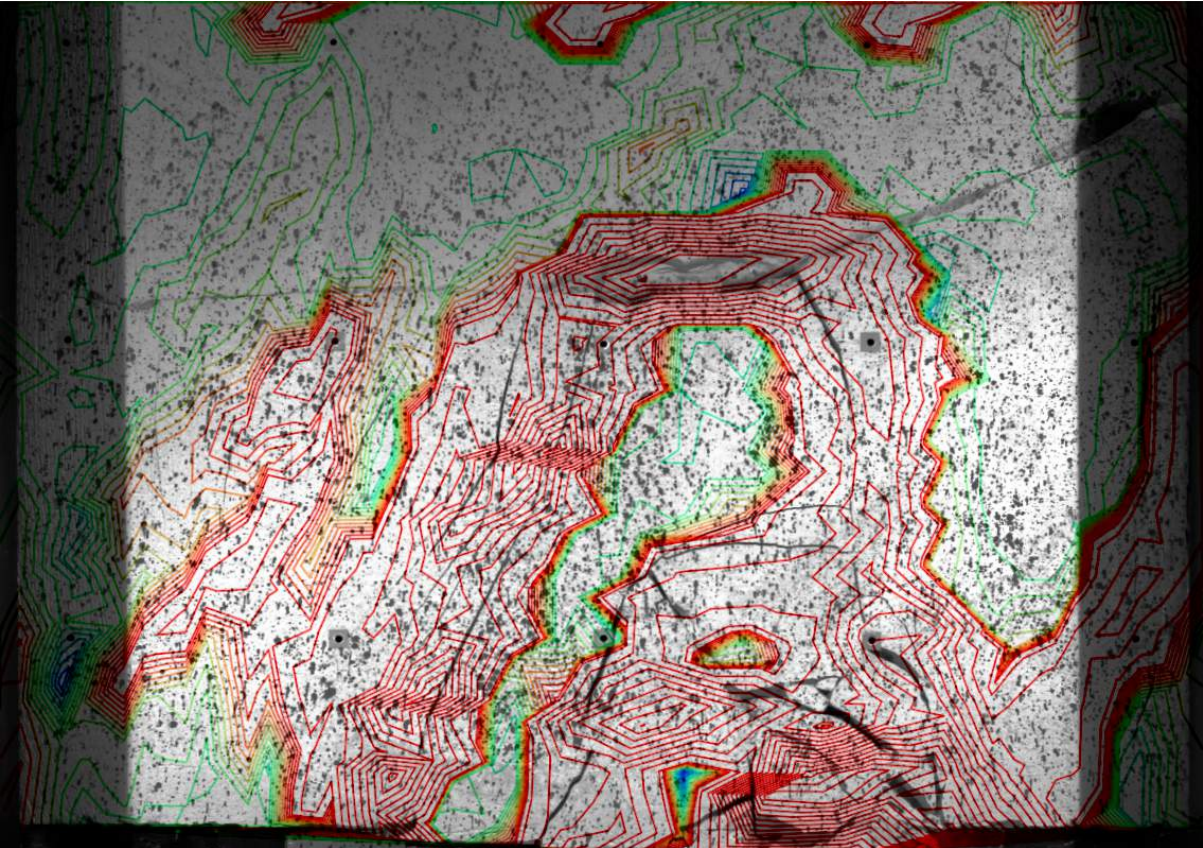


Figure 5.21: Step 4 of test 1 — superimposed contour plot.

Referring to Figure 5.22, it should be noted that the middle critical region at the sample surface in step 4 also met the growing cave-back in step 5. There was also a region of material in-between that did not display red, which indicates that cracks propagated around sections of material thereby suggesting parallel fracturing from strain analysis as well.

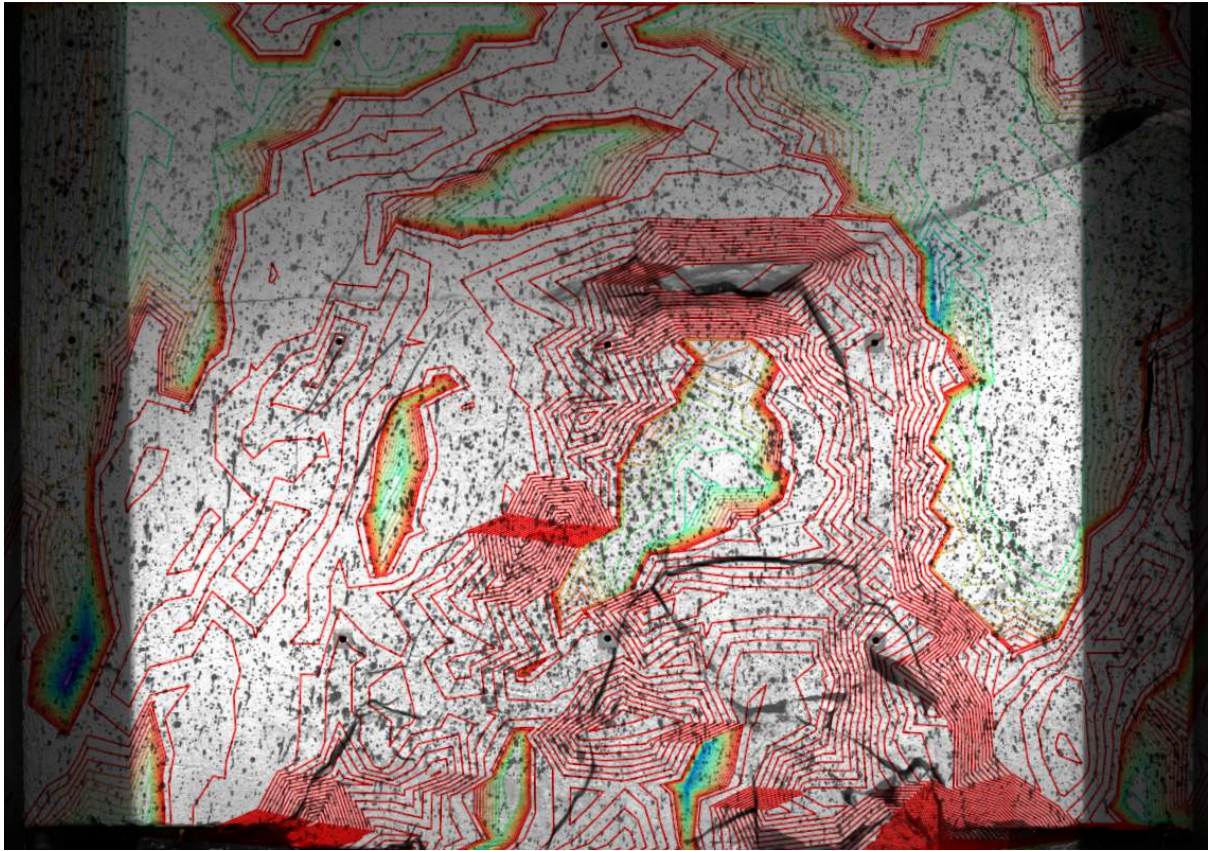


Figure 5.22: Step 5 of test 1 — superimposed contour plot.

The cave formation of test 2 can be described as having a low profile and being rapidly initiated. In step 1 of test 2, as indicated in Figure 5.23, cave initiation had already commenced with the material reaching a minor principal strain of -0.0154% and a major principal strain of 0.2171% . In step 2, a relatively large fracture propagated to the left, two-thirds of the full undercut width. Once again, outermost critical strain contours were observed to have overlapped with the relatively large advancing cave-back (this is shown in Figure 5.24).

On closer examination of the actuators from steps 0 to 1, actuator head E caused D to move downwards slightly due to the two actuators being pushed up against each other, thereby causing a hairline fracture in the sample above actuator head D. This is shown in the superimposed surface plot of step 1 in Figure 5.23 by the overhanging red crack at the bottom of the sample. Due to the actuators being in a position where they made contact with other, the withdrawal of actuator E placed friction upon actuator D which caused it to be lowered simultaneously. In this Figure, not much can be accounted for in terms of strain since the movement of the two actuators was minimal causing only a hairline fracture to form. It is possible that this fracture (although indicated in red to show cave growth) was first propagated during centrifuge acceleration to 80 g.

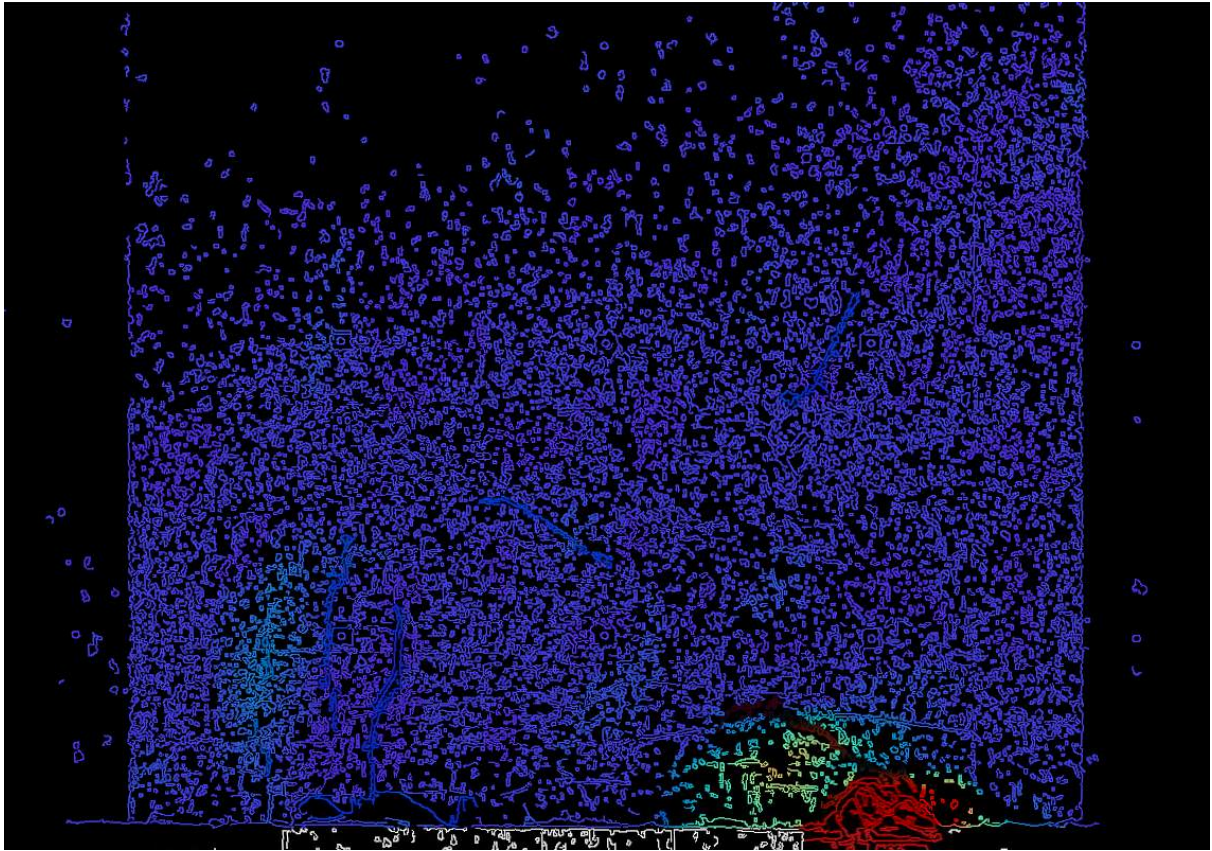


Figure 5.23: Step 1 of test 2 — superimposed surface plot.

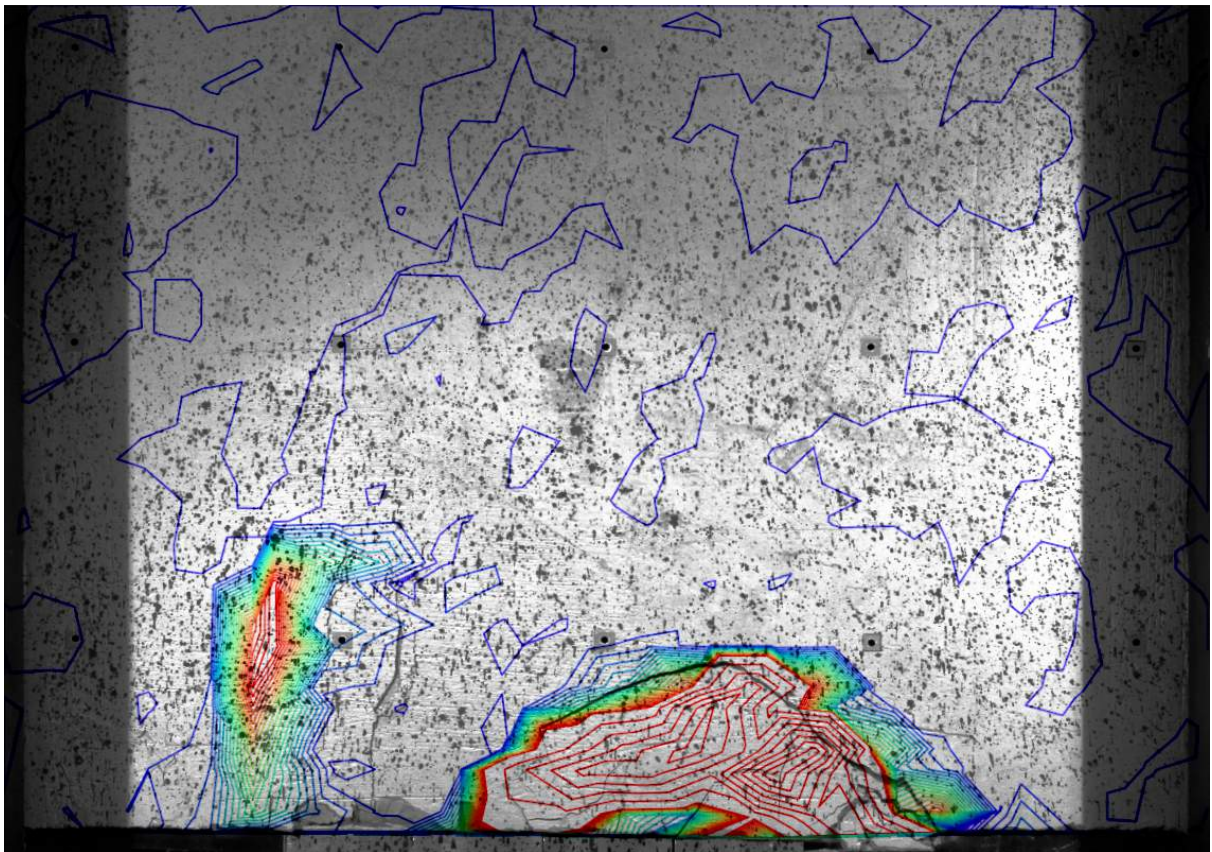


Figure 5.24: Step 2 of test 2 — superimposed contour plot.

Investigating the transition of steps 1 to 2, it was apparent that actuators D and C were withdrawn concurrently as well but with more movement this time. This could be the reason for the rapid cave propagation in this test since step 2 was intended for only moving actuator head D as per Figure 4.6. The mapped minor principal strain grew considerably in step 2, which occurred above actuator C and parts of B.

Figure 5.25 shows the caving progression superimposed with the strains at step 3 in test 2. As expected, when actuator head C was lowered conventionally in this step, strains in the model increased, which resulted in the two already existing red zones enlarging slightly from step 2. Furthermore, from a fracture standpoint, cave propagation did not advance and existing cracks outlining the cave-back were merely widened.

Returning from contours back to superimposed surface plots, Figure 5.26 can be used to identify the pre-existing cracks more clearly to show the anticipation of cave progression in further steps. In the left part of the sample at this stage, five defined pre-existing fractures have developed since step 0 of Figure 5.23 with the one on the extreme left showing as critical. The other four can be identified by the blue-coloured pixels in line formation. Progressing from step 3 to step 4 (shown in Figure 5.27), one can see that by lowering actuator head B, the cracks due to caving have propagated in the most direct way to reach the pre-existing fractures in left-hand side of the sample in step 3.

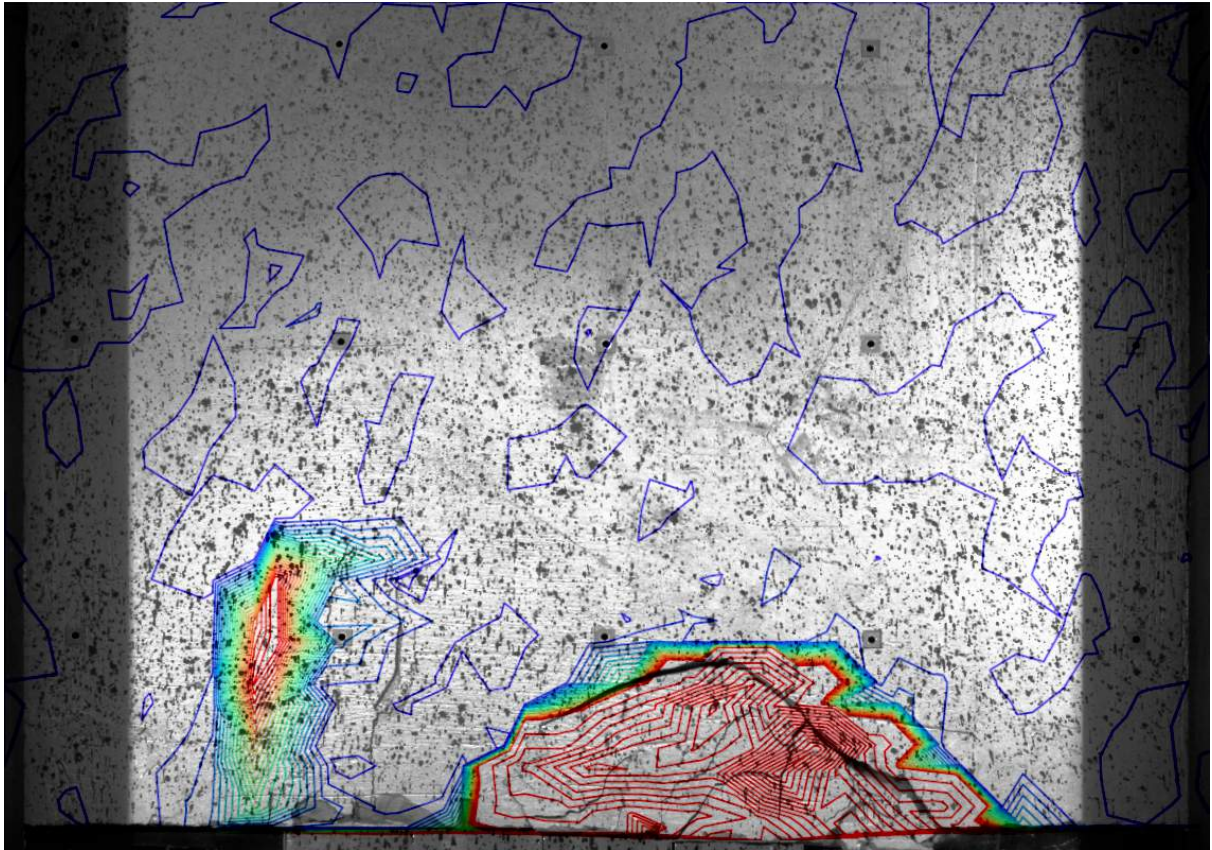


Figure 5.25: Step 3 of test 2 — superimposed contour plot.

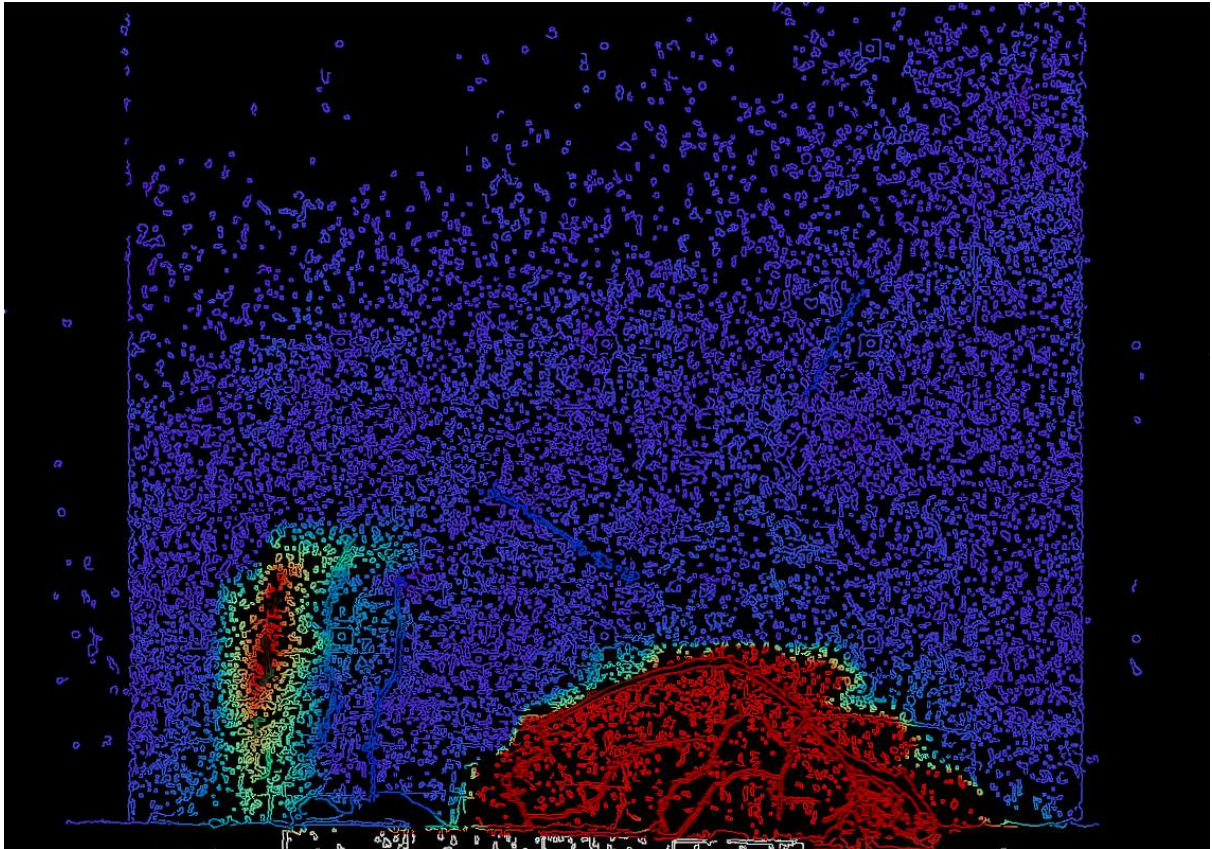


Figure 5.26: Step 3 of test 2 — superimposed surface plot.

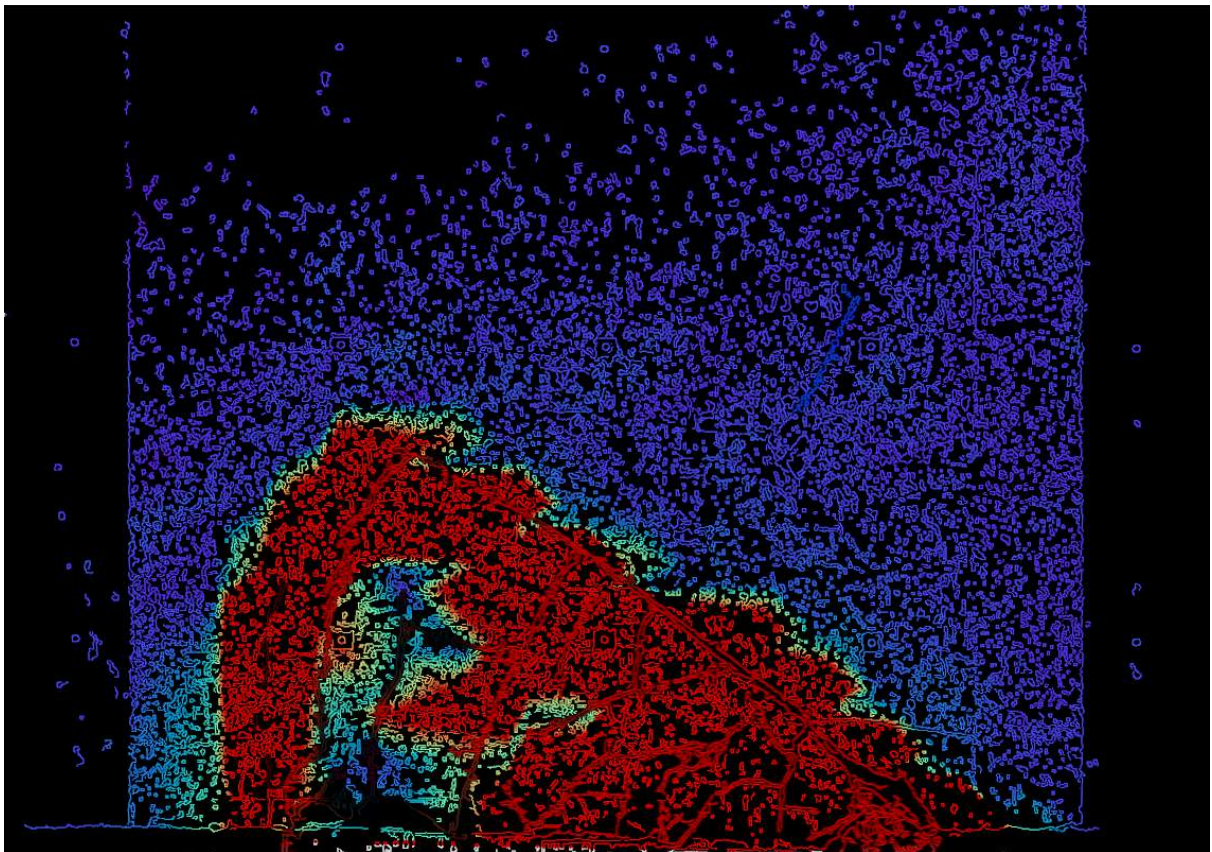


Figure 5.27: Step 4 of test 2 — superimposed surface plot.

Critical strains (indicated by red zones in Figure 5.27) can be reported in areas inside the crack boundaries on the right half of the cave-back and are seen to extend, having the inside of the red zone coincide with the crack in the left half of the cave-back. This follows the trend that critical strains converge from the source of where undercutting began. Step 5 has a similar shape in cave-back geometry to step 4; however, the zone of critical extensional strain was observed to have grown wider around the perimeter of the cave-back. Cave stalling was apparent until the test was increased to 110 g; after which subsidence occurred.

The discussion of test 3 commences with step 2 which resulted in a low profile cave-back that bisects the zone of critical extensional strain as shown when actuator head D is lowered in Figure 5.28. Similarly to previous tests, the strain was observed to originate from the bottom right corner before radiating upward and to the left when the cave propagated. Noting the pre-existing fractures of the sample in test 3 discussed in Section 5.2.3 and using the superimposed surface plots in steps 3 and 4 as can be seen in Figure 5.29 and Figure 5.30 respectively, was determined that upon lowering actuator head C, the cave back advanced upward in parallel fracturing until making contact with these pre-existing cracks. Large (red) regions of material that have exceeded the critical value are observed in these figures, which may make the point that an increased overburden could cause larger tensile strains when compared to step 4 of test 1 and 2.

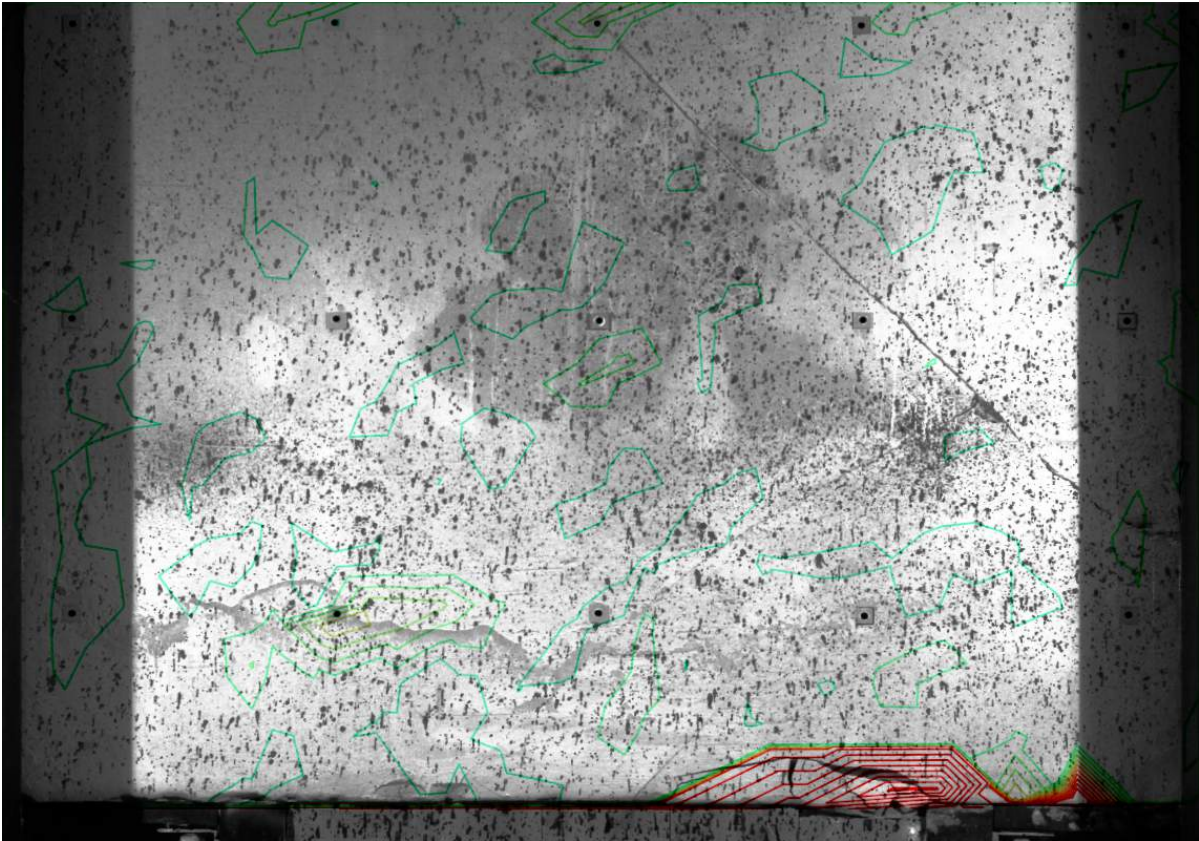


Figure 5.28: Step 2 of test 3 — superimposed contour plot.

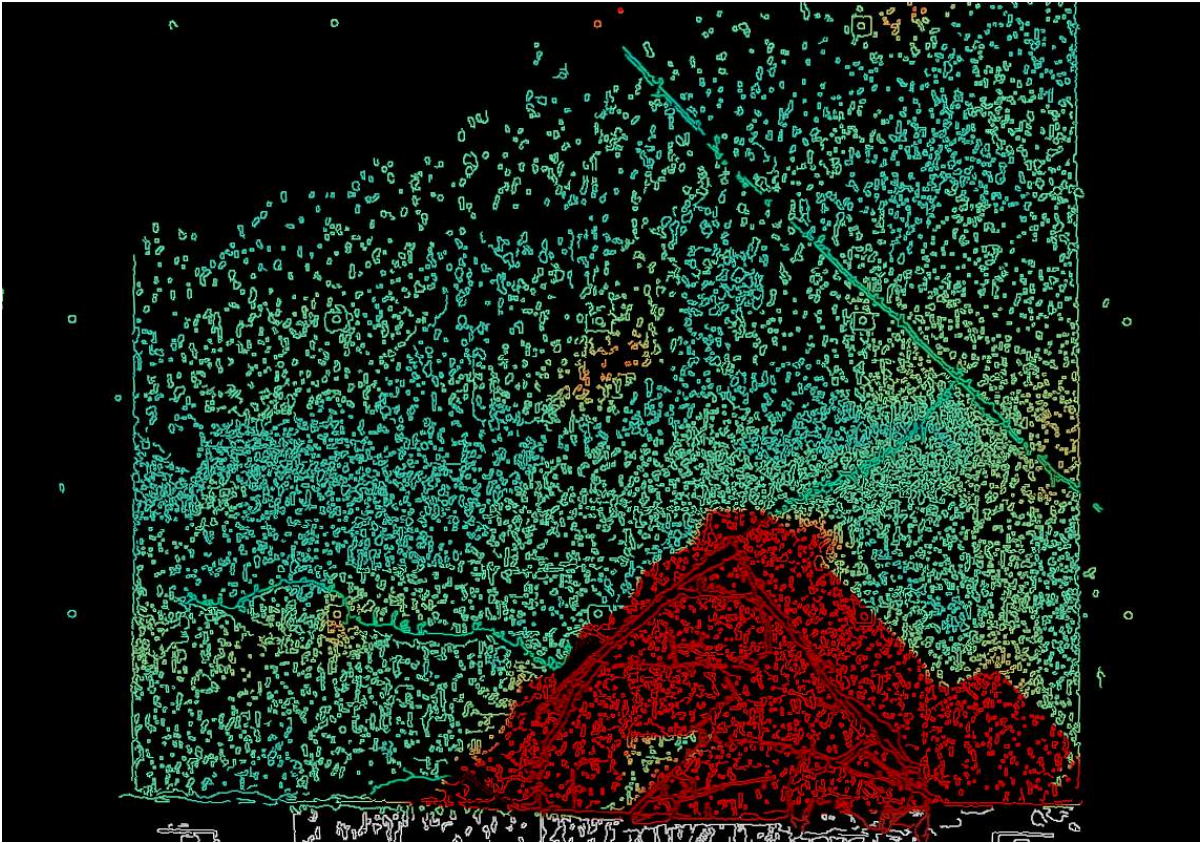


Figure 5.29: Step 3 of test 3 — superimposed surface plot.

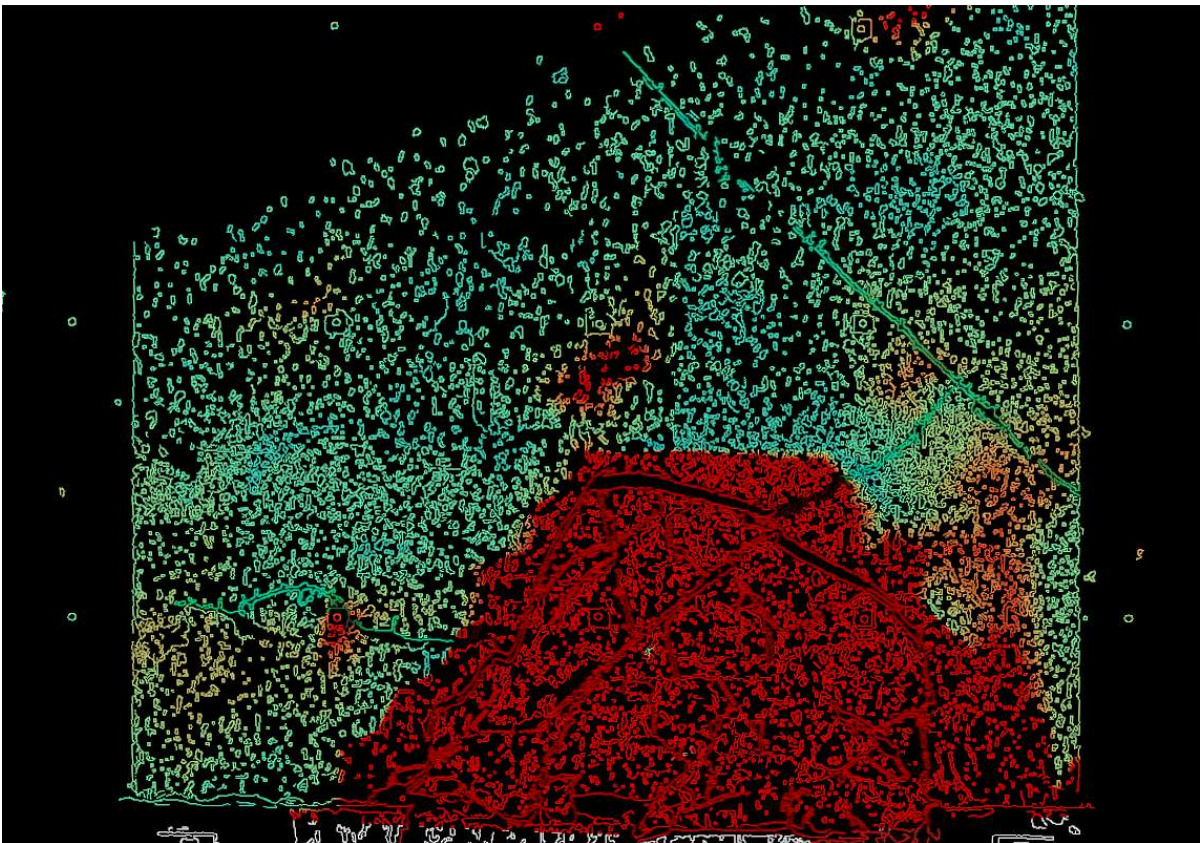


Figure 5.30: Step 4 of test 3 — superimposed surface plot.

In Figure 5.30, it is easily observed that the region of critical strain covers the entire area of caved material. Finally, in step 5 of test 3, the cave holds relatively the same magnitudes with respect to tensile strain around the caved section of the sample, but as shown in Figure 5.31, contours of strain exceeding the critical value can be observed in zones at the top surface of the sample and are present through lines indicating shear transition at the point of subsidence.

The strain on the top surface is a result of the deflection of material from overburden weights lying directly above the sample after transition cracks made their way to the top of the sample causing the formation of the ‘chimney’ when actuator head A was lowered. The transition lines (which are the vertical cracks on either side of the cave) seem to be located on the inside of the strains which link the caved material strains to those on the top surface of the sample. These strains that are along the transition lines are in the order of -0.014% to -0.088% . The strains near actuator head A have also passed critical and are identified as the root cause for the transition lines propagating upwards.

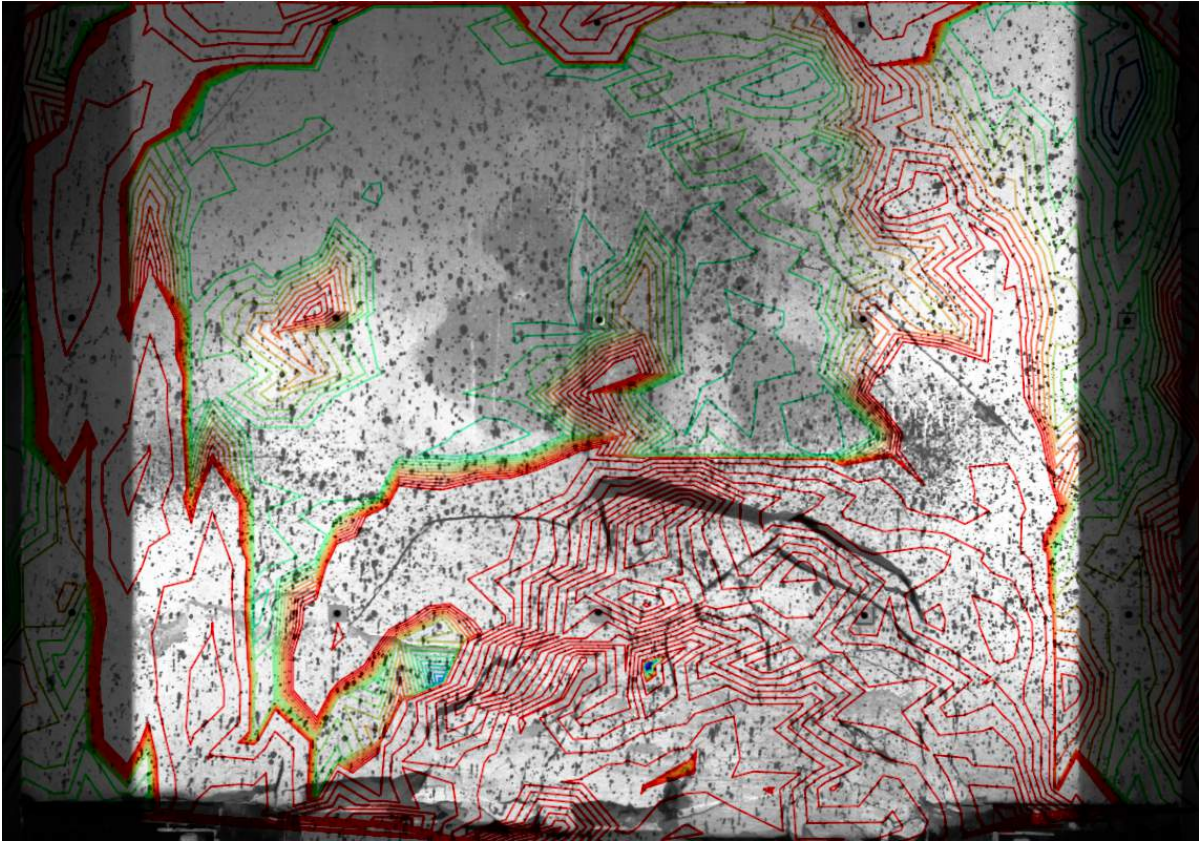


Figure 5.31: Step 5 of test 3 — superimposed contour plot.

As mentioned in Section 5.2.4, the material at the bottom of the sample in test 4 was crushed from centrifuge swing-up and once actuator D was withdrawn in step 2 of this test, material around the bottom right side of the sample (as well as in other places within the model) failed at critical values of minor principal strain. Re-iterating steps 2 to 3, subsidence occurred at the point when critical strains had reached the top surface

of the sample. This can be shown by moving from Figure 5.32 to Figure 5.33. From the indication of strains in step 2 (in Figure 5.32), it seems as though the right side was mobilised first, with the left side only reaching critical strains following this.

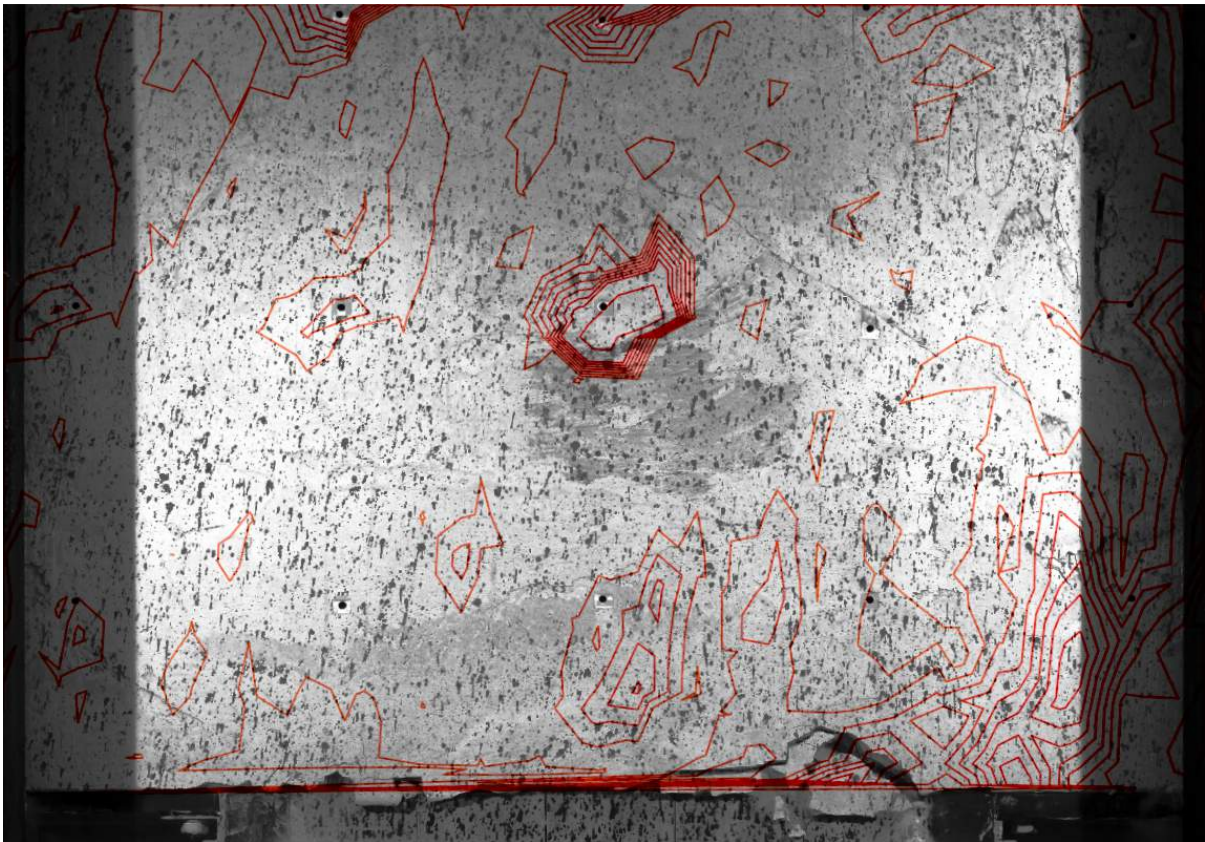


Figure 5.32: Step 2 of test 4 — superimposed contour plot.

While most of the strains in step 2 were near critical (orange), in step 3, the widest crack defined within the cave-back coincided with the orientation of several critical strain contours. Although the entire sample had reached the red zone in step 3, what is important to take note of are the directions of the red contours which also seem to outline the transition lines, indicating subsidence. From steps 3 to 4, parallel fracturing was identified when the cave-back advanced upward with zones throughout the model remaining critical. Not much in terms of significant magnitude was identified from step 3 to step 4 (in Figure 5.34), but the directions of strain contours (particularly at the bottom of the sample) had changed. Note that Figure 5.32 to Figure 5.34 contain strains that are present around locations of control point due to the movement of these artefacts; and not the material itself.

In Figure 5.35, the overview of cave progression test 4 can be given in terms of defined contour plots illustrating the progression of these strains in the model. Even though some material was crushed during swing-up, strains can be still be identified similarly to those found in test 3 where in both cases vertical strain bands formed outside the transition lines (fractures which define shear movement). This comparison can be observed in Figure 5.36.



Figure 5.33: Step 3 of test 4 — superimposed contour plot.

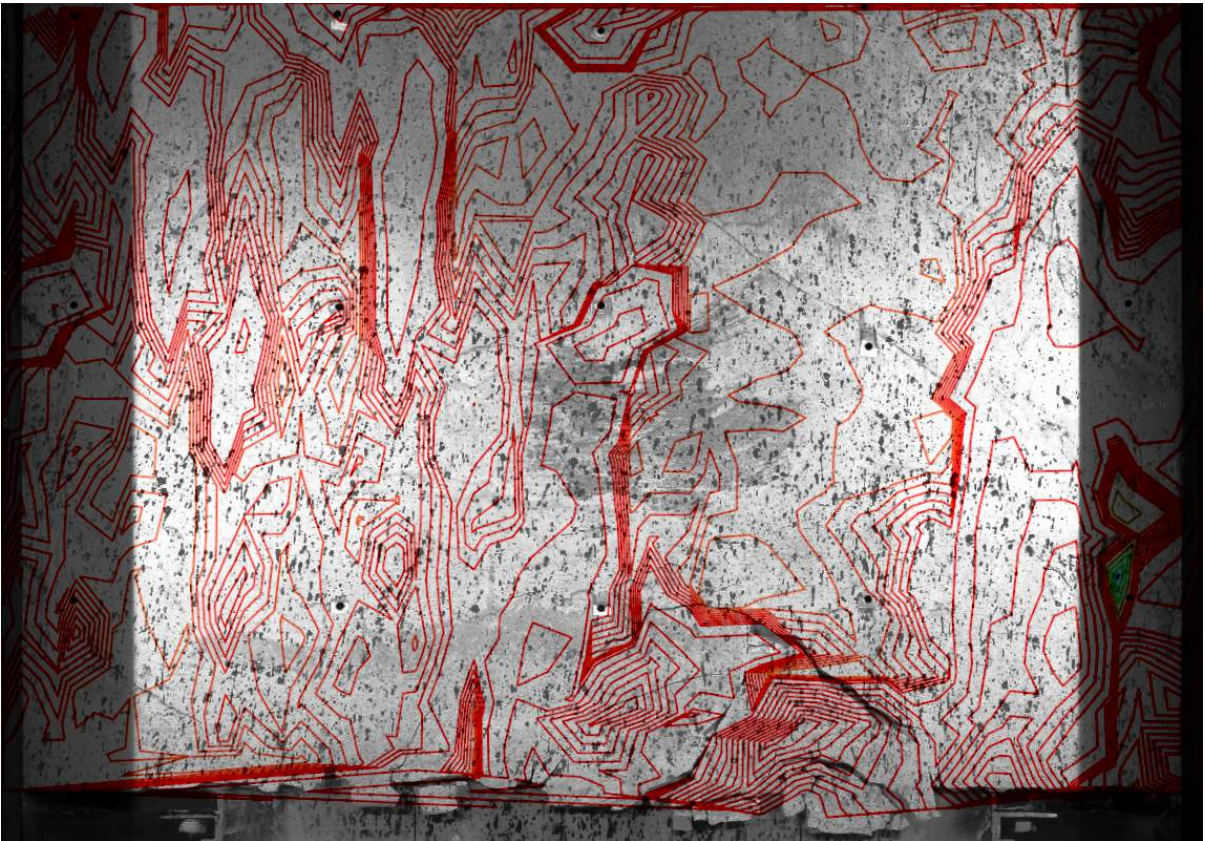


Figure 5.34: Step 4 of test 4 — superimposed contour plot.

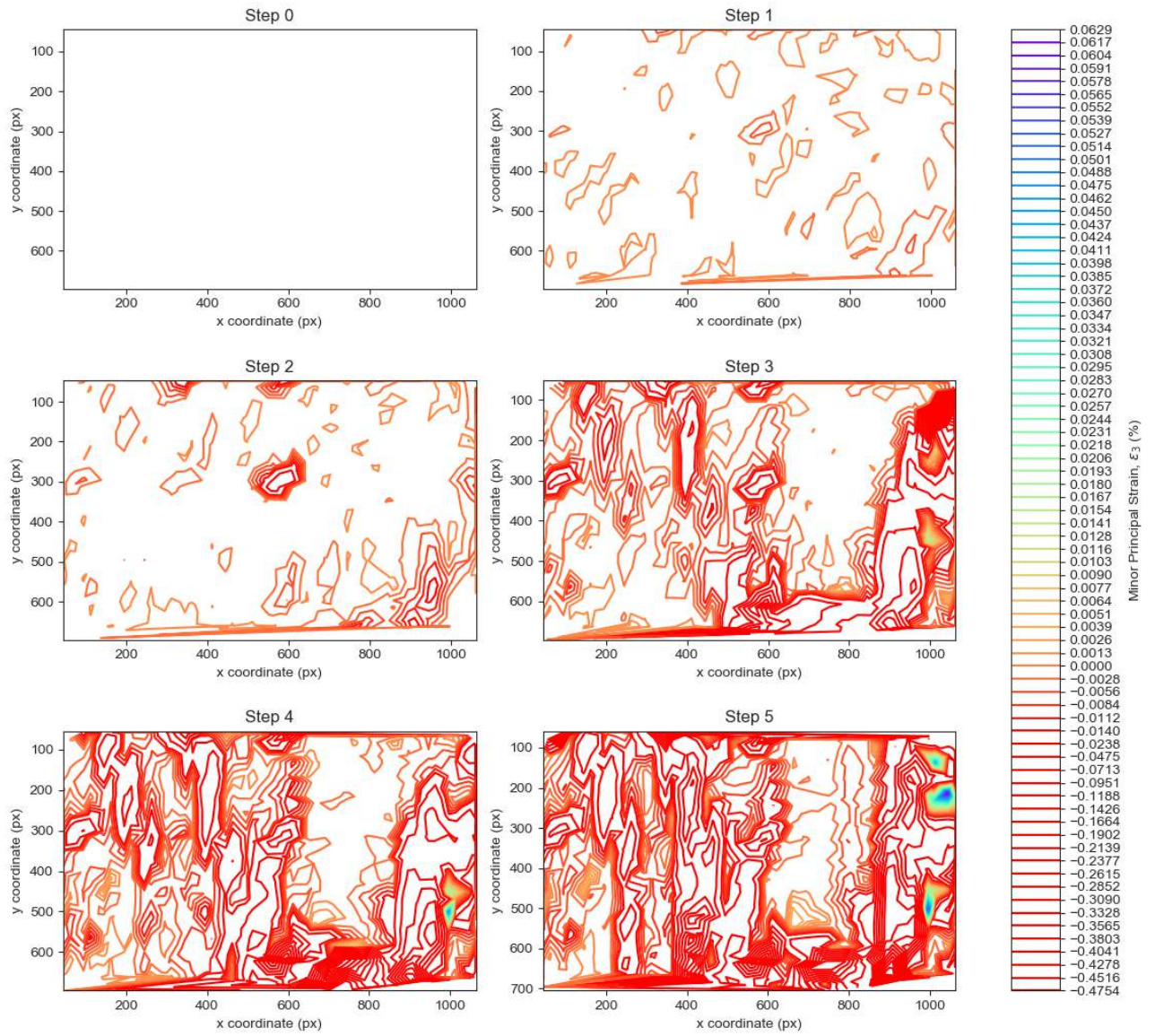


Figure 5.35: Cave progression overview of strain contours — test 4.

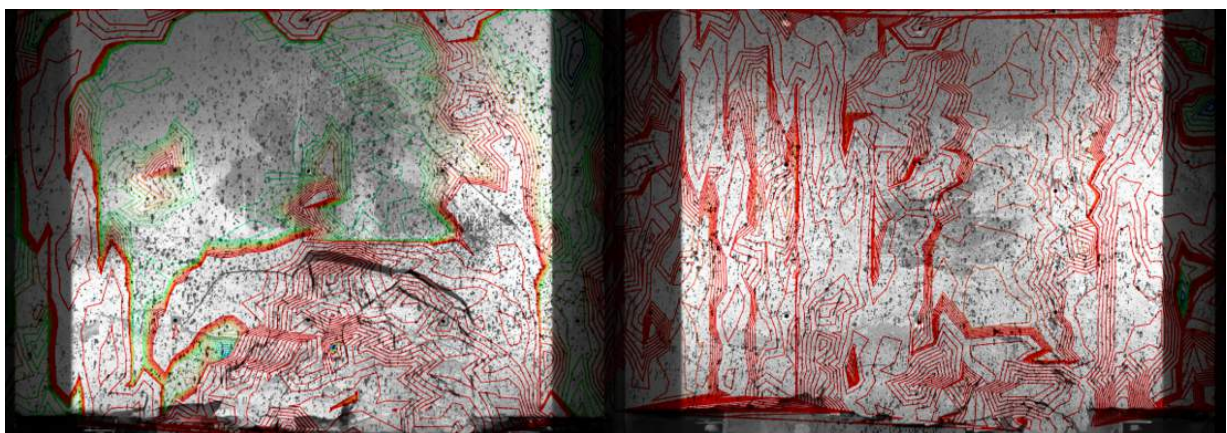


Figure 5.36: Test 3 (left) and test 4 (right) comparison at step 5.

5.3.4 Summary of Discussion

In terms of the results pertaining to cave progression geometry, the parameters of caved perimeter and caved area were similar in identifying the trend that at higher horizontal confinement (larger K values), the perimeter of the caved zone and particularly the caved area increased at a rate more rapid than under lower lateral confinement conditions. Conversely, tests that were conducted at smaller K values, take on slopes that are initially gradual due to the lack of horizontal confinement but steepen upon the cave-back reaching a certain height.

Combining the parameters of caved perimeter and caved area into caved hydraulic radius, the trend mentioned above still holds; however, it is less useful when identified in steps 1 to 2. Gradient values (particularly in Step 2 and onward) show that at higher degrees of horizontal to vertical stress, hydraulic radii increase at higher rates than in conditions of lower horizontal to vertical stress ratios. Test 1 to 4 yielded gradients of 19.18, 20.62, 14.86 and 15.97 between Steps 1 and 2, respectively. What still stands out is the point of subsidence in test 4.

Regarding the plot of cave height and width in Figure 5.17, the same trend can be identified even more explicitly by the changes in gradients of the lines at relevant steps of the caving progression. Finally, focusing on the data points when plotting the K of tests 1, 2 and 3 against the H/B ratio acquired at each step of the test, the trend can once again be seen. Lower K values result in H/B ratios that are initially low but grow rapidly in subsequent steps compared to those subjected to higher K values (i.e. more horizontal confinement). Larger K values result in H/B ratios that are initially higher but whose growth is less rapid and possibly stalling. Thus, it seemed that high lateral stress ratios were more prone to stalling since the lateral earth pressures effectively supported the arch.

From what was observed in test 1, the critical extensional strains were mapped around the perimeter of the cave-back clearly defining the area of cracks where the absolute critical value was exceeded. From step 2 onwards, strains are observed to exceed the critical value at the point where crack propagation takes places — providing relevance that the chosen strain criterion is valuable for detecting cracks within the model, thereby highlighting the tensile failure of the material. In test 2, cracks propagated as tensile strains reached the critical value; and on closer inspection seemed to have reached pre-existing fractures within the model. Strains were once again mapped around clearly defined fractures with red zones rendered where cracks had formed. In steps 2 and 3, the outermost critical strains were seen to overlap with the cave-back in certain positions. Test 3 revealed strains exceeding their critical values from the start of crack propagation in large zones which were bisected by these fractures. No gaps of non-critical strain contours were

observed which was different from that of tests 1 and 2. Transition lines formed to allow for subsidence in step 5 where strains outside of these lines were also clearly detected as critical. In test 4, fractures propagated to pre-existing ones when critical values were reached very early (in step 2) due to crushed material at the bottom of the sample from excessive overburden stresses. Subsidence looked to start on the right side of the sample and rapidly formed in step 3 of the caving progression test.

The method of superposition of strain contours on identified cracks using image analysis has allowed for the identification of tensile failure within the experimental models. In all tests, the observations seem to correspond well with the mode of cave mining failure identified by Cumming-Potvin (2018). The notion of ‘parallel fracturing’ and ‘gravity caving’ seem to be prominent in the four cases of centrifuge test results; and the identified tensile strains exceeding the critical extensional strain value for artificial material used, seemed adequate in estimating when and where crack propagation would occur. Both extreme cases of tests 1 and 2 with K values 0.50 and 0.94, respectively, show promise in the failure mechanism of parallel fracturing as a cave mechanics concept. Both tests 3 and 4, although having a K value within the extremes, demonstrated parallel fracturing (extensional failure) at steps before and after the event of subsidence.

6 Conclusions and Recommendations

The industry-accepted Duplancic model (Duplancic, 2001) and the Extended Conceptual Model for Caving Mechanics (Cumming-Potvin, 2018) are valuable postulations in quantifying the formation of cave mining propagation phenomena; however, the mechanism in which cave mining propagation occurs is still reliant on the in-situ stresses within the pre-caving rock-mass. These stresses, inferred by the horizontal to vertical stress ratio, are one such governing factor in influencing cave-back geometry and mapping cave mining propagation.

The research presented in this dissertation emphasises the effect of stress state and orientation on cave mining propagation which is location-specific. The results of this investigation are concluded in this section with respect to the applicability of the artificial rock-material, cave geometry and lateral earth pressure, as well as the mapping of critical extensional strain relative to caving events. Limitations of the study as well as recommendations for future research are highlighted at the end of this chapter.

6.1 Conclusions

The conclusions are presented in sections which aim to address the individual objectives originally established in Section 1.2.

6.1.1 Applicability of the Artificial Rock Material

The rock material provided adequate resemblance to the properties of rock, thus it can be concluded that ‘fracture banding’ can be said to occur for a material that is brittle and fragments like rock. In Chapter 2, typical rock properties were given for various rock types, and in Chapter 3, the artificial rock material was characterised using geotechnical laboratory testing to gain insight into the material properties. The following conclusions can be reported as to the suitability of the artificial rock material in replicating the characteristics of rock found in cave mines:

- The range of scale factors used in this experiment with regard to the artificial rock material is of the order of 12–9 291 when taking into account the evaluated critical extensional strain value of -0.014 %. Although the original scale factor range was quite variable, it does cater for a range of rock types and was curtailed upon the introduction of the critical extensional strain parameter; thereby highlighting its significance.

- The artificial rock material has a tensile to compressive strength ratio of 8.46 which is in the range of most rocks, and conforms to the ratio assumed from Griffith's theory of fracture.
- The artificial rock material has a porosity slightly higher than that of shale and shows similar visual qualities of blockiness upon break-up. Thus, the artificial rock material could be regarded to imitate clastic rock types since it shows similar rock-like fragmentation.
- The artificial rock material fails in uniaxial compression at a strain between 0.25 % and 0.36 %, which correlates well to failure strain of underground rock (especially Indiana limestone and shale). This is a good comparison with concrete (which has an assumed failure strain of 0.30–0.35 %) and for this reason the artificial rock material can be seen to exhibit brittleness.
- The Poisson's ratio of the artificial rock material compares well with most rock-types.

In light of the extensional mode of failure proposed by Cumming-Potvin, all tests conducted in this investigation can be noted to have failed in this failure mechanism for the various stress states experienced by samples. It can therefore be shown that the extensional failure mechanism (i.e. 'fracture banding') is applicable for a more brittle, rock-like artificial rock material.

6.1.2 Cave Geometry and Lateral Earth Pressure

Firstly, it should re-iterated that the failure mechanisms for all caving progression tests seemed to have followed the nature of tensile failure which implies a gravity type caving failure. Test 1, having the lowest K value, resulted in the most linear response when plotting the cave perimeter and hydraulic radius against undercutting steps 0 to 5. The proposed reason for this was that the lack of confinement could have caused the most natural environment for gravity caving to occur. Test 2 showed the lowest resulting cave-back profile in latter cave progression steps (3–5) and resulted in a cave stall (having the highest K value).

In step 2 of test 2; however, cave formation was the most rapid owing to the high probability of tension build up early on in the test. Test 3, similarly to test 1, was observed to propagate laterally before subsiding and causing break-through to the top surface. Subsidence occurred earlier in test 3 than in test 1 due to the higher overburden stresses. Test 4 clearly showed early subsidence due to the UCS strength of the artificial rock material being exceeded by the applied stress at 80 g. Material crushing was applicable in this test and although not much geometry could be observed with regard to the cave-back,

the geometry plots still indicate that subsidence occurred early on in the test. From the trends observed with regard to plotting the geometry parameters against the cave progression steps 1 to 5, it was concluded that higher K values result in gradient curves that are initially steep and tend to flatten off when the cave-back advances. Whereas smaller K values take on slopes that are initially flat due to the lack of horizontal confinement; but however, steepen upon the cave-back reaching a certain height. This behaviour is noticed particularly in tests 1, 2 and 3 with a K value of 0.50, 0.94 and 0.69, respectively. Like the gradients, the same trend is identified when plotting the H/B ratios at different cave progression steps against the K values of tests.

6.1.3 Critical Extensional Strain in Mapping Cave Propagation

As mentioned in Section 6.1.2, the experimental models were proposed to have failed in a gravity caving mechanism which implies the mobilisation of tension failure within the sample. Evidence of this is applicable when superimposing canny-edge binary images (from which fractures can be identified) with surface plots where zones of tensile strains are present. As presented in Chapter 5, an alternative superposition of the high-contrast photographs with strain contours also revealed the location of cracks relative to zones of tensile strains. From utilising the simple model of Critical Extensional Strain (Stacey, 1981), it was manageable to identify areas from where cracks originated as well as at what point propagation took place. The value chosen and used in the analyses was estimated conservatively using the approaches of Section 3.6.3.

The propagation of the tensile strains could be tracked conveniently from the source and it could be identified that strains formed outside the cracks which propagated upwards toward the surface upon the occurrence of subsidence. In all test cases, cracks propagated at the point of the material exceeding the absolute critical value of 0.014 % in either new fractures via cave-back progression or reaching pre-existing fractures. In most cases, the regions of tensile strains were observed to have been bisected by visual fractures in samples and from the results it was indicative that extensional strains were exceeded upon formation of the cracks. This suggests that cave failure was tensile. The utilisation of minor principal strains in the models also exhibited, in some cases, that the outermost tensile strain contours approximately coincided with the advancing cave-back. Critical strains were observed to have converged from the source of where undercutting began. Lastly, subsidence was detected and identified through strain contours.

A short summary of the tests can be given to make specific conclusions with regard to the four experiments conducted in this investigation. From the test 1 ($K = 0.50$), mapping of critical strains were easily made around the cave perimeter, showing that the crack propagation was expected since the strains exceeded their critical value. In test 2

($K = 0.94$), cracks propagated as tensile strains reached the critical value; and on closer inspection seemed to have reached pre-existing fractures within the model. Strains were once again mapped around clearly defined fractures with red zones rendered where cracks had formed. Strains were once again mapped around clearly defined fractures with red zones rendered after cracks had formed. Test 3 ($K = 0.69$) revealed strains exceeding their critical values from the start of crack propagation in large zones which were bisected by these fractures. Test 4 ($K = 0.69$) saw fractures propagate to pre-existing ones when critical values were reached very early in the test due to crushed material at the bottom of the sample from excessive overburden stresses.

6.2 Recommendations

Recommendations for conducting future research include:

- Once the water bladders had exerted enough pressure on the sample and cave propagation had occurred, the relaxation of the water bladders was not representative of the constant horizontal stresses that exists in real cave mines. Future research concerning a remedy for this problem would be valuable.
- Utilising various other procedures for undercutting under different stress state conditions.
- Unfortunately, due to the strength and brittleness of the material used in this study, K ratios of more than 1 could not be reached at the bottom of samples. It should be noted since the K values used in this investigation are slightly less than that which was specified based on literature. Future work to improve the artificial rock material still needs to be conducted in order to exert larger stresses on samples, thus obtaining higher K ratios. This could be done by using a tungsten based heavy-liquid as confinement in the bladders during centrifuge testing.
- A method of carefully transporting samples to the centrifuge without any damage was a challenging task. Special attention should be given to this process to orchestrate the transition whilst rendering the samples unfractured.
- A technique of reducing the porosity of the artificial rock material would be valuable in future research.
- A material that accounts for all rock types existing in one model — since the artificial rock material in this investigation mostly accounted for sedimentary rock type characteristics.

References

- Adrian, R.J. (1984). ‘Scattering particle characteristics and their effect on pulsed laser measurements of fluid flow: speckle velocimetry vs particle image velocimetry’. In: *Applied Optics*. Vol. 23. 11. Optical Society of America, pp. 1690–1691.
- Aghamelu, O.P., Nnabo, P.N. and Ezeh, H.N. (2011). ‘Geotechnical and environmental problems related to shales in the Abakaliki area, southeastern Nigeria’. In: *African Journal of Environmental Science and Technology*. Vol. 5. 2. Academic Journals, pp. 80–88.
- ASTM (2008). *Standard test method for splitting tensile strength of intact rock core specimens*. D 3967-08. ASTM International, West Conshohocken, USA.
- Attewell, P.B. and Farmer, I.W. (1988). *Principles of Engineering Geology*, pp. 217–249.
- Bandis, S., Lumsden, A. and Barton, N. (1983). ‘Fundamentals of rock joint deformation’. In: *International Journal of Rock Mechanics and Mining Sciences* 20.6, pp. 249–268.
- Barla, G., Boshkov, S. and Pariseau, W. (1980). ‘Numerical modeling of block caving at the Grace Mine’. In: *Geomechanics Applications in Underground Hardrock Mining, Turyn, Włochy*, pp. 241–256.
- Barton, N. (1968). *Private communication from Barton to Stimpson before ‘Modelling Materials for Engineering Rock Mechanics’ was published*. Imperial College of Science and Technology, London.
- Barton, N. (1976). ‘The shear strength of rock and rock joints’. In: *International Journal of Rock Mechanics and Mining Sciences and Geomechanics Abstracts*. Vol. 13. 9. Elsevier, pp. 255–279.
- Barton, N. (2002). ‘Some new Q-value correlations to assist in site characterisation and tunnel design’. In: *International Journal of Rock Mechanics and Mining Sciences* 39.2, pp. 185–216.
- Baumgartner, P. and Stimpson, B. (1979). ‘Development of a tiltable base friction frame for kinematic studies of caving at various depths’. In: *International Journal of Rock Mechanics and Mining Sciences & Geomechanics Abstracts*. Vol. 16. 4. Elsevier, pp. 265–267.
- Benito, C. (1968). ‘Essais Comparatifs pour le Choix d’une Forme Résistante’. In: *Proceedings of the Symposium on Shell Research, Delft*, pp. 282–286.

- Benz, T., Schwab, R., Kauther, R.A. and Vermeer, P.A. (2008). 'A Hoek-Brown criterion with intrinsic material strength factorization'. In: *International Journal of Rock Mechanics and Mining Sciences*. Vol. 45. 2. Elsevier, pp. 210–222.
- Bewick, R.P., Kaiser, P.K. and Valley, B. (2011). 'Interpretation of triaxial testing data for estimation of the Hoek-Brown strength parameter m_i '. In: *45th US Rock Mechanics/Geomechanics Symposium*. American Rock Mechanics Association.
- Bieniawski, Z.T. (1976). 'Rock mass classification of jointed rock masses'. In: *Exploration for Rock Engineering*. Vol. 97. Balkema, Johannesburg, p. 106.
- Bieniawski, Z.T. (1978). 'Determining rock mass deformability: experience from case histories'. In: *International Journal of Rock Mechanics and Mining Sciences and Geomechanics Abstracts*. Vol. 15. 5. Elsevier, pp. 237–247.
- Biswas, R. and Sil, J. (2012). 'An improved canny edge detection algorithm based on type-2 fuzzy sets'. In: *Procedia Technology*. Vol. 4. Elsevier, pp. 820–824.
- Brace, N.F., Voegle, M. and Pratt, H. (1982). *Porosity, Permeability, and their Relationship in Granite, Basalt, and Tuff*. Tech. rep. ONWI/E512-02900/TR-10, report prepared for Office of Nuclear Waste Isolation. Battelle Memorial Institute, Columbus, Ohio.
- Brady, B.H.G. and Brown, E.T. (2006). 'Rock Mechanics for underground mining'. In: *Springer, Netherlands*, pp. xviii, 626.
- Bray, J.W., Brown, E.T., Ladanyi, B. and Hoek, E. (1983). 'Ground response curves for rock tunnels'. In: *Journal of Geotechnical Engineering*. Vol. 109. 1. American Society of Civil Engineers, pp. 15–39.
- Briševac, Z., Kujundžić, T. and Čajić, S. (2015). 'Current cognition of rock tensile strength testing by Brazilian test'. In: *Rudarsko-Geološko-Naftni Zbornik* 30.2, pp. 101–114.
- Brock, G.C. (1959). *Direct models as an aid to reinforced concrete design*. Vol. 187. 4857. Engineering, London, pp. 468–470.
- Brock, G.C. (1960). *Effect of shear on ultimate strength of rectangular beams with tensile reinforcements*. Vol. 31. American Concrete Institute, pp. 619–638.
- Brock, G.C. (1964). 'Predicting the Plasticity of Reinforced Concrete Shell Structures by Model Experiment'. In: *Proceedings of the Symposium on Non-classical Shell Problems*, Warsaw, pp. 1101–1110.
- Brock, G.C. (1968). *Reinforced plaster models for bridge structures*. Vol. 36. Highway Public Works, pp. 6–10.

- Broekman, A., Jacobsz, S.W., Louw, H., Kearsley, E.P., Gaspar, T.A.V. and Da Silva Burke, T.S. (2020). ‘Fly-by-Pi: Open source closed-loop control for geotechnical centrifuge testing applications’. In: *Hardware X 8, Elsevier*.
- Brown, E. (2003). ‘Block caving geomechanics (International Caving Study I, 1997–2000)’. In: *University of Queensland, JKMRRC monograph series in mining and mineral processing, Brisbane*.
- Brown, E.T. (2007). *Block caving geomechanics: International Caving Study 1997-2004*. English. 2nd ed. Indooroopilly, Qld. Julius Kruttschnitt Mineral Research Centre, The University of Queensland. ISBN: 9780980362206.
- Brown, E.T. and Trollope, D.H. (1970). ‘Strength of a model of jointed rock’. In: *Journal of Soil Mechanics; Foundations Division ASCE* 96.2, pp. 685–704.
- BS:1881 (1983). *Testing Concrete. Method for determination of Compressive Strength of Concrete cubes*. Part 166. British Standards Institute. London, United Kingdom.
- Buckingham, E. (1914). ‘On physically similar systems; illustrations of the use of dimensional equations’. In: *Physical Review, APS* 4.4, p. 345.
- Canny, J. (1986). ‘A computational approach to edge detection’. In: *IEEE Transactions on pattern analysis and machine intelligence* 6, pp. 679–698.
- Carlson, G. and Golden Jr, R. (2008). ‘Initiation, Growth, Monitoring and Management of the 7210 Cave at Henderson Mine—A Case Study’. In: *5th International Conference and Exhibition on Mass Mining*. Vol. 9. University of Technology Press, Lulea, Sweden, pp. 97–106.
- Castro, R., Trueman, R. and Halim, A. (2007). ‘A study of isolated draw zones in block caving mines by means of a large 3D physical model’. In: *International Journal of Rock Mechanics and Mining Sciences* 44.6, pp. 860–870.
- Chen, Y.F., Wei, K., Liu, W., Hu, S.H., Hu, R. and Zhou, C.B. (2016). ‘Experimental characterization and micromechanical modelling of anisotropic slates’. In: *Rock Mechanics and Rock Engineering*. Vol. 49. 9. Springer, pp. 3541–3557.
- Christensen, N.I. (1996). ‘Poisson’s ratio and crustal seismology’. In: *Journal of Geophysical Research: Solid Earth*. Vol. 101. B2. Wiley Online Library, pp. 3139–3156.
- Chuanliang, Y., Jingen, D., Lianbo, H., Zijian, C., Xinjiang, Y., Hai, L., Qiang, T. and Baohua, Y. (2015). ‘Brittle failure of shale under uniaxial compression’. In: *Arabian Journal of Geosciences*. Vol. 8. 5. Springer, pp. 2467–2475.

- Clough, G., Sitar, N., Bachus, R. and Rad, N. (1981). 'Cemented sands under static loading'. In: *Journal of Geotechnical and Geo-environmental Engineering*. Vol. 107. ASCE 16319 Proceeding.
- Collins, B. and Sitar, N. (2009). 'Geotechnical properties of cemented sands in steep slopes'. In: *Journal of Geotechnical and Geo-environmental Engineering*. Vol. 135. 10. American Society of Civil Engineers, pp. 1359–1366.
- Colmenares, L.B. and Zoback, M.D. (2002). 'A statistical evaluation of intact rock failure criteria constrained by polyaxial test data for five different rocks'. In: *International Journal of Rock Mechanics and Mining Sciences*. Vol. 39. 6. Elsevier, pp. 695–729.
- Cumming-Potvin, D. (2018). 'An Extended Conceptual Model of Caving Mechanics'. PhD thesis. The University of Western Australia, Perth.
- Cumming-Potvin, D., Wesseloo, J., Jacobsz, S.W. and Kearsley, E.P. (2016a). 'Fracture banding in caving mines'. In: *Journal of the Southern African Institute of Mining and Metallurgy*. Vol. 116. 8. The Southern African Institute of Mining and Metallurgy, pp. 753–761.
- Cumming-Potvin, D., Wesseloo, J., Jacobsz, S.W. and Kearsley, E.P. (2016b). 'Results from physical models of block caving'. In: *7th International Conference & Exhibition on Mass Mining (MassMin 2016), 9-11 May 2016, Sydney, New South Wales, Australia*. Australasian Institute of Mining and Metallurgy, pp. 329–340.
- Das, B., Yen, S. and Dass, R. (1995). 'Brazilian tensile strength test of lightly cemented sand'. In: *Canadian Geotechnical Journal*. Vol. 32. 1. NRC Research Press, pp. 166–171.
- Davidovits, J. (2008). *Geopolymer Chemistry and Applications*. 2nd ed. Saint Quentin: Geopolymer Institute, pp. 131–145.
- De Nicola Escobar, R. and Fishwick Tapia, M. (2000). 'An underground airblast–CODELCO Chile–Division Salvador'. In: *Proceedings of MassMin 2000*, pp. 173–178.
- Deere, D.U. (1968). *Rock mechanics in engineering practice*. Technical Report No. AWWL-TR-116. Air Force Weapons Laboratory Kirtland Air Force Base, New Mexico.
- Diederichs, M. (2007). 'The 2003 Canadian Geotechnical Colloquium: Mechanistic interpretation and practical application of damage and spalling prediction criteria for deep tunnelling'. In: *Canadian Geotechnical Journal*. Vol. 44. 9. NRC Research Press, pp. 1082–1116.

- Diering, J. and Laubscher, D. (1986). 'Practical approach to the numerical stress analysis of mass mining operations'. In: *Mining Latin America*. Springer, pp. 87–99.
- Dinsdale, A. (1986). 'Pottery Science: Materials, process and products'. In: *Ellis Horwood Limited*, pp. 137–143.
- Duplancic, P. (2001). 'Characterisation of caving mechanisms through analysis of stress and seismicity'. PhD thesis. University of Western Australia, Perth.
- Duplancic, P. and Brady, B. (1999). 'Characterisation of caving mechanisms by analysis of seismicity and rock stress'. In: *9th ISRM Congress*. International Society for Rock Mechanics and Rock Engineering.
- Durelli, A.J. and Jacobsen, R.H. (1962). *Brittle material failure as indicators of stress concentration factors*. Int. J. Rock Mech. Min. Sci. 3, pp. 65–74.
- Dusseault, M. and Morgenstern, N. (1979). 'Locked sands'. In: *Quarterly Journal of Engineering Geology and Hydrogeology*. Vol. 12. 2. Geological Society of London, pp. 117–131.
- Fairhurst, C. (1964). 'On the validity of the 'Brazilian' test for brittle materials'. In: *International Journal of Rock Mechanics and Mining Sciences* 1.4, pp. 535–546.
- Farmer, I.W. (2012). *Engineering behaviour of rocks*. Springer Science and Business Media.
- Gaspar, T.A.V. (2017). 'Investigating the tensile behaviour of unsaturated soils using the Brazilian disc test'. MA thesis. University of Pretoria.
- Gaudin, C., Randolph, M. and O'Loughlin, C. (2006). 'New insights from model tests of foundation and anchoring systems in offshore geomechanics'. In: *Proc. 6th Int. Conf. on Physical Modelling in Geotechnics*. Vol. 1, pp. 47–62.
- Gercek, H. (2007). 'Poisson's ratio values for rocks'. In: *International Journal of Rock Mechanics and Mining Sciences*. Vol. 44. 1. Elsevier, pp. 1–13.
- Goodman, R.E. (1989). *Introduction to Rock Mechanics*. Vol. 2. Wiley New York, pp. 57–100.
- Gramberg, J. (1965). 'The axial cleavage fracture 1 Axial cleavage fracturing, a significant process in mining and geology'. In: *Engineering Geology*. Vol. 1. 1. Elsevier, pp. 31–72.
- Griffith, A.A. (1920). 'The phenomena of rupture and flow in solids'. In: *Philosophical Transactions of the Royal Society of London. Series A, containing papers of a mathematical or physical character*. Vol. 221. 582-593. The Royal Society London, pp. 163–198.

- Hajiabdolmajid, V., Kaiser, P. and Martin, C. (2002). 'Modelling brittle failure of rock'. In: *International Journal of Rock Mechanics and Mining Sciences*. Vol. 39. 6. Elsevier, pp. 731–741.
- Handin, J., Heard, H.C. and Magouirk, J.N. (1967). 'Effects of the intermediate principal stress on the failure of limestone, dolomite, and glass at different temperatures and strain rates'. In: *Journal of Geophysical Research*. Vol. 72. 2. Wiley Online Library, pp. 611–640.
- Hatheway, A.W. and Kiersch, G.A. (1986). 'Engineering properties of rocks'. In: *Carmichael RS, editor. Handbook of physical properties of rocks and minerals*. Vol. 2. CRC Press, pp. 289–331.
- Heah, C.Y., Kamarudin, H., Mustafa Al Bakri, A.M., Binhussain, M., Luqman, M., Khairul Nizar, I., Ruzaidi, C.M. and Liew, Y.M. (2011). 'Effect of curing profile on kaolin-based geopolymers'. In: *Physics Procedia*. Vol. 22. Elsevier, pp. 305–311.
- Heah, C.Y., Kamarudin, H., Mustafa Al Bakri, A.M., Binhussain, M., Luqman, M., Khairul Nizar, I., Ruzaidi, C.M. and Liew, Y.M. (2012). 'Study on solids-to-liquid and alkaline activator ratios on kaolin-based geopolymers'. In: *Construction and Building Materials*. Vol. 35. Elsevier, pp. 912–922.
- Heslop, T. (1978). 'Rock Mechanics Aspects of Block Caving Chrysotile Asbestose Orebodies at Shabanie Mine, Rhodesia.' MA thesis. University Of Witwatersrand, Johannesburg, South Africa.
- Hillis, R.R., Enever, J.R. and Reynolds, S.D. (1999). 'In situ stress field of eastern Australia'. In: *Australian Journal of Earth Sciences*. Vol. 46. 5. Taylor & Francis, pp. 813–825.
- Hobbs, D.W. (1966). 'Scale model studies of strata movement around mine roadways. Apparatus, technique and some preliminary results'. In: *International Journal of Rock Mechanics and Mining Science* 3, pp. 101–127.
- Hoek, E. (1965a). 'Rock fracture under Static Stress Conditions'. In: *Council for Science and Industrial Research*. National Mechanical Engineering Research Institute, pp. 1–237.
- Hoek, E. (1965b). 'The design of a centrifuge for the simulation of gravitational force fields in mine models'. In: *Journal of the Southern African Institute of Mining and Metallurgy*. Vol. 65. 9. Southern African Institute of Mining and Metallurgy, pp. 455–487.

- Hoek, E. (1968). 'Brittle fracture of rock'. In: *Rock Mechanics in Engineering Practice*. Vol. 130. John Wiley and Sons, Inc., London, England, pp. 9–124.
- Hoek, E. (1983). 'Strength of jointed rock masses'. In: *Geotechnique*. Vol. 33. 3. Thomas Telford Ltd, pp. 187–223.
- Hoek, E. and Brown, E.T. (1980). *Underground Excavations in Rock*. London: Institution of Mining and Metallurgy.
- Hoek, E. and Brown, E.T. (2019). 'The Hoek–Brown failure criterion and GSI – 2018 edition'. In: *Journal of Rock Mechanics and Geotechnical Engineering*. Vol. 11. 3. Elsevier Ltd, pp. 445–463.
- Hoek, E., Carranza-Torres, C. and Corkum, B. (2002). 'Hoek-Brown failure criterion-2002 edition'. In: *Proceedings of NARMS-Tac*. Vol. 1. 1. TAC Conference Toronto, pp. 267–273.
- Hoek, E. and Diederichs, M. (2006). 'Empirical estimation of rock mass modulus'. In: *International Journal of Rock Mechanics and Mining Sciences*. Vol. 43. 2. Elsevier, pp. 203–215.
- Hoek, E., Marinos, P. and Benissi, M. (1998). 'Applicability of the Geological Strength Index (GSI) classification for very weak and sheared rock masses. The case of the Athens Schist Formation'. In: *Bulletin of Engineering Geology and the Environment*. Vol. 57. 2. Springer, pp. 151–160.
- Hoek, E. and Martin, C.D. (2014). 'Fracture initiation and propagation in intact rock — a review.' In: *Journal of Rock Mechanics and Geotechnical Engineering*. 6, pp. 287–300.
- ISRM (1981). *Rock characterization, testing and monitoring - ISRM suggested methods*. Tech. rep. International Society for Rock Mechanics, Oxford, Pergamon.
- Ivars, D.M., Pierce, M.E., Darcel, C., Reyes-Montes, J., Potyondy, D.O., Young, P.R. and Cundall, P.A. (2011). 'The synthetic rock mass approach for jointed rock mass modelling'. In: *International Journal of Rock Mechanics and Mining Sciences* 48, pp. 211–244.
- Jacobsz, S.W., Kearsley, E.P., Cumming-Potvin, D. and Wesseloo, J. (2018). 'Modelling cave mining in the geotechnical centrifuge'. In: *Physical Modelling in Geotechnics*. Vol. 2. CRC Press, pp. 809–814.
- Jacobsz, S.W., Kearsley, E.P. and Kock, J.H.L. (2014). 'The geotechnical centrifuge facility at the University of Pretoria'. In: *Physical Modelling in Geotechnics*. Taylor & Francis Group, London. ISBN: 978-1-138-00152-7.

- Jaky, J. (1944). 'The coefficient of earth pressure at rest'. In: *Journal of the Society of Hungarian Architects and Engineers*, pp. 355–358.
- Karzulovic, A. and Flores, G. (2003). 'Geotechnical guidelines for a transition from open pit to underground mining'. In: *Report to International Caving Study*, pp. 421–434.
- Kirsten, H.A.D. and Klokow, J.W. (1979). 'Control of fracturing in mine rock passes'. In: *4th ISRM Congress*. International Society for Rock Mechanics and Rock Engineering.
- Knappett, J. and Craig, R. (2012). *Craig's soil mechanics*. CRC press.
- Kvapil, R. (1965). 'Gravity flow of granular materials in Hoppers and bins in mines—II. Coarse material'. In: *International Journal of Rock Mechanics and Mining Sciences and Geomechanics Abstracts*. Vol. 2. 3. Elsevier, pp. 277–292.
- Laubscher, D. (1975). 'Class distinction in rock masses.' In: *Pascal and Francis Bibliographic Databases*.
- Laubscher, D. (1990). 'A geomechanics classification system for the rating of rock mass in mine design'. In: *Journal of the Southern African Institute of Mining and Metallurgy*. Vol. 90. 10. Sabinet, pp. 257–273.
- Laubscher, D. (1994). 'Cave mining—the state of the art'. In: *Journal of The Southern African Institute of Mining and Metallurgy*. Vol. 94. 10. Sabinet, pp. 279–293.
- Lee, H. and Haimson, B.C. (2011). 'True triaxial strength, deformability, and brittle failure of granodiorite from the San Andreas Fault Observatory at Depth'. In: *International Journal of Rock Mechanics and Mining Sciences* 48.7, pp. 1199–1207.
- Li, A.J., Merifield, R.S. and Lyamin, A.V. (2008). 'Stability charts for rock slopes based on the Hoek-Brown failure criterion'. In: *International Journal of Rock Mechanics and Mining Sciences* 45, pp. 689–700.
- Li, D. and Wong, L. (2013). 'The Brazilian disc test for rock mechanics applications: review and new insights'. In: *Rock Mechanics and Rock Engineering*. Vol. 46. 2. Springer, pp. 269–287.
- Li, Z., Wang, L., Lu, Y., Li, W. and Wang, K. (2018). 'Experimental Investigation on the Deformation, Strength, and Acoustic Emission Characteristics of Sandstone under True Triaxial Compression'. In: *Advances in Materials Science and Engineering*. Vol. 2018. Article ID 5241386. Hindawi Publishing Corporation, pp. 1–16.
- Ljunggren, C., Stephansson, O., Alm, O., Hakami, H. and Mattila, U. (1985). *Mechanical properties of granitic rocks from Gideå, Sweden*. Tech. rep. Swedish Nuclear Fuel and Waste Management Co.

- Lorig, L., Board, M., Potyondy, D. and Coetzee, M. (1995). 'Numerical modelling of caving using continuum and micro-mechanical models'. In: *Proc. of CAMI'95 Canadian Conference on Computer Applications in the Mining Industry, Montreal, Quebec, Canada*, pp. 416–424.
- Lorig, L., Hart, R., Board, M. and Swan, G. (1989). 'Influence of discontinuity orientations and strength on cavability in a confined environment'. In: *The 30th US Symposium on Rock Mechanics (USRMS)*. American Rock Mechanics Association.
- Lye, A., Crook, G., Kolff van Oosterwijk, L. and Lewis, P.C. (2006). 'The discovery history of the Northparkes deposits'. In: *Mineral Exploration Geoscience in New South Wales*, pp. 21–25.
- Malik, A., Chakraborty, T. and Rao, K.S. (2018). 'Strain rate effect on the mechanical behavior of basalt: Observations from static and dynamic tests'. In: *Thin-Walled Structures*. Vol. 126. Elsevier, pp. 127–137.
- Marinos, P., Marinos, V. and Hoek, E. (2007). 'Geological Strength Index (GSI). A characterization tool for assessing engineering properties for rock masses'. In: *Proceedings of the Workshop (W1) on Underground Works under Special Conditions* January 2015, pp. 13–21.
- Mark, C.M. and Gadde, M.B. (2008). 'Global Trends in Coal Mine Horizontal Stress Measurements'. In: *27th International Conference Ground Control in Mining*, pp. 319–331.
- Martins, F., Ferreira, P., Flores, J., Bressani, L. and Bica, A. (2005). 'Interaction between geological and geotechnical investigations of a sandstone residual soil'. In: *Engineering Geology*. Vol. 78. 1-2. Elsevier, pp. 1–9.
- Mathews, K.E., Hoek, E., Wyllie, D.C. and Stewart, S. (1981). 'Prediction of stable excavation spans for mining at depths below 1000m in hard rock'. In: *Report No. DSS, Serial No. OSQ80-00081*.
- McNearney, R. and Abel Jr, J.F. (1993). 'Large-scale two-dimensional block caving model tests'. In: *International Journal of Rock Mechanics and Mining Sciences & Geomechanics Abstracts*. Vol. 30. 2. Elsevier, pp. 93–109.
- Meng, Y., Li, Z. and Lai, F. (2015). 'Experimental study on porosity and permeability of anthracite coal under different stresses'. In: *Journal of Petroleum Science and Engineering*. Vol. 133. Elsevier, pp. 810–817.

- Milne, D., Hadjigeorgiou, J. and Pakalnis, R. (1998). 'Rock mass characterization for underground hard rock mines'. In: *Tunnelling and underground space technology*. Vol. 13. 4. Elsevier, pp. 383–391.
- Mogi, K. (1966). 'Pressure dependence of rock strength and transition from brittle fracture to ductile flow'. In: *Bulletin Earthquake Research Institute* 32, pp. 44–215.
- Nemcik, J., Gale, W. and Mills, K. (2005). 'Statistical Analysis of Underground Stress Measurements in Australian Coal Mines.' In: *Proceedings of the Bowen Basin Symposium*, pp. 117–122.
- Nieuwoudt, A.P.C. and Rozendaal, A. (1990). 'In situ stress determinations in mines located in two major structural domains in South Africa'. In: *ISRM International Symposium*. International Society for Rock Mechanics and Rock Engineering.
- Nishida, T., Esaki, T. and Kameda, N. (1988). 'A development of the base friction technique and its application to subsidence engineering'. In: *Proceedings of the International Symposium on Engineering in Complex Rock Formations*. Elsevier, pp. 386–392.
- Okoye, F.N., Durgaprasad, J. and Singh, N.B. (2015). 'Mechanical properties of alkali activated Fly Ash/Kaolin based geopolymer concrete'. In: *Construction and Building Materials*. Vol. 98. Elsevier, pp. 685–691.
- Okubo, S., Fukui, K. and Qingxin, Q. (2006). 'Uniaxial compression and tension tests of anthracite and loading rate dependence of peak strength'. In: *International Journal of Coal Geology*. Vol. 68. 3-4. Elsevier, pp. 196–204.
- Palma, R. and Agarwal, R. (1973). *A study of the cavability of primary ore at the El Teniente Mine*. Technical Report from Colombia University, New York.
- Pancini, M. (1961). *Results of the first series of tests performed on a model reproducing the actual structure of the abutment of the Vaiont Dam*. *Geologie Bauwes.* 27, pp. 105–119.
- Panek, L.A. (1981). 'Ground movements near a caving stope'. In: *Stewart, D. (ed.). Proceedings of the International Conference on Caving and Sublevel Stopping: Design and Operation of Caving and Sublevel Stopping Mines*. Society of Mining Engineers of the American Institute of Mining, Metallurgical, and Petroleum Engineers, New York, USA, pp. 329–354.
- Panek, L.A. (1984). 'Subsidence in undercut-cave operations, subsidence resulting from limited extraction of two neighbouring-cave operations'. In: *Geomechanical Applica-*

- tions in Hard Rock Mining*. Department of Mining Engineering, Michigan Technological University, Houghton, Michigan, pp. 225–240.
- Paredas, P.S. and Pineda, M.F. (2014). ‘An analysis of the lateral dilution entry mechanisms in panel caving’. In: *Proceedings of Third International Symposium on Block and Sub-level Caving*. Vol. 3. Universidad de Chile: Santiago, pp. 118–127.
- Parry, R. (2004). *Mohr circles, stress paths and geotechnics*. CRC Press.
- Patton, F.D. (1966). ‘Multiple Modes of Shear Failure in Rock and Related Materials’. PhD thesis. University of Illinois.
- Perras, M. and Diederichs, M. (2014). ‘A review of the tensile strength of rock: concepts and testing’. In: *Geotechnical and Geological Engineering*. Vol. 32. 2. Springer, pp. 525–546.
- Pickering, C.J.D. and Halliwell, N.A. (1984). ‘Speckle photography in fluid flows: signal recovery with two-step processing’. In: *Applied Optics*. Vol. 23. 8. Optical Society of America, pp. 1128–1129.
- Pierce, M.E., Cundall, P.A., Ivars, D.M., Darcel, C., Young, R., Reyes-Montes, J. and Pettitt, W. (2006). *Mass Mining Technology Project: Six Monthly Technical Report, Caving Mechanics, Sub-Project No. 4.2: Research and Methodology Improvement, and Sub-Project 4.3, Case Study Application*. Tech. rep. ICG06-2292-1-Tasks 2-3-14, Itasca Consulting Group, Inc., Minneapolis.
- Pratt, H.R., Black, A.D., Brown, W.S. and Brace, W.F. (1972). ‘The effect of specimen size on the mechanical properties of unjointed diorite’. In: *International Journal of Rock Mechanics and Mining Sciences and Geomechanics Abstract* 9.5, pp. 513–529.
- Rahn, P.H. (1996). ‘Engineering Geology, An Environmental Approach’. In: *Environmental and Engineering Geoscience*. Prentice Hall, Inc., Upper Saddle River, N.J.
- Ramsey, J.M. and Chester, F.M. (2004). ‘Hybrid fracture and the transition from extension fracture to shear fracture’. In: *Nature*. Vol. 428. 6978. Nature Publishing Group, pp. 63–66.
- Randolph, M. and Gourvenec, S. (2017). *Offshore geotechnical engineering*. CRC press.
- Rao, M.V.M.S., Prasanna Lakshmi, K.J., Nagaraja Rao, G.M., Vijayakumar, K. and Udayakumar, S. (2011). ‘Precursory microcracking and brittle failure of Latur basalt and migmatite gneiss under compressive loading’. In: *Current Science*. Vol. 101. 8, pp. 1053–1059.

- Razi, P.Z., Abdul, R., Hashim, A.R. and Khalid, N.H.A. (2016). 'Sustainability, eco-point and engineering performance of different workability OPC fly-ash mortar mixes'. In: *Materials*. Vol. 9. 5. Multidisciplinary Digital Publishing Institute, p. 341.
- Read, S., Perrin, N. and Richards, L. (1999). 'Applicability of the Hoek-Brown failure criterion to New Zealand greywacke rocks'. In: *9th ISRM Congress*. International Society for Rock Mechanics and Rock Engineering.
- Rech, W. and Lorig, L. (1992). 'Predictive numerical stress analysis of panel caving at the Henderson Mine'. In: *Proceedings of MASSMIN*. Vol. 92, pp. 55–62.
- Rodriguez-Sastre, M.A. and Calleja, L. (2006). 'The determination of elastic modulus of slates from ultrasonic velocity measurements'. In: *The Geological Society of London*. Vol. 775. IAEG, pp. 1–11.
- Rohatgi, A. (2020). *Webplottedigitizer: Version 4.4*. <https://automeris.io/WebPlotDigitizer>.
- Ros, H.C. and Eichinger, A. (1928). 'Experimental Attempt to Solve the Problem of Failure in Materials-Non-Metallic Materials'. In: *Federal Materials Testing Lab. ETH, Rept 28*.
- Sahouryeh, E., Dyskin, A.V. and Germanovich, L.N. (2002). 'Crack growth under biaxial compression'. In: *Engineering Fracture Mechanics*. Vol. 69. 18. Elsevier, pp. 2187–2198.
- Sainsbury, B.L. (2012). 'A Model for Cave Propagation and Subsidence Assessment in Jointed Rock Masses'. PhD thesis. The University of New South Wales, Sydney, pp. 1–300.
- Saucier, K.L. (1961). *Development of Material for Modelling Rock*. Paper 6-934. U.S. Army Waterways Experimental Station, Vicksburg, Mississippi, pp. 105–119.
- Schmertmann, J. and Osterberg, J. (1960). 'An experimental study of the development of cohesion and friction with axial strain in saturated cohesive soils'. In: *Research conference on shear strength of cohesive soils*. ASCE, pp. 643–694.
- Serafim, J.L. (1983). 'Consideration of the geomechanical classification of Bieniawski'. In: *Proceedings of the International Symposium on Engineering Geology and Underground Construction*. Vol. 1, pp. 33–44.
- Sharrock, G., Slade, N., Thin, I. and Duplancic, P. (2002). 'The prediction of stress induced caving on a mining abutment'. In: *Proceedings First International Seminar on Deep and High Stress Mining (Deep Mining 2002)*, pp. 6–8.
- Sheorey, P.R. (1997). *Empirical Rock Failure Criteria*. Rotterdam, Brookfield, VT: A.A. Balkema, Netherlands, pp. 1–200. ISBN: 9789054106708.

- Singh, M., Raj, A. and Singh, B. (2011). 'Modified Mohr–Coulomb criterion for non-linear triaxial and polyaxial strength of intact rocks'. In: *International Journal of Rock Mechanics and Mining Sciences*. Vol. 48. 4. Elsevier, pp. 546–555.
- Siratovich, P.A., Davidson, J., Villeneuve, M., Gravley, D., Kennedy, B., Cole, J., Wyring, L. and Price, L. (2012). 'Physical and mechanical properties of the Rotokawa Andesite from production wells RK 27_L2, RK28 and RK30'. In: *Proceedings, NZ Geothermal Workshop*.
- Sitar, N. and Clough, G. (1983). 'Seismic response of steep slopes in cemented soils'. In: *Journal of Geotechnical Engineering*. Vol. 109. 2. American Society of Civil Engineers, pp. 210–227.
- Stacey, T.R. (1981). 'A simple extension strain criterion for fracture of brittle rock'. In: *International Journal of Rock Mechanics and Mining Sciences & Geomechanics Abstracts*. Vol. 18. 6. Elsevier, pp. 469–474.
- Stacey, T.R. and De Jongh, C.L. (1977). 'Stress fracturing around a deep-level bored tunnel'. In: *Journal of the Southern African Institute of Mining and Metallurgy*. Vol. 78. 5. Sabinet, pp. 124–133.
- Stacey, T.R. and Wesseloo, J. (1998). 'In situ stresses in mining areas in South Africa'. In: *Journal of the Southern African Institute of Mining and Metallurgy*. Vol. 98. 7. Southern African Institute of Mining and Metallurgy, pp. 365–368.
- Stanier, S.A., Blaber, J., Take, W.A. and White, D.J. (2016). 'Improved image-based deformation measurement for geotechnical applications'. In: *Canadian Geotechnical Journal*. Vol. 53. 5. NRC Research Press, pp. 727–739.
- Stephens, R. and Banks, D. (1989). 'Moduli of deformation studies of the foundation and abutments of the Portugues Dam-Puerto Rico'. In: *The 30th US Symposium on Rock Mechanics (USRMS)*. American Rock Mechanics Association.
- Stimpson, B. (1970). 'Modelling materials for engineering rock mechanics'. In: *International Journal of Rock Mechanics and Mining Sciences & Geomechanics Abstracts*. Vol. 7. 1. Elsevier, pp. 77–121.
- Sygała, A., Bukowska, M. and Janoszek, T. (2013). 'High temperature versus geomechanical parameters of selected rocks—the present state of research'. In: *Journal of Sustainable Mining*. Vol. 12. 4. Elsevier, pp. 45–51.

- Tiwari, R. and Rao, K. (2006). 'Post failure behaviour of a rock mass under the influence of triaxial and true triaxial confinement'. In: *Engineering Geology*. Vol. 84. 3-4. Elsevier, pp. 112–129.
- Townend, J. and Zoback, M.D. (2000). 'How faulting keeps the crust strong'. In: *Geology* 28.5, pp. 399–402.
- Trueman, R. and Mawdesley, C. (2003). 'Predicting cave initiation and propagation'. In: *CIM bulletin* 96.1071, pp. 54–59.
- Ulusay, R. (2014). *The ISRM suggested methods for rock characterisation, testing and monitoring: 2007-2014*. Springer.
- Van As, A. and Jeffrey, R. (2000). 'Hydraulic fracturing as a cave inducement technique at Northparkes Mines'. In: The Australian Institute of Mining and Metallurgy, pp. 165–172.
- Van der Pluijm, B.A. and Marshak, S. (2004). *Earth structure: An introduction to structural geology and tectonics*. WW Norton.
- Van Jaarsveld, J.G.S., Van Deventer, J.S.J. and Lukey, G.C. (2002). 'The effect of composition and temperature on the properties of fly ash and kaolinite-based geopolymers'. In: *Chemical Engineering Journal*. Vol. 89. 1-3. Elsevier, pp. 63–73.
- Vekinis, G., Ashby, M.F. and Beaumont, P.W.R. (1993). 'Plaster of Paris as a model material for brittle porous solids'. In: *Journal of Materials Science*. Vol. 28. 12. Springer, pp. 3221–3227.
- Vorobjev, B.M. (1963). *Studies of strata movement and rock pressure on models*. J. Mines Metals. Fuels 11, (10) 1 12, pp. 105–119.
- Vutukuri, V.S., Lama, R.D. and Saluja, S.S. (1974). 'Handbook on mechanical properties of rocks, Volume 1: Clausthal'. In: *Trans Tech Publications*, p. 280.
- Waldeck, H.G. (1979). 'The design and support of large underground chambers at depth in gold mines of the Gold Fields Group of South Africa'. In: *4th ISRM Congress*. Vol. 1. International Society for Rock Mechanics and Rock Engineering, pp. 565–571.
- Wawersik, W.R. and Fairhurst, C.H. (1970). 'A study of brittle rock fracture in laboratory compression experiments'. In: *International Journal of Rock Mechanics and Mining Sciences & Geomechanics Abstracts*. Vol. 7. 5. Elsevier, pp. 561–575.
- Wesseloo, J. (2019). *Private communication via email with Prof. J. Wesseloo*. University of Pretoria, Pretoria, South Africa.

- Wesseloo, J. and Stacey, T.R. (2016). ‘A reconsideration of the extension strain criterion for fracture and failure of rock’. In: *Rock Mechanics and Rock Engineering*. Vol. 49. 12. Springer, pp. 4667–4679.
- West, T.R. (2010). *Geology applied to engineering*. Waveland Press.
- Xu, H., Zhou, W., Xie, R., Da, L., Xiao, C., Shan, Y. and Zhang, H. (2016). ‘Characterization of rock mechanical properties using lab tests and numerical interpretation model of well logs’. In: *Mathematical Problems in Engineering*. Vol. 2016. Article ID 5967159. Hindawi Publishing Corporation, pp. 1–13.
- Yahya, Z., Abdullah, M.M.A.B., Ramli, N.M., Burduhos-Nergis, D.D. and Razak, R.A. (2018). ‘Influence of Kaolin in Fly Ash Based Geopolymer Concrete: Destructive and Non-Destructive Testing’. In: *IOP Conference Series: Materials Science and Engineering*. Vol. 374. 1. IOP Publishing, p. 012068.
- Zhang, H., Zhou, W. and Zhao, C. (2015). ‘The Brittleness Evaluation of Sand and Shale based on the Stress-Strain Curve in Fifth Member of Xujiahe Formation, Xinchang Gas Field, Sichuan Province’. In: *Acta Geologica Sinica-English Edition* 1.89, pp. 433–433.
- Zoback, M.L. and Zoback, M.D. (1989). ‘Tectonic stress field of the continental United States’. In: *Geophysical framework of the continental United States: Geological Society of America Memoir* 172, pp. 523–539.
- Zoback, M.L. and Zoback, M.D. (2002). *State of Stress in the Earth’s Lithosphere. International Handbook of Earthquake and Engineering Seismology, Vol. 81A*. Elsevier Science Publishing Co Inc, pp. 559–568.
- Zoback, M.L. and Zoback, M.D. (2007). *Lithosphere Stress and Deformation. Chapter 6.06 in Treatise on Geophysics, vol. 6, Crust and Lithosphere Dynamics*. Elsevier, pp. 253–273.

A Appendix A

Images of meshed subsets for each significant Brazilian disc test.

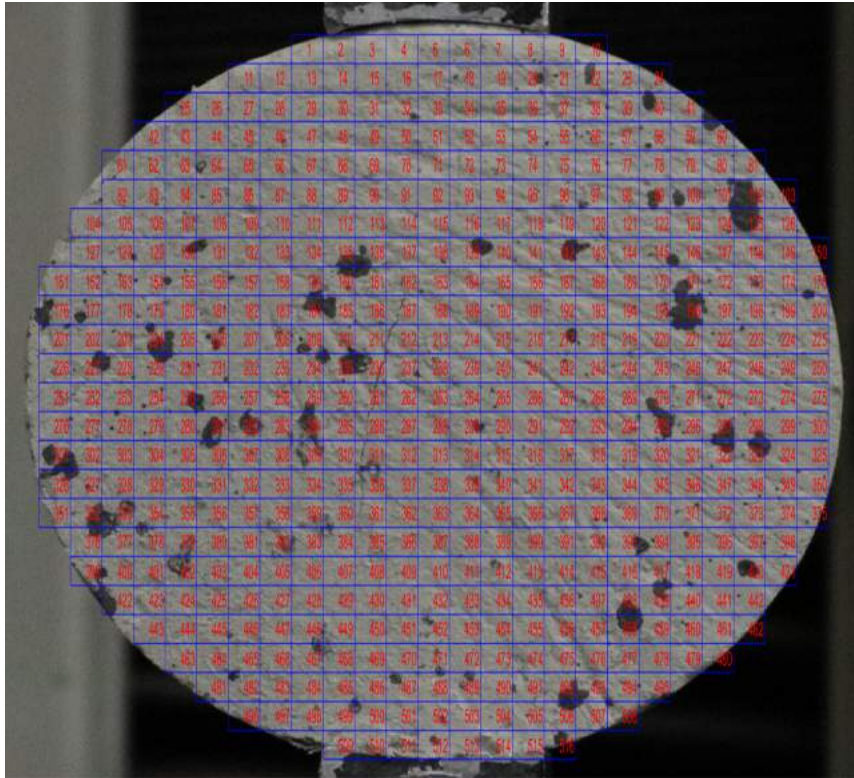


Figure A.1: Post fracture image of Brazilian disc test 3 (with subset mesh)

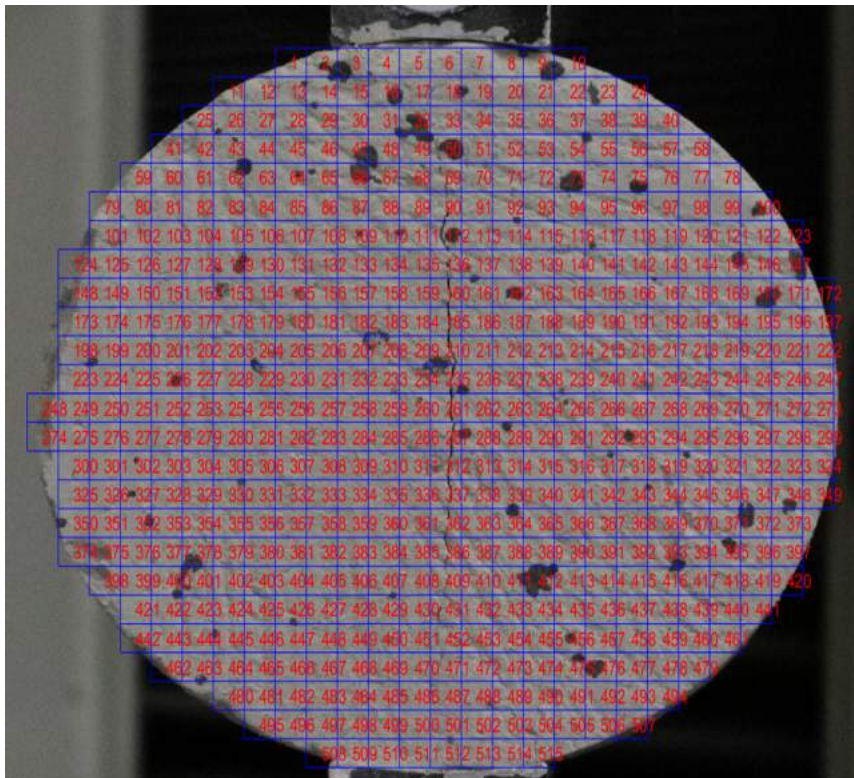


Figure A.2: Post fracture image of Brazilian disc test 4 (with subset mesh).

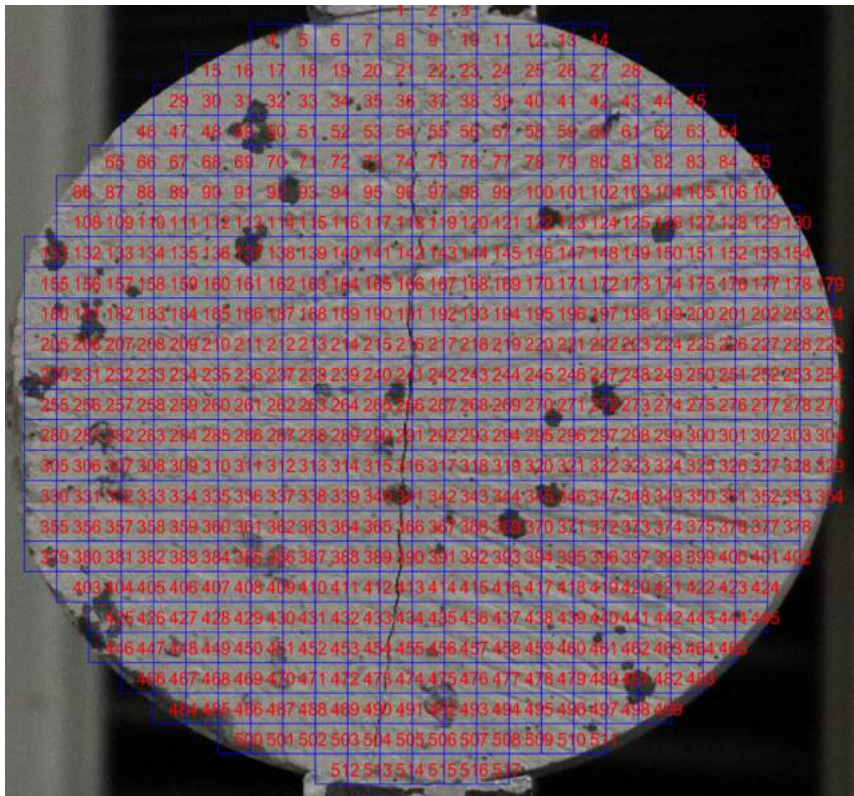


Figure A.3: Post fracture image of Brazilian disc test 5 (with subset mesh).

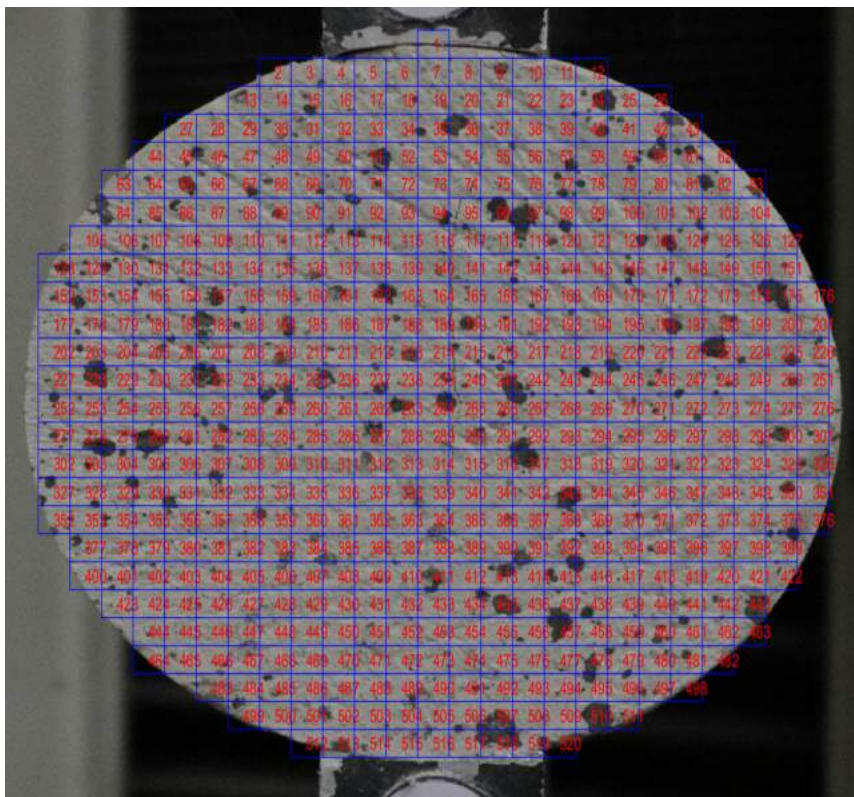


Figure A.4: Post fracture image of Brazilian disc test 7 (with subset mesh).

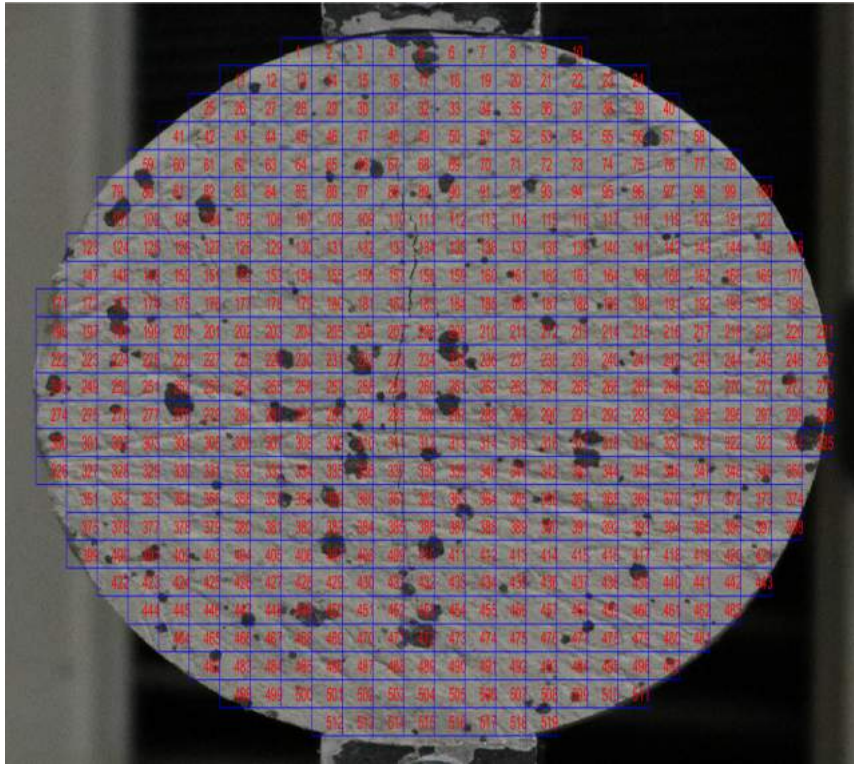


Figure A.5: Post fracture image of Brazilian disc test 11 (with subset mesh).

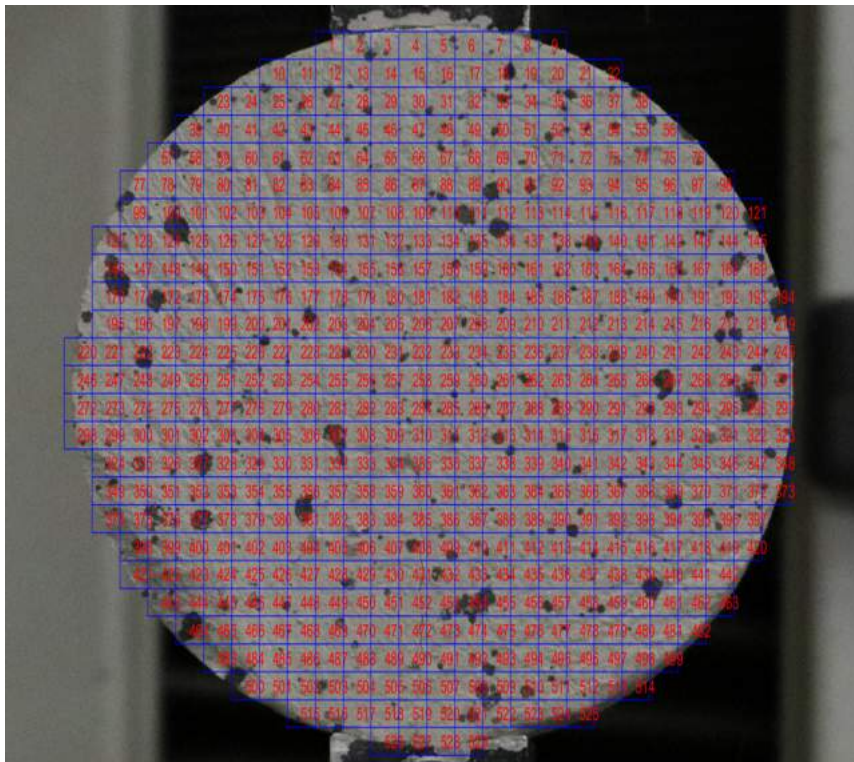


Figure A.6: Post fracture image of Brazilian disc test 13 (with subset mesh).

B Appendix B

The dimensioned Auto-CAD drawings of the test frame and various components which were used for physical modelling in the investigation.

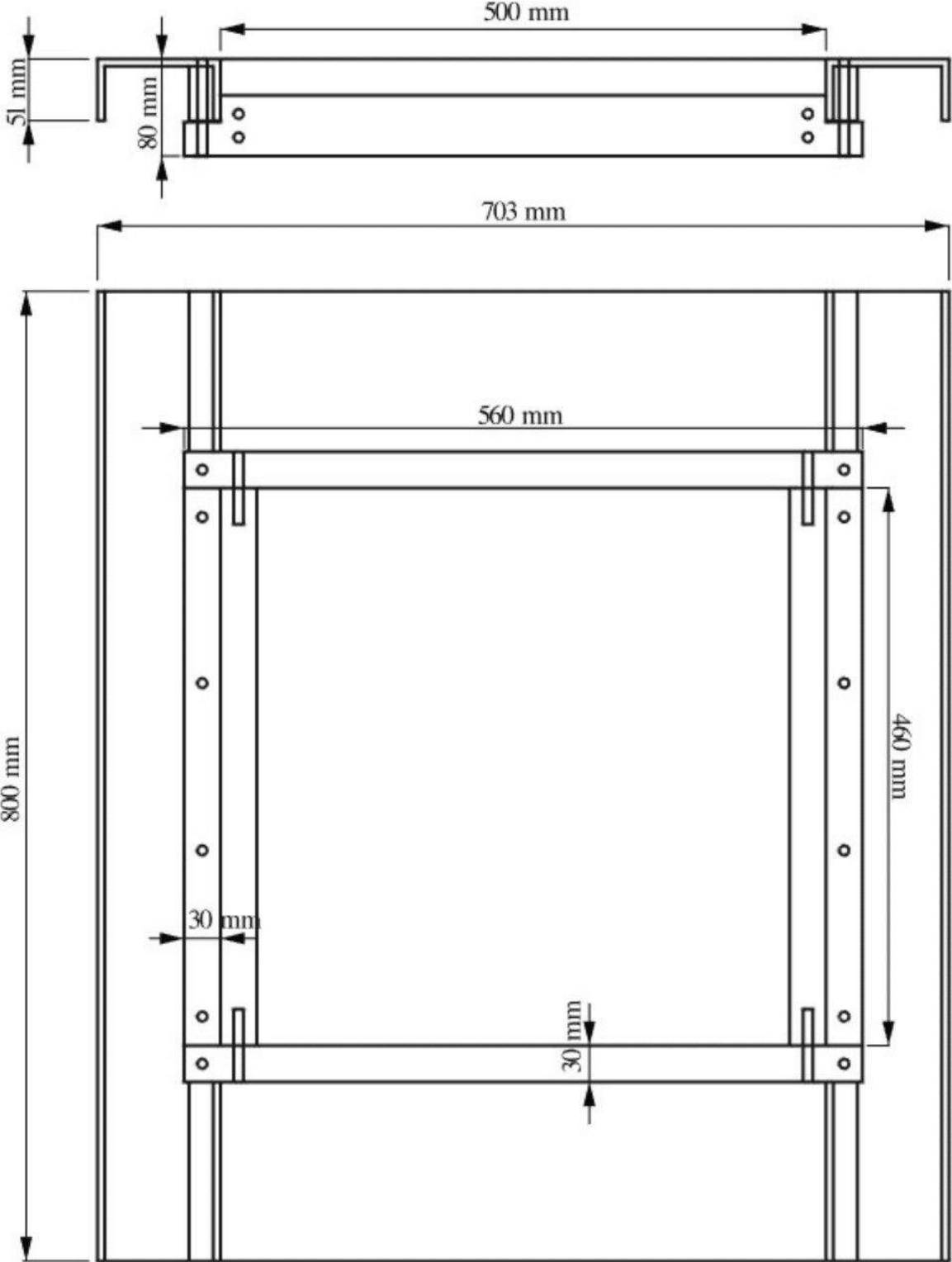


Figure B.1: Dimensioned schematic of the test frame (front window) used in centrifuge testing.



Figure B.2: Dimensioned schematic of the actuators used in centrifuge testing.

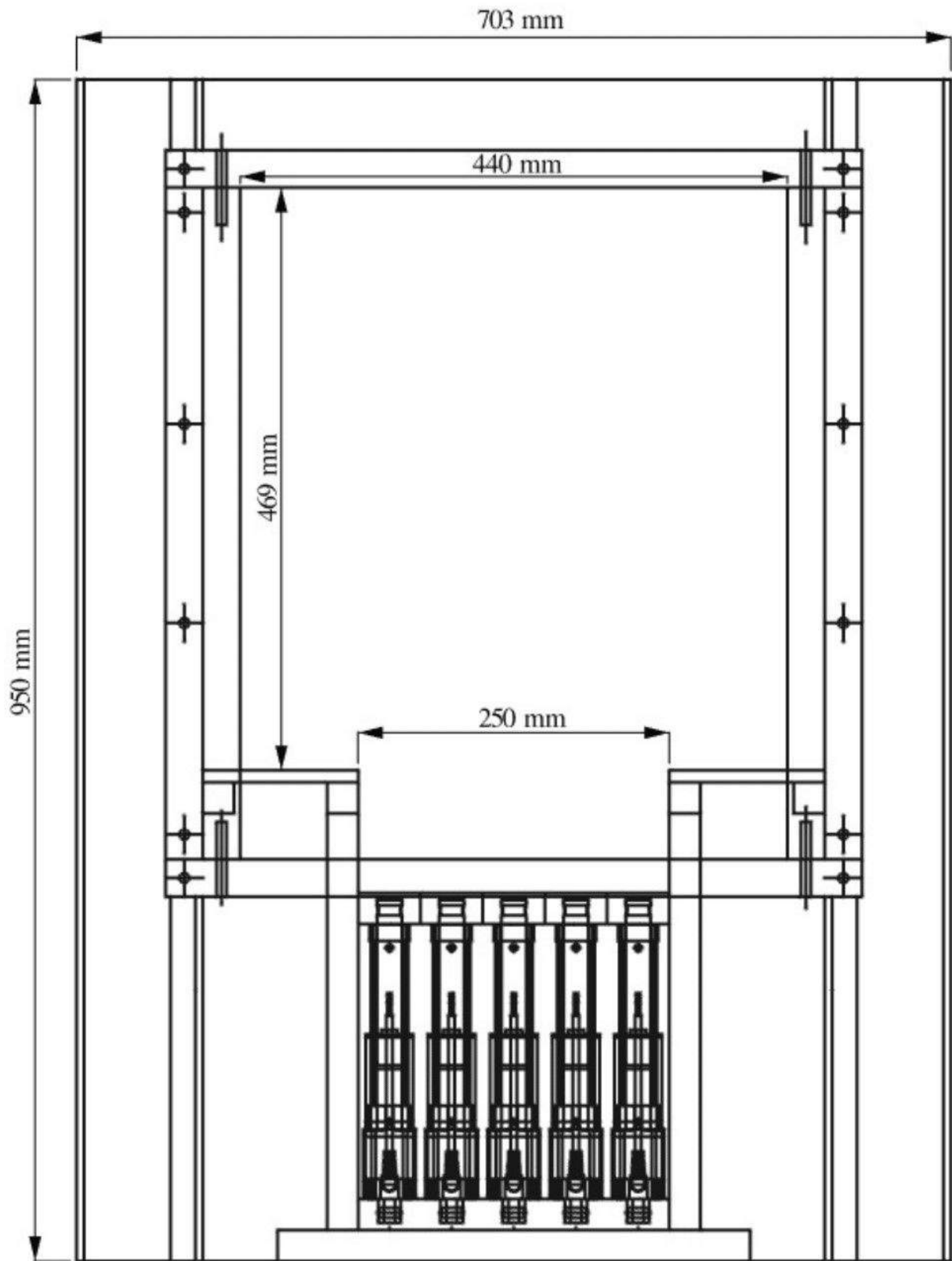


Figure B.3: Dimensioned schematic of the complete test frame used in centrifuge testing.

C Appendix C

The facilities/machines used in the geotechnical laboratory of the University of Pretoria.



Figure C.1: Geotechnical Centrifuge at the University of Pretoria



Figure C.2: Shear Mixer used to manufacture the artificial rock material.

D Appendix D

The superposition of images in overview of cave progression tests are shown for steps 0 to 5 in the following figures. Superimposed surfaces are shown followed by superimposed contours.

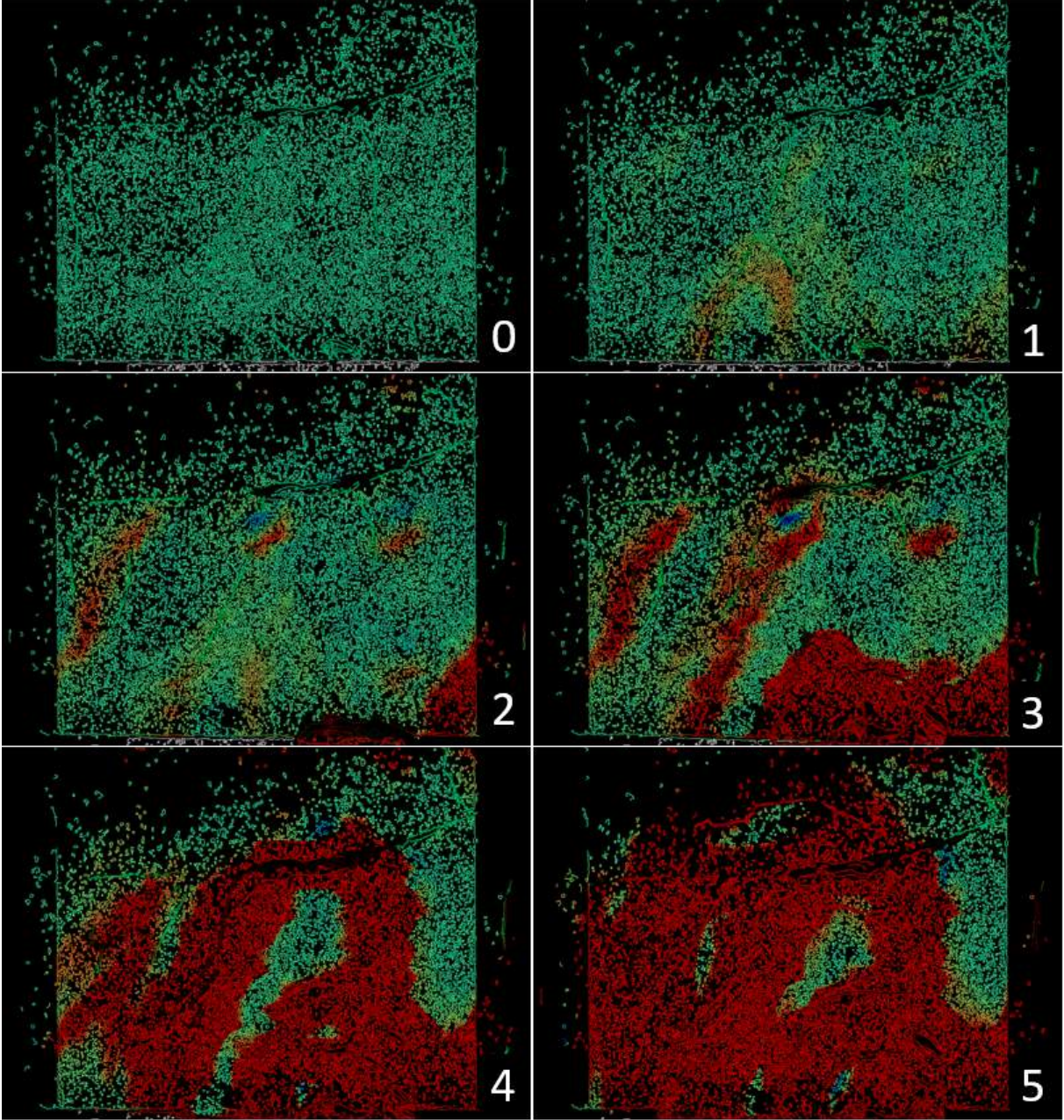


Figure D.1: Superimposed Surface Overview of cave progression test 1 over steps 0-5.

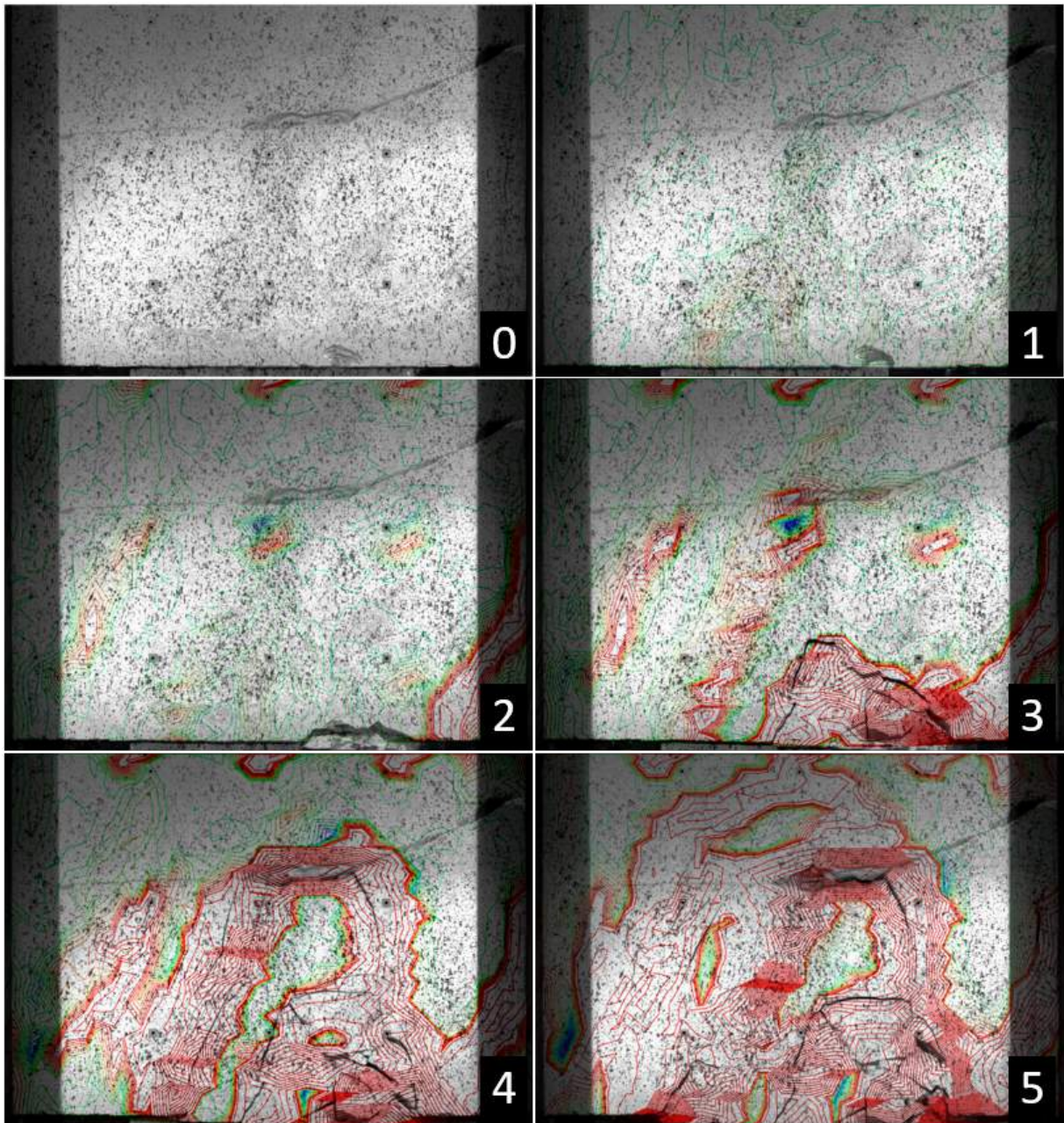


Figure D.2: Superimposed Contour Overview of cave progression test 1 over steps 0–5.

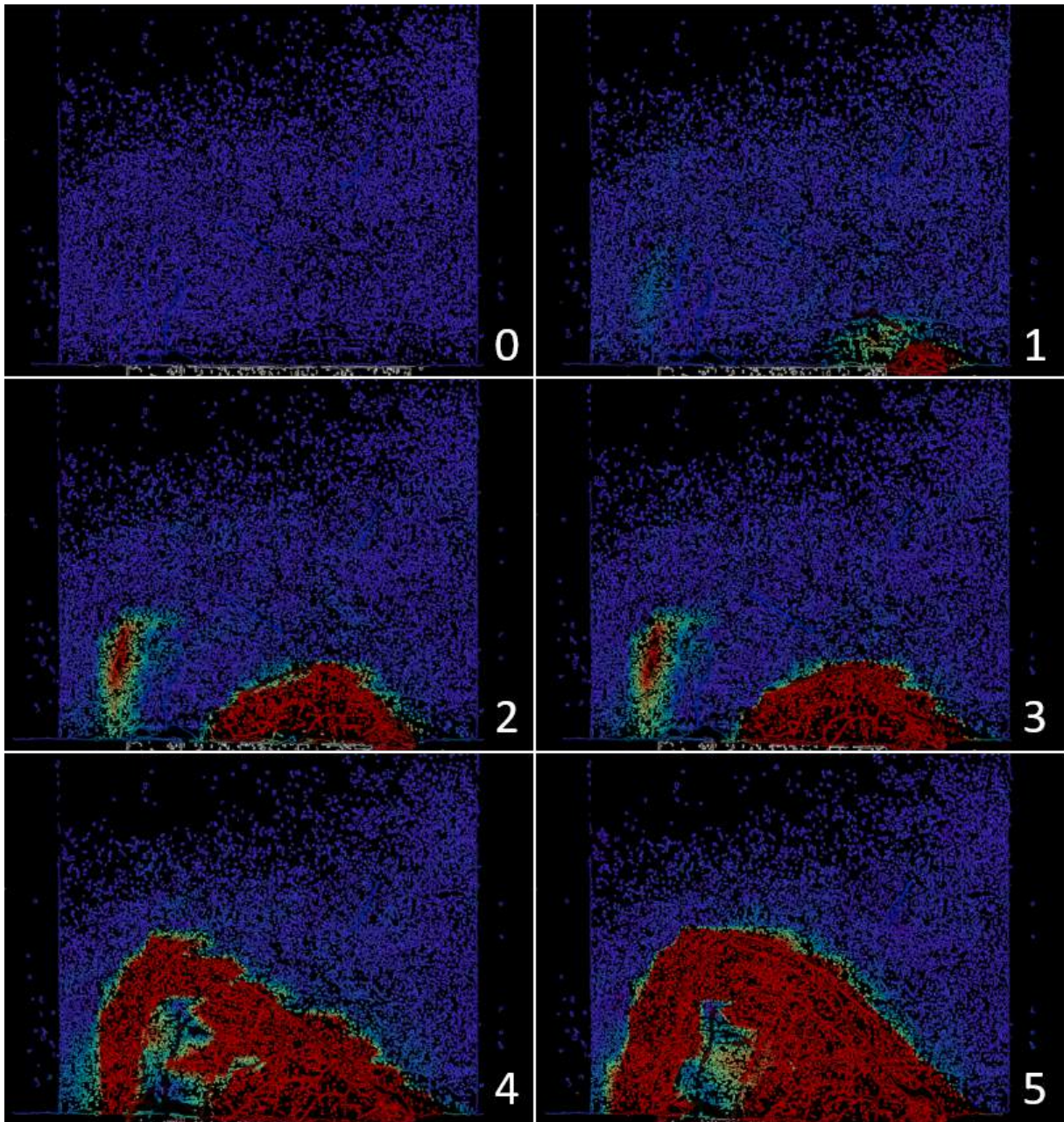


Figure D.3: Superimposed Surface Overview of cave progression test 2 over steps 0-5.

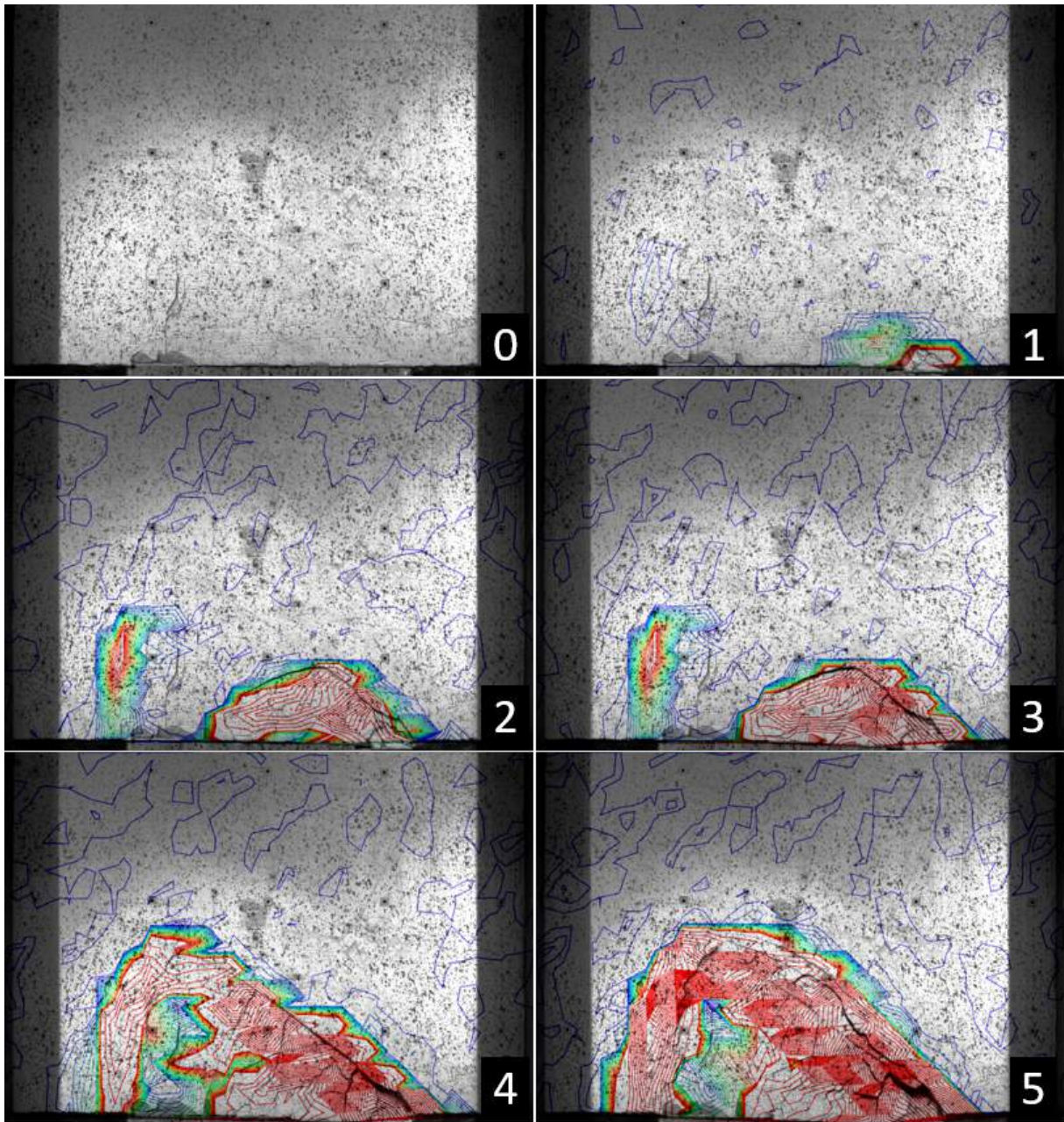


Figure D.4: Superimposed Contour Overview of cave progression test 2 over steps 0–5.

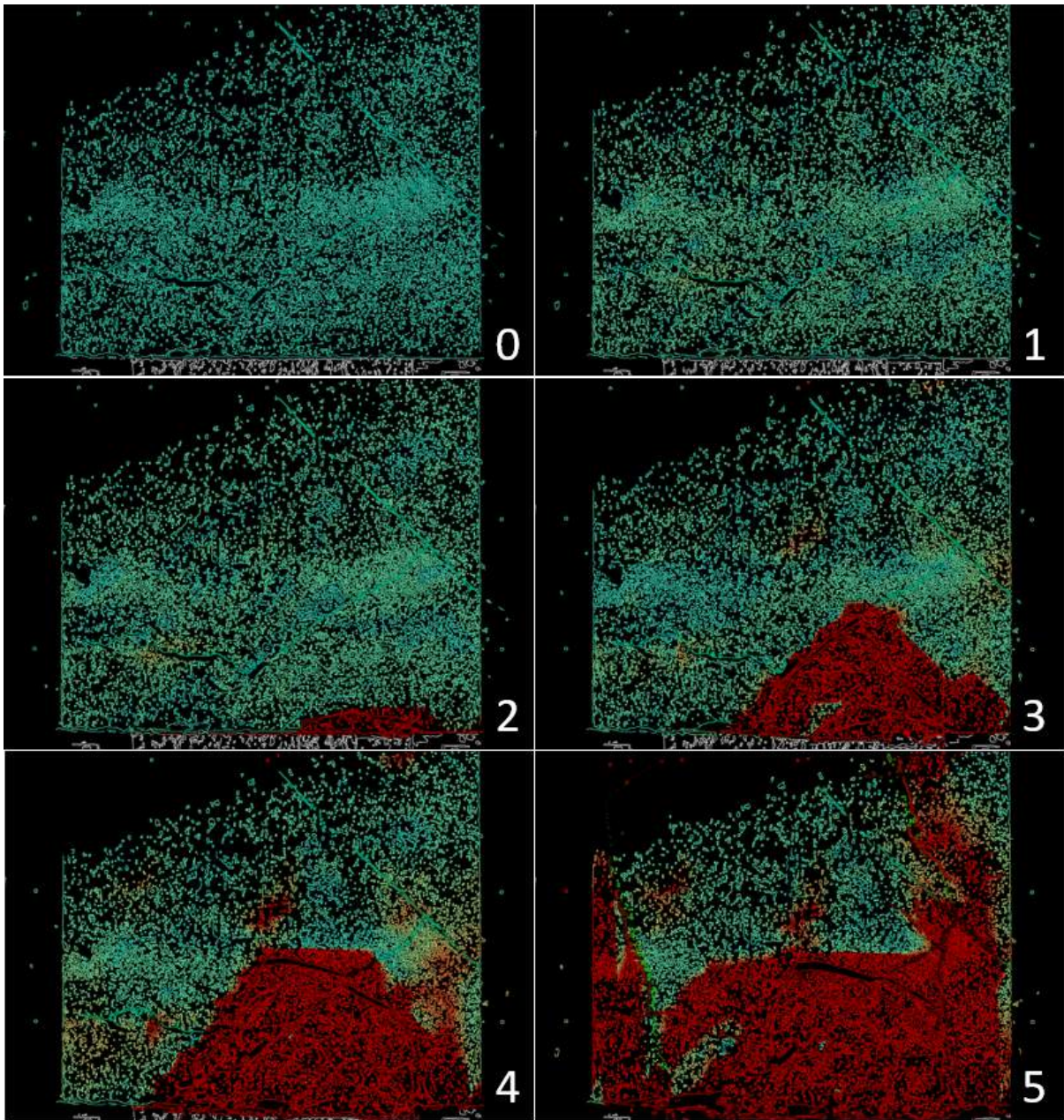


Figure D.5: Superimposed Surface Overview of cave progression test 3 over steps 0–5.

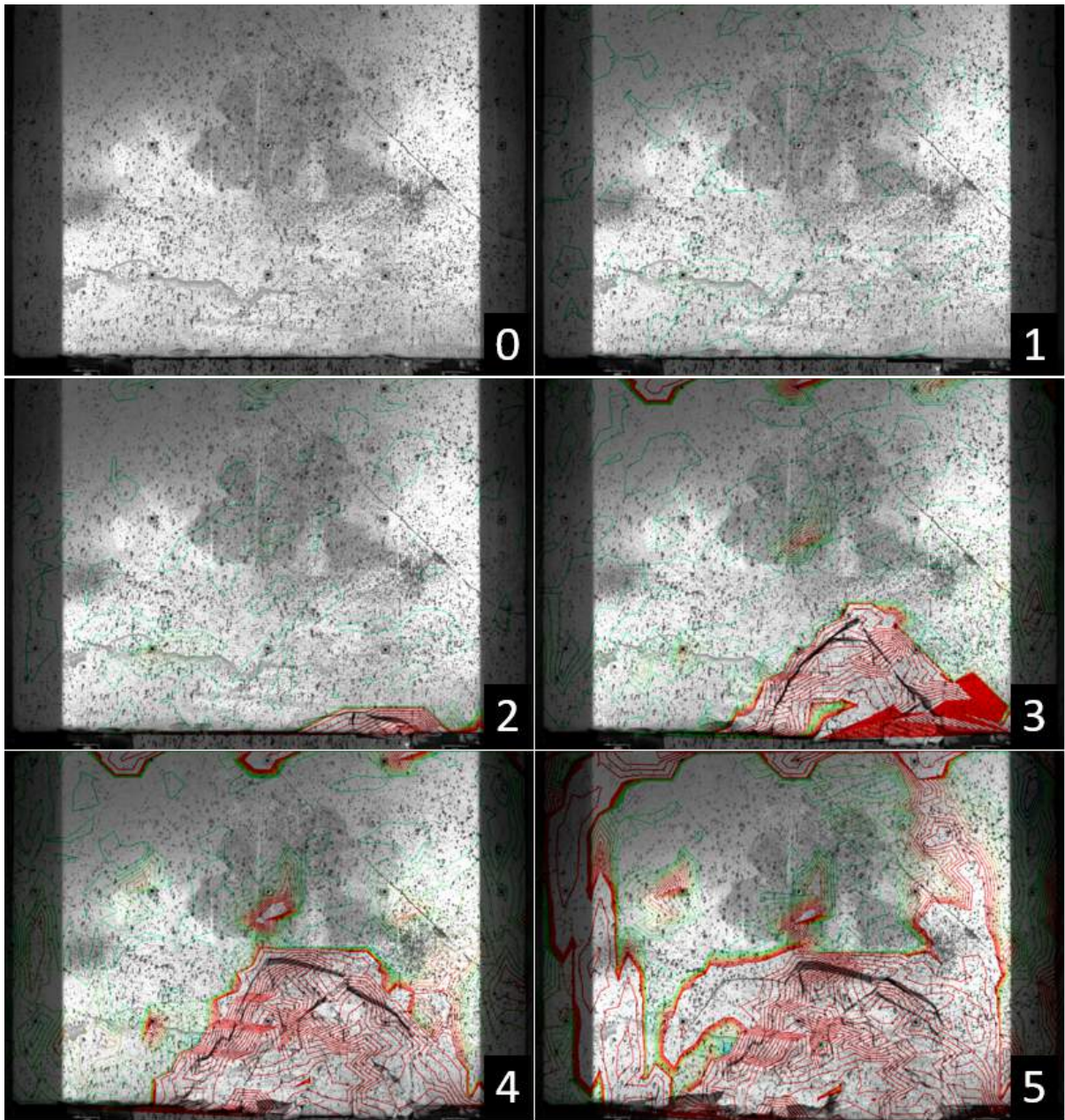


Figure D.6: Superimposed Contour Overview of cave progression test 3 over steps 0–5.

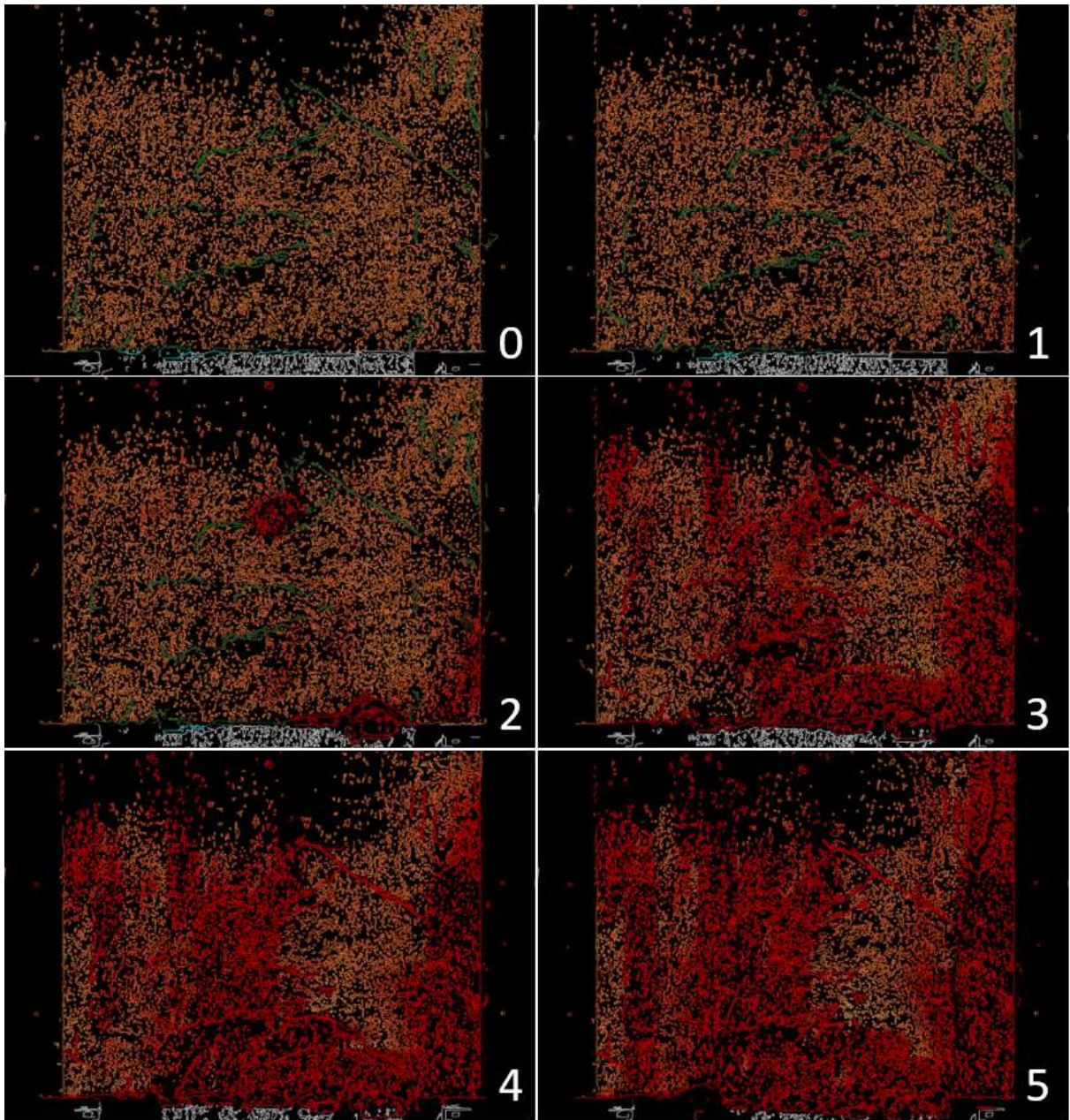


Figure D.7: Superimposed Surface Overview of cave progression test 4 over steps 0-5.

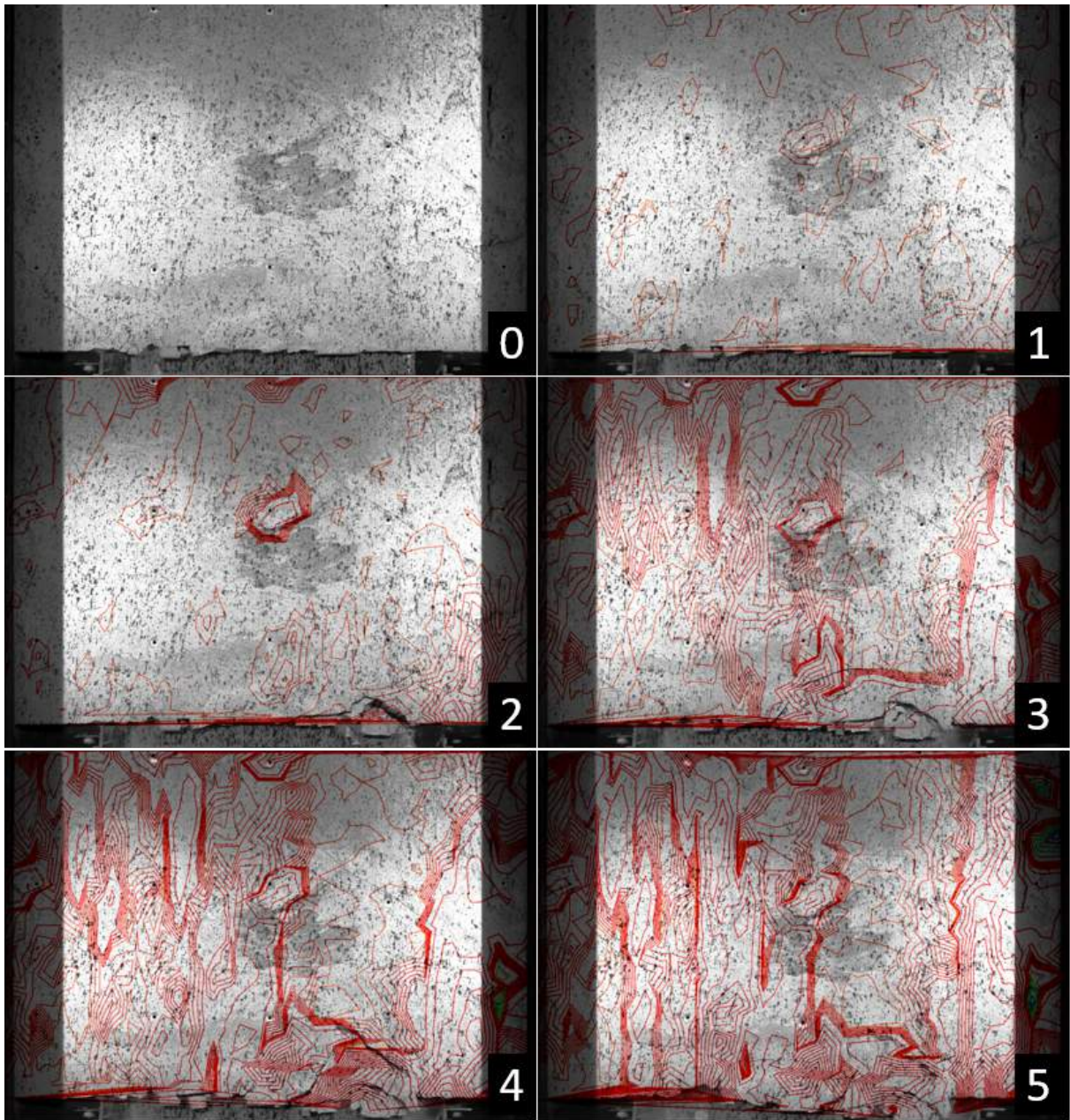


Figure D.8: Superimposed Contour Overview of cave progression test 4 over steps 0–5.